

Lecture Notes on Multidisciplinary Industrial Engineering
Series Editor: J. Paulo Davim

Chenfeng Li
U. Chandrasekhar
Godfrey Onwubolu *Editors*

Advances in Engineering Design and Simulation

Select Proceedings of NIRC 2018

 Springer

Lecture Notes on Multidisciplinary Industrial Engineering

Series Editor

J. Paulo Davim, Department of Mechanical Engineering, University of Aveiro, Aveiro, Portugal

“Lecture Notes on Multidisciplinary Industrial Engineering” publishes special volumes of conferences, workshops and symposia in interdisciplinary topics of interest. Disciplines such as materials science, nanosciences, sustainability science, management sciences, computational sciences, mechanical engineering, industrial engineering, manufacturing, mechatronics, electrical engineering, environmental and civil engineering, chemical engineering, systems engineering and biomedical engineering are covered. Selected and peer-reviewed papers from events in these fields can be considered for publication in this series.

More information about this series at <http://www.springer.com/series/15734>

Chenfeng Li · U. Chandrasekhar ·
Godfrey Onwubolu
Editors

Advances in Engineering Design and Simulation

Select Proceedings of NIRC 2018

 Springer

Editors

Chenfeng Li
Swansea University
Swansea, UK

Godfrey Onwubolu
Sheridan College
Oakville, ON, Canada

U. Chandrasekhar
Vel Tech Dr. RR & Dr. SR Technical
University
Chennai, Tamil Nadu, India

ISSN 2522-5022

ISSN 2522-5030 (electronic)

Lecture Notes on Multidisciplinary Industrial Engineering

ISBN 978-981-13-8467-7

ISBN 978-981-13-8468-4 (eBook)

<https://doi.org/10.1007/978-981-13-8468-4>

© Springer Nature Singapore Pte Ltd. 2020

This work is subject to copyright. All rights are reserved by the Publisher, whether the whole or part of the material is concerned, specifically the rights of translation, reprinting, reuse of illustrations, recitation, broadcasting, reproduction on microfilms or in any other physical way, and transmission or information storage and retrieval, electronic adaptation, computer software, or by similar or dissimilar methodology now known or hereafter developed.

The use of general descriptive names, registered names, trademarks, service marks, etc. in this publication does not imply, even in the absence of a specific statement, that such names are exempt from the relevant protective laws and regulations and therefore free for general use.

The publisher, the authors and the editors are safe to assume that the advice and information in this book are believed to be true and accurate at the date of publication. Neither the publisher nor the authors or the editors give a warranty, expressed or implied, with respect to the material contained herein or for any errors or omissions that may have been made. The publisher remains neutral with regard to jurisdictional claims in published maps and institutional affiliations.

This Springer imprint is published by the registered company Springer Nature Singapore Pte Ltd. The registered company address is: 152 Beach Road, #21-01/04 Gateway East, Singapore 189721, Singapore

Preface

With the impact of digitization on every stage of product development starting from conceptualization till realization, the role of engineering analysis and simulation has become more prominent than ever before. While the analysis tools have become more and more versatile, high power computation has become ubiquitous, thus enhancing the penetration and reach of engineering simulation to most of the sectors. This phenomenon is readily visible in high-technology sectors like aerospace, defense, automotive, biotechnology, and energy as the thrust on making the products lighter, smarter, and more efficient is ever present. Even in sectors like consumer goods, manufacturing, and tooling, the tendency to use simulation tools is increasing due to not only technological demands but also market needs. The conference conducted by NAFEMS has served as an inspiring platform for greater exchange and learning, deepening of technological abilities engineering analysis, synergistic utilization of resources, and partnership development. This proceedings is an effort to encapsulate these interactions and presents in a form that could potentially serve the needs of future practitioners. The diversity of practices and depth of coverage is reflected in the selected articles that typify the comprehensive use of finite element methods and computational fluid dynamics for simulating the operational conditions and providing useful input to the product development efforts. It is inferred that in the current industrial scenario wherein humongous amount of data is being generated through sensors and readily transmitted through networks, the synergistic use of data sciences, AI, and machine learning in tandem with engineering analysis would greatly aid the upkeep of the infrastructure and aid superior utilization.

Swansea, UK
Chennai, India
Oakville, Canada

Chenfeng Li
U. Chandrasekhar
Godfrey Onwubolu

Contents

1	Optimization for Position of Heat Loop in Refrigerator Using Steady-State Thermal Analysis	1
	Pushpendra Mahajan, Arunachalam Nagarajan and Vishal Marathe	
2	Refrigerator Structural Stability Analysis and Correlation	17
	Vikram Suriyanarayanan, Arunachalam Nagarajan, Mike Fiori, Pushpendra Mahajan and Aditya Nalwade	
3	Thermomechanical Analysis of a Cylindrical Liner	33
	Subhadip Roy, N. Ganesh, A. Kumarasamy and P. Viswanathan	
4	Mathematical Model for Built-in Dishwasher to Study Door Open and Close Forces and Sealing with Monte Carlo Simulations	41
	Krishna Chaitanya Kusupudi, Amit Mandal and Deeptiranjana Barik	
5	Numerical Simulation of Electric-Bus Windshield Demisting in Winter Conditions	53
	Bharat Kumar Nuthi, S. Vijayaraghavan and D. Govindaraj	
6	Simulation of a Screw Self-tapping Process	61
	Kushagr Goyal, Sivaraman Rajan, Harish Krishnamurthy and Ravindra Venkataramu	
7	Washing Machine Outlet Hose Analysis in Full Water Condition	71
	Changadevkumar Desai, Sushilkumar Vishwakarma and Pavol Vasko	
8	Performance Study of a Twisted Vaned Diffuser in a Compressor Stage	81
	Venkateswara Rao Pothuri, Venkata Ramana Murthy Govindaraju, Amogh Baraar and C. Pradeep Reddy	

9	Computational Study on the Effect of Aft-Body Attachments on Base Drag Using Locked Vortex Flow Management Technique	97
	Thippeswamy Sanjitha, Kailas S. Jagtap, Karthik Sundararaj, Prakash S. Kulkarni, Manoj Veetil, Arun Mallappa Bagewadi, Syed Sameer Mujaawar and Kothnur Narayanaswamy Ramyashree	
10	Reconstruction of Femur Bone from DICOM Files and FEA on Fractured Human Femur Bone with PEEK Thermoplastic Prosthetic Plate Implantation	109
	S. Kirthana and Mohammed Khaja Nizamuddin	
11	Numerical Simulation of Electrical Operated Mechanism Considering Impact Force	121
	Abhimanyu Kumar Singh, Parkash Kumar and Mahesh Ranade	
12	Vibrational Study of Labyrinth Seals for Turbomachines	133
	S. M. Sanjay kumar and C. Suresh	
13	Refrigerant Gas Leakage in ISO Room: A Comparative CFD Study	147
	Sangamesh Hosur, Sachin Kumar Rai and Mahmood Tabaddor	
14	Forced Vibration Harmonic Response Analysis of Semi-mobile Crusher Station	157
	Shanmugam Perumal, Raghunathan Swaminathan and Mike Christensen	
15	Comparative Study of Material Approximation Methods for Fatigue Life Prediction of Steels, Aluminum and Titanium . . .	171
	Majnoo M. Gawture and Tanmay Tamhane	
16	Recurrence Perspective of Forces Generated by Flapping Wing Under Different Frontal Inflow Conditions	197
	M. De Manabendra, J. S. Mathur and S. Vengadesan	
17	Convergence Studies in the Finite Element Analysis of CFRP Shaft Under Torsion Using Shell281, Shell181, and Comparison with Analytical Results	219
	Akshay Kumar and H. K. Rangavittal	
18	Testing a Fire Door Through Simulation	233
	Amita Tripathi, Chenthil Kumar, Thomas Grinnaert and Anil Kumar	
19	Modeling of Aircraft Arresting Gear System by Multibody Dynamics Approach and Co-Simulation of Multibody Dynamics With Hydraulic System Using Adams and Easy5	249
	S. Mohan Raju, H. G. Manjunath, Naveen Narayan and C. Ganga Reddy	

20 Design and Optimization of Knuckle of an All-Terrain Vehicle 263
 Aditya Kulkarni, Aditi Bang, Akanksha Hundekari, B. G. Akshata, Arun Y. Patil and B. B. Kotturshettar

21 Modeling and Analysis of ATV Roll Cage 281
 A. S. Shridhar, Abhilash Tukkar, Akshay Vernekar, Vinod Badderu, Arun Y. Patil and Basavaraj B. Kotturshettar

22 Computational Flow Analysis of a Blade Wedge Duct 293
 K. R. Deepthi and S. Shankar

23 Computational Fluid Dynamic Analysis of Amphibious Vehicle 303
 H. Jaouad, P. Vikram, E. Balasubramanian and G. Surendar

24 Finite Element Analysis of Amphibian UAV Structure 315
 Ting Kee Sheng, Balasubramanian Esakki and Arunkumar Ponnambalam

25 Investigation of 3D Printed Jet Fuel Atomizer 325
 Raja Marudhappan, U. Chandrasekhar and K. Hemachandra Reddy

About the Editors

Dr. Chenfeng Li obtained his PhD in computational engineering (Swansea University), Masters in solid mechanics (Tsinghua University), and his Bachelors in engineering mechanics (Tsinghua University). Since 2013, he has been working as an associate professor at the Civil & Computational Engineering department, College of Engineering at Swansea University. His research is largely centered around computational science and engineering, with a special focus on stochastic modeling and its applications in energy, environmental and biomedical engineering; and physical modeling for graphics applications. He develops novel probabilistic models that allow accurate quantitative measurement and description of various practical random media that are non-Gaussian, non-stationary and nonlinear. Dr. Chenfeng also develops efficient numerical simulation techniques that can analyze and evaluate the uncertainty propagation through complex physical and engineering systems, which can guide the associated risk assessment and management.

Dr. U. Chandrasekhar is a scientist and academician with more than three decades of experience in research and project management. He received his bachelors from NIT Surathkal, Karnataka, and his masters from IIT Madras in mechanical engineering. He received his PhD from VTU for his research in additive manufacturing carried out at the Defense Research and Development Organisation (DRDO). He also hold an advanced diploma in management. Currently, he is the pro Vice-Chancellor of Vel Tech University. His areas of research include mechanical analysis of aero gas turbine engine modules, additive manufacturing, micro aerial vehicles, and sensors for harsh environments. He received a Gold Medal from the former President of India Dr. APJ Abdul Kalam for his academic achievements. After serving the Ministry of Defence in several capacities, he became Additional Director, DRDO in 2010. He set up India's first-ever rapid prototyping laboratory at GTRE, Bangalore. During his tenure at DRDO, he carried

out several technology development projects and also led a senior group of scientists in Moscow during the testing phase of a developmental aero gas turbine engine. He received commendation medal from the Scientific Advisor to the Defence Minister in recognition of his contributions to rapid prototyping of complex aeronautical systems.

Dr. Godfrey Onwubolu holds a Bachelors in engineering (University of Benin), a Masters in mechanical engineering (Aston University), and a PhD in computer-aided design (Aston University). He is internationally recognized for his work in inductive modeling, especially in Europe, where he gives public lectures and examines doctoral theses on the subject. He is currently the lead researcher at Sheridan College in applying this technology to the joint Sheridan-Nexflow project for studying the behaviours of Nexflow air products based on their operational parameters. He continues to use his expertise in the domains of computer-aided design, additive manufacturing, and inductive modeling to impart knowledge to students as an engineering and technology educator, and to advance productivity in the manufacturing industry sector in Canada and other countries.

Chapter 1

Optimization for Position of Heat Loop in Refrigerator Using Steady-State Thermal Analysis



Pushpendra Mahajan, Arunachalam Nagarajan and Vishal Marathe

Abstract Heat loop is an integral part of the household refrigerator, which helps to avoid external condensation on the refrigerator but also increases its energy consumption. Hence, heat loop position inside foam needs to be carefully chosen to provide an optimum trade-off between the robustness of refrigerator to external condensation and minimum energy consumption. The present study aims to develop a simulation methodology for the selection of heat loop position which gives minimum energy consumption and maximum robustness for external condensation. Optimization problem definition discussed in the study led to the creation of full factorial design of experiment (DoE) setup which is solved using the finite element methods. The output from full factorial design of experiment is utilized to perform sensitivity analysis and trade-off analysis to find the optimum heat loop position. The work thus helps to have a systematic and optimum selection of input parameters so as to predict and design the refrigerator with desired attributes.

Keywords Refrigerator · External condensation · Heat gain · Energy · Optimization · Sensitivity

Nomenclature

E	Energy consumption (dimensionless since this is considered as ratio in current study)
R	Robustness to external condensation (dimensionless)
T_{ambient}	Ambient temperature of air ($^{\circ}\text{C}$)
T_{dp}	Dew point temperature ($^{\circ}\text{C}$)
RH	Relative humidity (dimensionless)
T_{H}	Temperature of refrigerant in heat loop ($^{\circ}\text{C}$)
T_{I}	Inside temperature in refrigerator ($^{\circ}\text{C}$)

P. Mahajan (✉) · A. Nagarajan · V. Marathe
Global Technology and Engineering Centre, Whirlpool of India Ltd., Pune, India
e-mail: pushpendra_p_mahajan@whirlpool.com

© Springer Nature Singapore Pte Ltd. 2020
C. Li et al. (eds.), *Advances in Engineering Design and Simulation*,
Lecture Notes on Multidisciplinary Industrial Engineering,
https://doi.org/10.1007/978-981-13-8468-4_1

T_A	External temperature on refrigerator surfaces ($^{\circ}\text{C}$)
x, y	Decision variables representing heat loop coordinates (position) (m)
U_x	Upper bound for x -values (m)
U_y	Upper bound for y -values (m)
L_x	Lower bound for x -values (m)
L_y	Lower bound for y -values (m)
q	Heat flux (W)
h	Convection coefficient ($\text{W}/\text{m}^2\text{-}^{\circ}\text{C}$)
A	Surface area (m^2)
T_{surface}	Surface temperature ($^{\circ}\text{C}$)

1.1 Introduction

A refrigerator is a household appliance that comprises a compartment which is thermally insulated and transfers heat from the items placed inside the compartment to the external environment [1]. This ensures that the temperature of items placed in the refrigerator is maintained below the external ambient temperature [1]. The foam which is popular insulation acts as a thermal barrier to heat flow due to very low thermal conductivity which is in the range of 0.01–0.05 W/m-K [2]. Cooling effect inside the refrigerator is provided by the continuous flow of refrigerant in the refrigerator tubes. Refrigerant follows vapor compression cycle to absorb the heat from refrigerator space (evaporator) and dissipate the heat to the atmosphere using a heat exchanger (condenser) [3]. Generally, the refrigerator comprises two basic compartments such as freezer and refrigeration section. Flow and compression of refrigerant and operation of auxiliary components like motor, fan, and lighting require energy that is supplied in the form of electrical energy. Energy consumption is an important attribute and sales feature in the cost competitive appliances industry [4]. Use of finite element analysis (FEA) to predict and optimize the energy consumption of the refrigerator is widespread in the appliances industry [4].

As a known fact, dew point temperature is the temperature at which water vapor in the air at constant pressure begins to condense into water [5]. Further, the rate of condensation is equal to the rate of evaporation of water vapor at the dew point temperature. When the ambient temperature is equal to or below the dew point, condensation occurs. This means that water vapor in the air gets converted to water and appears as dew drops on surfaces [5]. Since the refrigerator has a larger temperature difference between the inner surface and the ambient, there is a possibility that the external surface temperature of the refrigerator may drop below ambient air temperature. Freezer section in the refrigerator is affected more than the refrigeration section as the freezer section has to be maintained at a lower temperature with approximately -18°C , whereas the refrigeration section is maintained at 5°C . Since the temperature difference between ambient and freezer section is higher as compared to the refrigeration section, utmost care has to be taken while designing. In such a scenario, ambient air flowing over the refrigerator external surfaces gets cooled. If

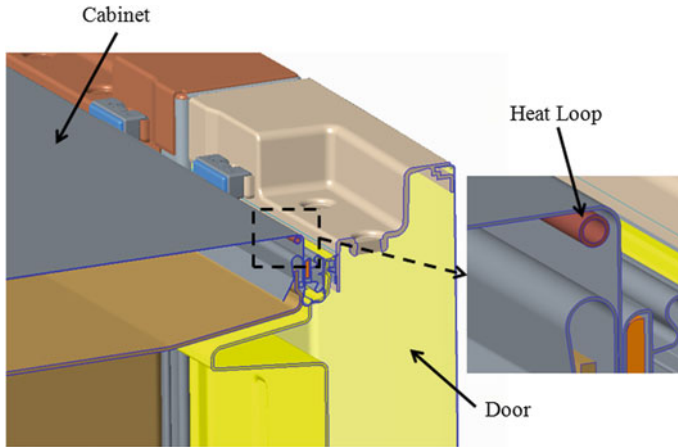


Fig. 1.1 Heat loop position

the temperature of air falls below dew point temperature, it will result in condensation of water vapor on the refrigerator surface. This leads to accumulation of a pool of water droplets on the refrigerator surface and is commonly termed as external condensation in the appliances industry. External condensation hampers perceived the quality of refrigerator and impacts aesthetics. Heat loop in the refrigerator plays a vital role to avoid external condensation.

Refrigerator normally has compressor and condenser at the rear side. These components are at significantly higher temperatures as compared to ambient. Hence, the external surfaces of refrigerator adjoining to these components (rear surfaces) are hotter than ambient air. Front flange is the outside surface of the refrigerator cabinet which is adjoining to the gasket. Since it is close to gasket interface and far from rear surfaces of the cabinet, the front flange is prone to condensation. Heat loop is a tube made of steel or copper and contains warm refrigerant that exits from the condenser. Heat loop is routed behind the front flange. Hence, it allows the front flange portion of the refrigerator to be warm. Heating the flange is considered necessary to prevent condensation in high humidity environment [4]. Figure 1.1 shows the position of heat loop in the refrigerator. It is an in the foamed part where foam helps to maintain its position and shape. Heat loop thus increases the robustness of refrigerator to external condensation. A lot of effort has gone into heat loop joint technique with condenser, whereas the impact of heat loop position on refrigerator energy consumption is still an un-researched area [4].

Heat loop acts as heat producing source inside the insulation and thus allows the flow of some heat into the refrigerator interior area. It thus increases the temperature of the refrigerator interior area and compels the refrigerator to consume more energy to maintain the cooler temperature [4]. Thus, the heat loop tube helps to avoid external condensation but at the same time increases energy consumption. Amount of heat leak to the refrigerator interior area depends on the heat loop position inside the

foam. This demands a detailed study for heat loop position inside the foam and analysis to obtain an optimum trade-off between external condensation and energy consumption. Thus, various heat loop positions have to be analyzed, and the optimum position needs to be selected. The work thus intends to study the impact of variation in heat loop position on robustness to external condensation and energy consumption.

1.2 Methodology

This section presents the strategy adopted to achieve the optimization of heat loop position. Schematic of the proposed strategy is shown in Fig. 1.2. Proposed strategy includes two distinct methodologies named as Simulator and Optimizer integrated to achieve an optimum position of heat loop. The Simulator comprises FEA model, and Optimizer comprises design of experiments (DoE)-based optimization technique.

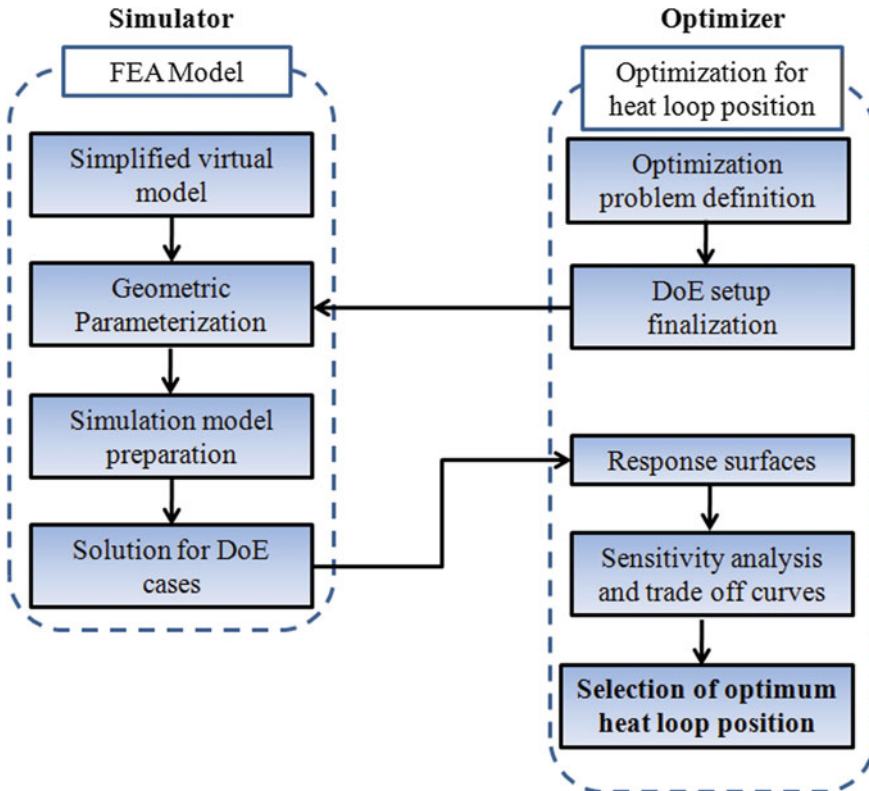


Fig. 1.2 Schematic for proposed strategy

The study is performed using steady-state thermal analysis. The building of the FEA model starts with the simplification of the 3D CAD model. In the present work, the heat loop region is considered. As shown, geometric parameterization is the next step in the FEA model. Herein, the decision variables which are chosen for DoE setup are parameterized in the simulation tool. By parameterization, we mean that the chosen decision variables along with their levels should be defined in the simulation environment so that they can be dynamically varied by the simulation solver to generate DoE results. This step requires the input of detailed DoE setup which comes from the Optimizer methodology.

Geometric parameterization from Simulator and DoE setup finalization from Optimizer work in parallel with each other. Optimizer starts with the definition of the optimization problem which includes the objective function, constraints, and decision variables. The range of decision variables is a vital part that has to be considered. Once the optimization problem is defined, we can now define the DoE setup. DoE setup contains the number of cases to be run and details of each case. This input needs to be passed on to geometric parameterization. Simulation model with boundary conditions, loads, and mesh details needs to be defined in simulation software. Next step consists of solving the FEA model to generate results for DoE cases.

Some common surfaces (response surfaces) should be chosen in the solved FEA model to generate results for energy consumption and robustness to external condensation. These results can be then further analyzed using statistical or mathematical tools such as sensitivity analysis and trade-off plots. Sensitivity analysis helps us to understand the effect of each decision variable. Trade-off plots help us overlap the energy consumption and external condensation results in order to analyze the optimum heat loop position. The above-proposed strategy provides a systematic way of performing DoE-based optimization work.

1.3 Modeling Strategy

1.3.1 Assumptions

1. The refrigerant temperature that has just exited the condenser is assumed in the range of 35–45 °C.
2. Freezer section temperature is assumed as –18 °C.
3. The ambient temperature of outside air is assumed in the range of 25–40 °C.
4. Considering the worst humidity values of coastal belts and high rainfall zones, the relative humidity of 80% is assumed in the study.
5. Dew point temperature is calculated using the ambient air temperature of 32 °C by approximation given below in Eq. 1.1 [6]:

$$T_{dp} = T_{ambient} - \left(\frac{100 - RH}{5} \right) \quad (1.1)$$

1.3.2 Modeling Approach

A sectional simulation model of depth 10 mm in the heat loop region is considered as shown in Fig. 1.3. Length and width of the section are chosen so as to adequately capture the heat loop region along with gasket interface. The sectional model considered has dimensions of $150 \times 100 \times 10$ mm. Figure 1.3 shows the detail of the simulation model considered. External condensation situation is more likely to occur on freezer doors. Hence, it is advisable to consider the heat loop in freezer door region for analysis. Also, heat loop is present behind the front flange of the cabinet, and hence, its impact is also limited on to the front flange region. Generally, dimensions and boundary conditions in the heat loop region are uniform across the profile of the cabinet and door. Hence, energy consumption value obtained for small depth section can easily be extrapolated for a total profile of cabinet and door. Also, the temperature gradient plot obtained for small depth sectional models can be used to understand temperature distribution across the profile.

As shown in Fig. 1.3, parts considered for analysis are cabinet assembly, door assembly, gasket, trapped air and heat loop along with the refrigerant. Cabinet assembly and door assembly each consists of steel wrapper, plastic liner, and foam. Foam is constructed using volume extraction between wrapper and liner in CAD software. Similarly, trapped air inside gasket and refrigerant inside heat loop are also constructed using volume extraction. In order to avoid the complexity of contact

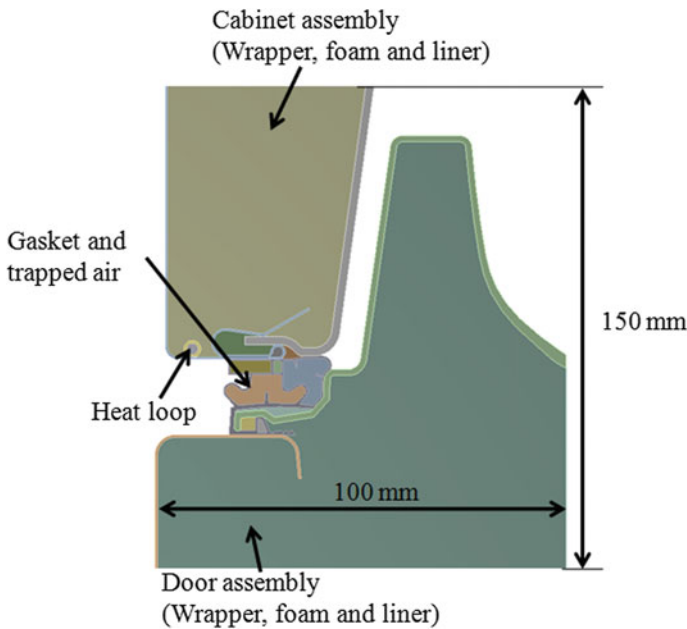


Fig. 1.3 Details of the simulation model

algorithms, multibody single-part approach is followed using ANSYS software. In this approach, we merge all the bodies inside a single part. Bodies inside the part can be applied different material properties and mesh properties. Material properties are determined using experimental investigations.

With the single-part multibody approach, care is taken to ensure mesh connectivity across bodies. Mesh connectivity is thoroughly checked while meshing the part. All the bodies are meshed with solid elements. Mesh used consists of linear tetrahedral elements with nodal degrees of freedom (DoF) of 1. Soft element sizing of 2×10^{-3} m is applied for all bodies to adequately capture intricate shapes and contours. Figure 1.4 shows the meshed model used in the analysis.

Mesh size suitable for the model is determined by the grid independence test. This test is performed by successively reducing the mesh size until we see a negligible divergence between successive iterations. Allowable or targeted divergence value in this test is taken as 0.5%. Results for this test are mentioned in Table 1.1. The table shows that, a mesh size of 2 mm, the divergence between successive mesh sizes is 0.32%. Thus, we can say that results are independent of mesh size at 2 mm element size. Hence, a mesh size of 2 mm is used in the analysis. Actual heat gain values cannot be disclosed here. Hence, the values in the table are in relative terms.

Boundary conditions used in the FEA model are shown in Fig. 1.5. The refrigerant that exits from the condenser is at a fixed temperature, T_H °C. Hence, a fixed temperature boundary condition of T_H °C is applied to the refrigerant body. T_H varies in the range of 35–45 °C. All the nodes of the refrigerant body are maintained at a fixed temperature during runtime on account of this boundary condition. External surfaces of the cabinet and door that are exposed to ambient air are applied with convection boundary condition with an ambient temperature of T_A °C and convection coefficient that is experimentally determined. Inside surfaces of the refrigerator that are exposed to cool air are applied with convection boundary condition with an inside temperature

Fig. 1.4 Mesh details

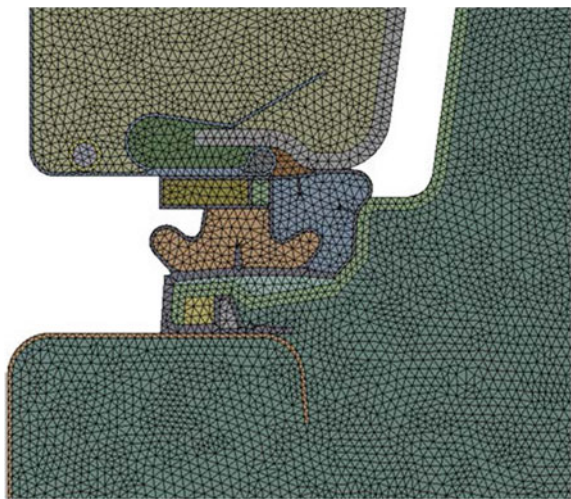


Table 1.1 Grid independence test

Mesh size ($\times 10^{-3}$ m)	Energy consumption (relative terms)	% Divergence
10	1	–
8	0.985	1.5%
6	0.992	0.72%
4	0.985	0.61%
2	0.981	0.32%

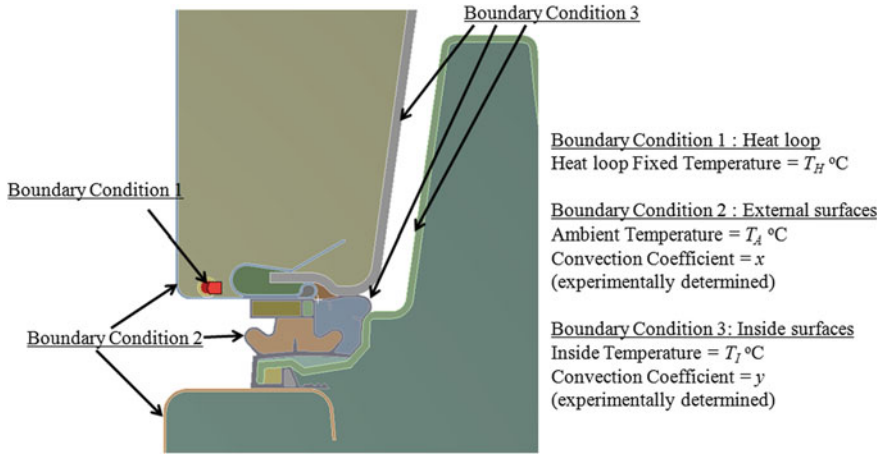


Fig. 1.5 Boundary conditions

of T_I °C and convection coefficient which is experimentally determined. T_A varies in the range of 25–40 °C, while T_I is assumed as -18 °C. Convection coefficients cannot be disclosed since these values are company proprietary and confidential.

1.4 Optimization Problem

Efforts to increase robustness to avoid external condensation leads to an increase in energy consumption. Thus, there must be a trade-off between these two. This trade-off is considered as an optimization problem. The objective of this optimization problem is to minimize energy consumption. Let us denote the energy consumption value of the refrigerator as E .

The implicit constraint for the problem is to avoid external condensation on the refrigerator. In quantifiable terms, this constraint can be stated as temperatures on exterior faces of the refrigerator should be greater than dew point temperature. In order to simplify the interpretation of constraint, Let us convert the minimum temperature on external faces of a refrigerator to a parameter called robustness to external

Table 1.2 Scale for robustness to external condensation

Minimum temperature (°C)		Robustness to external condensation (R)
Lower bound	Upper bound	
27.00	27.99	-1
28.00	28.00	0
28.01	28.99	1
29.00	29.99	2
30.00	30.99	3
31.00	31.99	4

condensation. Let us denote this parameter as R . With the current ambient temperature and relative humidity assumptions, dew point temperature of 28 °C is obtained. Hence, any temperature above 28 °C indicates that the model is robust to prevent external condensation on the external flange. Further, higher is temperature, as compared to the dew point, more robust, is the model. Considering this, we define robustness scale, where the temperature of 28 °C corresponds to $R = 0$. Table 1.2 defines the robustness scale. Thus, as per the below scale, any positive robustness score ($R \geq 1$) indicates that there is no condensation on the external flange. Zero or negative score ($R \leq 0$) indicates there is an external condensation in the model. Thus, the implicit constraint for the optimization problem is $R \geq 1$.

The explicit constraint for this optimization problem would define the maximum allowable range for decision variables. Let us discuss details for the choice of decision variables as given in Sect. 1.4.1.

1.4.1 Choice of Decision Variables

Decision variables for the problem comprise of x - and y -coordinates of heat loop position with respect to the coordinate axes defined subsequently. Quantifiable and measurable decision variables in order to define the heat loop position are chosen. A coordinate system (X, Y) is chosen as shown in Fig. 1.6 where X -axis is taken as inside wall of cabinet side face and Y -axis is taken as inside wall of the front flange of the cabinet. In this way, x -coordinate represents lateral (sidewise) position of heat loop from side face, while y -coordinate represents the depth-wise position of heat loop from the front flange.

Next step is deciding bounds for decision variables. It is advisable to consider the heat loop as close as possible to the front flange to avoid external condensation. $y = 0$ m represents that heat loop is just below the flange which is the most favorable position to avoid external condensation. As y increases, heat loop moves further away from front flange resulting in lesser heating of front flange. If it crosses an allowable distance, it will become ineffective in heating the flange. Considering this aspect,

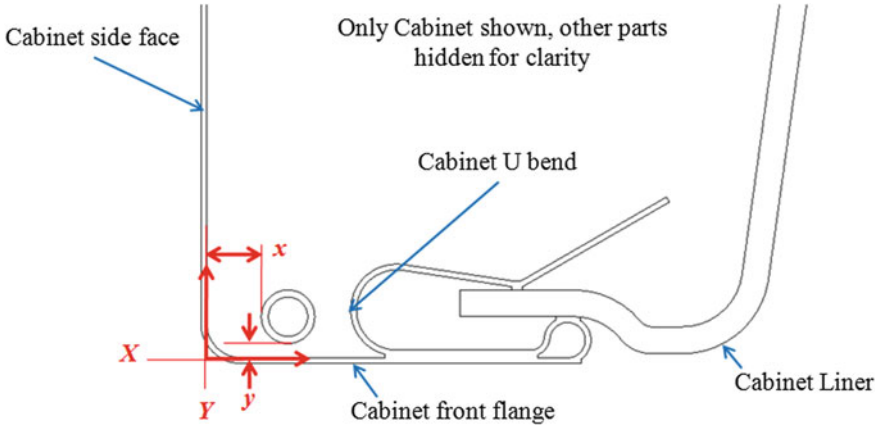


Fig. 1.6 Coordinate axes definition

the upper limit is 4×10^{-3} m for y . As a parametric study, values for y considered in the study are from 0 to (4×10^{-3}) m with a step size of 1×10^{-3} m.

For x -position, heat loop in contact with U-bend of the cabinet should be avoided. This is because U-bend of the cabinet is in direct contact with refrigerator interior liner. Also, there is a 2×10^{-3} m fillet distance between the coordinate axes (between the front flange and side face). Hence, x -values should start from $x = 2 \times 10^{-3}$ m. Values till $x = 6 \times 10^{-3}$ m are considered. This is because, beyond 6×10^{-3} m, heat loop comes in the close vicinity of U-bend. Thus, values from $x = (2-6) \times 10^{-3}$ m with the step of 1×10^{-3} m are considered. In this way, we will have full factorials DoE with two factors (x and y) each having five levels. These decision variables should be reflected in the simulation model as parameters in ANSYS tool [7].

1.4.2 Formulation of the Optimization Problem

Considering the above discussion, the optimization problem is defined by Eqs. 1.2, 1.3a, and b. Equation 1.2 represents the objective function, while Eq. 1.3a and b represent implicit constraint and explicit constraint, respectively.

$$\text{Objective: Minimize } E = f(x, y) \quad (1.2)$$

Subject to:

$$R = g(x, y) \geq 1 \quad (1.3a)$$

$$L_x \leq x \leq U_x$$

$$L_y \leq y \leq U_y \quad (1.3b)$$

In Eq. 1.3b, L_x and U_x are lower and upper bounds for variable x . L_y and U_y are lower and upper bounds for variable y . The functions $f(x, y)$ and $g(x, y)$ for E (energy consumption) and R (robustness to external condensation), respectively, cannot be analytically defined. This is because E and temperature R are outputs of 3D conduction and convection effects which cannot be manually evaluated. Geometry also consists of complex contours. Hence, problem solving using finite element analysis with the help of ANSYS as a tool for analyzing these two functions is considered to be appropriate.

Reason for choosing a full factorial DoE is twofold. The first reason is that since this is a decision-making point in the project, it is best to extract maximum information about levels and all interactions of the factors before taking a final decision about the values of x and y . Partial factor or screening DoEs are conducted during initial stages to eliminate weak or unimportant factors. In other words, when factors are large and the goal is to narrow down to few important factors, the partial factorial DoE is preferred. Here, only two factors are present, and the goal of DoE is not to eliminate the factor but to determine the most favorable levels for factors to satisfy optimization requirement (objective function). Hence, a full factorial approach is selected for DoE. For a full factorial DoE with n levels and k factors, a number of iterations (cases) m can be determined using Eq. 1.4.

$$m = n^k \quad (1.4)$$

Hence, DoE with m cases needs to be performed for optimization work. Consider, $n = 5$ and $k = 2$ for the present study; then, a number of cases m are 25. Parametric modeling in ANSYS modeling interface which is the Design Modeler is used to complete this task. Boolean operations are set parametrically in Design Modeler to achieve different heat loop positions. DoE setup is obtained by setting up all combinations of variables x and y in the ranges specified in the above optimum optimization problem.

1.5 Solution Strategy

Model is solved using the physics of steady-state thermal analysis. Instantaneous heat flow and energy consumption are efficiently predicted by the solver. Governing equation of the analysis is as depicted in Eq. 1.5 below [8].

$$[K(T)]\{T\} = \{Q(T)\} \quad (1.5)$$

In Eq. 1.5, K stands for the thermal conductivity of the materials involved. K can be constant or temperature dependent. Q matrix is for boundary conditions and

loads applied in the model. Solver solves for nodal temperatures using Eq. 1.5. This is basically a conduction-based equation based on Fourier's law. Heat flux, fixed temperature imposition, and convection are treated as boundary conditions represented by $\{Q\}$ in the above equation. In the present analysis, convection on external and inside surfaces of the refrigerator is considered. Further, a fixed temperature boundary condition is considered on the heat loop. Convection boundary condition incorporates heat flow dependant on the temperature differential between the surface and ambient temperature with the help of Eq. 1.6 below [8].

$$q = hA(T_{\text{surface}} - T_{\text{ambient}}) \quad (1.6)$$

The solver uses implicit iterative algorithms to solve Eq. 1.5. Loads are applied incrementally through substeps. Each substep is started by randomly assuming temperature at nodes and calculating the internal load based on assumption. Difference between internal and external load is then computed. Based on this result, the next iteration is chosen by the solver so that this difference is reduced sequentially. When this difference falls below convergence criteria (tolerance), load substep is said to be converged and next load substep is taken up for solving [7].

1.6 Results and Discussion

1.6.1 Results and Post-processing

Response surfaces chosen for post-processing are shown in Fig. 1.7. Since the cabinet front flange is prone to condensation, cabinet front flange is chosen as response surface for external condensation. Further, in order to evaluate E (energy consumption), all the inside surfaces of the refrigerator (surfaces of liners and gasket) are chosen as response surfaces, and heat gain for the model is evaluated by running a post-processing script on these response surfaces.

Sample results for one of the heat loop positions are shown in Fig. 1.8. Temperature scale and exact temperature values are not shown for the purpose of confidentiality.

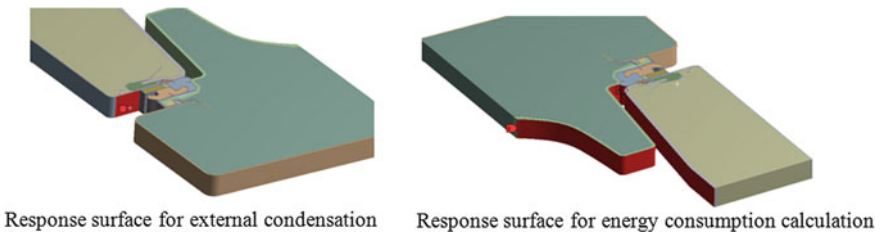


Fig. 1.7 Response surfaces

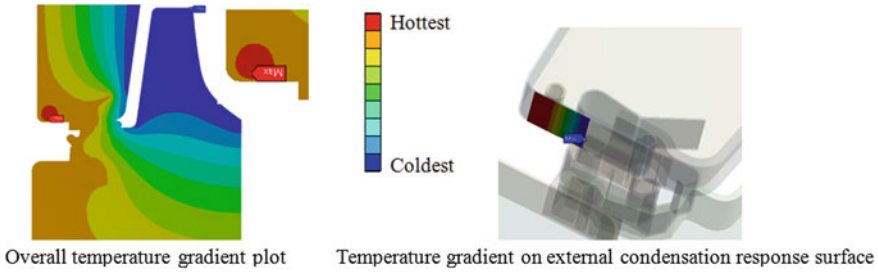


Fig. 1.8 Sample output plots

Note that, in the below temperature gradient plots, red color shows hottest zones, while blue color shows coldest zones.

The minimum temperature on external condensation response surfaces is obtained by analyzing temperature gradient plots. This data is converted to R (robustness to external condensation) using Table 1.1.

Since our study is based on comparative assessment and selection, we treat E value for DoE case 1 as a reference and express E values for other cases as ratios with respect to reference E value. E value for DoE case 1 is then considered as unity to allow comparison with other values. With these considerations, consolidated data is populated in Table 1.3 as shown.

1.6.2 Sensitivity Analysis of Factors

In order to evaluate the sensitivity for each factor on respective outputs, multiple variable regression analysis is conducted. P values and coefficients of both factors for each of the two outputs are studied to determine the dominant factor in the analysis. An approximate equation is built between decision variables and output. Equations 1.7 and 1.8 below show the approximate relations obtained between decision variables and outputs. Values of variables x and y should be used in ($\times 10^{-3}$ m) or mm format to use the below equations.

$$R = 1.44 + 0.4x - 1.1y \tag{1.7}$$

$$E = 0.978 + 0.002x - 0.0117y \tag{1.8}$$

As shown above Eqs. 1.7 and 1.8, it is said that both external condensation and energy consumption are strongly dependant on decision variable y . In other words, y is the dominant factor in DoE. This is also reflected in significantly lower P values obtained for y as compared to x .

Table 1.3 Post-processed DoE results

Case No.	Heat loop x -coordinate ($\times 10^{-3}$ m)	Heat loop y -coordinate ($\times 10^{-3}$ m)	R	E
1	2	0	3	1 (reference)
2		1	1	0.958
3		2	-1	0.952
4		3	-1	0.949
5		4	-1	0.948
6	3	0	4	1.001
7		1	1	0.957
8		2	-1	0.951
9		3	-1	0.949
10		4	-1	0.947
11	4	0	4	1.008
12		1	1	0.955
13		2	1	0.953
14		3	-1	0.950
15		4	-1	0.948
16	5	0	4	1.006
17		1	1	0.958
18		2	1	0.956
19		3	-1	0.953
20		4	-1	0.951
21	6	0	5	1.011
22		1	2	0.968
23		2	1	0.963
24		3	1	0.957
25		4	1	0.957

1.6.3 Trade-off Plots and Selection of Optimum Position

In order to select the optimum position of heat loop, we need to create trade-off plots between E and R . Using Eqs. 1.2, 1.3a, and b, an optimum x and y position can then be selected. The optimization problem is to minimize E with the implicit constraint of $R \geq 1$. Five trade-off plots are generated keeping x as constant with varying y -coordinates. Consider Fig. 1.9a, the plot for $x = 2 \times 10^{-3}$ m which is L_x . An optimum point is obtained in the plot by selecting the point with minimum energy consumption (E) and robustness to external condensation ($R \geq 1$). This point is highlighted by a green balloon in the plot. A similar exercise is repeated for $x =$

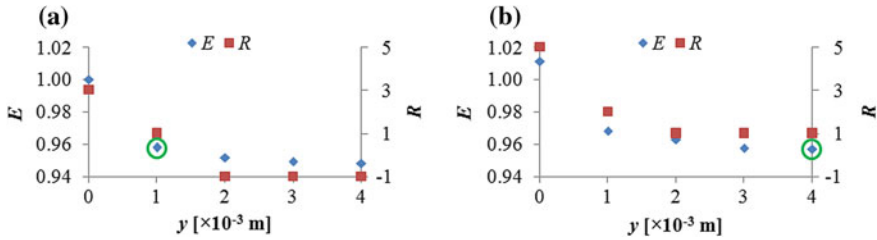
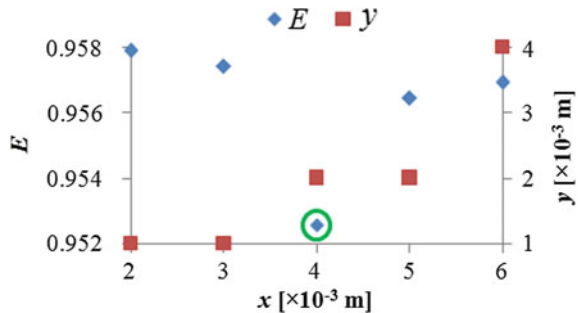


Fig. 1.9 **a** Trade-off plot at $x = 2 \times 10^{-3}$ m, **b** trade-off plot at $x = 6 \times 10^{-3}$ m

Fig. 1.10 Selection of most optimum heat loop position



(3, 4 and 5) $\times 10^{-3}$ m by generating respective trade-off plots. In this way, optimum points at each x -position are obtained. Position (x, y) data for each optimum point is recorded. Figure 1.9b shows the trade-off plot for $x = 6 \times 10^{-3}$ m which is U_x .

Next, five optimum points with varying x are plotted against E to select least energy consumption (E_m) out of the above-mentioned optimum points as shown in Fig. 1.10. This position is highlighted by a green balloon in Fig. 1.10. The heat loop position thus obtained is the final solution of the optimization problem. Thus, the heat loop position is one with least E and also satisfies the constraint of $R \geq 1$. After plotting the data in Figs. 1.9 and 1.10, we note that most optimum heat loop position is at $x = 4 \times 10^{-3}$ m with $y = 2 \times 10^{-3}$ m.

1.7 Conclusion

Heat loop placement provides a unique challenge of satisfying contradictory requirements which are minimizing energy consumption and maximizing the robustness of refrigerator to external condensation. This challenge was solved by building a comprehensive methodology for optimum selection of heat loop. This methodology comprises framing an optimization problem and solving the problem using DoE-based optimization approach. Full factorial DoE was executed using steady-state thermal FEA model built in software ANSYS. An efficient modeling approach for FEA was developed which can be utilized across different types of refrigerators like a single

door, top mount, bottom mount, multidoor bottom mount, and side-by-side refrigerators. Appropriate response surfaces were plotted and chosen to compare DoE cases. Sensitivity analysis was conducted to identify a dominant factor which was found to be depth-wise position of heat loop. Due to rigorous analysis, trade-off plots helped to select the most optimum heat loop position. From the trade-off analysis, the optimum position of heat loop for the present study was found to be $x = 4 \times 10^{-3}$ m (lateral position) and $y = 2 \times 10^{-3}$ m (depth-wise position).

This work would be helpful in providing a systematic and efficient methodology for the selection of heat loop position for complex designs of future refrigerators. The proposed methodology can be effectively utilized in the early design phase of a refrigerator to cut down design time and expensive experimental efforts. Physical testing can be completely eliminated in the early design phase and replaced by virtual experiments using simulation. This work also promotes the rigorous use of simulation for design evaluation.

As a future scope, refrigerant fluid flow in heat loop and its effect on energy consumption and external condensation are planned to be studied using computational fluid dynamics. Incorporation of transient effects to study the impact on the energy rating of the refrigerator can also improve the analysis.

References

1. Sreejith, K., Sushmitha, S., Das, V.: Experimental investigation of a household refrigerator using air-cooled and water-cooled condenser. *Int. J. Eng. Sci.* **4**(6) (2014)
2. Matweb Online Library Material Property Data. <http://www.matweb.com/index.aspx>
3. Arora, C.P.: Refrigeration and Air Conditioning. Tata McGraw Hill Publishing Company Limited, New Delhi (2006)
4. Rasche, K.J.: Probabilistic study of a refrigerator steel heat loop tube joint. In: Proceedings of the 10th International Ansys Conference, Pittsburgh, USA (2002)
5. Jones, W.P.: Air Conditioning Engineering. CRC Press, Boca Raton (2007)
6. Lawrence, M.G.: The relationship between relative humidity and the dewpoint temperature in moist air: a simple conversion and applications. *Bull. Am. Meteorol. Soc.* **86**(2) (2005)
7. Ansys User Manual.: Steady-State Thermal Analysis. Ansys Inc. (2005)
8. Lienhard IV, J.H., Lienhard V.J.H.: A Heat Transfer Textbook. Phlogiston Press, Cambridge (2017)

Chapter 2

Refrigerator Structural Stability Analysis and Correlation



Vikram Suriyanarayanan, Arunachalam Nagarajan, Mike Fiori, Pushendra Mahajan and Aditya Nalwade

Abstract The work intends to develop a robust simulation methodology that is capable of evaluating the stability of a refrigerator body that resists tipping for test specified tipping load and loading conditions. Simulation methodology involves a detailed study of testing conditions and replicating the loading and boundary conditions in the simulation environment. Simulation is performed using the physics of nonlinear static structural analysis with iterative solution algorithms in commercial software package ANSYS. Further, simulation involves the technical complexity of incorporating varied test conditions from safety regulations, handling complex contact algorithms, overcoming nonlinearity, and obtaining model behavior with product falling. The simulation results are validated using experimental studies. It is observed that they are in good agreement within the margin of error range. The work intends to have robust simulation methodology and proven correlation so that simulation can be effectively incorporated in the early design cycle to optimize the design parts so as to satisfy tipping loads before tooling investment. The obtained results proved to be reliable and useful to predict and avoid failure in the final product and thus helped to ensure safety compliant designs.

Keywords Refrigerator · FEA · MSA · CG · Tipping · Correlation

Nomenclature

FEA	Finite element analysis
CG	Center of gravity
MSA	Measurement system analysis
FC	Freezer compartment

V. Suriyanarayanan (✉) · A. Nagarajan · P. Mahajan · A. Nalwade
Global Technology and Engineering Center, Whirlpool of India Ltd., Pune, India
e-mail: vikram_suriyanarayanan@whirlpool.com

M. Fiori
Whirlpool Corporation, Benton Harbor, MI, USA

© Springer Nature Singapore Pte Ltd. 2020
C. Li et al. (eds.), *Advances in Engineering Design and Simulation*,
Lecture Notes on Multidisciplinary Industrial Engineering,
https://doi.org/10.1007/978-981-13-8468-4_2

RC	Refrigerator compartment
x	Displacement
t	Time
m	Mass of the objects being modeled
c	Damping factor
k	Stiffness coefficient of the system
F^{external}	External forces being applied on the system
LC	Load cell
RP	Reference point
LCO	Load cell offset
W_{case}	Weight of the refrigerator case
H_{case}	Height of the refrigerator case
RTT	Distance between rear roller to tip load
RD	Distance between front and rear support rollers

2.1 Introduction

The refrigerator is a very common household appliance that is a necessity in today's world and is widely used. Certain large volume refrigerators tend to become extremely bulky and in a scenario like a child hanging may tip over and cause serious injuries and in certain extreme cases result in a fatality. Based on a study conducted by the US consumer product safety division, the annual average tip-over injuries for the year 2013–2015 is 1100, which shows that it is a relevant and a widespread problem occurring in the day-to-day lives [1].

ANSYS Workbench [2, 3] is a powerful and a user-friendly finite element analysis (FEA) software that is widely used to model and analyze different types of problems ranging from linear static problems to complex dynamic problems involving vibrations, etc. because of its multiphysics capabilities and availability of comprehensive online documentation. ANSYS uses an implicit scheme to solve the finite element-based mathematical model [3]. During the design of a refrigerator, it is subjected to several product stability tests and it is mandatory for the refrigerator to pass in them in order to be released to the market. One such important test is the cabinet tipping test, wherein the load at which static refrigerator topples and falls over is determined as shown in Fig. 2.1. Figure 2.1a, b shows the side and top view of the case, respectively. This load is called the tipping load. Generally, commercial refrigerators follow a thumb line rule which dictates the tipping load to be no lesser than one-fifth the weight of the empty product or 22.5 kg, whichever is lesser. Hence, a need for building a robust system level FEA model exists which would accurately capture the physics behind tipping that would reduce the need for successive physical tests or iterations.

Kesani et al. [4] describe a methodology developed using ANSYS APDL to predict the critical angle of tilt during transportation. Kesani carries out three optimization exercises to reduce the mass of the product successively, and then, deflections are

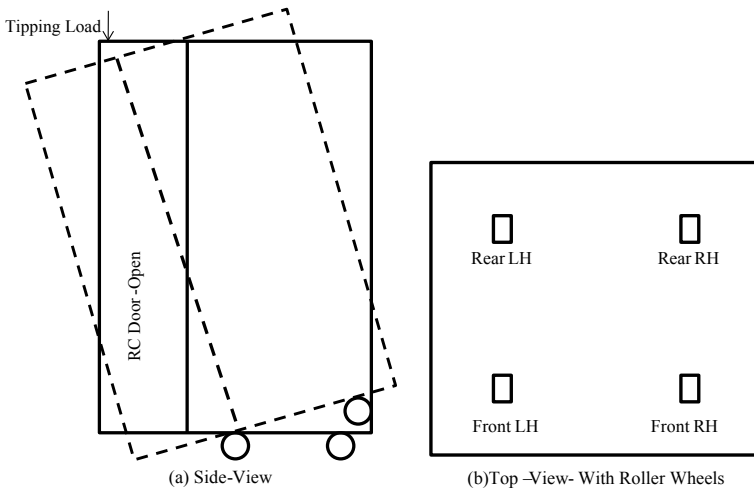


Fig. 2.1 a General schematic showing the tipping process, b top view of the refrigerator

recorded. Furthermore, toppling analysis was carried out to determine the critical tilt angle and was determined to be 35.18° .

Kumar and coworkers [5] have described a methodology that has been developed to predict cabinet deflection of an entire refrigerator by taking into consideration the cabinet wrapper, foam, and liners. The outcome of the analysis is to determine the cabinet twist and sway which is to be kept below a certain allowable limit.

The aim of the work described here is to accurately determine the tipping load of the refrigerator. During the course of the design, if it is determined that the tipping load is less than a certain allowable load, then design improvements can be implemented in the refrigerator to have stability. The methodology adopted to determine the tipping load of the refrigerator system is presented in the study. All the critical components of the refrigerator such as wrappers, liners, bracket reinforcement bars, back panel, deck, and cabinet foam are modeled in order to consider the entire stiffness of the system. The physical measurement tests to determine the center of gravity and tipping load of the refrigerator are also discussed. Furthermore, the validation of the simulation result is carried out by comparing it with physical results. The word ‘case’ refers to the refrigerator model and ‘sample’ refers to multiple instances of the same model. Refrigerator compartment is abbreviated as RC, and the freezer compartment is abbreviated as FC. In general, a refrigerator has two compartments and two doors to cover each compartment.

2.2 Methodology

In Fig. 2.2, the flowchart shows the parallel track for experimental and simulation approach. In the experimental approach, two cases (named as Case-1 and Case-2) are chosen, and the center of gravity is determined by using the experimental setup. The reactions from the load cells are obtained, and CG is calculated in x -, y -, and z -directions. Experiments are carried on further to determine the tipping load.

In the simulation approach, the finite element model is developed wherein the CAD model is taken through three stages:

1. Preprocessing: The model is simplified by suppressing unwanted parts and by removing small fillets and features in order to reduce the mesh count.
2. Meshing: The preprocessed CAD model is meshed using suitable mesh elements.
3. Boundary Conditions and Loading: Appropriate boundary conditions and loads are applied in order to capture the physics of the testing conditions.
4. Run: Typical runtimes for a tipping simulation takes 8–10 h based on the model and mesh count in a 64 GB RAM machine.

Results from both the approaches are compared, and the model is validated to gain confidence.

2.2.1 Measurement System Analysis

In order to evaluate the center of gravity values accurately through experiments and to capture the variations of the values obtained, a measurement system analysis sampling plan has been devised, and the data is stored in the form of the matrix as explained below.

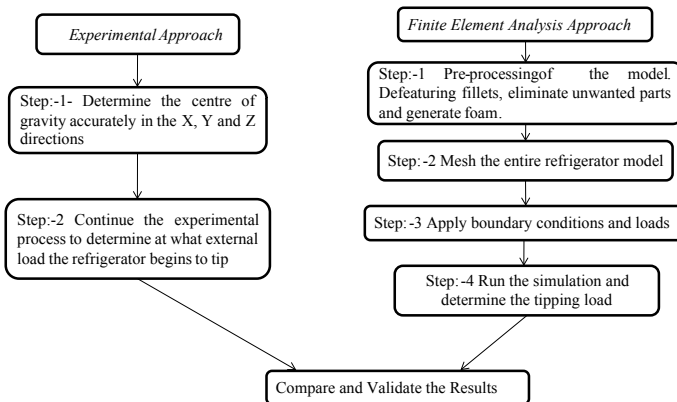


Fig. 2.2 Flowchart illustrating the overall methodology adopted to solve the problem

$$\begin{bmatrix} a_{111} & a_{112} & \cdot & \cdot & a_{11k} & \cdot & \cdot & a_{i11} & a_{i12} & \cdot & \cdot & a_{ik} & \cdot & \cdot & a_{m11} & a_{m12} & \cdot & \cdot & a_{m1k} \\ \cdot & \cdot & \cdot & \cdot & \cdot & \cdot & \cdot & \cdot & \cdot & \cdot & \cdot & \cdot & \cdot & \cdot & \cdot & \cdot & \cdot & \cdot & \cdot \\ \cdot & \cdot & \cdot & \cdot & \cdot & \cdot & \cdot & \cdot & \cdot & \cdot & \cdot & \cdot & \cdot & \cdot & \cdot & \cdot & \cdot & \cdot & \cdot \\ a_{1j1} & a_{1j2} & \cdot & \cdot & a_{1jk} & \cdot & \cdot & a_{ij1} & a_{ij2} & \cdot & \cdot & a_{ijk} & \cdot & \cdot & a_{mj1} & a_{mj2} & \cdot & \cdot & a_{mjk} \\ \cdot & \cdot & \cdot & \cdot & \cdot & \cdot & \cdot & \cdot & \cdot & \cdot & \cdot & \cdot & \cdot & \cdot & \cdot & \cdot & \cdot & \cdot & \cdot \\ \cdot & \cdot & \cdot & \cdot & \cdot & \cdot & \cdot & \cdot & \cdot & \cdot & \cdot & \cdot & \cdot & \cdot & \cdot & \cdot & \cdot & \cdot & \cdot \\ a_{1n1} & a_{1n2} & \cdot & \cdot & a_{1nk} & \cdot & \cdot & a_{in1} & a_{in2} & \cdot & \cdot & a_{ink} & \cdot & \cdot & a_{mn1} & a_{mn2} & \cdot & \cdot & a_{mnk} \end{bmatrix}$$

Fig. 2.3 General matrix form to store the CG values for m samples, n operators, and k setups for a single case

$$\begin{bmatrix} a_{111} & a_{112} & a_{113} & a_{211} & a_{212} & a_{213} & a_{311} & a_{312} & a_{313} \\ a_{121} & a_{122} & a_{123} & a_{221} & a_{222} & a_{223} & a_{321} & a_{322} & a_{323} \end{bmatrix}$$

Fig. 2.4 Specific matrix entry for three samples, two operators and three setups for a single case

The matrix with ' m ' samples, ' n ' operators, and ' k ' number of setups for a single case has been developed and is shown in Fig. 2.3. General matrix form to store the CG values for m samples, n operators and k set-ups for a single case.

a_{111} is the reading obtained by the first operator for sample-1 for the first setup; similarly, a_{112} is the reading obtained by the first operator for sample-1 for the second setup. a_{11k} is the reading obtained by the first operator for sample-1 for the k th setup. a_{ik} is the reading obtained for i th sample by operator-1 for the k th setup. a_{m11} is the reading obtained for the m th sample by the first operator for the first setup. a_{m1k} is the reading obtained for the m th sample by the first operator for the k th setup. Moving downwards in the matrix a_{1j1} is the reading obtained by the j th operator for sample-1 and setup 1. a_{ijk} is the reading obtained for i th sample by the j th operator for the k th setup.

Let us discuss a simple example to understand the matrix shown in Fig. 2.3. Let us assume that there is one refrigerator case and there are three different samples of the same. Now, there are two operators performing an experiment on each of the samples for three setups and record the readings. So each operator will have three sets of readings for each of the sample, and two operators would have six sets of reading for the same sample. In all for three different samples, this experiment would contain 18 different readings as shown in Fig. 2.4.

For this particular study, two cases (Case-1 and Case-2) are considered, and three samples of each case were considered. The experiments were carried out by two operators for three setups of each case. Thus, 36 readings were recorded to study the center of gravity.

The above system of measurement has been as this is an established and accepted process in the industry and the organization. It enables us to obtain data in a structured

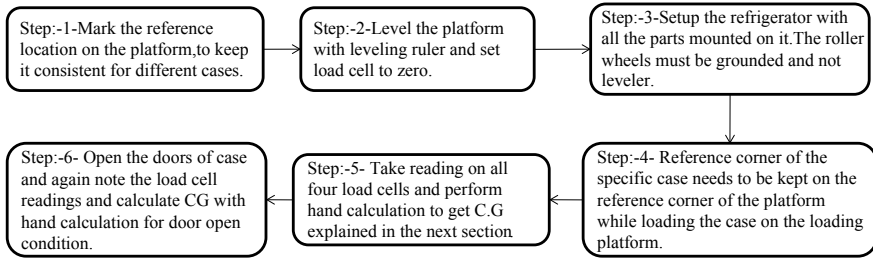


Fig. 2.5 Center of gravity experimental measurement process map

and detailed manner that is extremely beneficial in capturing variation in the output data that may arise due to operator change or sample differences.

2.2.2 Center of Gravity Experimental Measurement and Calculation

An accurate measurement of the center of gravity is important in order to assess the tipping load. Figure 2.5 shows the methodology adopted to measure the center of gravity for different refrigerator cases. During step-1, a reference location is marked on the measurement platform which will help in the accurate and consistent setup of different samples on the measurement platform. Since it is important for all the four roller wheels to rest on the surface equally on a single plane in order to capture reaction forces correctly, it is essential to level the cases (Case-1 and Case-2) using a leveling screw. Once appropriately leveled, the load cell reading is set to zero. Once the sample is mounted on the platform with the reference points aligned, the readings from all the four load cells are recorded. This information is then used to calculate the center of gravity. Finally, open the doors and record the load cells reading again.

Figure 2.6 shows the top view of the loading platform on to which the refrigerator cases are loaded. It shows the alignment of the x - and z -directions. In Fig. 2.6, LC-1, LC-2, LC-3, and LC-4 show the location for placing the load cells. RP-1 and RP-2 represent the reference points with which the refrigerator case will be aligned. Offset- X and Offset- Z represent the distance of the reference point from the platform edges. LCO- X and LCO- Z represent the load cell offset from the edges of the platform in the X - and Z -directions, respectively. The rear side denotes the rear side of the sample with the back wrapper, etc., and the front side denotes the door side of the sample.

2.2.2.1 X-CG Location Calculation

Figure 2.7 shows a schematic of the front view of the refrigerator case which is resting on the loading platform with the load cells. LCO refers to the distance of the load cell

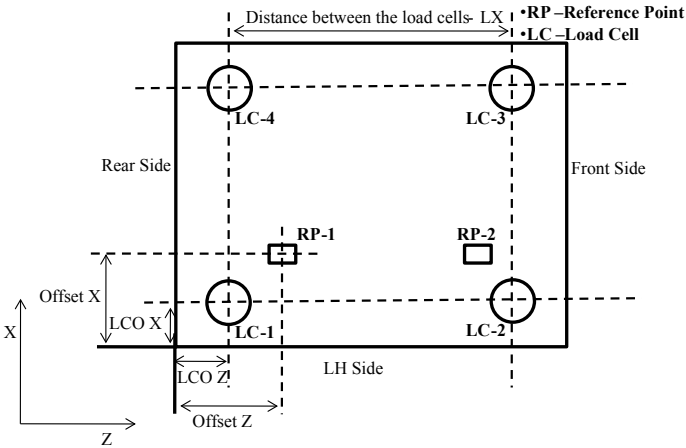


Fig. 2.6 Schematic illustrating the layout of the loading platform with load cells and a reference coordinate system

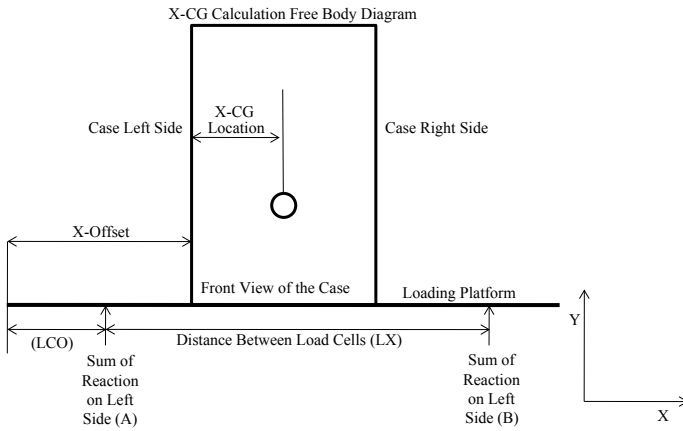


Fig. 2.7 Free-body diagram to calculate the X-CG coordinate of the system

from the edge of the platform. X -offset refers to the distance of the refrigerator left side wall from the edge of the loading platform. X -CG location denotes the distance between the refrigerator side wall and the location of the center of gravity. L_x refers to the distance between the load cells located at the left and right side. ‘**A**’ refers to the sum of force reactions obtained by the load cells on the left side, and ‘**B**’ refers to the sum of the force reactions obtained by the load cells on the right side. W_{case} is the weight of the refrigerator case.

Referring to Fig. 2.7, Eq. 2.1 represents the balancing of ‘ z ’ moment at location A.

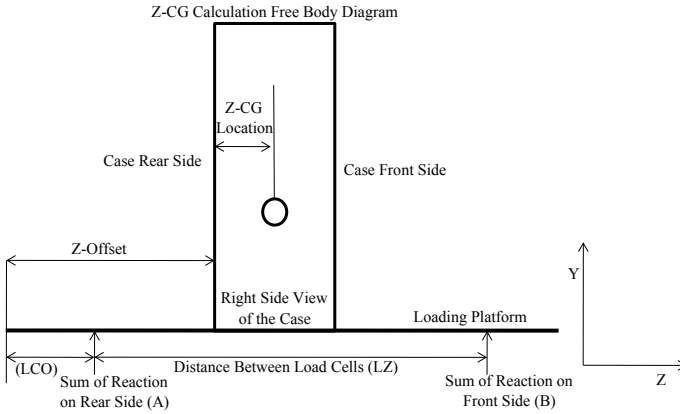


Fig. 2.8 Free-body diagram to calculate the Z-CG coordinate of the system

$$W_{\text{case}} * ((X_{\text{offset}} + X_{\text{CGLocation}}) - \text{LCO}) = B * L_x \quad (2.1)$$

After the rearrangement of Eq. 2.1, the x -coordinate of the center of gravity is expressed as in Eq. 2.2.

$$X_{\text{CGLocation}} = \frac{(B * L_x - (W_{\text{case}} * (X_{\text{offset}} - \text{LCO})))}{W_{\text{case}}} \quad (2.2)$$

2.2.2.2 Z-CG Location Calculation

Figure 2.8 shows a schematic of the right side view of the refrigerator case which is resting on the loading platform with the load cells. LCO refers to the distance of the load cell from the edge of the platform. Z-offset refers to the distance of the refrigerator rear side from the edge of the loading platform. Z-CG location denotes the distance between the refrigerator rear side and the location of the center of gravity. L_z refers to the distance between the load cells located at the front and rear side. ‘A’ refers to the sum of force reactions obtained by the load cells on the rear side, and ‘B’ refers to the sum of the force reactions obtained by the load cells on the front side. W_{case} is the weight of the refrigerator case.

Referring to Fig. 2.8, Eq. 2.3 represents the balancing of ‘ x ’ moment at location A.

$$W_{\text{case}} * ((Z_{\text{offset}} + Z_{\text{CGLocation}}) - \text{LCO}) = B * L_z \quad (2.3)$$

After the rearrangement of Eq. 2.3, the z -coordinate of the center of gravity is expressed as in Eq. 2.4.

$$Z_{CGLocation} = \frac{(B * L_z - (W_{case} * (Z_{offset} - LCO)))}{W_{case}} \tag{2.4}$$

2.2.2.3 Y-CG Location Calculation

Figure 2.9 shows the side view of the refrigerator case which is resting horizontally on the loading platform with the doors facing upwards. This particular setup is different from others in the sense that here the refrigerator is resting horizontally instead of vertically. LCO refers to the distance of the load cell from the edge of the platform. Y-offset refers to the distance of the refrigerator case top side from the edge of the loading platform. Y-CG location denotes the distance between the refrigerator bottom side and the location of the center of gravity. L_y refers to the distance between the load cells located at the left and right side. ‘A’ refers to the sum of force reactions obtained by the load cells on the left side, and ‘B’ refers to the sum of the force reactions obtained by the load cells on the right side H_{case} refers to the height of the refrigerator case. W_{case} is the weight of the refrigerator case.

Referring to Fig. 2.9, Eq. 2.5 represents the balancing of ‘y’ moment at location B.

$$W_{case} * ((Y_{CGLocation} - LCO - (H_{case} - Y_{offset} - depth_{platform}) - LCO) = A * L_y \tag{2.5}$$

After the rearrangement of Eq. 2.5, the y-coordinate of the center of gravity is expressed as in Eq. 2.6

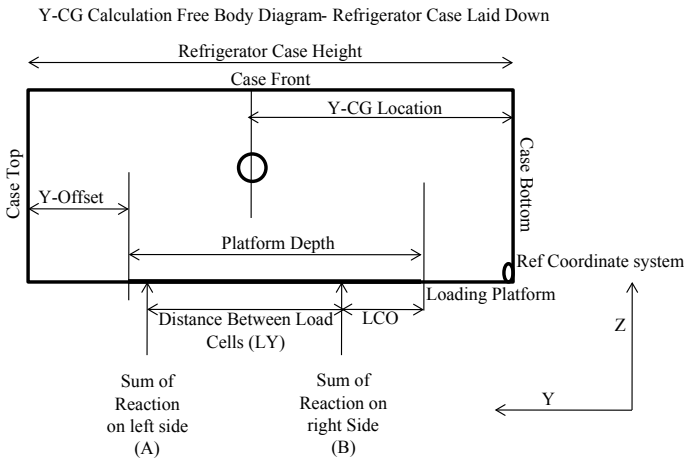


Fig. 2.9 Free-body diagram to calculate the Y-CG coordinate of the system

$$Y_{CGLocation} = \frac{(A * L_y)}{W_{case}} + LCO + H_{case} - Y_{offset} - depth_{platform} \quad (2.6)$$

2.2.3 Tipping Load Experimental Measurement Process Map and Calculation

Figure 2.10 shows the methodology to calculate the tipping load. Firstly set up the refrigerator case in the same manner as for the CG measurement. Open both the doors of the sample at 90°. Place an expanded polystyrene (EPS) block below one of the doors with a slight clearance in order to prevent a complete product falls down. Now start applying the tipping load on the freezer compartment door of the sample in the form of block weights. Continue applying the loads until the product starts tipping which is defined as the point where one of the rollers is lifted off the ground.

Tipping Load Calculation

Figure 2.11 shows a schematic of the right side view of the refrigerator case which is standing vertically on the loading platform. **R1** refers to the force reaction exerted on the load cells on the refrigerator case front side, and **R2** refers to the reaction exerted on the refrigerator case rear side. Z-CG location denotes the distance between the refrigerator rear side and the location of the center of gravity. RTT refers to the distance between the rear roller to tip load. RD refers to the distance between the front and rear support rollers. Tipping load refers to the load at which the product starts tipping or the load at which the rear rollers lose contact with the ground. W_{case} is the weight of the refrigerator case.

Referring to Fig. 2.11, the overall force balance in ‘y’ direction is given in Eq. 2.7.

$$R1 + R2 = \text{Tipping Load} + W_{case} \quad (2.7)$$

When the refrigerator case is about to tip, no reaction is exerted on the rear wheel, and hence, $R2 = 0$, so $R1$ is expressed as given in Eq. 2.8

$$R1 = \text{Tipping Load} + W_{case} \quad (2.8)$$

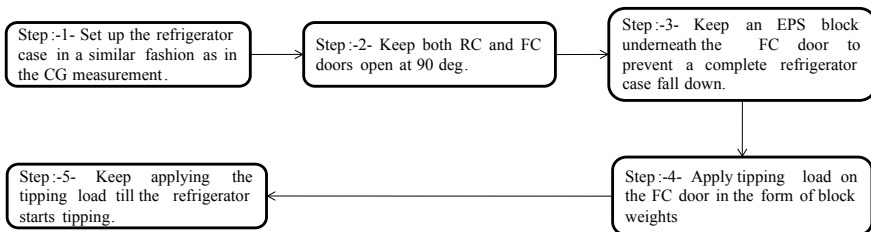
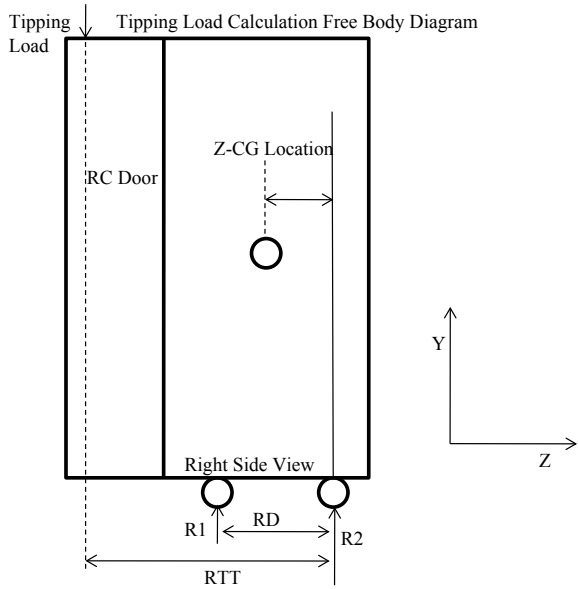


Fig. 2.10 Tipping load experimental measurement process map

Fig. 2.11 Schematic illustrating the free-body diagram to determine the tipping load through hand calculation



Equation 2.9 gives the moment balance at front roller

$$\text{Tipping Load} = W_{\text{case}} * \frac{(RD - Z_{CG\text{location}})}{(RTT - RD)} \tag{2.9}$$

2.2.4 Modeling the Tipping Problem Using FEA

2.2.4.1 Input Parameters Required to Model

See Fig. 2.12 and Table 2.1.

2.2.4.2 Preprocessing

For preprocessing, the necessary parts such as the door and cabinet liners, wrappers, and foam are retained. The other additional features such as bins, drawers, and crispers are not physically modeled but are considered by adding respective weights into the foam. This is done so that the weight of the refrigerator case in the physical test should match that of the model used in the simulation. Once the required numbers of parts are considered, complex and minute features such as fillets on the liners are defeatured as they may drive down the size of the element and hence increasing the mesh count. This is an important part of the process as it enables us to develop a robust

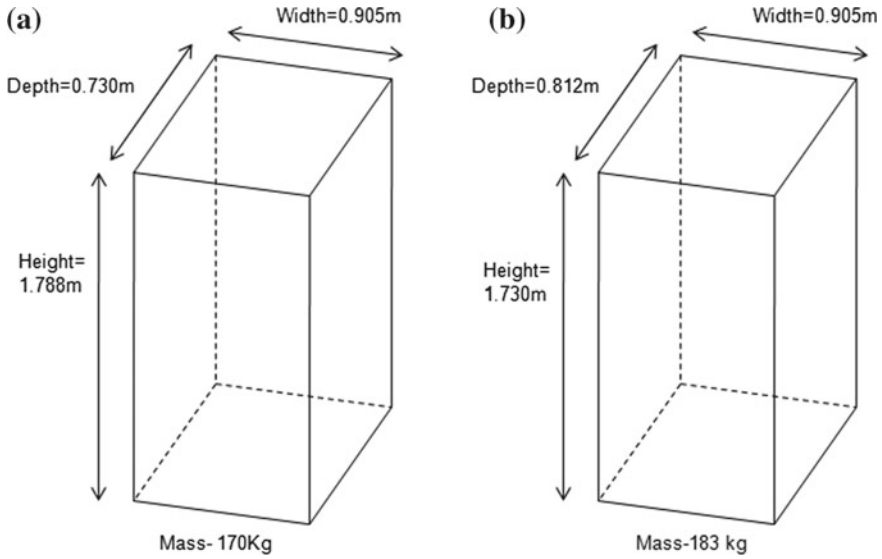


Fig. 2.12 Schematic illustrating the difference b/w the two cases **a** Case-1, **b** Case-2

Table 2.1 Comparison of the parameters of the two cases

Parameter	Case-1	Case-2
Cabinet width (m)	0.905	0.905
Cabinet height (m)	1.788	1.730
Cabinet depth (m)	0.730	0.812
Product mass (kg)	170	183

FEA model with minimal computational effort. The cabinet and door foam are also generated at this step using ANSYS design modeler. Foam is an important structural component in the refrigerator as it takes up a significant amount of structural load by adding to the stiffness.

2.2.4.3 Meshing

Meshing is performed primarily by using second-order tetrahedral elements. The foam, however, is meshed using first-order tetrahedral elements as modeling them with second-order elements may lead to a high number of elements. A lower value of Young’s modulus is chosen in order to offset the excessively stiff elements.

Structural parts like cabinet wrapper, door wrapper, deck, and back wrapper are made of steel and are thin members whose thickness values are much smaller in comparison with the length and width of the member. These parts are modeled as shell elements which help in a significant reduction in the computation time

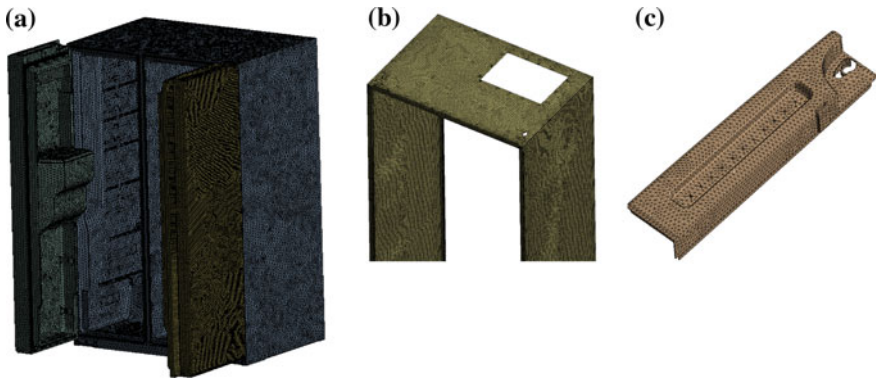


Fig. 2.13 a Cabinet and door foam mesh, b body wrapper mesh, and c door endcap mesh

by reducing the mesh count. The entire cabinet model typically consists of about 8,00,000–10,00,000 nodes depending upon the capacity of the model.

The primary reason for choosing second-order tetrahedral elements for most parts is because of the complex geometry involved, and the foam is primarily meshed using first-order tetrahedral elements because using second-order elements would increase the element count significantly (Fig. 2.13).

2.2.4.4 Mechanical Modeling and Boundary Conditions

Screw fasteners and other connections are modeled as rigid connections by using the remote point feature available in ANSYS Workbench.

Since this is a system-level tipping problem where local effects are not of interest, all the contacts in the product are modeled as bonded contacts, which do not take frictional effects into consideration. All food loads, cabinet loads, and compressor loads are applied as point masses. Furthermore, the densities of cabinet foam and door foam are modified in order to match the product weight with bins and shelves.

Once the weight of the product is matched, the rear rollers are subjected to a compression only support boundary condition which replicates the physical situation of the rollers resting on a hard surface. As far as front rollers are concerned, a patch created at the bottom of the LH roller is fixed and the RH roller is constrained in such a way that it is free to move in the lateral direction as shown in Fig. 2.14.

The tipping load is applied on the edge of the widest exterior door with doors open at 90°. The load is linearly ramped, and with each time step, the force reaction is measured at the rollers. The time instant where the roller reaction becomes zero is recorded, and the corresponding applied force is measured. This is the tipping load obtained during the simulation.

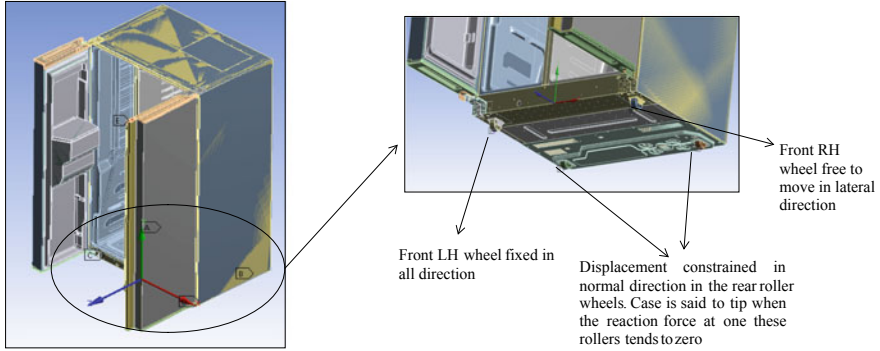


Fig. 2.14 Schematic illustrating the application of boundary conditions for the refrigerator model

2.2.4.5 Mathematical Equations

ANSYS mechanical [3] solves the general structural dynamics equation given in Eq. 2.10 in the background in order to obtain a solution to dynamic structural problems.

$$m \frac{d^2x}{dt^2} + c \frac{dx}{dt} + kx = F^{\text{external}} \quad (2.10)$$

While solving the linear static problems, however, the inertial and the damping components of the equation reduce to zero, thereby reducing Eqs. 2.10–2.11.

$$kx = F^{\text{external}} \quad (2.11)$$

The above equation is then solved using the finite element method wherein the continuous differential equations are transformed into a discrete form by converting them into blocks of matrices and then using implicit Newton–Raphson method to determine solutions for the algebraic system [3]. The deformations are then obtained, and subsequently, the strains and stresses are evaluated.

2.3 Results and Discussion

2.3.1 Validation with Simulation for CG Results

A total of 36 CG measurements obtained from experiments outlined in Sect. 2.2.1 are compared against the values obtained through FEA simulations and correlation levels are determined and shown in Tables 2.2 and 2.3. Please note that the values

Table 2.2 Table displaying the percentage correlation b/w simulation and physical test results for CG for Case-1

Results	CG door closed			CG door open		
	X-CG position	Z-CG position	Y-CG position	X-CG position	Z-CG position	Y-CG position
Average physical test data	1.000	0.822	1.921	0.990	1.016	1.921
Simulation result	1.028	0.831	1.989	1.021	1.024	1.989
% Correlation	97.2	98.9	96.4	96.8	99.1	96.4

Table 2.3 Table displaying the percentage correlation b/w simulation and physical test results for CG for Case-2

Results	CG door closed (mm)			CG door open (mm)		
	X-CG position	Z-CG position	Y-CG position	X-CG position	Z-CG position	Y-CG position
Average physical test data	1.000	1.032	1.856	0.991	1.263	1.856
Simulation result	1.017	1.023	1.912	1.010	1.276	1.913
% Correlation	98.2	99.0	96.9	98.0	98.9	96.9

are normalized with the X-CG position obtained through the physical test when the door is closed.

2.3.2 Validation with Simulation for Tipping Load Results

Validation for tipping load has been performed on Case-1 and Case-2, and the results are shown in Table 2.4. Please note that the tipping load is normalized with the value obtained in the physical test. In Case-1, about 80% correlation is observed between physical tests and simulation and in Case-2 about 94% correlation is observed between the same. In both cases, simulation results tend to overpredict the physical results.

Table 2.4 Table displaying the correlation % b/w simulation and physical test results for tipping load for Case-1 and Case-2

Results	Tipping load (Case-1)	Tipping load (Case-2)
Average physical test data	1.000	1.000
Simulation result	1.209	1.059
% Correlation	80	94

2.4 Conclusion

A robust FEA methodology has been developed in order to predict the tipping load for a refrigerator. Measurement system analysis has been used to devise a data collection scheme to obtain CG information through physical tests. Good correlations between simulation and physical tests are observed with respect to the CG measurement, which is critical to predicting the tipping load. Almost all the values obtained through simulations are more than 95% in agreement with physical tests.

Good correlations are obtained with respect to the measurement of tipping loads. Based on the two cases that have been considered to determine the tipping load, it is observed that simulation tends to overpredict the tipping load in comparison with the actual physical tests. It is highly likely that the refrigerator cabinet dimensions play a strong role in the stability of the product. For example, increasing cabinet, depth is highly likely to increase the tipping load, thereby adding to the stability. The same can be said about the height of the cabinet, increasing the height is likely to make the product tip over easily. Even though these conclusions seem intuitive in nature, the FEA methodology developed provides a quantitative and reliable basis to draw design conclusions and decreasing the product design cycle time.

Future work would involve carrying out the validation for a higher number of cases to gain confidence and potentially identify issues that will help to close the gaps between simulation and physical tests.

Acknowledgements We would like to express sincere thanks to Dr. Biswadip Shome for his guidance and review of our technical paper.

References

- Suchy, A.: Product Instability or Tip Over Injuries and Fatalities Associated with Television, Furniture and Appliances: 2016 Report, Division of Hazard Analysis, U.S. Consumer Product Safety Commission (2016)
- Lee, H.-H.: Finite Element Simulation with ANSYS Workbench 17. SDC Publications, Kansas (2017)
- Ansys Mechanical User's Guide-Release 18.1, Apr 2017
- Kesani, D.: Finite element analysis and optimization of refrigerator structure. *Int. J. Eng. Res. Rev.* **3**(1), 136–144 (2015)
- Kumar, G., Maheswari, U., Kulkarni, A., Gopal, S.T.: FEA simulation of refrigerator cabinet deflection. In: ANSYS India User Conference, Nov 2003

Chapter 3

Thermomechanical Analysis of a Cylindrical Liner



Subhadip Roy, N. Ganesh, A. Kumarasamy and P. Viswanathan

Abstract The liner of an internal combustion engine is subjected to a high temperature of combustion gas, which leads to high thermal stresses. In the present study, the thermomechanical analysis of a cylindrical liner was carried out to estimate the temperature profile and stress distribution. For thermal analysis, the input values of combustion gas temperature and its heat transfer coefficient were obtained by carrying out 1D thermodynamic cycle simulation using AVL BOOST[®] software. The temperature of the liner reduces from TDC to BDC. The temperature distribution of the liner was obtained by conjugate heat transfer analysis using ANSYS Fluent[®]. This temperature distribution was used for stress analysis of the liner using ANSYS[®]. The stress and deformation become maximum at an intermediate point near TDC. Near TDC, the gas pressure is more, but it acts on a smaller surface, as the piston goes towards BDC pressure force reduces and the surface area on which it acts increases gradually.

Keywords Liner · CFD · Heat transfer coefficient · Stress

3.1 Introduction

The reliability and performance of an internal combustion engine are limited by the maximum temperature of its components. Thermal loading of the engine components is increasing because of its increased output. This, in turn, causes higher thermal stress on the components. Hence, the temperature distribution and evaluation of stress on engine components, e.g. piston, liner, cylinder head, are important parameters for engine durability. Work has been carried out by various researchers to determine the temperature of the engine components, and various materials have been used to control their temperature and stress.

S. Roy (✉) · N. Ganesh · A. Kumarasamy · P. Viswanathan
Combat Vehicles Research and Development Establishment, Chennai, India
e-mail: subhadip.roy@cvrde.drdo.in

Heat transfer model to predict the transient operation of the turbocharged diesel engine was developed. This model included correlations for the convective heat transfer coefficient of a different part of the engine [1]. The piston was analysed by considering the lubricating oil film, the secondary motion of piston and piston ring. The boundary conditions for numerical simulation were verified with experimental results and were used to predict the temperature distribution of a newly developed engine [2]. The performance of the diesel engine was studied by using various materials of the liner. The aim was to select suitable material in order to minimize the heat loss through the cylinder wall. Low thermal conductivity materials with the required mechanical properties were considered for this purpose [3]. The effects of three types of coating, viz. ceramic (PSZ), Al_2O_3 and nickel chrome, on the liner were compared in terms of thermal stress, heat flux, thermal gradient and nodal temperature. The analysis was done numerically by ANSYS software. Al_2O_3 was found to be the best in this respect [4]. Finite element analysis is very helpful for the thermomechanical analysis of the liner, as it is difficult to analyse the actual working condition. This helps in designing the component with more durability [5].

Considering the previous research work, it can be concluded that the thermomechanical analysis of the liner is very important to ensure the proper operation of the engine. Hence, the aim of the present paper is to study the temperature distribution of a liner of a 600 hp engine and stress developed in the liner at full load condition rated speed (3300 rpm).

3.2 Methodology

CAD model of the liner analysed in the present study is shown in Fig. 3.1. The liner is surrounded by coolant passage with one inlet and two outlets. The geometric model was created using Creo Elements/Pro (Pro/ENGINEER) software and was transferred to ANSYS Fluent[®] software to carry out CFD study. The temperature distribution was obtained from this study, and the obtained distribution was used to carry out a stress analysis.

3.2.1 CFD Study

During the CFD study, steady-state conjugate heat transfer analysis was carried out to analyse conduction through the liner and convection of coolant together. For carrying out the analysis, the heat transfer coefficients and temperatures of combustion gas at the various positions of the piston in the liner are required. They were obtained (at an interval of 20° rotation of crank angle) at full load condition from the thermodynamic

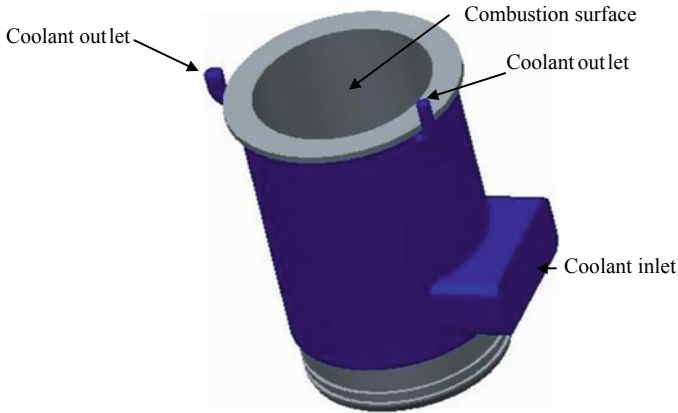


Fig. 3.1 Liner with the coolant passage

simulation by AVL BOOST® software. As the analysis was carried out in the steady state, the heat transfer coefficients and temperatures of combustion gas at the various positions of the liner needed to be averaged. During this averaging, data for all positions of the piston (0–720°) were used.

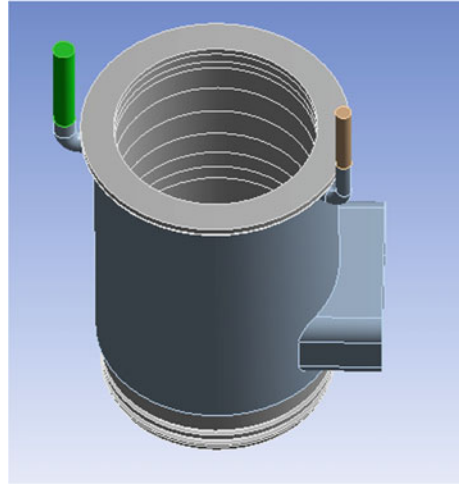
The liner is not subjected to the same combustion gas temperature and heat transfer coefficient from TDC to BDC. Hence, it was divided into nine segments (Fig. 3.2). The height of each segment corresponds to the height traversed by the piston during 20° crankshaft rotation (e.g. the distance covered during 0–20° crankshaft rotation represented the height of the first segment from TDC, and the distance covered during 160–180° crankshaft rotation represented the height of the segment just before BDC). Depending on the movement of the piston, each segment is subjected to different combustion gas temperatures and heat transfer coefficients. Crankcase temperature and heat transfer coefficient were applied to the portion below BDC. During the averaging procedure, it was assumed that, at any stage, the segments above and below the piston are at combustion temperature and heat transfer coefficient and at crankcase temperature and heat transfer coefficient, respectively.

Finally, the temperature and heat transfer coefficient of each segment were averaged as follows.

$$t_{g,average} = \frac{\sum ht}{\sum h}$$

$$h_{g,average} = \frac{\sum h}{\text{Number of segment}}$$

Fig. 3.2 Liner after segmentation



The coolant flow rate around the liner was considered to be 52 lpm. The velocity inlet was applied to the coolant inlet and pressure outlet was applied to the coolant outlet. The averaged temperatures and heat transfer coefficients were applied to each segment of the inner side of the liner. The coolant inlet temperature was assumed to be 118 °C.

The model used for the analysis was SST $k-\omega$. This model takes advantage of both $k-\omega$ and $k-\varepsilon$ models. It uses the $k-\omega$ method near the wall and $k-\varepsilon$ method away from the wall.

3.2.2 Stress Analysis

The temperature distribution was obtained by CFD analysis. Subsequently, the resultant temperature and heat transfer coefficient were used for stress analysis of the liner (Fig. 3.3). During stress analysis, the coolant domain was suppressed. Fixed boundary condition in the radial direction was applied to the top rim of the piston (Fig. 3.4). The stress analysis of the liner was carried out for various positions of the piston. In the first case, the pressure was applied only in the topmost segment, as pressure due to combustion gas acts on this segment only. The value of applied pressure was equal to that of combustion gas during first 20° rotation of the crankshaft from TDC (obtained by AVL BOOST® software). By this analysis, the stress and deformation of the liner for this position of the piston were evaluated. In the next study, the pressure was applied only in the topmost and the next segment, as pressure due to combustion

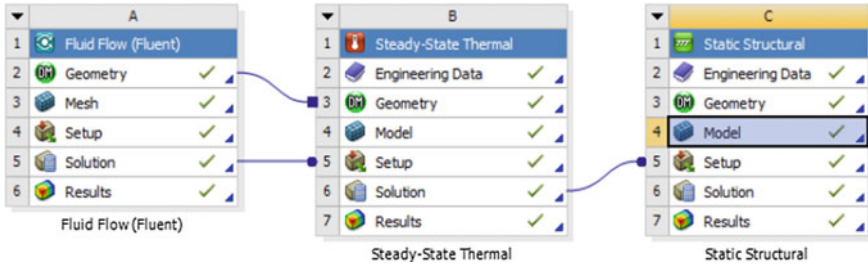


Fig. 3.3 Coupled analysis sequence

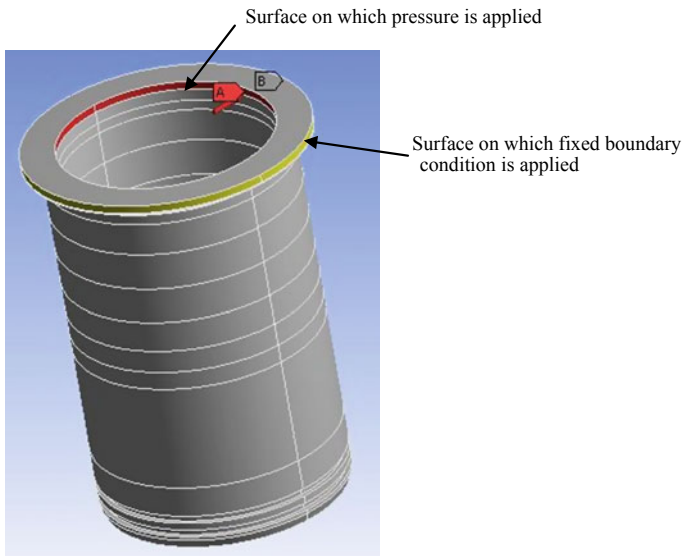


Fig. 3.4 Stress analysis of the liner at piston position of 20° crankshaft rotation from TDC

gas acts on this segment only. The pressure value equals the value during the first 20–40° rotation of the crankshaft from TDC (obtained by AVL BOOST® software). The process was continued for 9 cases (180° crankshaft rotation).

3.3 Results and Discussion

The temperature distribution, stress and deformation of the liner were obtained by CFD study (conjugate heat transfer analysis) and stress analysis.

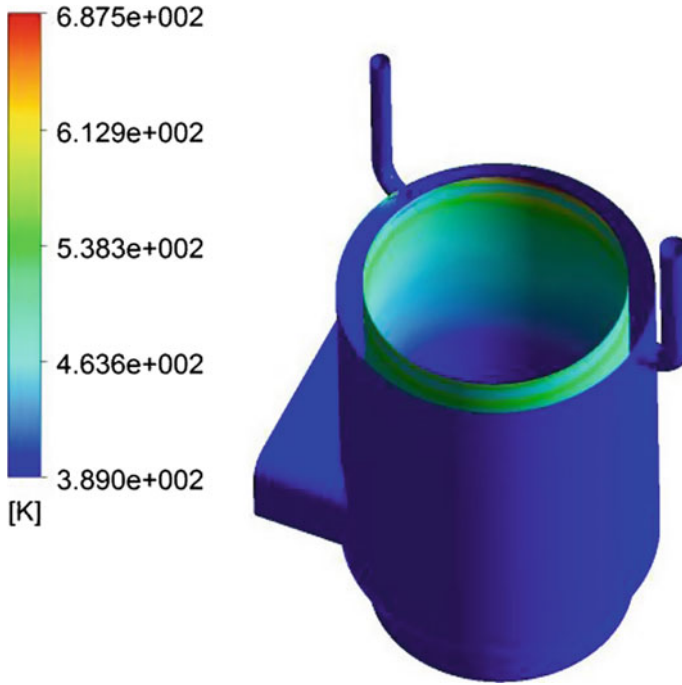


Fig. 3.5 Temperature distribution obtained by CFD analysis

3.3.1 *CFD Study*

The temperature distribution was obtained by CFD study (conjugate heat transfer analysis) and is shown in Fig. 3.5. It shows that the temperature of the inner side of the liner decreases gradually from top to bottom. It can be explained by considering the fact that the upper portion of the liner remains exposed to combustion gas to a more extent. The time for exposure to combustion gas reduces gradually from top to bottom.

3.3.2 *Stress Analysis*

Stress analysis was carried out for 9 positions of the piston in the liner during the power stroke (at a 20° interval from TDC to BDC). Equivalent stress (von Mises stress), shear stress and total deformation were evaluated at each position. It was observed that at each position of the piston, stress and deformation at a different location of the liner follow a similar pattern (maximum and minimum values occur

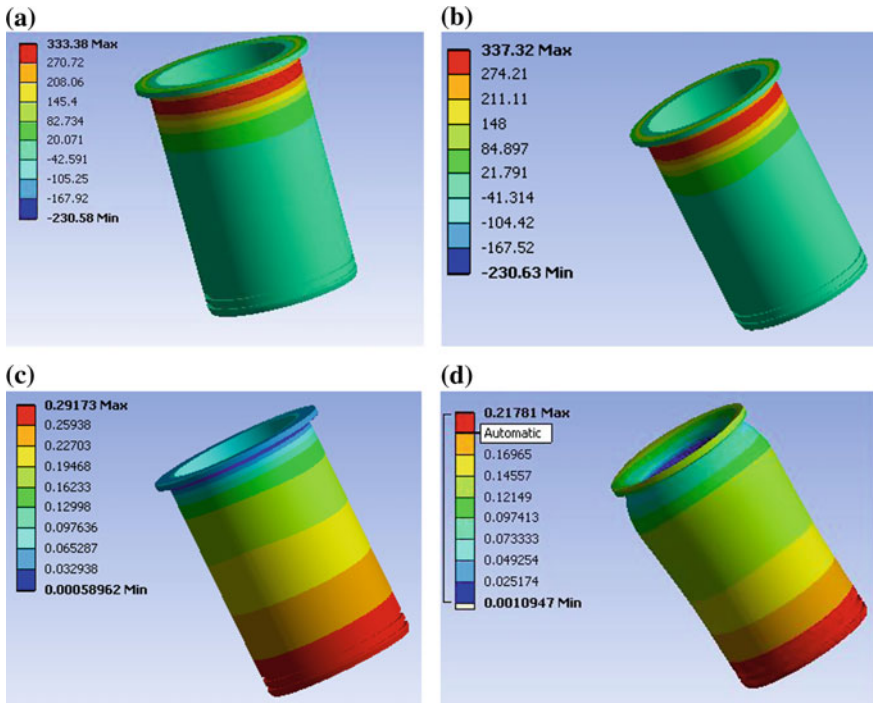


Fig. 3.6 **a** von Mises stress of the liner at piston position of 20° crankshaft rotation from TDC. **b** von Mises stress of the liner when the piston is at BDC. **c** Deformation of the liner at piston position of 20° crankshaft rotation from TDC. **d** Deformation of the liner when the piston is at BDC

at the similar places in all cases). Stress and deformation pattern for the two extreme cases (at TDC and BDC of the piston in the liner) are shown in Fig. 3.6. In all conditions, stress reduces from top to bottom and deflection increases from top to bottom. It can be explained by considering the fact that pressure and displacement constrained are applied only in the top position.

The maximum values of stresses and deformation of the liner at each position of the piston are shown in Fig. 3.7. It is seen that the maximum value takes place at some intermediate position of the piston. It can be explained by considering the fact that the gas pressure is the maximum when the piston is at TDC, but it acts on the minimum surface area. The value of pressure starts to decrease as the piston moves down, but the area exposed to pressure starts to increase simultaneously. Hence, the effect of pressure becomes the maximum at some intermediate position. The value of stress and deformation changes accordingly.

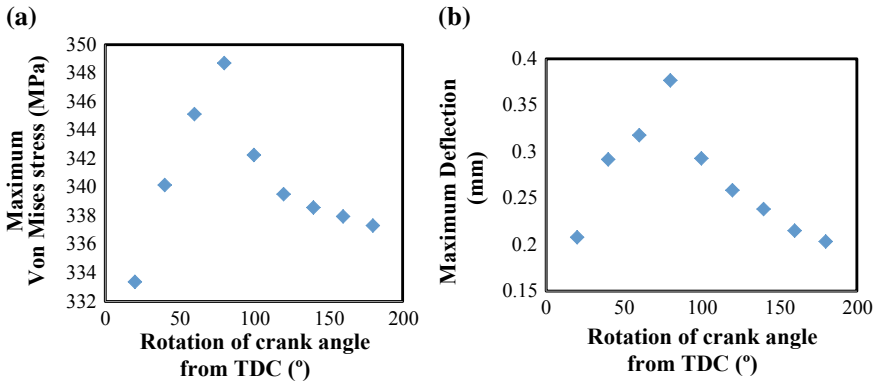


Fig. 3.7 **a** Maximum value of von Mises stress of the liner w.r.t different positions of the piston. **b** Maximum value of deflection of the liner w.r.t different positions of the piston

3.4 Conclusion

The temperature of the liner decreases from top to bottom. Stress and deformation of the liner at different positions follow the same pattern during all positions of the piston (maximum and minimum values occur at the similar places in all cases). Both maximum stress and deformation become maximum at some intermediate position of the piston. In all positions, the stress values reduce from top to bottom as the displacement was arrested at the top rim of the liner and deflection gradually increases from top to bottom.

References

- Galindo, J., Lujan, J.M., Serrano, J.R., Dolz, V., Guilain, S.: Description of a heat transfer model suitable to calculate transient processes of turbocharged diesel engines with one-dimensional gas-dynamic codes. *Appl. Therm. Eng.* **26**, 66–76 (2006)
- Lu, X., Li, Q., Zhang, W., Guo, Y., He, T., Zou, D.: Thermal analysis on piston of marine diesel engine. *Appl. Therm. Eng.* **50**, 168–176 (2013)
- Dineshkumar, S., Sriprashanth, V.: IC engine wet liners thermal analysis. *Int. J. Eng. Sci. Res. Technol.* **4**, 489–496 (2015)
- Anand Kumar, M., Prasad Rao, A.A.V., Hari Narayana Rao, J.: Design and analysis of dry cylinder liners used in diesel engines. *Int. J. Sci. Eng. Adv.* **3**, 518–526 (2015)
- Shinde, S., Jadhav, P.V., Jadhav, D.B.: Thermo mechanical analysis of cylinder liner. *Int. J. Eng. Res. General Sci.* **4**(3), 296–306 (2016)

Chapter 4

Mathematical Model for Built-in Dishwasher to Study Door Open and Close Forces and Sealing with Monte Carlo Simulations



Krishna Chaitanya Kusupudi, Amit Mandal and Deeptiranjana Barik

Abstract The objective of the study is to demonstrate the development of a mathematical model for a built-in dishwasher to study door open and close forces and sealing. A mathematical model is used to compute several characteristics associated with the closing and latching of the door of built-in dishwasher. The input file to the mathematical model consists of rows and columns of numerical data. Most of the columns represent relevant drawing dimensions that influence the door close and latch event. Each row represents a unique value of drawing dimension and the variance that is determined using the tolerance of the dimension. The outputs of the mathematical model are door open and close forces, gasket compressions (minimum and maximum), force gradient and door angle at the final position. This mathematical model is further used in Monte Carlo simulation to optimize door opening/closing forces and robust sealing design. To carry out Monte Carlo simulations, a mathematical model is embedded and the input file is modified in such a way that each unique value is statistically determined. Each row represents a scenario of values corresponding to the drawing dimensions. The output of this study needs data analysis of different outcomes and their chances of occurrence.

Keywords Door forces · Sealing · Latch · Tub seal · Mathcad · Monte Carlo

Nomenclature

$f(x)$	Seal force (N)
$h(x)$	Height of the compressed area (mm)
$L(x)$	Latch force (N)
LL	Lower limit (dimensionless)
$M1$	Seal moment (N-mm)
$M2$	Latch moment (N-mm)

K. C. Kusupudi (✉) · A. Mandal · D. Barik
Global Technology and Engineering Centre, Whirlpool of India Ltd., Pune, India
e-mail: krishna_c_kusupudi@whirlpool.com

© Springer Nature Singapore Pte Ltd. 2020
C. Li et al. (eds.), *Advances in Engineering Design and Simulation*,
Lecture Notes on Multidisciplinary Industrial Engineering,
https://doi.org/10.1007/978-981-13-8468-4_4

TL Threshold limit (dimensionless)

UL Upper limit (dimensionless)

4.1 Introduction

A dishwasher is an electrically operated device for washing dishes and cutlery [1]. Unlike manual cleaning, which relies mainly on hand washing to remove soil, the mechanical dishwasher cleans by spraying hot water onto the dishes. It starts with the wash cycle, and a mixture of water and dish soap is pumped into rotating spray arms which spray on dishware [2]. Once the wash cycle is completed, the water is drained and freshwater enters the tub by means of an electromechanical solenoid, and then the rinse cycle begins. In the final drying cycle, the water is drained and the moisture on dishes is taken away using one of the drying methods.

Dishwashers are typically available to choose between built-in and free-standing model. The best choice depends on individual needs, kitchen layout and preferences. A built-in dishwasher as shown in Fig. 4.1 which fits beneath the countertop flushes to kitchen cabinets. This provides a neat, streamlined look, which homeowners generally prefer. A free-standing dishwasher is covered on all sides and on the top, so one can place it anywhere in the kitchen.

The appropriate door opening and closing forces and proper sealing are essential prerequisites for the acceptable functioning of a built-in dishwasher and very critical from the quality point of view. The door opening and closing forces must be in the acceptable range so that customers feel comfortable in opening and closing the door. Sealing must be water leak proof since water leakage is not acceptable. Door forces and sealing depend on multiple factors such as the latch system, sealing interface, gasket compressions, and door- and tub-dimensional variations.

The sealing of a dishwasher occurs when the sealing surface of the inner door as shown in Fig. 4.1 comes in contact with tub seal and compresses it to an increasing extent as the door is closed. The extent of the tub seal that is compressed increases with decreasing door angle. The door latch engages the strike plate at the small door opening angles. The latch provides pull-in force that is balanced by the force required to compress the tub seal. The final angle of the door is when the seal compression is balanced by latch pull-in. A mathematical model is developed for a built-in dishwasher to study door open and close forces and sealing. The outputs of the mathematical model are door open and close forces, gasket compressions (minimum and maximum), force gradient and door angle at the final position. This mathematical model is further used in Monte Carlo studies to understand all different part variations which could occur due to the manufacturing process. It is important to capture a larger sample size, and Monte Carlo simulations really help to simulate a large sample size in quick time.

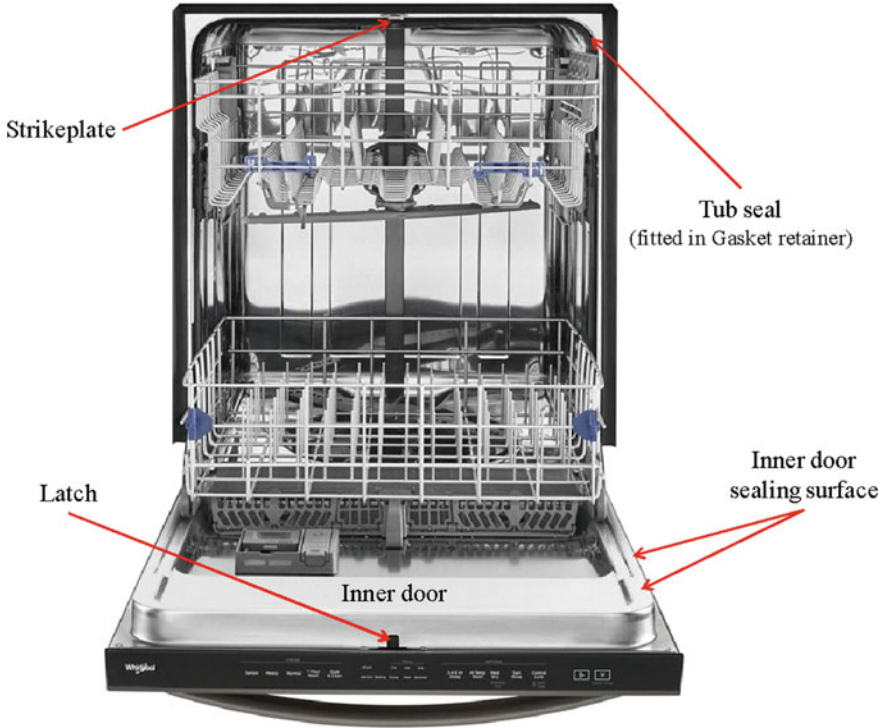


Fig. 4.1 Dishwasher parts influencing door open and close forces and sealing

4.2 Mathematical Model

Conventional FEA-based simulation method (a three-dimensional simulation carried out in LS-DYNA implicit [3] or ANSYS [4]) is used to calculate door open and close forces, gasket compressions and door angle at the final position of the dishwasher door at closed and latched conditions. The method is limited to study fewer sample sizes due to preprocessing and solving time. To perform variation studies on a larger sample size, the conventional FEA simulation method was found to be inefficient. It is observed that there is a need of alternative methods to perform variation studies on a larger scale, using 500 sample sizes or greater to understand the robustness of the dishwasher sealing system and door open and close forces.

A mathematical model is developed in Mathcad [5] to replace the conventional FEA simulation method and also to carry out variation studies. The mathematical model has the following assumptions:

- Two-dimensional model [dimensions of dishwasher are considered from left to right (X) and bottom to top (Y)].
- Tub seal channel represented by a vertical line.

- Tub seal cross section is uniform throughout the channel length.
- Friction between parts is not considered.

Figure 4.2 shows the schematic that describes the methodology for working of a mathematical model. From the figure, it can be seen that inputs to the mathematical model are tub seal closure load deflection (CLD) curve, latch curves (latch pull-in and pull-out force versus strike plate travel) and part dimensions. Outputs are balance point, door angle, maximum forces to open and close the door, minimum force gradient, minimum and maximum seal compressions. Table 4.1 compares the attributes for the conventional FEA simulation method and the mathematical model. It can be seen from the table, the time taken by a mathematical model to solve one iteration is remarkably fast as compared to the conventional FEA simulation method.

The general workflow of the mathematical model is shown in Fig. 4.3. It comprises of seven steps that have to be followed. In Step 1, need to read all inputs which are tub seal CLD, latch curves and part dimensions. The curves obtained for the latch and seal are converted to linear piecewise functions in Step 2. In Step 3, the dimensions

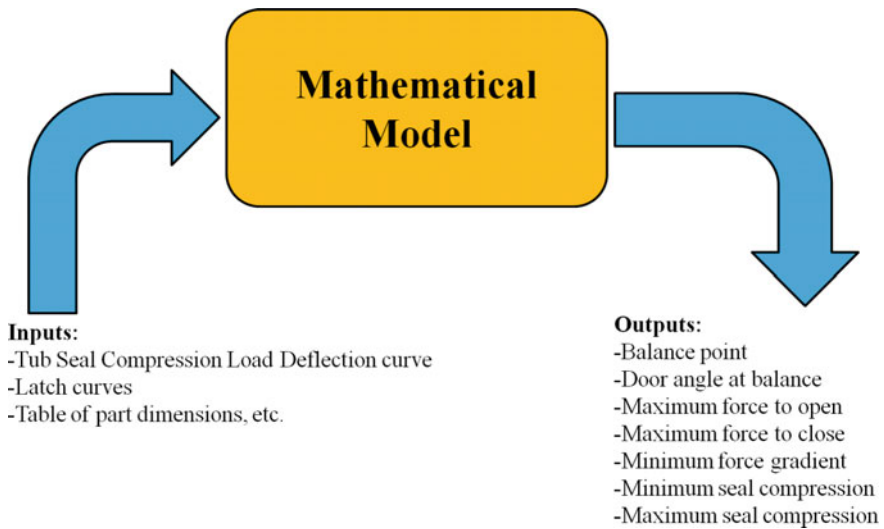


Fig. 4.2 Inputs and outputs of a mathematical model

Table 4.1 Comparison of conventional FEA simulation method and the mathematical model

Attributes	Conventional FEA simulation method	Mathematical model
Preprocessing time	~12 h	~5 min
Solving time	~4 h	~10 s
Feasibility	Only for fewer samples	A large number of samples
Automation	Difficult	Easy

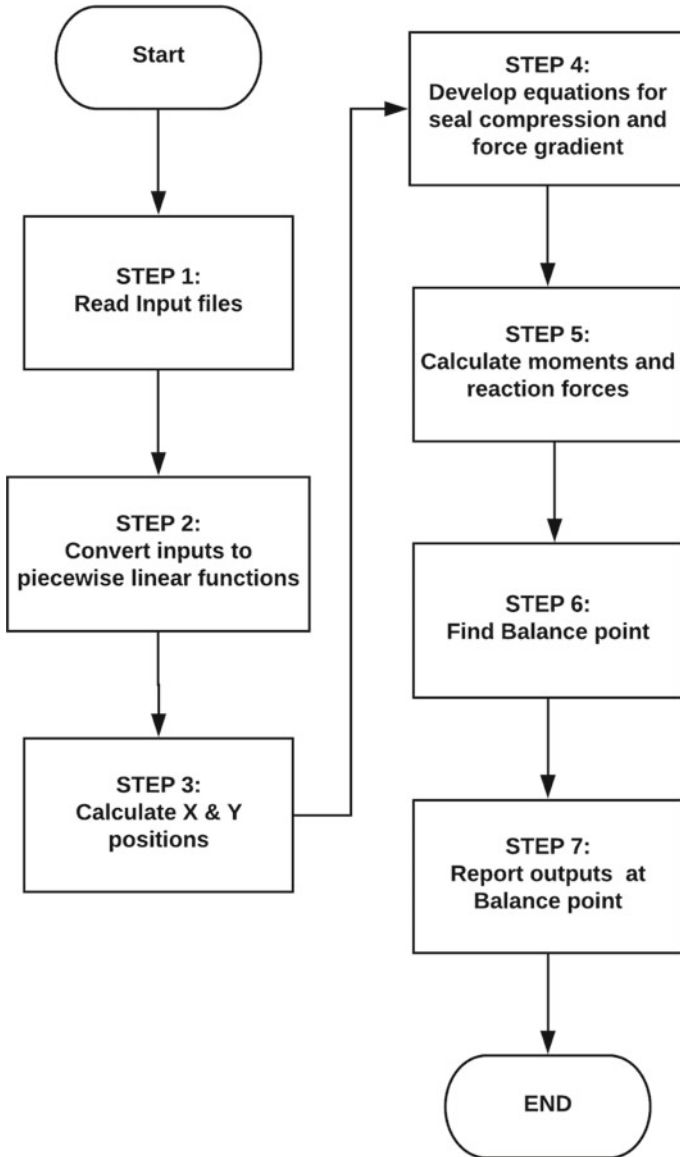


Fig. 4.3 Workflow in a mathematical model

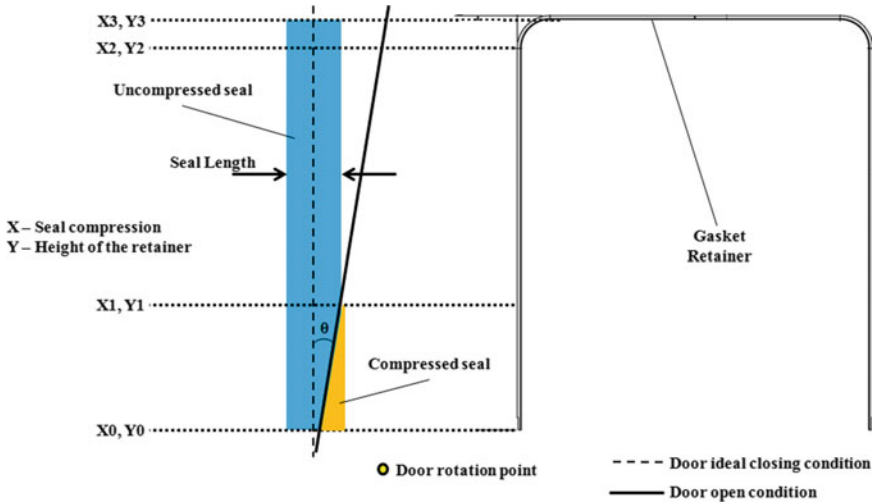


Fig. 4.4 Representation of sealing system of a dishwasher

are stacked up to calculate the X and Y position of the top and bottom sealing surfaces. This is generally done at a vertical position (door opening angle, $\theta = 0^\circ$) as shown in Fig. 4.4. Step 4 comprises of equations to calculate seal compression as a function of elevation and seal gradient. In Step 5, moments and resultant forces are calculated at every small door angles. Intervals depend on the speed of calculation and accuracy. In Step 6, the balance point is obtained where seal moment equals to latch moment. Finally, in Step 7, outputs are reported out at the balance point.

A schematic diagram of the built-in dishwasher sealing system is shown in Fig. 4.4. Tub seal is fitted in a channel called gasket retainer. At an angle θ , uncompressed and compressed seal areas are shown. X represents seal compression, and Y represents the height of the retainer which is used to calculate seal force at different door angles.

In Fig. 4.5,

- Seal force is represented by $f(x)$ for the compressed area (Y_0 to Y_1) at door angle θ .
- The height of the compressed area is represented by $h(x)$.
- Seal moment is represented by

$$M1 = \int_{x_0}^{x_1} f(x) * h(x) \tag{4.1}$$

- During door closure, strike plate on tub travels into the latch mechanism of the door. Due to this travel, a force is exerted which is called latch force and it is represented by $L(x)$.
- Latch moment is represented by

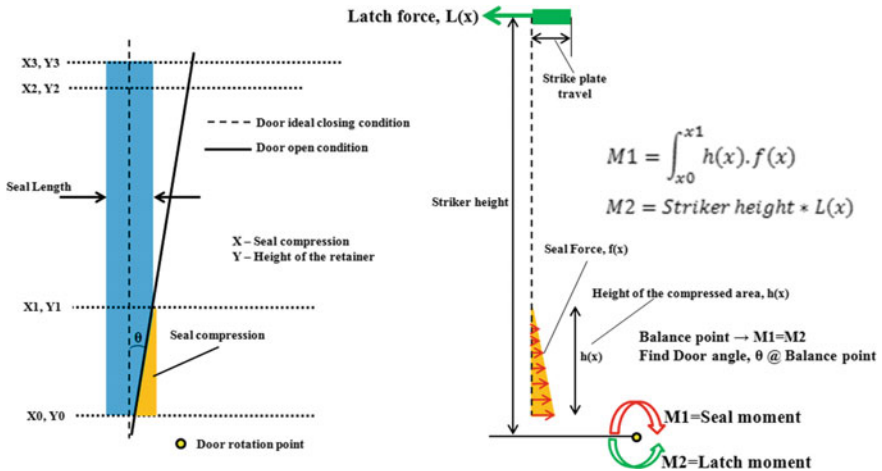


Fig. 4.5 Door balance representation of a dishwasher

$$M2 = \text{Striker height} * L(x) \tag{4.2}$$

- When dishwasher door is latched, there must be balance attained in the system which is represented by

$$M1 = M2 \tag{4.3}$$

During the dishwasher door closure, tub seal compression increases with a decrease in door angle. The door latch engages the strike plate at the small door opening angles as shown in Fig. 4.5. The latch provides pull-in force that is balanced by the force required to compress the tub seal. The final angle of the door is considered when the seal compression is balanced by latch pull-in and that is called as a balance point as shown in Fig. 4.6 where all the outputs are calculated.

4.3 Monte Carlo Simulations

Monte Carlo simulation popularly known as the Monte Carlo method is used to model the probability of various outcomes in a process that are tedious to predict due to the intervention of random variables. This technique is used to understand the impact of risk and uncertainty in prediction and forecasting models [6]. In our current work, Monte Carlo simulations (variation studies) are performed to understand the robustness of the sealing system and door open and close forces which are essential prerequisites for the acceptable functioning of a built-in dishwasher.

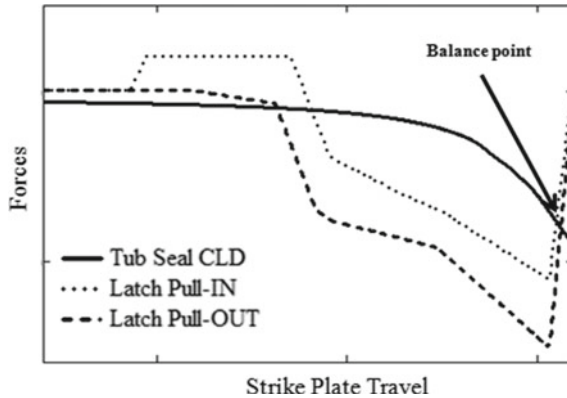


Fig. 4.6 Graphical representation of balance point in the mathematical model

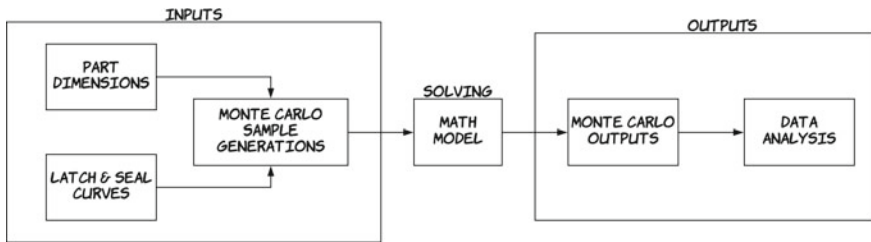


Fig. 4.7 Flowchart of a Monte Carlo simulation

Monte Carlo simulation setup is generated by embedding mathematical model into an MS Excel workbook. Flowchart of a Monte Carlo simulation used in this work is shown in Fig. 4.7. A dedicated MS Excel workbook is employed by the user to prepare the input file for Monte Carlo simulations. It contains a collection of worksheets, each of which represents a drawing with one or more views from the drawing. The user enters a nominal value and tolerance for each selected dimension of the drawing. The user also specifies the number of simulation runs to construct in the input file. A normal distribution is calculated using the nominal and tolerance assigned by the user. The MS Excel workbook automatically generates an input file with each value randomly selected from the corresponding normal distribution. Each row in the input file represents a unique scenario. Other user-defined inputs are the seal CLD curve and latch curves which are also defined with some tolerances.

To carry out Monte Carlo simulations, a macro was executed to run a Mathcad program embedded in MS Excel with inputs defined in respective worksheets. Macro was executed based on a number of samples (e.g., for 500 sample runs, the macro is executed 500 times) and reported output in a separate worksheet. Each row in the output worksheet defines the outcome of a unique scenario; see Fig. 4.8.

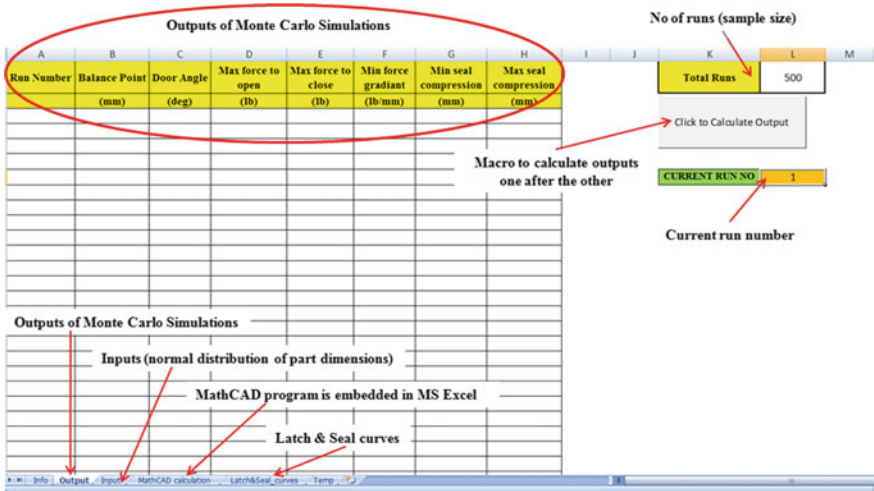


Fig. 4.8 Snapshot of a Monte Carlo simulation template in MS Excel workbook

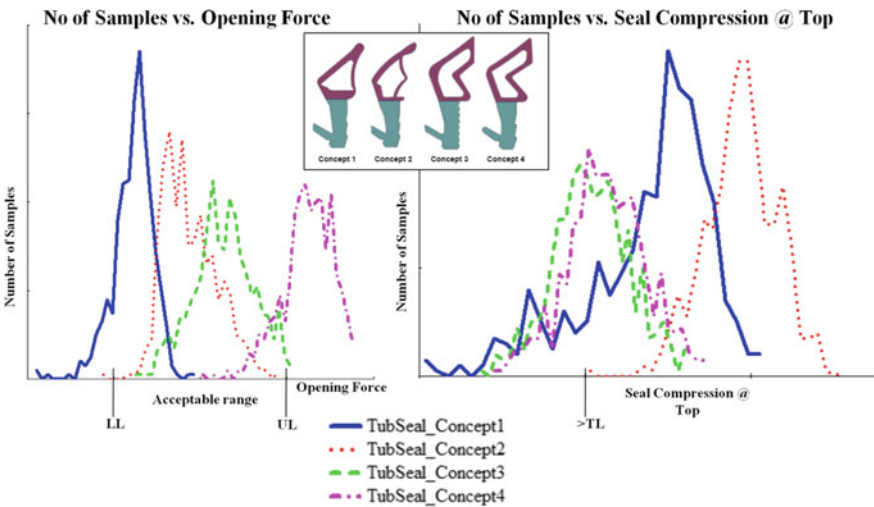


Fig. 4.9 Example of a data analysis of Monte Carlo outputs of various tub seal concepts

In Fig. 4.9, an example of Monte Carlo simulation results is shown for four different tub seal concepts which vary in design. For all concepts, the larger sample size was considered and sample data kept the same to choose the best concept which survives variation in the system. Opening forces must be in the acceptable range between lower limit (LL) and upper limit (UL). Seal compressions at the top must be greater than a certain threshold limit (TL). Opening forces in concept 2 and concept 3 are in an acceptable range for a maximum number of samples. Seal compression

at the top in concept 2 is greater than TL for all samples. A similar study was carried out for the remaining outputs as well. This study needs data analysis of different outcomes and their chances of occurrence. Trade-offs need to be understood well. Finally, the concept which was most favorable in all outputs was recommended to the design team for prototyping.

4.4 Correlation

Tub seal design concept 2 was finalized through data analysis of Monte Carlo outputs and proceeded for physical prototyping. New tub seal physical prototypes were installed in built-in dishwashers. A large number of physical samples were tested to capture all possible variations affecting door open and closing forces and seal compressions. Door open and close forces and balance point were tested on random samples.

Physical test results were compared with Monte Carlo simulation results. There is a quite good correlation achieved. For example, a comparison of door opening force between physical test and Monte Carlo simulation results is shown in Fig. 4.10.

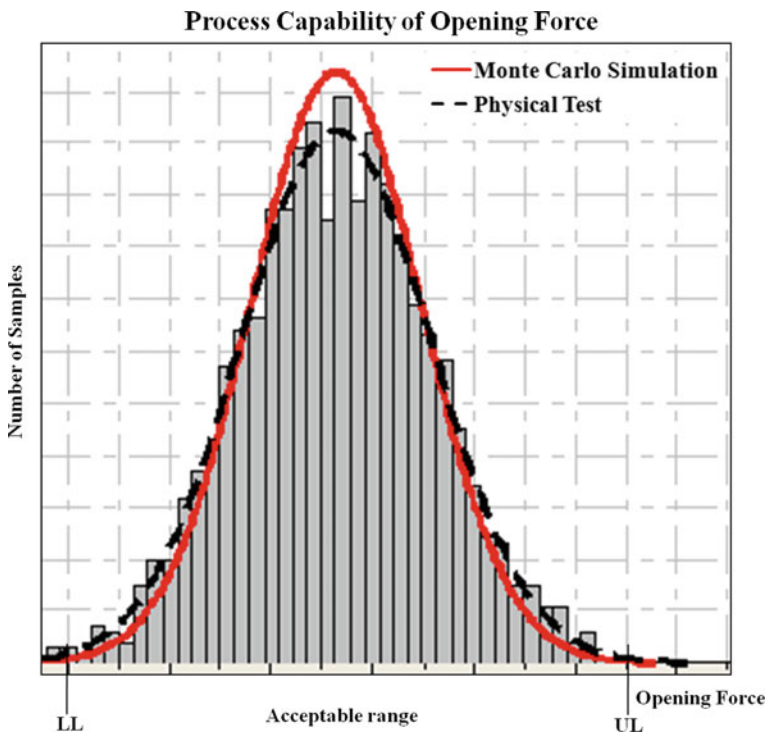


Fig. 4.10 Example of a correlation between the physical test and Monte Carlo simulation results

Simulation captured most of the variation as in physical scenario. From this study, it shows that the system is very robust in which physical variations are within predicted limits.

4.5 Conclusion

Conventional FEA-based simulation method was used to calculate door open and close forces, gasket compressions and door angle at the final position of the dishwasher door at closed and latched conditions. This method was limited to study fewer sample sizes (<10 samples) due to computational time and cost. To perform variation studies on a larger sample size (>500 samples), conventional FEA-based simulation method is not feasible. As an alternative method, a mathematical model was developed in Mathcad which reduced solving time tremendously (less than 10 s). This gave us the opportunity to carry out variation studies with larger sample size. Monte Carlo simulations carried out with all feasible variations which are statistically determined. The output of these studies is analyzed based on their outcomes and chances of occurrence. Quite good correlation is observed between physical test and Monte Carlo simulation results.

This work has helped us to optimize the design development of tub seal, strike plate, latch mechanism and inner door sealing surface and also provided us with a lot of insight considering all possible variations. Trade-offs are obtained and help us to take the right design decision to make the highest quality product.

Note: Due to a client confidentiality agreement, math model and exact values are not provided.

References

1. Yashwant, C.Y., Kawade Sudhir, B., Dhumal Chetan, A., Take Pradip, R.: Automatic dishwashing machine. *IJSRD Int. J. Sci. Res. Dev.* **3**(11) (2016)
2. Leipnitz, A.W.: Automatic dishwashing products. In: *Proceedings of the Detergents in Depth '80 Symposium* sponsored by the Soap and Detergent Association (1980)
3. LS-DYNA Implicit Support [Online]. Available: <https://www.dynasupport.com/howtos/implicit>
4. ANSYS Support [Online]. Available: <https://www.ansys.com/en-in/support>
5. Aan, A., Heinloo, M., Aarend, E., Mikita V.: Analysis of four-stroke cycle internal combustion V-Engine in MathCAD environment. In: *8th International DAAAM Baltic Conference "Industrial Engineering"*, 19–21 Apr 2012
6. Pons, D.J., Raine, J.K.: Simulation of key performance characteristics under uncertainty. *J. Eng. Manuf. (Proceedings of the Institution of Mechanical Engineers Part B)*. First submitted 24 June (2003) as 'Combining quantitative and qualitative variables in engineering design', revised 28 Nov 2003, revised 10 Mar (2004)

Chapter 5

Numerical Simulation of Electric-Bus Windshield Demisting in Winter Conditions



Bharat Kumar Nuthi, S. Vijayaraghavan and D. Govindaraj

Abstract Driver visibility in the automotive industry is a major source of safety design concern for the manufacturers. The mist that forms on the windshield during winter season would affect the driver's visibility, so in winter climate the water vapor film is originated inside the windshield. In order to demist, warm air is passed at a certain velocity and relative angle to the windshield, so that it will reduce the thickness of this water vapor film on the windshield, which improves driver's visibility. Experimental testing is extremely time-consuming as well as quite expensive. CFD simulations have been able to shorten the development cycle and reduce cost. Numerical simulation has been studied for the demisting process under a transient condition of condensed water vapor thickness on the windshield. Therefore, a well-designed HVAC system will help to reduce this water vapor film thickness to an accepted level for driver visibility as per safety norms.

Keywords Defogging · Windshield demister · Bus demister · CFD simulation · Star CCM+ · HVAC · Demist unit

List of Notations

HVAC Heating, Ventilation and Air Conditioning
PTC Positive Temperature Coefficient
CFD Computational Fluid Dynamics
 μm Micrometer

B. K. Nuthi · S. Vijayaraghavan (✉) · D. Govindaraj
Pranav Vikas India Pvt Ltd., Faridabad, India
e-mail: Vijay.raghavan@pranavvikas.com

B. K. Nuthi
e-mail: Bharat.nuthi@pranavvikas.com

D. Govindaraj
e-mail: Govindarajd@pranavvikas.com

© Springer Nature Singapore Pte Ltd. 2020
C. Li et al. (eds.), *Advances in Engineering Design and Simulation*,
Lecture Notes on Multidisciplinary Industrial Engineering,
https://doi.org/10.1007/978-981-13-8468-4_5

5.1 Introduction

Automobiles are developed to minimize the travel time from one location to another. Nevertheless to function under any weather conditions is always a big challenge for manufacturers or OEMs. It is always important that one should feel comfortable inside it. As well as, it is more significant to provide proper visibility [1] conditions for the driver too. Visibility in the automotive industry is a major source of safety design concern. As per the vehicle test standard, 90% of driver's vision zone and 80% of overall windshield should be cleared within 10 min. Problems related to visibility can be in any form like rainwater on windshield, mist or fog inside or outside windshield or ice formation. To regulate all these and other comfort like cooling, heating, etc., inside cabin HVAC unit comes into action.

HVAC systems are quite helpful to regulate climate control and safety regulations in many ambient conditions. These units mostly control the cabin environment compare to outside surroundings. These units are very helpful to cool down the cabin temperature during the hot summer season and keep warm and cozy during winter conditions. HVAC units also play a key role in the defogging and deicing process. These units consist of several components like filter, heater, and evaporator which treats ambient air with respect to the application required inside the cabin.

This document basically presents the application of CFD to study demist or defog process with the help of hot air from the heaters by monitoring vapor film with respect to time on bus windshield. The airflow distribution on the windshield is also taken into consideration for this simulation because linearity in airflow on the windshield is the optimum parameter. All the necessary operations (pre-processing, solving, and post-processing) are performed in STAR CCM+.

5.1.1 Computational Modeling

Computational fluid dynamics is the approach to solve flow problems using numerical methods. It uses continuity equations of mass, momentum, and energy to solve the problems. These equations result into solution when boundary conditions are applied. Computational fluid dynamics is vastly used across different engineering domains to optimize efficient designs. This technique is also used in our current problem for simulating defogging phenomenon. As fog is formed inside the cabin of an automobile in low temperature or high humid conditions, it is important to eliminate this for safety regulations and visibility.

Computational domain for this simulation consists of a demist unit. This unit basically consists set of filter, blower, and PTC heater. There are two blowers placed inside the casing which draws ambient cold air, which then blows through the heater. The air gets warms up and passes through multiple ducts and enters into dashboard panel before hitting the windshield. The air which is having high temperature comes out from the multiple openings in the dashboard panel. When this hot air hits the

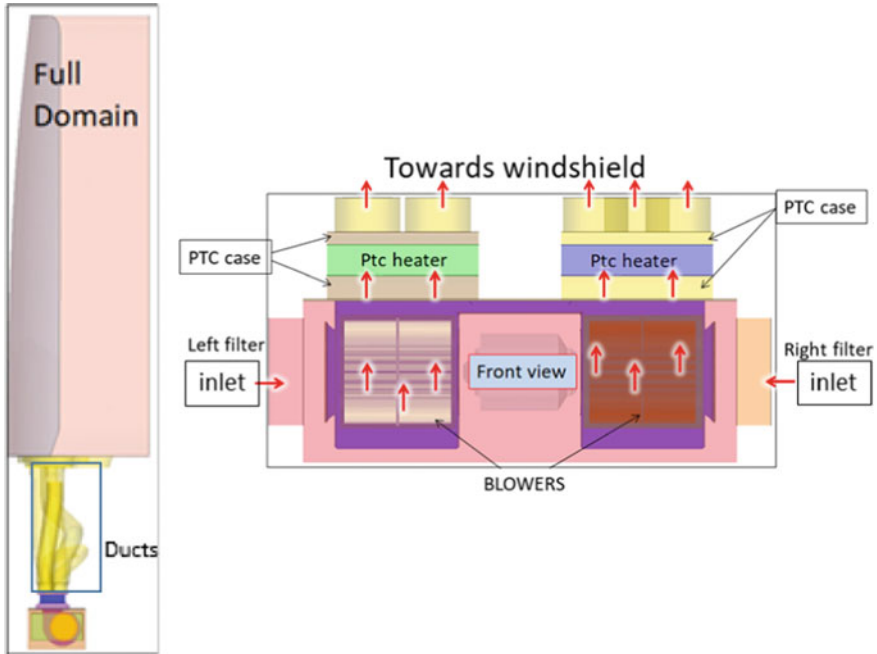


Fig. 5.1 Description of the full computational domain (left) and components of demist unit (right)

windshield, fog present on it starts to fade away. Indeed, this solves visibility issues faced by the driver. This computational problem is solved in two parts [2], due to its complex physics. Initially, CFD calculations ran for airflow distribution (to obtain airflow distribution and temperature) [2]. Later, defogging calculations were performed.

Initial calculations were performed for airflow and temperature distribution. The overall and complete geometry such as demist unit, ducts, and part of the cabin is considered for CFD simulation and is shown in Fig. 5.1. In left image (side view), complete domain is shown, whereas the image on the right describes the flow path from ambient to windshield.

Figure 5.2 (CFD calculations for defogging) shows a closer view of air escaping through small openings in dashboard panel, and these parts are considered for defog simulation.

As per the visibility zones, windshield is divided into different visible zones. Zones that are defined below (Fig. 5.3) are purely for simulation purpose, to resemble vision zones defined on the windshield.

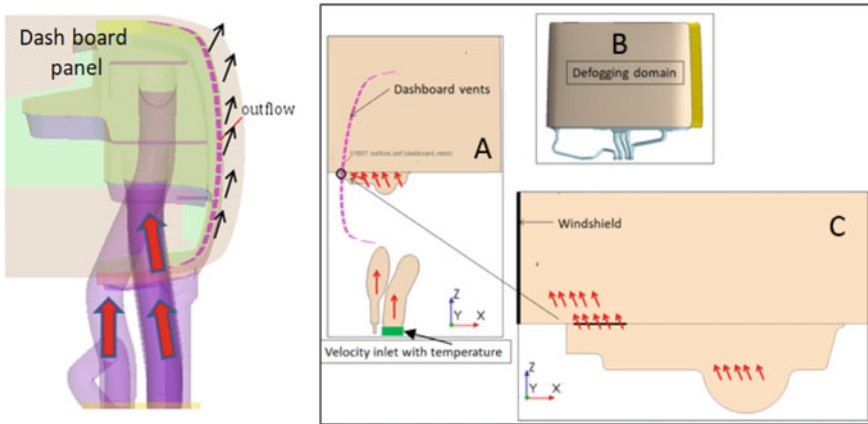
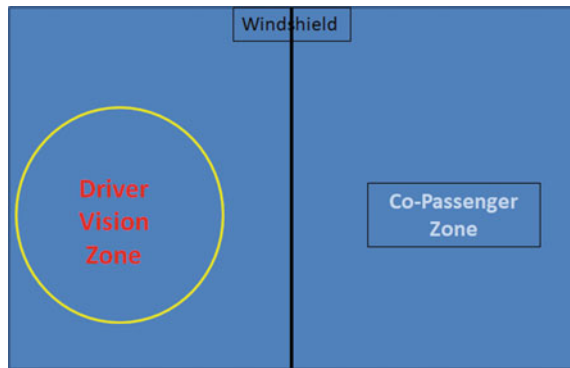


Fig. 5.2 Hot air passing through multiple ducts (left), flow description on plane section (right)

Fig. 5.3 Visibility zones on windshield (frontal view)



5.2 CFD Simulation

CFD plays a key role in estimating the results for different design iterations by solving partial equations which govern the fluid flow. As mentioned earlier, this problem is solved in two segments [2] due to complex physics. The first part of the calculation is performed for airflow distribution and temperature [2]. Volume mesh is generated using polyhedral cells. Realizable k-epsilon [1–3] is used to model turbulence. Here, “ k ” is a measure of energy in the flow and “ e ” is a measure of the dissipation rate. This turbulence model has well-established regime of predictive capability, numerically robust and stable. It exhibits superior performance for flows involving adverse pressure gradients, rotation, recirculation, and separation. Corresponding modeling approach is mentioned in Table 5.1. As for the first segment, steady-state calculation is considered [2]. Mesh independency was studied on both segments. Initial mesh was refined by 1.5 times, and acceptable solution convergence was achieved, respectively. With this change in mesh, refinement results have shown improvement

Table 5.1 Model used

Parameters	Model
Mesh count	16 million cells
Filters and PTC heaters	Porous region
Blowers	Moving reference frame
Turbulence	<i>k</i> -epsilon
Gas	Ideal gas
Energy source option	Total heat source

Table 5.2 Boundary conditions for defog simulation

Parameters	Boundary conditions
Fog layer thickness	10 μm
Vapor humidity	70%
Ambient temperature	-5 °C
Angle of attack (dashboard openings)	90°

in monitored values like velocities and temperatures, etc. Likewise, another iteration was carried out, again mesh was refined with the same order, and the results were alike. There was no change in the results, which confirms no further refinement of the mesh is required.

Once the flow velocities and temperature in each duct are obtained, these obtained values are mapped to the inlets of the individual ducts (portion just above the PTC heater casing highlighted in green. Image “A” of flow description on the plane section in Fig. 5.2). Once these values are mapped, the second segment of the simulation comes into the calculation. This simulation includes defogging [4] model while modeling the physics. It is a simplified approach to obtain defogging phenomenon in any fog-forming areas (like windshield, headlamps, etc.) [4]. This option consists of a film option which lets the user define its physics. Transient simulation was performed to monitor the defog effect with respect to time. Table 5.2 represents some of the boundary conditions.

5.3 Results

This section presents results for both cases steady-state results for velocity and temperature and transient results for defogging. Figure 5.4 shows the velocity distribution on the windshield. It’s observed that flow is much more evenly distributed on windshield toward co-passenger zone, whereas on the driver’s zone it needs to be improved. Figure 5.5 shows the temperature distribution on the windshield.

Flow from the demist unit develops and spreads over the windshield; the heat in the air starts effecting the thickness of the fog layer (Initial fog thickness 10 μm). As time progresses, fog starts to diminish and visibility is clear for the driver. This

Fig. 5.4 Velocity distribution on windshield

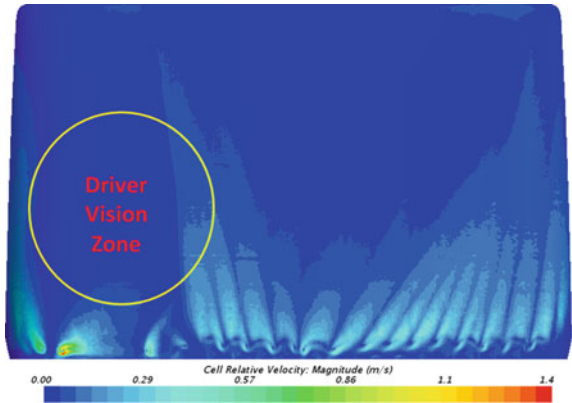
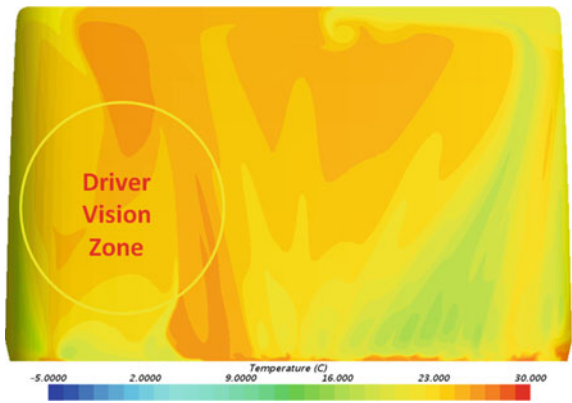


Fig. 5.5 Temperature distribution on the windshield



phenomenon is monitored with images captured for every half a second during the simulation process. The overview is presented in the below set of images at every half a minute [3]. At time zero seconds, the fog layer is completely blocking the visibility of the driver. Legend scale is shown from 0 to 8 μm for better visualization. It starts to defog from the bottom as the hot air is striking on the windshield and at time 210 s almost 95% of the fog is disappeared (Fig. 5.6).

5.4 Conclusion

The transient approach in CFD is useful in optimizing such phenomenon related to defogging and deicing. The existing design is in the further scope of improvement. It is observed the zone defined for driver visibility is receiving less flow and is not uniformly distributed on the windshield. If the flow is evenly distributed, it is possible that demist will occur in less time. As per the vehicle test standard guidelines 90% of

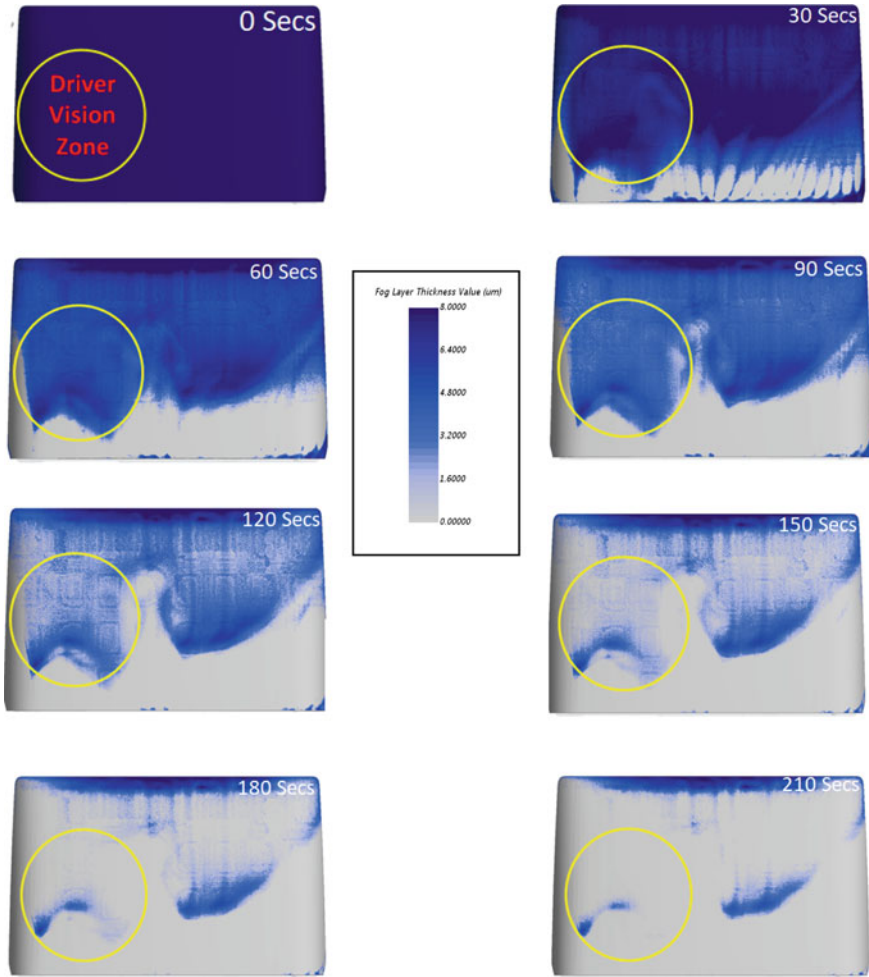


Fig. 5.6 Defog area on windshield

driver’s vision zone and 80% of overall windshield should be cleared within 10 min, however, in existing design, most of the windshield area is cleared in 210 s. Further optimization also includes an angle of openings as well as the shape of these openings present on dashboard panel. With proper opening shape and angle of attack, even flow distribution can be achieved. Considering all the change in parameters, over several iterations a proper efficient design, with the uniformly distributed flow over the windshield and fast defogging can be achieved, and CFD is the key approach.

References

1. Zolet TL, de Freitas Maia GF, Dutra GG, Pereira LV CFD and experimental correlation of the defrost flow and vehicle's windshield defogging COBEM, 24–28 October 2011. <https://docplayer.net/46849329-Cfd-and-experimental-correlation-of-the-defrost-flow-and-vehicle-s-windshield-defogging.html>
2. Sandhu, K.: Simulation of the windscreen defrost performance. Star European User Conference, 22–23 March 2011. <http://mdx2.plm.automation.siemens.com/sites/default/files/Presentation/15-jaguar.pdf>
3. Kitada, M., Asano, H., Kataoka, T., Hirayama, S. and Maruta, Y.: Prediction technology of transient defogging pattern by CFD—denso technical levi. 8(2) 2003. https://www.denso.com/jp/ja/innovation/technology/dtr/v08_2/dissertation19ic.pdf
4. Star CCM+ User manual, Version 11.06

Chapter 6

Simulation of a Screw Self-tapping Process



Kushagr Goyal, Sivaraman Rajan, Harish Krishnamurthy and Ravindra Venkataramu

Abstract With the ever-increasing demand to use lightweight materials in the automotive industry, automakers are keen on using plastics across their products. Plastics are predominantly held together using adhesives, screws, or snaps. Screws are promising when axial reinforcement between the components is desired. Self-tapping screws are now the preferred type, for its ease of assembly and cost. A self-tapping screw can tap its own hole as it is driven into the material. Such screws can be broadly classified into two categories: Thread-cutting screws (woods and metals) and thread-forming screws (plastics and thin metal sheets). Thread-forming screws form the threads by local deformation by displacing the material along its travel. Generation of these threads in plastic components using FE simulation is often tricky as it undergoes severe localized plastic deformations. This calls for the use of a unique FEM approach called Combined Eulerian Lagrangian (CEL), in which the screw and the plastic screw post are modeled using Lagrangian and Eulerian formulations, respectively. The Eulerian domain allows large localized deformations to accommodate plastic flow. This approach also enables the evaluation of the tightening torque in addition to the thread-formation pattern on the plastic component.

Keywords Combined Eulerian Lagrangian (CEL) · Self-tapping screw · Thread-forming and tightening torque

6.1 Introduction

The present times call for improved efficiency at a system level in pretty much every industry. One of the most important factors in improving efficiency and life of component systems is to reduce their weight. This leads to reduced inertial loads during dynamic operations and less wear and tear. The automotive industry is no different,

K. Goyal · S. Rajan · H. Krishnamurthy · R. Venkataramu (✉)
Inteva Products India Automotive Private Limited, Bengaluru, India
e-mail: RVenkataramu@intevaproducts.com

© Springer Nature Singapore Pte Ltd. 2020
C. Li et al. (eds.), *Advances in Engineering Design and Simulation*,
Lecture Notes on Multidisciplinary Industrial Engineering,
https://doi.org/10.1007/978-981-13-8468-4_6







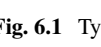
with its focus on weight reduction. It's also a very crucial factor in enhancing the performance and dropping the overall emission levels of a motor vehicle.

With the advent of new manufacturing technologies and research on polymer plastics, it has become ever more possible to replace more and more metal components with plastics. With clever design and careful material selection, plastic components can replace the metals in several areas. The plastic components are much lighter than their metal counterparts. They can also be manufactured at a much faster rate and at a lower cost (considering larger volumes). Plastic parts also do not suffer from any type of corrosion.

However, the plastic parts usually tend to display higher sensitivity to temperature, humidity, etc. They are also more susceptible to higher levels of wear and tear. Connecting these plastic components to each other requires different processes than metal parts. One of such processes is to use a self-tapping screw for assembly. Self-tapping screws tap their own hole as they are driven into the material. There are several different designs of self-tapping screws based on their ends, as shown in the image below (Fig. 6.1).

The type of screw to be used depends upon the application, material of the components to be fastened together, availability, and cost. Here, this work deals with the Type "B" self-tapping screw. Threads are created by the process of forming or cutting depending on the material. In plastics, these screws can displace the material and "form" the threads. On the assembly line, these screws reduce the process time by reducing the number of operations required for fastening the components together.

Self-tapping screws can produce a lot of stress in a component as they are driven into the material. They also cause severe localized deformations in order to form threads. This becomes a particularly difficult problem to simulate because of the large localized deformation. The usual approach of structural simulations is found to

TYPE DESIGNATIONS FOR TAPPING AND METALLIC DRIVE SCREWS				
Thread-Forming				
Type	Manuf.	A.S.A.	Federal	Notes
	A	A	A	Being replaced by Type AB
	AB	AB	none	Type B with Gimlet Point
	B	B	B	
	BP	BP	BP	Type B Thread with a Pointed Pilot
	C	C	C	
	SWAGE-FORM	SW	SW	
	U	U	U	






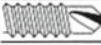


Type	Manuf.	A.S.A.	Federal	Notes
	F	F	CF	Thread-Cutting
	BF	BF	BF	
	1	D	CS	
	23	T	CG	
	25	BT	BG	
	InFast	none	none	Self-Drilling
	Teks	none	none	
	none	none	none	Thread-Rolling

Fig. 6.1 Types of self-tapping screws

be inadequate. This calls for a unique approach for simulating self-tapping process, called the Combined Eulerian Lagrangian (CEL) approach.

6.2 Combined Eulerian Lagrangian (CEL) Approach

The most common method of modelling in finite element analysis is considered to be the Lagrangian model of the elements. This type of element formulation is easy to implement and computationally less expensive to solve [1]. Here, the nodes are coincident with the material, and therefore, under the application of load, they both move together. Furthermore, the material inside each element is fixed and cannot move in or out of the element. This allows for easy application of boundary conditions and tracking of the free surfaces.

[2] However, with all its advantages, the Lagrangian formulation does suffer from the reduced accuracy of results in simulations with large deformations/strains. There are a couple of techniques used to reduce the effect of these large deformations. One of these techniques works by locally remeshing the domain as the simulation progresses. Another technique that can be used deletes the elements based on predefined criteria. Though these techniques can help improve the accuracy of the model, they increase the simulation time as they are more computationally expensive.

The Eulerian formulation of the elements can get us around the issue of large deformation/strain. Unlike a Lagrangian mesh, here the elements don't deform themselves but the material flows through them. Since the material can flow through elements, the domain must be modeled larger than required so that no material can flow out of it; otherwise, the material that leaves the domain is no longer considered in the simulation. The basic difference between the Lagrangian and the Eulerian formulations can be visualized in the image below (Fig. 6.2).

It may be observed that since the mesh itself does not deform, it can handle large deformations easily. However, there is difficulty in tracking the free surfaces as the material boundary differs from the nodal boundary. This also makes it difficult to apply boundary conditions to the model.

Hence, here it is proposed to use the Combined Eulerian and Lagrangian (CEL) approach. Usually, this approach is used for fluid-structure interactions. It combines

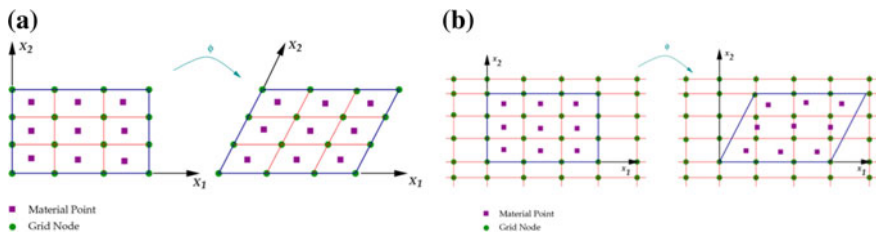


Fig. 6.2 a Lagrangian mesh model b Eulerian mesh model

both the Eulerian and Lagrangian meshes in the same model. Regions which are expected to undergo large deformation are modeled using Eulerian formulation, and the remaining regions can be modeled using Lagrangian formulation. The Eulerian mesh allows for evaluation of deformations with reasonable accuracy in the regions of interest.

6.3 Model Setup

This work deals with a plastic component which the self-tapping screw is fastened into. The screw is fastened into a hollow cylindrical part of this component called the screw post. The aim is to evaluate the fastening torque and strength and performance of this screw post during the self-tapping process. Three distinct designs of this screw post are evaluated in order to find out the design that's most suitable for self-tapping.

6.3.1 Material Model

The model setup of the simulation for this work, as it may be observed from Fig. 6.3c, considers only two components, namely the screw and the screw post. The screw is made of steel, and the screw post is made up of a plastic material. For computational efficiency and practical purpose, the screw is considered to be rigid, for there is a large difference between the stiffness of steel and plastic and marginal deformation is assumed in the screw during the self-tapping process.

Typical FEM solvers offer several material models for simulating different types of materials like metals, plastics, rubbers, etc. The choice of the material model depends upon the type of the material itself, the loading conditions, temperature, strain rate dependency, anisotropy, etc.

[3] Material nonlinearity is caused by a nonlinear relationship between the stress and strain after the yield limit is reached. Beyond the yield limit, some part of the material will start yielding and the stress starts to respond in a nonlinear fashion to applied strain. This is what causes the change in the stiffness of the component, and it depends upon a material behavior called Elasto-plastic behavior. For the work presented here, this material model is assumed for the screw post (Fig. 6.4).

Such materials exhibit a characteristic called work or strain hardening. This increases the yield stress of the material when it is taken in the plastic region. This increase in strength is eventually followed by softening if the external load keeps increasing, and ultimately leads to the failure of the material.

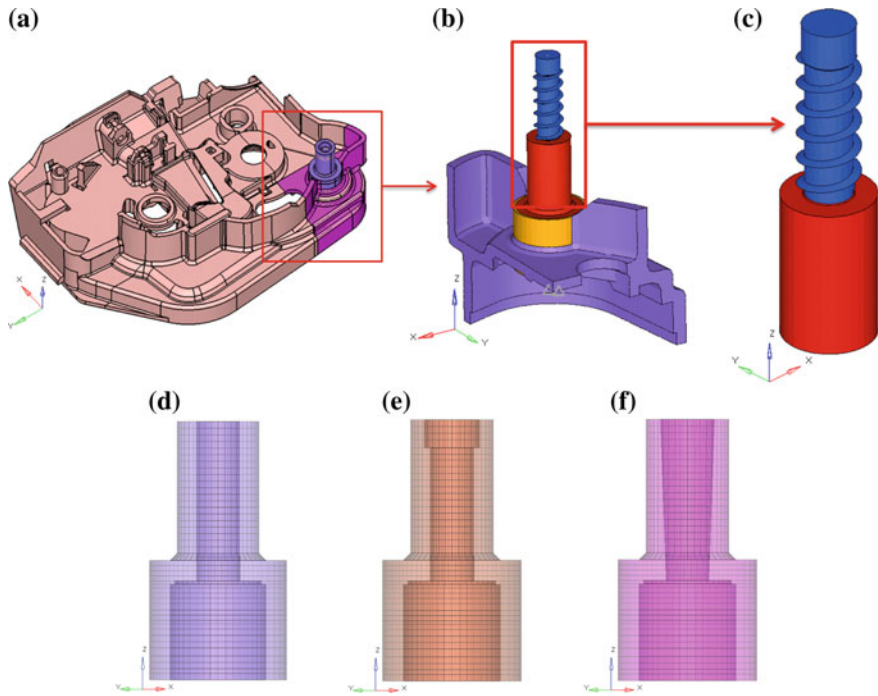
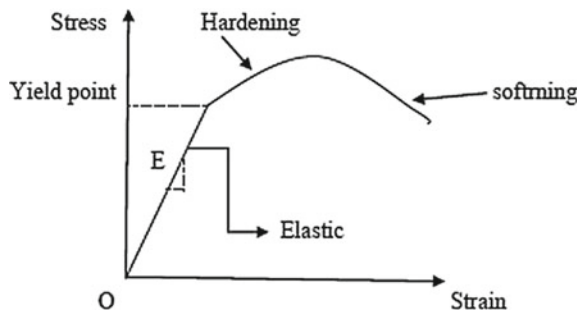


Fig. 6.3 a Component considered b Simplification of geometry c Region of interest: Screw post d Design 1 e Design 2 f Design 3

Fig. 6.4 Strain hardening behavior



6.3.2 Eulerian Domain

Here, our region of interest, the screw post, is modeled using Eulerian formulation. Unlike Lagrangian elements, the Eulerian elements are not completely filled with material. Instead, each Eulerian element has a particular volume fraction value associated with it, indicating how much volume of the element is full of material. Usually, the Eulerian mesh is made larger than the actual geometry. This is done so that the material inside the Eulerian mesh has adequate space available to flow.

[4] The Eulerian mesh, when created, by default, is empty, i.e., without any material. The material distribution needs to be defined in the Eulerian mesh in the initial step of the simulation, by calculating the volume fraction of this mesh with respect to a reference Lagrangian mesh. Reference Lagrangian mesh represents the actual geometry. This volume fraction is called Eulerian volume fraction (EVF). An element can take all the values from completely filled ($EVF = 1.0$) to completely empty ($EVF = 0.0$). Eulerian elements are capable of containing multiple materials at the same time. The sum of volume fractions of all these materials (including void material) equals one.

[5] The time incrementation algorithm is based on an operator split of the governing equations. This results in Lagrangian phase, followed by the Eulerian phase. This formulation is called “Lagrange-plus-remap.” During the Lagrangian phase, the nodes are assumed to be temporarily fixed to the material and material and elements deform together. During the Eulerian phase, deformation is suspended; the elements experiencing large deformation are automatically remeshed, and the material flow between neighboring elements is calculated.

6.3.3 Eulerian–Lagrangian Contact Model

The rigid screw is discretized using elements with the Lagrangian formulation. The Lagrangian object can move through the Eulerian mesh until it encounters any material. Then, the contact algorithm starts to act.

[6] The Eulerian–Lagrangian contact formulation used in this work is based on an enhanced immersed boundary method. It is called general surface-to-surface contact. Here, the Lagrangian object is placed in the void region of the Eulerian mesh. The contact algorithm automatically calculates and tracks the contact interface between the Eulerian and Lagrangian domains. This contact method also does not require conforming mesh in the Eulerian region. It is observed that, often, a regular grid of Eulerian elements gives good accuracy.

[7] The surface-to-surface contact formulation enforces the contact conditions as average over nearby slave nodes. This differs from node-to-surface contact as that enforces the contact conditions only on individual nodes. The averaged regions are approximately centered on the slave nodes but also consider adjacent slave nodes. This may lead to small penetrations of the master surface into slave surface, but it also allows the forces to spread out over multiple slave nodes. The spread of the forces leads to a smoothing effect, i.e., for a given mesh refinement in master and slave surfaces the stresses observed are more accurate.

Table 6.1 shows the element types considered for the simulation.

Table 6.1 Element types used in the simulation

Component	Formulation	Element type	No. of elements
Self-tapping screw	Lagrangian	R3D3 and R3D4 (Tria and Quad)	1109
Screw post	Eulerian	EC3D8R (Hex)	30,000
Screw post (reference)	Lagrangian	C3D8 (Hex)	4800

6.3.4 Boundary and Loading Conditions

Symmetry boundary conditions are applied on the bottom surface of the post. The screw is given translational and rotational displacements along the axis of the screw post. The values for the displacements are calculated based on the design of the screw thread.

6.4 Results and Discussions

The threads can be visualized using a special output variable specific only to Eulerian regions, called EVF—Void (Eulerian Volume Fraction—Void). This variable shows the value of the volume fraction of the Eulerian elements with respect to the void. Hence, the value of EVF—Void = 1 signifies the presence of a complete void, i.e., no material filled in the elements. Here, the value of 0.5 is observed to provide the best visualization of the tapped threads.

Three unique designs are chosen, and identical boundary and loading conditions are applied to all. Based on the design, the number of threads engaged during fastening is different and the same can be noticed in Table 6.2.

Here, it is observed that the Design 1 and Design 2 have the highest number of engaged threads. However, since the hole available for self-tapping itself is tapered, in Design 2, the initial threads may not be able to provide adequate holding strength. This can be seen from the formed threads after the simulation below (Fig. 6.5).

Further, the reaction moment (output variable: RM) for the self-tapping process is obtained from the simulation as an output. The complete simulation for each design

Table 6.2 Number of threads engaged

Design	No. of threads engaged
Design 1	5.47
Design 2	4.32
Design 3	5.47

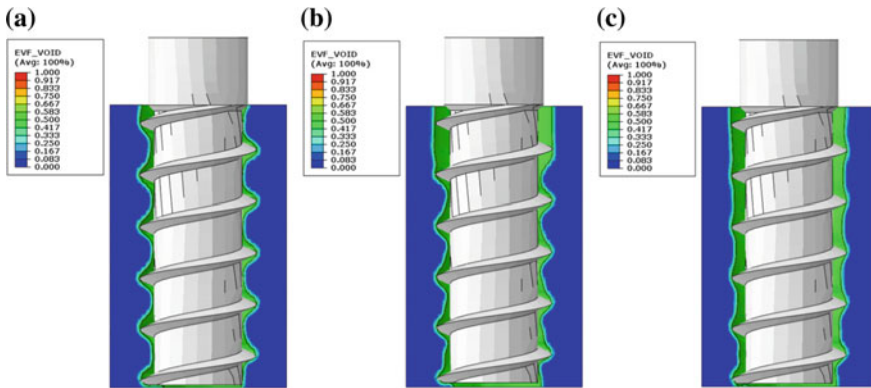


Fig. 6.5 a Design 1 b Design 2 c Design 3

Table 6.3 Maximum moment during a step

Design	Self-tapping process (step 1) (N-m)	Unscrewing process (step 2) (N-m)	Retightening process (step 3) (N-m)
Design 1	0.90	0.62	0.73
Design 2	0.86	0.76	0.61
Design 3	0.99	0.78	0.55

takes place in three steps. The first step deals with the actual self-tapping process, and the maximum moment required by the process is calculated. The second step involves unscrewing of the screw, and the third step calculates the moment required to retighten the screw into the tapped hole. Table 6.3 provides the values for the maximum moments in each of the above-mentioned steps for all three designs.

It is evident that the moment required to fasten the screw is high for the very first time and then reduces for the next steps. This is because, the first time, the material is formed into the shape of the threads by the screw. In the later steps, the screw just retraces its path through the screw post.

6.5 Conclusion

The current work presents the methodology for simulating a self-tapping process using the CEL approach. This approach, though computationally expensive, yields acceptable results for evaluation of torque required for self-tapping and clear visualization of the threads. This methodology may be used to evaluate different designs for self-tapping and tightening torques with sufficient accuracy.

References

1. Aryal, A.: A coupled Eulerian-Lagrangian extended finite element formulation for moving interface problems and damage transport in hyperelastic media. Graduate School of Vanderbilt University (2014)
2. Duobu, F.: The CEL method as an alternative to the current modelling approaches for Ti6Al4 V orthogonal cutting simulation. Proc. CIRP **58**, 245–250 (2017)
3. Roy, R.G.: Elasto-plastic analysis of plate using ABAQUS. National Institute of Rourkela (2015)
4. Abaqus Analysis User's Guide, Section: 14.1.1 Eulerian Analysis, Material Interfaces
5. Abaqus Analysis User's Guide, Section: 14.1.1 Eulerian Analysis, Eulerian Volume Fraction
6. Abaqus Analysis User's Guide, Section: 14.1.1 Eulerian Analysis, Interactions, Formulation of Eulerian-Lagrangian contact
7. Abaqus Analysis User's Guide, Section: 38.1.1 Contact formulations in Abaqus/Standard, Discretization of contact pair surfaces

Chapter 7

Washing Machine Outlet Hose Analysis in Full Water Condition



Changadevkumar Desai, Sushilkumar Vishwakarma and Pavol Vasko

Abstract Outlet hose is a flexible connection between washtub outlet and drain pump inlet in front-load washing machine. Its purpose is to carry water, keep a constant connection during machine operation, avoid water leakage, and reduce force transmission. Rib pattern provided on hose introduces flexibility in hose allows it to remain intact without transferring forces to the machine structure. But the excessive flexibility of hose may cause over-bending, and it may also lead to collapse due to water load which leads to air clogging or self-rubbing issues. The hose may also hit surrounding components like metal brackets continuously during washing cycle which causes wear and in turn, leads to water leakage over a period of time. To avoid the above circumstances, it is necessary to study the behavior and movement of the outlet hose in full water condition for static and dynamic cases and provide design solutions. Using various simulation tools, the hose design is developed and further analyzed to have an improvised and efficient design. In the present study, the finite element method is used for the analysis of the outlet hose due to its complex material and loading conditions. Explicit finite element code LS-DYNA is used to generate static and dynamic loading environment in the simulation. Smoothed-particle hydrodynamics (SPH) method is used for water modeling and fluid–structure interaction study. Using this technique, different hose design concepts are evaluated and refined to improve the design.

Keywords SPH · FSI · LS-DYNA · Washing machine · Outlet hose · Rubber

C. Desai (✉) · S. Vishwakarma
Global Technology and Engineering Center, Whirlpool of India Ltd., Pune, India
e-mail: changadev_desai@whirlpool.com

P. Vasko
Whirlpool Slovakia Ltd., Poprad, Slovakia

© Springer Nature Singapore Pte Ltd. 2020
C. Li et al. (eds.), *Advances in Engineering Design and Simulation*,
Lecture Notes on Multidisciplinary Industrial Engineering,
https://doi.org/10.1007/978-981-13-8468-4_7

7.1 Introduction

Wash unit assembly is an important subassembly in the washing machine. It contains a washtub, drum assembly, drive system, counterweights, and flexible hoses. Washtub is connected with machine structure through springs and dampers only. Drum assembly directly mounted on washtub with help of bearings and receives motion from drive system during the wash and spin cycle. The hose is a flexible part attached to washtub inlet and the outlet port. The hose is either made of rubber or plastic and plays an important role in the washing machine. Their purposes are to carry water, keep a constant connection during machine operation, avoid water leakage, and reduce force transmission. In front-load washing machines, there are mainly two flexible hoses connected to the washtub. First is an inlet hose connected between the outlet of the inlet pump and washtub inlet. It is used to supply clean water into the washtub. Second is an outlet hose connected between the washtub outlet and drain pump inlet as shown in Fig. 7.1. It is used to drain dirty water from the washtub during spin and wash cycle of washing machine. Based on their application, it is clear that the outlet hose has full water condition during most of the machine wash cycle. So the analysis of outlet hose is more critical and complex than inlet hose analysis. In the present study, more focus has given on outlet hose analysis under static and dynamic conditions.

Outlet hose is made of rubber in front-load washing machine. It has a rib pattern provided on its circumference. Ribs provide additional flexibility in the hose which allows it to remain intact without transferring forces to the machine structure. Hose flexibility increases with an increase in its overall length and increase in a number of ribs. The excessive flexibility of hose may result in over-bending due to water load. It may also lead to collapse due to water load which leads to air clogging or self-rubbing issues of the hose. Air clogging inside hose generates gravel-type noise in the pump during the suction cycle and affects pump efficiency as well.

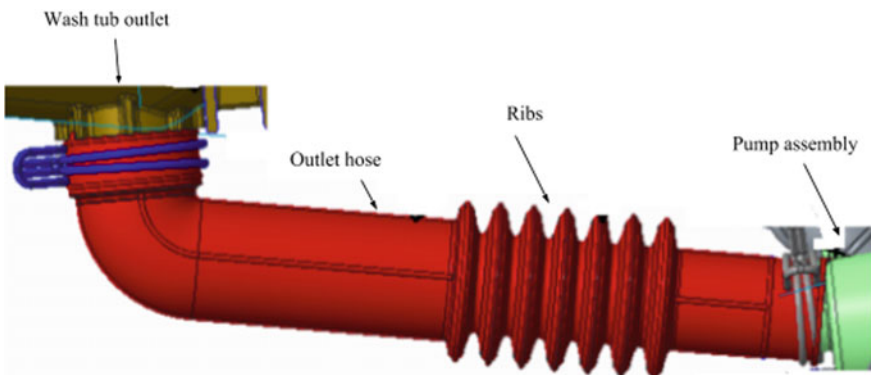


Fig. 7.1 Outlet hose structure and connection details

During the wash or spin cycle, the hose may hit surrounding components like metal brackets, counterweights continuously which causes wear and in turn, leads to water leakage over a period of time. To avoid the above circumstances, it was necessary to study the behavior and movement of outlet hose in full water condition for static and dynamic cases and provide design solutions. The proposed design solution on air clogging issue was to reduce hose deflection in static under full water condition as much as possible.

To reduce cost and design, lead time finite element method is used for the analysis of outlet hose. Explicit finite element code LS-DYNA [1] is used for the static and dynamic analysis of hose. It has the capability to handle fluid–structure interaction (FSI) simulations.

7.2 Methodology

In the present study, an attempt has been made to analyze outlet hose with full water condition. First, the finite element model of outlet hose along with washtub and drain hose was developed in HyperMesh [2] for LS-DYNA solver. Then outlet hose was assembled between washtub and drain hose through simulation in LS-DYNA implicit. Later, a literature review was carried out to study different water modeling approaches in LS-DYNA. Static analysis was performed on the hose in full water condition applying gravity load, and few water modeling approaches were evaluated. Static simulation results were compared with physical test results and selected suitable water modeling approach. In addition, different rib patterns were evaluated to reduce hose bending in the static simulation. To perform dynamic analysis of hose, critical load case was identified and simulated in multi-body dynamics (MBD). The output of MBD simulation was used for dynamic analysis of different hose rib concepts. In the next section, physical test results are discussed.

7.3 Physical Test Results

Outlet hose CAD model represents the undeformed shape of the hose. Original length and shape of hose change during its assembly process. Hose gets stretched by a certain amount while assembling between washtub and drain pump. This stretch creates initial tension in the hose and does not allow the hose to bend in its assembled position as shown in Fig. 7.2a. When water enters into the washtub through the inlet hose, first it fills the empty volume of the outlet hose. During this stage, drain pump seals the water and does not allow it to drain. Once the water fills into the hose completely, it starts occupying the space in the washtub. In the physical test, water was completely filled into the outlet hose and maintained 50 mm water height in tub above the tub outlet. At this stage, the outlet hose was in full water condition and

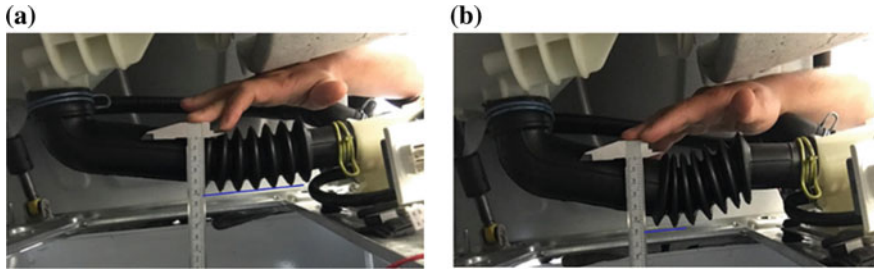


Fig. 7.2 a Outlet hose in empty condition b Outlet hose with full water condition

water height pressure was constantly acting on the hose. Outlet hose bent in the rib region due to water load as shown in Fig. 7.2b.

Hose bending pattern along with maximum hose bending was used for validation of simulation model in a static condition. Finite element modeling details are discussed in details in the next section.

7.4 Analysis of Outlet Hose

7.4.1 Finite Element Modeling

CAD model of outlet hose, washtub, drain pump, and surrounding metal structure was considered in the analysis. Finite element (FE) models were created in HyperMesh for LS-DYNA solver. Outlet hose was meshed using QUAD shell elements of 5 mm global element size. Element formulation 16 along with NIP = 5 was used for shell elements of the hose. Rubber material modeling was challenging due to its complex nature. Mooney–Rivlin rubber material model was used for hose material modeling. To reduce computational time, a lower half model of washtub was considered and the tub was modeled as a rigid component. Counterweight outer surface was also modeled as a rigid component. Washtub outer surface and counterweight surface were meshed with QUAD shell elements size 5 mm. Drain pump was modeled as a rigid component and meshed with TETRA elements. Outlet hose assembly is shown in Fig. 7.3.

7.4.2 Boundary Conditions and Loading

The drain pump is directly mounted on washing machine structure and assumed that the pump is fixed in all degree of freedom (DOF) in the static and dynamic analyses. This assumption fixed all DOF of the respective end of outlet hose in the

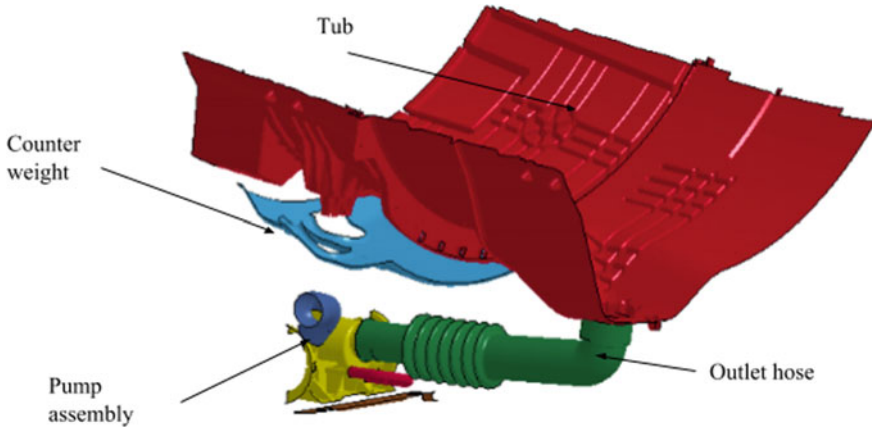


Fig. 7.3 Outlet hose assembly details

complete analysis. Other ends of outlet hose attached to washtub which directly receives motion of washtub. In the static condition, washtub does not move, so it is considered as a fixed part. First, the outlet hose was assembled with drain pump using LS-DYNA implicit code. After completion of assembly simulation, hose initial shape was updated with the assembled shape of hose. Then static and dynamic simulations were performed in LS-DYNA explicit solver. In static analysis, both ends of the outlet hose were fixed in all direction by applying fixed boundary conditions to washtub as well as drain pump. Gravity load gradually applied to the entire model by ramping up linearly over a period of time. A dynamic analysis was carried out after the static analysis.

During the wash or spin cycle, washtub moves in all degree of freedom due to motor and cloth unbalance load. This washtub motion was considered in the dynamic analysis of the outlet hose. To carry out dynamic analysis, critical load case was identified based on the past experience. Particular load case was simulated in multi-body dynamics (MBD) and time history of washtub motion at bearing center location was recorded. Tub motion from MBD simulation was taken as input in LS-DYNA software and directly applied to washtub bearing center to make its motion according to the load case.

In this study, most challenging tasks were water modeling inside the outlet hose. Different water modeling techniques were studied. Few water modeling approaches are discussed in the next topic.

7.4.3 Water Modeling Approach

Water presents inside the outlet hose during most of the washing machine cycle. It makes outlet hose analysis more complex than inlet hose. FE modeling of water

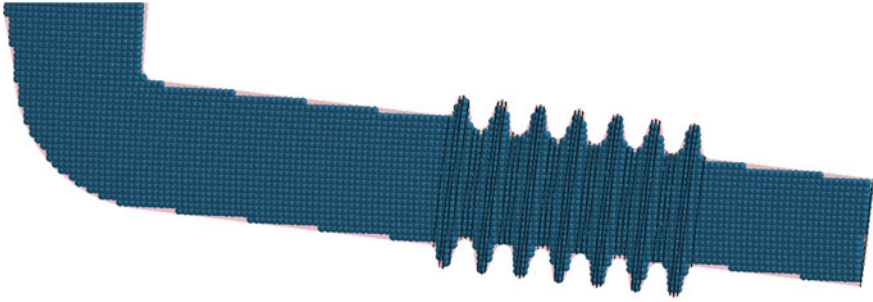


Fig. 7.4 Outlet hose FE model with water SPH elements

Table 7.1 Gruneisen parameters for water [10]

	∇_o (kg/m ³)	C_o (m/s)	S	Γ_o
Water	1000	1490	1.79	1.65

and water interaction with the hose were challenging tasks in this study. Different approaches were tried to model water in the simulation. In the first approach, water was modeled as mass elements on the nodes of the outlet hose, and then water weight was assigned to those mass elements. In the second approach, RBE3 elements were used for water modeling. These are generally used for load distribution. Static analysis was performed on hose considering two approaches and measured corresponding peak hose deflection. It was observed that peak deflection was less than physical test measurement in both cases due to lack of mass elements uniform distribution and water head pressure. This motivated to think about mesh-free methods [3]. Nowadays these methods are widely used for various applications, but these methods increase the simulation time. Liu [4] highlighted the needs of mesh-free methods in large deformations problems. One of the mesh-free methods is smoothed-particle hydrodynamics (SPH) mostly used for modeling free fluid flows [5, 6].

In the SPH method, the fluid is represented as particles (nodes). Each particle possesses its individual material properties, velocity, and position [7]. This method makes use of smoothing kernel functions to obtain the governing equations of the system [8]. Fluid particles material properties changes due to interaction with neighboring particles. This makes SPH, mesh-free Lagrangian method [9].

In this paper, the SPH method is used to simulate water inside the outlet hose. SPH elements were created in HyperMesh considering washtub up to 50 mm height and outlet hose as a closed volume. Elements were uniformly distributed inside the closed volume with a spacing of 3 mm as shown in Fig. 7.4.

Water density 1000 kg/m³ has assigned to SPH elements. SPH elements were defined with equation of state (EOS) such as Gruneisen equation for pressure response [10]. Gruneisen constant parameters for water are mentioned in Table 7.1.

After FE modeling of water, node to surface contact defined between water SPH particles and outlet hose. SPH elements are not supported by implicit solver, so static and dynamic analyses were performed in LS-DYNA explicit solver.

7.5 Results and Discussion

7.5.1 Static Simulation Results

Gravity load applied on outlet hose and water SPH elements to perform its static analysis. As rubber is hyperelastic material, the hose did not reach to its stable position immediately in the explicit solver. Outlet hose was oscillating about mean position. To identify hose mean position, nodal displacement time history was plotted. Using a time history plot, hose stable position was decided. Figure 7.5a shows the mean position of outlet hose obtained from static simulation and (b) shows the physical test position.

Outlet hose bending was measured at this mean position. Hose displacement pattern was well correlating with the physical test results. Maximum displacement has observed in hose rib region and left side ribs were displaced more compared to right side ribs. Maximum hose displacement was 16 mm near left side ribs, and it is 80% close to physical test measurement. The main reason for result variation was tub displacement in a downward direction due to water weight has not considered in the simulation model. The next step was to reduce hose bending by changing rib shapes, a number of ribs and rib patterns. Figure 7.6 shows a summary of hose concepts evaluated in this study.

Five hose design concepts were evaluated in static simulation. Peak displacement of all design concepts is shown in Fig. 7.7. In each design concept, the minimum gap between ribs was also measured. In concept 3 and 4, total ribs were split into two sections lead to a reduction in hose deflection by 44% compared to the baseline design. Both concepts were showed 9 mm deflection in the static simulation. Concept 3 has shown maximum deflection toward the pump side, and concept 4 has shown

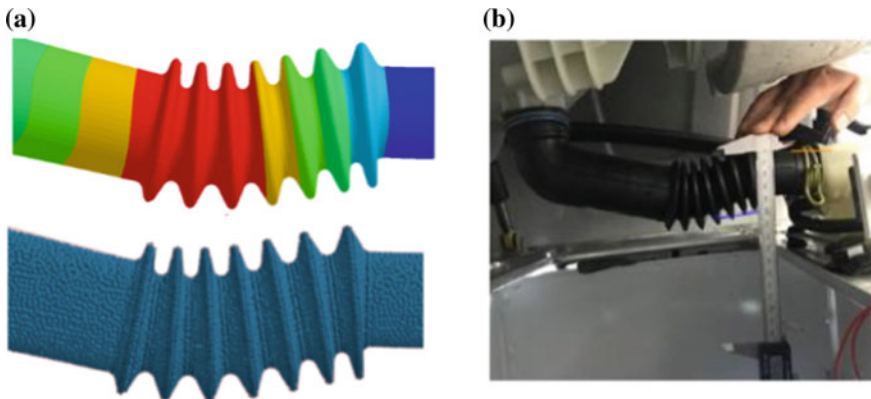


Fig. 7.5 a Outlet hose (Base design) mean position static simulation b Physical test position

maximum deflection toward the washtub side. Concept 4 is a better option as it is having less deflection at the pump side compare to concept 3 which may avoid bubble formation.

7.5.2 Dynamic Simulation Result

After finalizing the outlet hose design, the dynamic simulation was performed. Critical load case output taken from MBD simulation was used for the dynamic analysis. In the dynamic analysis, the outlet hose movement was monitored and checked for any interaction with surrounding components. Hose kinematic is shown in Fig. 7.8.

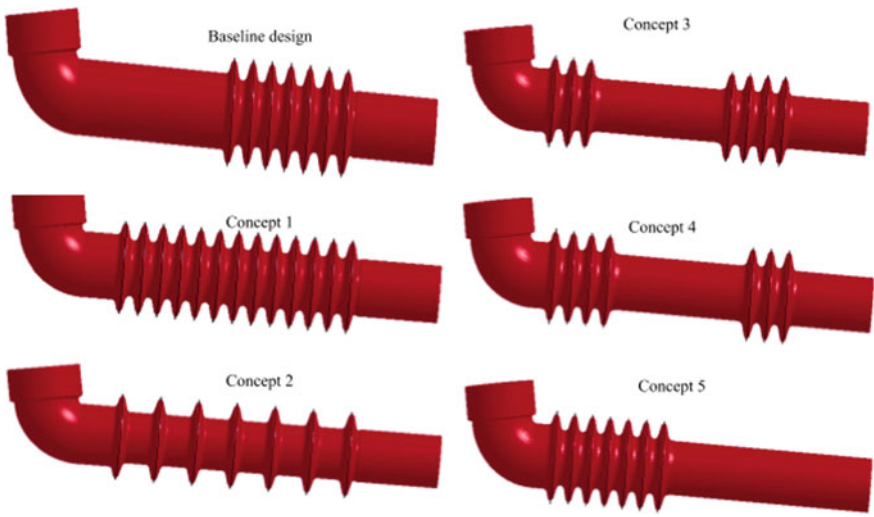


Fig. 7.6 Outlet hose design concepts

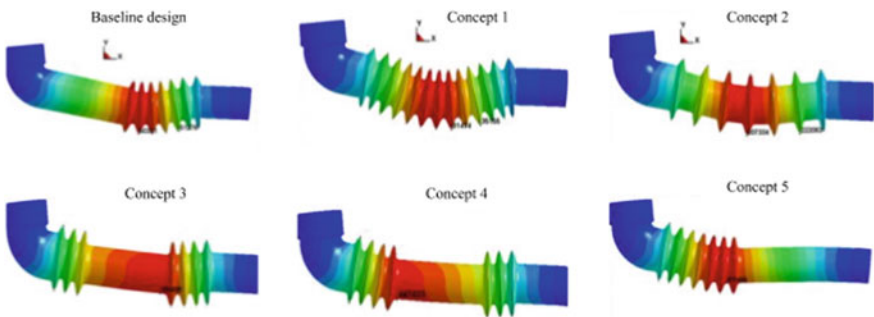


Fig. 7.7 Peak displacements of outlet hose design concepts

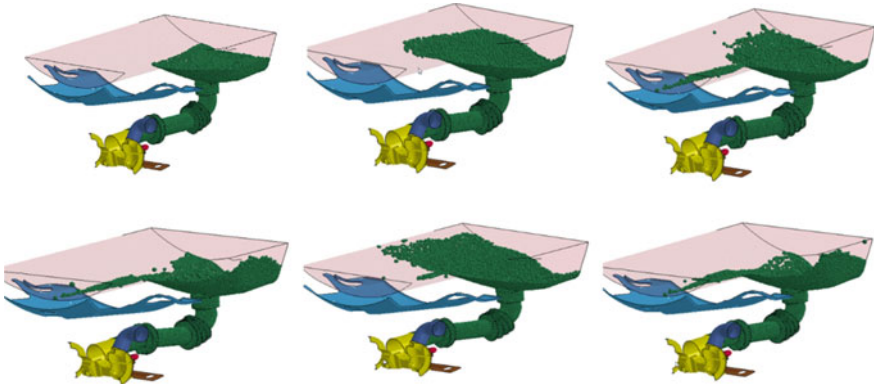


Fig. 7.8 Outlet hose kinematic of dynamic analysis

Forces transmitted by hose to pump were within permissible limit. Hose ribs were not touching each other.

7.6 Conclusions

This paper has described an analysis of washing machine outlet hose in full water condition using SPH elements. LS-DYNA explicit solver was successfully used for static and dynamic simulations of the hose. The goal of the study was to validate simulation results with the physical test result and further evaluate different hose design concepts. Outlet hose maximum bending and hose bending pattern were compared to and validated with physical test results. The simulation results showed 80% correlation with the physical test result. Different hose design concepts were evaluated through static simulations. Physical test results required for correlation of dynamic analysis of hose in full water condition. Also, need to explore air particle modeling to capture air bubble formation in outlet hose.

Acknowledgements The authors would like to express their gratitude to Whirlpool Corporation. The authors would also like to appreciate the efforts of all those individuals who directly or indirectly helped in this work.

References

1. Livermore Software Technology Corporation. LS-DYNA keyword user's manual Volume 1 R10.0
2. Altair HYPERWORKS User Manual

3. Vesenjak, M., Ren, Z.: Application aspects of the meshless SPH method. *J. Serb. Soc. Comput. Mech.* **1**, 74 (2007)
4. Liu, G.R., Liu, M.B.: *Smoothed Particle Hydrodynamics: A Meshfree Particle Method*. World Scientific Publishing Company, Singapore, 10 October 2003
5. Valizadeh, A., Shafieefar, M., Monaghan, J.J., Salehi Neyshaboori, S.A.A.: Modeling two-phase flows using SPH method. *J. Appl. Sci.* **8**(21), 3817 (2008)
6. Lobovsky, L., Kren, J.: Smoothed particle hydrodynamics modelling of fluids and solids. *Appl. Comput. Mech.* **1**, 521 (2007)
7. Bisagni, C., Pigazzini, M.S.: Modelling strategies for numerical simulation of aircraft ditching. *Int. J. Crashworthiness* (2017)
8. Masahiko, O., Yamato, M., Kenji, M., Yukio, K., Shigeru, I.: A study on shock wave propagation process in the smooth blasting technique. In: 8th International LS-DYNA Users Conference, p. 7 (2004)
9. Liu, G.R.: *Mesh Free Methods: Moving Beyond the Finite Element Method*, 2nd edn. CRC Press LLC, Washington D.C., 6 October 2009, ISBN 9781420082098 - CAT# 82094
10. Limido, J., Espinosa, C., Salaun, M., Lacombe, J.L.: A new approach of high speed cutting modelling: SPH method. In: 8th International Conference on Mechanical and Physical Behaviour of Materials under Dynamic Loading, p. 11 (2006)

Chapter 8

Performance Study of a Twisted Vaned Diffuser in a Compressor Stage



Venkateswara Rao Pothuri, Venkata Ramana Murty Govindaraju,
Amogh Baraar and C. Pradeep Reddy

Abstract The current study compares the centrifugal compressor stage performance employed with vaneless and twisted vaned diffusers and in turn establishes the effect of diffuser parameters such as chord length and twist angle of the twisted vaned diffuser on its performance. The chosen diffuser has a uncambered aerofoil section with solidity varying due to blade twist from hub to shroud. To provide a twist to the diffuser blade, it is rotated in the direction opposite to that of the impeller, the origin being placed at the profile's leading edge. The analysis is performed at 0.35 Mach at the tip of the impeller. For the analysis, chord length is varied from 80 to 120-mm insteps of 10 mm and the twist angle from 5° to 11° insteps of 2°. The mass flow rate is altered from 80 to 120% of design flow rate insteps of 10%, thus considering both design and off-design conditions. The overall stage performance is evaluated by means of different performance parameters like total-to-static stage efficiency, static pressure recovery coefficient, static head coefficient and power coefficient. The conclusion from the study is that using TVD results in better performance than VLD and TVD with chord length 100 mm, and twist 9° operating at design conditions results in the best performance for the chosen configuration.

Keywords Impeller · Diffuser · Hub · Shroud · Chord length · Twist · Solidity · Performance parameters

V. R. Pothuri (✉) · V. R. M. Govindaraju · A. Baraar · C. Pradeep Reddy
Department of Mechanical Engineering, Vasavi College of Engineering, Hyderabad, Telangana,
India
e-mail: pothuri26@gmail.com

V. R. M. Govindaraju
e-mail: directoraa@staff.vce.ac.in

A. Baraar
e-mail: baraaramogh@gmail.com

© Springer Nature Singapore Pte Ltd. 2020
C. Li et al. (eds.), *Advances in Engineering Design and Simulation*,
Lecture Notes on Multidisciplinary Industrial Engineering,
https://doi.org/10.1007/978-981-13-8468-4_8

Nomenclature

C_p	Static pressure recovery coefficient, $(p_4 - p_2)/(p_{02} - p_2)$
D	Diameter (m)
g	Acceleration due to gravity (m/s^2)
H	Total head (m), $\frac{\gamma}{\gamma-1} RT_{01} \left[\left(\frac{P_{04}}{P_{01}} \right)^{\gamma-1/\gamma} - 1 \right] \frac{1}{g}$
l	Vane chord length (m)
LE	Leading edge
LSVD	Low solidity vaned diffuser
m	Mass flow rate (kg/s)
n	Speed (rpm)
p	Pressure (Pa)
r	Radius (m)
S	Pitch (m), $\pi D_3/Z$
TVD	Twisted vaned diffuser
u	Peripheral velocity (m/s), $\pi Dn/60$
VLD	Vaneless diffuser
Z	Number of diffuser vanes
α	Flow angle (deg)
β	Blade angle (deg)
η	Total-to-static stage efficiency (%), $\left[\left(\frac{P_4}{P_1} \right)^{\gamma/\gamma-1} - 1 / \left(\frac{T_{04}}{T_{01}} - 1 \right) \right] * 100$
λ	Power coefficient, $\phi\psi/\eta$
ω	Angular velocity (rad/s)
ϕ	Flow coefficient, $m/(\rho u_2 \pi D_2^2/4)$
γ	Ratio of specific heats
ρ	Inlet density (kg/m^3)
σ	Solidity, l/s
ψ	Head coefficient, $H/(u_2^2/2g)$
CL*	Chord length of * mm
T*	Twist of * degree

Subscripts

- 0 Total quantities
- 1 Impeller inlet
- 2 Impeller exit
- 3 Diffuser inlet
- 4 Diffuser exit

8.1 Introduction

The widespread use of centrifugal compressors for industrial and non-industrial applications necessitates a study on their performance in terms of stage efficiency and pressure rise across the machine. A typical multi-stage centrifugal compressor consists of rotating impellers, stationary diffusers and return channels. A casing houses the stationary and rotating components. Impellers consist of a set of blades and are driven by a prime mover; suction is created, and the air is sucked into the impeller stage and whirled outwards at high speed due to the centrifugal action, thereby imparting kinetic energy to the flow. The imparted kinetic energy is converted into pressure energy causing energy transformation in the diffuser. Return channels help in directing flow from one stage to the subsequent one, i.e. from radially outward to inward direction.

The performance of a multi-stage centrifugal compressor can be enhanced by modifying the design, geometry of impellers, diffusers and return channels. It is found from the literature that the study on impeller has reached saturation and hence studies are directed towards stationary components such as diffusers and return channels. The present paper confines to study flow through diffusers for a single-stage machine.

8.2 Literature Review

Diffusers are mainly categorised as vaneless and vaned diffusers. The annular space of diffuser surrounds impeller in a centrifugal compressor. If the annular does not have any vanes, it is called as 'vaneless diffuser', and if it has, then it is called a 'vaned diffuser'. A vaneless diffuser encompasses two parallel walls, forming a radial annular passage through the outlet radius of the impeller to that of diffuser which may be converging, diverging or parallel. Thus, the flow is allowed in the radial direction, such that the kinetic energy of the flow gets converted into the static pressure. For an incompressible, isentropic flow through a vaneless diffuser with constant height, the absolute flow angle is constant, resulting in 'logarithmic spiral path'. For compressible flows, the density varies with pressure and temperature in a manner such that there is an increase in absolute flow angle in the radial direction with increasing radius, facilitating the flow to turn more than the simple logarithmic spiral, thereby leading to increased friction losses. From the work of Anish and Sitaram [1], the flow entering the vaneless diffuser has a significant swirl; swirl angle varies typically between 10° and 30° with the tangential direction. Backflow is observed in the diffuser if the flow enters at a flow angle less than the critical flow angle. At larger flow coefficients, there is no flow separation from hub and shroud wall, as the flow turns more radial, which can be the main reason for effective pressure recovery at higher flow coefficients [2]. From the numerical study by Galerkin et al. [3], it can be seen that the flow separation possibility and friction losses are lower at higher flow angles.

For a better efficiency than the vaneless diffuser, vaned diffusers are developed. In a vaned-type diffuser, blades are connected to hub or shroud of the diffuser. The cross section of blades can be a constant transverse cross section or an aerofoil section. There is a vaneless gap between the outlet of the impeller and the leading edge of the vanes in a vaned diffuser. This helps in reducing the circumferential pressure gradient at the inlet of the diffuser and also smoothens out the velocity variations. Moreover, it reduces the Mach number at the leading edge of the diffuser vanes, thereby avoiding shocks or overspeeding on the vane profile. Introduction of the vane in a conventional vaned diffuser helps in deswirling the flow, providing a shortened flow path and thereby aids in achieving the desired pressure ratio at a reduced diameter. But the range at which the compressor operates is reduced by choking of the throat at high flow rates and stalling of the vane at low flow rates. Vaned diffusers facilitate better flow guidance, hence decelerating the flow more effectively than VLD, thus resulting in the better value of the static pressure recovery coefficient.

In an attempt to overcome the deficiencies of conventional vaned diffusers and vaneless diffusers, the concept of low solidity vaned diffusers was developed by Senoo [4] and later the results reported by Kaneki and Ohashi and Senoo et al. [5] have shown that by employing low solidity vaned diffusers, there is notable efficiency gain than vaneless diffusers with a negligible loss in flow range. The most striking feature of these diffusers is the absence of geometrical throat between the vanes, which improved the diffuser range both on the choke and on the stall side of the compressor operating range. These diffusers are a good compromise with better pressure recovery than the vaneless and wider flow range than the vaned diffusers.

The throat formation can be avoided by using partial vaned diffuser also. Yoshinaga et al. [6] was first to report about partial vaned diffuser which improved the centrifugal compressor performance with the height of diffuser vanes a little less than the width of diffuser passage, fixed to the shroud. However, the staggered configuration in which vanes are attached to both hub and shroud improved the performance substantially.

The patent of the twisted vaned diffuser is held by Abdelwahab [7] and Abdelwahab et al. [8, 9] who used an aerofoil diffuser in which the solidity varies from low solidity (<1) value at the hub to a high solidity (>1) at shroud. Twisted configuration is in the spanwise direction between the hub and the shroud, such that the inlet blade angle decreases. This leads to different blade angles at the hub and shroud. Venkateswara Rao et al. [10, 11] studied the twisted configuration in the spanwise direction between the hub and the shroud, in the direction of rotation of the impeller and in the opposite direction. From the literature, it is seen that not much research has been done on the twisted vane configuration which is the reason the present work is carried out and intended to ameliorate the performance of compressor stage.

Table 8.1 Details of the compressor

Speed, n	4500 rpm
Impeller vane radius at the inlet	150 mm
Impeller vane radius at the outlet	250 mm
Diffuser vane radius at the inlet	275 mm
Diffuser vane radius at the outlet	377 mm
Impeller width	24.5 mm
Blade angle at impeller inlet, β_1 w.r.t. tangential direction	27°
Blade angle at impeller exit, β_2 w.r.t. tangential direction	45°
Width of the diffuser passage, b	24.5 mm
Mass flow rate, \dot{m}	1.3 kg/s
Diffuser blade chord length at hub, l	Varying from 80 to 120 mm
Number of impeller blades	17
Number of diffuser blades, Z	14

8.3 Centrifugal Compressor Details

A centrifugal compressor design to operate at a flow rate by mass of 1.3 kg/s and the rotational speed of 4500 rpm is considered for this study. The details of the compressor are specified in Table 8.1. The impeller details are taken from Siva Reddy et al. [12]. The diffuser passage length is extended by 25 mm to facilitate the analysis with longer chord lengths.

8.4 Governing Equations

Governing equations used in the present analysis are RANS equations. These are shown below

$$\text{Continuity equation, } \frac{\partial \rho}{\partial t} + \nabla \cdot (\rho \bar{C}) = 0$$

$$\text{Momentum equation, } \frac{\partial (\rho \bar{C})}{\partial t} + \nabla \cdot (\rho \bar{C} \times \bar{C}) = \nabla \cdot \{ \tau - \overline{\rho C \times C} \} + S_M$$

The tensor $-\overline{\rho C \times C}$ is known as the Reynolds stress.

Energy equation,

$$\frac{\partial \rho h_{\text{tot}}}{\partial t} - \frac{\partial \rho}{\partial t} + \nabla \cdot (\rho \bar{C} h_{\text{tot}}) = \nabla \cdot (\lambda \nabla \tau - \overline{\rho C h}) + \nabla \cdot (\bar{C} \times \tau) + S_E$$

where, τ , stress tensor is,

$$\tau = \mu \left(\nabla \bar{C} + (\nabla \bar{C})^T \right) - \frac{2}{3} \delta \nabla \cdot \bar{C}$$

$$h_{\text{tot}} = h + k$$

k is the turbulent kinetic energy, $k = \frac{1}{2} \overline{C^2}$

S_M and S_E refer to momentum source and energy source, respectively.

For flows with a rotating frame of reference, rotating with constant angular velocity (ω) and additional sources of momentum are required to account for the effect of Coriolis force and the centrifugal force.

$$S_{M,\text{rot}} = S_{\text{cor}} + S_{\text{cfg}}$$

$$S_{\text{cor}} = -2\omega\rho \times C_{\text{rot}}$$

$$S_{\text{cfg}} = -\rho\omega \times (\omega \times r)$$

Similarly in the energy equation, the advection of total enthalpy is replaced by the advection enthalpy,

$$I = h + \frac{1}{2} C_{\text{rot}}^2 - \frac{1}{2} u^2$$

Apart from these equations, the standard k - Σ equations are used to solve the present problem.

8.5 Numerical Model and Meshing

As the geometry of impeller and diffuser domains is symmetric cyclically, the periodic boundary condition is applied which limits the CFD simulations to be performed only on a single impeller–diffuser passage, rather than modelling the entire model, which minimises the model size and hence computational time and effort. The impeller is a rotating domain, which accommodates a three-dimensional flow, while the diffuser is a stationary domain, which is modelled as a three-dimensional model for numerical simulation. Modelling of impeller and twisted vane diffuser geometry is performed with AutoCAD. For generating the co-ordinates of twisted vane diffuser at the base of the profile, AutoLISP code has been used. Along with this, a Python code is developed for the generation of co-ordinates at different spans with the desired twist angle.

ANSYS TurboGrid is used for discretising the bladed components. The machine type is specified as a centrifugal compressor with a blade set count of 17 for the impeller and 14 for a vane diffuser with z-axis as the principal axis. Then, 3D mesh is generated by which structured hexahedral grids are generated. Meshes of vaneless and twisted vane diffusers with various chord lengths and twist 9° are shown in Fig. 8.1. Around leading and trailing edges of the blades, ‘O’ and ‘C’

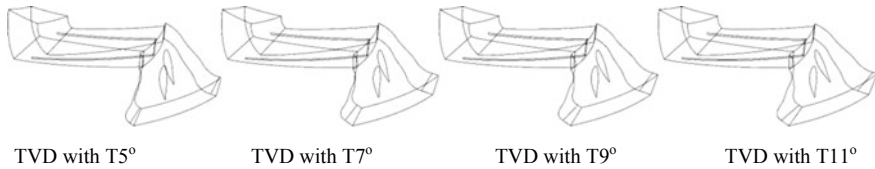


Fig. 8.1 Geometry of TVD with 100-mm chord length at the specified twist

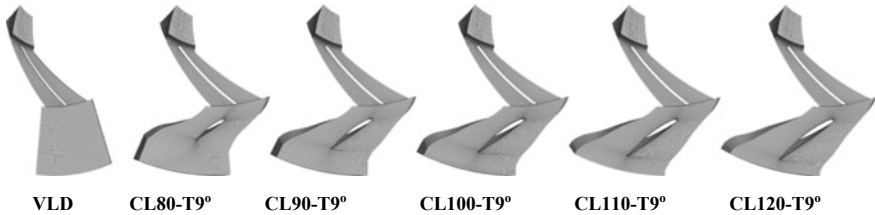


Fig. 8.2 Meshes of VLD and TVD with twist 9° at specified chord length

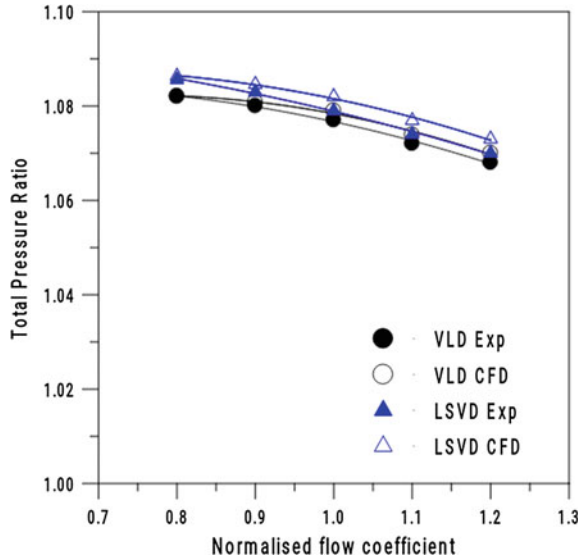
grid topologies are used to augment the mesh quality. Grid independence studies are carried out at design flow conditions. For a particular configuration, four grids, with the increasing number of elements from 75,000 to 150,000 in steps of 25,000, are generated. After solving all these meshes, best mesh with regard to the static pressure recovery coefficient is selected and with the best mesh, by varying the flow rates from 80 to 120% of design flow rate, solutions are generated (Fig. 8.2).

8.6 Boundary Conditions and Methodology

ANSYS CFX is incorporated for simulating all the configurations. For the impeller, wall configuration is specified as no-tip clearance at hub and shroud. To make sure that the boundary conditions at the inlet are not influenced by back pressure, computational domain inlet is considered aloof from the impeller eye. For the analysis, working fluid considered is air and assumed as an ideal gas, 95,000 Pa (reference absolute pressure); heat transfer model employed for determining temperature values is total energy model; the standard $k-\epsilon$ model is employed for turbulence modelling. The outlet boundary condition is the specified flow rate by mass. For side walls of impeller and diffuser, the rotational periodic boundary condition is used. For the region between impeller outlet and diffuser inlet, the stage-mixing interface is specified. The current model also facilitates for obtaining predictions of steady state for multi-stage machines. The advection terms are discretised using high-resolution scheme.

Reynolds averaged continuity, energy and momentum equations govern the physical model, simulations and the involved calculations in the mathematical model.

Fig. 8.3 Total pressure ratio variation



A time step of $0.1/\omega$ is used for controlling the solution convergence. Steady-state solutions are carried out for the convergence of the residual (RMS) values of computations to the order of 1×10^{-5} .

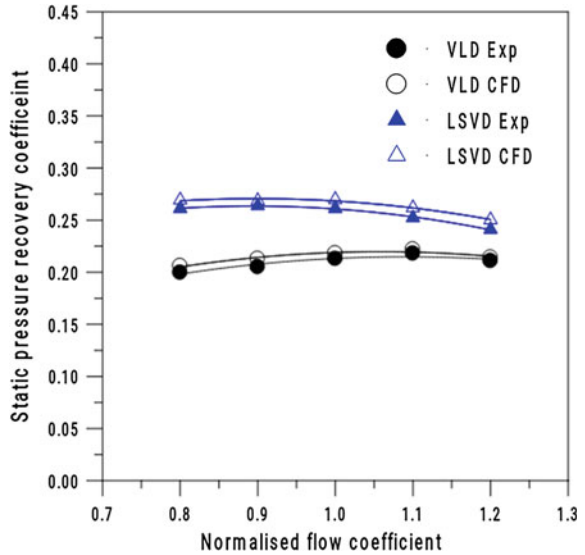
8.7 Numerical Validation

Siva Reddy (2007) conducted experiments on a compressor stage with Nq (specific speed) = 39.3 and Φ (design flow coefficient) = 0.053. A 2D impeller with blade count of 17 and 500-mm exit diameter was used. Mach number of 0.35 at impeller tip, nominal speed of 4500 r/min and a radius ratio of 1.4 at the exit section of VLD were used. The diffuser configurations (VLD and LSVD with solidity range 0.7–0.9) were investigated with the same impeller for setting angles varying from 16° to 32° in steps of 4° with same boundary conditions used in the CFD analysis. So, the experimental data of the Siva Reddy (2007) is used for the numeral validation of the CFD analysis.

8.7.1 Total Pressure Ratio

An inverse relation between total pressure ratio and mass flow rate is observed as shown in Fig. 8.3. Pressure lost at inlet cone and volute casing is not included in the CFD modelling. So, the predicted CFD results are marginally higher than experimental ones.

Fig. 8.4 SPR coefficient variation



8.7.2 Static Pressure Recovery Coefficient

Figure 8.4 depicts a variation of static pressure recovery (SPR) coefficient with flow coefficient normalised with the data of VLD, for compressor stage with VLD and LSVD. It is observed that SPR coefficient remains nearly unaffected with the increase in flow rate. From the experimental results, it is seen that this coefficient decreased with an increase in flow rate whereas it remained constant at 80 and 100% design flows. There is reasonable matching between experimental and CFD results.

From the results presented above, it is observed that there is an agreement with the test results of the earlier experimental investigations on a centrifugal compressor stage of the same configuration and size. It is concluded from this comparison that the methodology used for numerical computation can be relied upon to investigate the different aspects of the centrifugal compressor stage taken up in the present work.

8.8 Results and Discussion

The following figures depict the variation of normalised flow properties and static pressure recovery coefficient for different configurations of TVD with normalised flow coefficient. Normalisation is done with reference to the data of vaneless diffuser at design flow conditions.

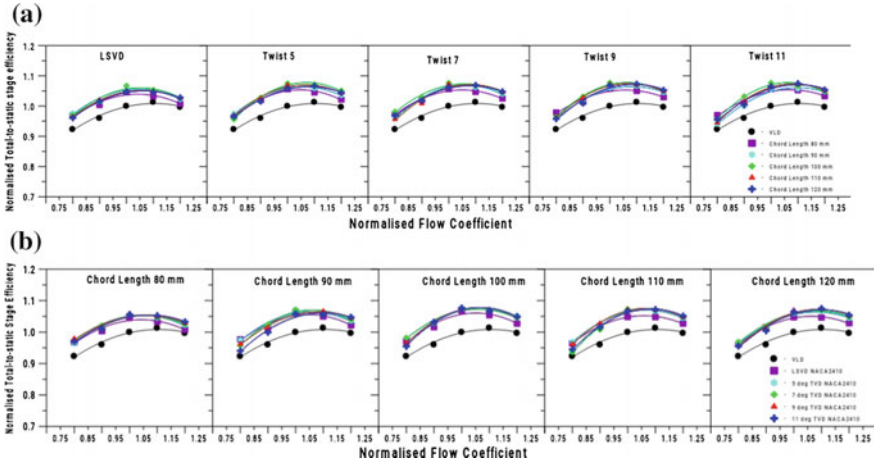


Fig. 8.5 a Variation of normalised total-to-static stage efficiency with normalised flow coefficient at a given twist for different chord lengths, b variation of normalised total-to-static stage efficiency with normalised flow coefficient for a given chord length at different twist angles

8.8.1 Stage Performance Analysis—Effect of Chord Length and Twist Angle

8.8.1.1 Stage Efficiency

Centrifugal compressor’s performance is evaluated in terms of stage efficiency. For evaluating stage efficiency, conditions at both impeller and diffuser are taken into account. Hence, this corresponds to the overall performance of the stage. Figure 8.5a shows the graph between normalised total-to-static stage efficiencies with normalised flow coefficient for VLD and TVD at a given twist for different chord lengths. It is observed that the stage efficiency of TVD with any configuration is higher than VLD. The maximum efficiency for TVD is observed at 100-mm chord length at any given twist. There is an increase in efficiency from chord length 80–100 mm and a decrease thereafter. Change in normalised total-to-static stage efficiency with normalised flow coefficient for a given chord length at different twist angles is shown in Fig. 8.5b. It is observed that with the introduction of twist, there is an increase in efficiency for all chord lengths relative to VLD. The reason for this can be the reduction of secondary flows. The efficiency has increased from twist 5° to 9°, and then there is a drop in it. Irrespective of chord length, the maximum efficiency is observed at design flow conditions at a given twist. There is an increase in efficiency up to design flow rate and decrease thereafter.

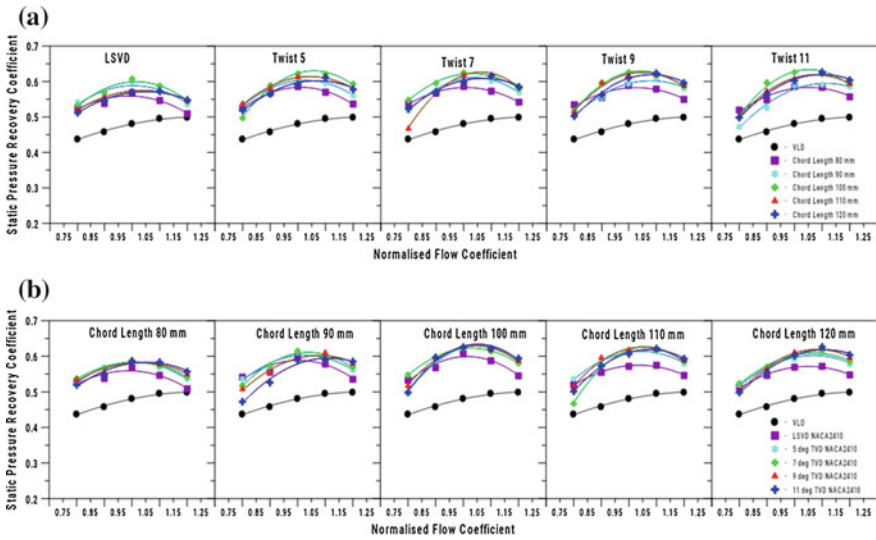


Fig. 8.6 **a** Variation of the static pressure recovery coefficient with a normalised flow coefficient at a given twist for different chord lengths, **b** Variation of the static pressure recovery coefficient with normalised flow coefficient for a given chord length at different twist angles

8.8.1.2 Static Pressure Recovery Coefficient

The kinetic energy of the flow leaving the tip of the impeller is transformed into the static pressure rise as the flow passes through the increasing area of diffuser passage. Static pressure recovery coefficient quantifies the static pressure recovered from the dynamic head available at the diffuser inlet. Figure 8.6a shows how the static pressure recovery coefficient varies with the normalised flow coefficient at a given twist for different chord lengths. It is evident that the static pressure recovery of TVD with any configuration is higher than VLD. In addition, the maximum recovery of the static pressure is for chord length 100 mm at any given twist. Static pressure recovery coefficient augmented from chord length 80–100 mm and decremented thereafter. This is due to the drag offered to the flow by longer chord lengths. Figure 8.6b describes how the static pressure recovery coefficient alters with the normalised flow coefficient at different twist angles for a given chord length. It is inferred that by introducing vane and providing a twist to it, the amount of the static pressure recovered from the flow is enhanced due to the retardation of flow. For any chord length, the maximum static pressure recovery is observed at design flow rate. It has increased from lower flow rates up to the design flow rate and then decreased.

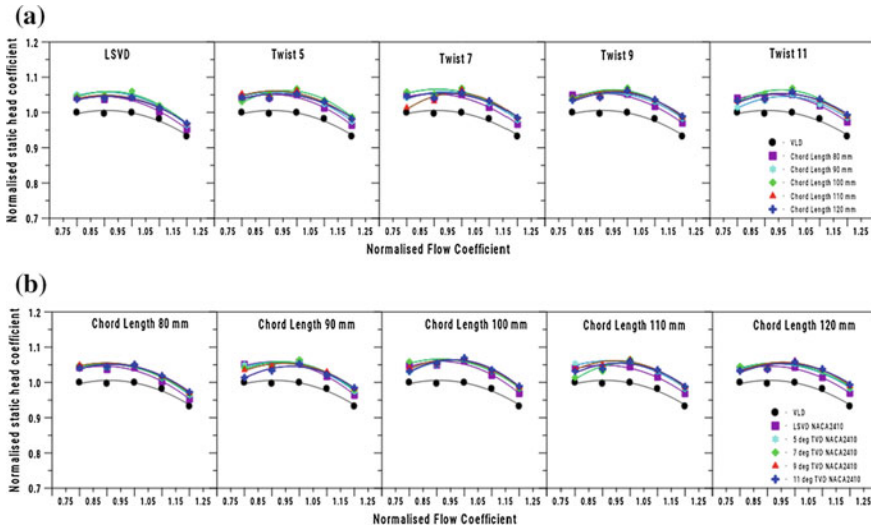


Fig. 8.7 a Variation of the normalised static head coefficient with a normalised flow coefficient at a given twist, b variation of the normalised static head coefficient with normalised flow coefficient for a given chord length

8.8.1.3 Head Coefficient

The head coefficient quantifies the amount of the static pressure increased, as the flow passes from the inlet of impeller, through the diffuser outlet. The variation of the normalised static head coefficient with a normalised flow coefficient at a given twist for different chord lengths is shown in Fig. 8.7a. It is clear that irrespective of twist, the maximum static head is obtained for 100-mm chord length. Figure 8.7b shows the variation of the normalised static head coefficient with a normalised flow coefficient for a specified chord length at different twist angles. Static head coefficient increased from twist 5° to 9° and then decreased. Among various twist angles, the highest static head is found for twist 9°. The rise in the static head has an inverse relation with flow rate because at higher velocities corresponding to higher flow rates, incidence angle increases which leads to incidence losses.

8.8.1.4 Power Coefficient

Power coefficient provides the information regarding the amount of power consumed or required by the compressor to pressurise the flow passing through impeller and diffuser. The change in normalised power coefficient with normalised flow coefficient at a specified twist for different chord lengths is shown in Fig. 8.8a. It is understood that as mass flow rate increases, the power consumed increases irrespective of the type of diffuser. It is seen that the power coefficient for TVD at any configuration is

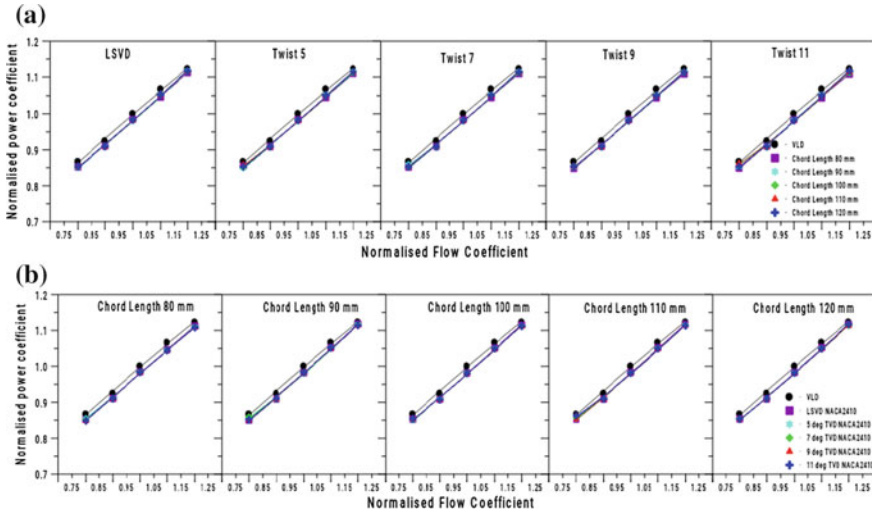


Fig. 8.8 a Variation of normalised power coefficient with normalised flow coefficient at a given twist, b variation of normalised power coefficient with normalised flow coefficient for a given chord length

less compared to VLD. The reason for this is an increase in the static head due to the introduction of the vane. Figure 8.8b shows the graph between normalised power coefficient and normalised flow coefficient for a given chord length at different twist angles, and it can be concluded that there is no considerable effect on the power consumption with the change in chord length and twist.

8.8.2 Absolute Pressure Variation in the Stage

The variation of normalised absolute pressure for TVD with 100-mm chord length and twist 9° at each of the specified flow rates is shown in Fig. 8.9. Variation is presented spanwise at three different spans 0.05, 0.5 and 0.95 from the hub. Normalisation is carried out using the dynamic head $0.5\rho_2u_2^2$, based on the impeller exit velocity and the rotational speed being 4500 rpm, by which the pressure recovery coefficient can be estimated. From the figure, it is clear that pressure augments from impeller inlet to diffuser outlet, which is the purpose of the compressor. With an increase in impeller speed, pressure decreases at the diffuser inlet and increases at its exit. The decrease in pressure at the impeller inlet is due to the increase in centrifugal action on the fluid as the impeller picks up speed. For all the chord lengths, pressure recovery is high at low flow rates (<100%) and it has increased from twist 5° to 9° and decreased to 11° and is highest for TVD with 100-mm chord length and 9° twist.

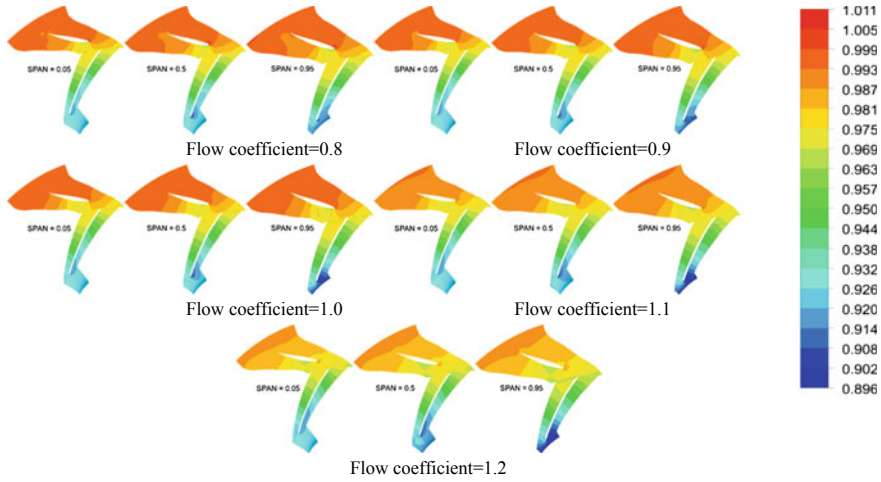


Fig. 8.9 Variation of normalised absolute pressure for TVD with 100-mm chord length and twist 9°

8.9 Variation of Velocity in the Diffuser

Variation of normalised absolute velocity in the diffuser along streamwise direction at mid-span (50%) is shown in Fig. 8.10. Variation is presented for the design mass flow rate for all the chord lengths at twist 9° considered in the present analysis. Normalisation is carried out with the impeller tip velocity (u_2). With the increase in chord length, average absolute velocity has decreased for all the mass flow rates under consideration in the analysis. Least average absolute velocity is observed for chord length 100 mm. This shows the superiority of 100-mm chord length over other chord lengths. This variation is in line with the fundamental that at higher pressures, the velocity of the flow is lower and vice versa.

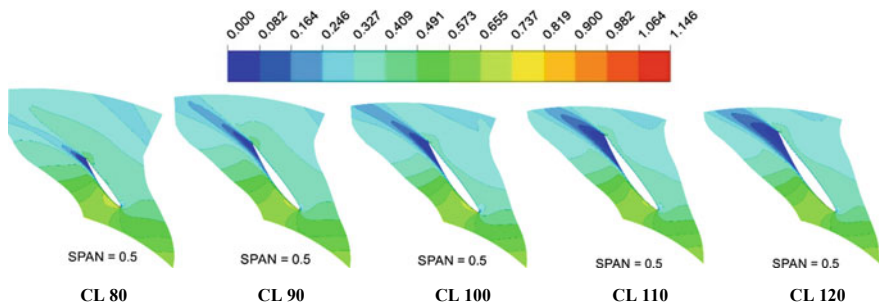


Fig. 8.10 Variation of normalised velocity for TVD with twist 9° and design flow rate at specified chord length

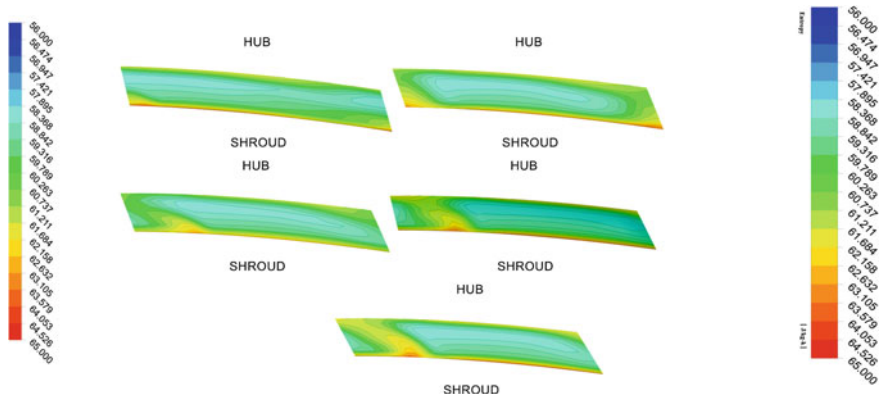


Fig. 8.11 Variation of static entropy at the diffuser exit for TVD at twist 9° and design flow rate with chord length 80, 90, 100, 110 and 120 mm, respectively

8.9.1 Variation of Entropy at Diffuser Outlet

Figure 8.11 shows the variation of entropy at diffuser outlet for TVD with the chord lengths considered for the present analysis. It can be observed from the contours that the static entropy at the diffuser exit has increased from chord length 80–90 mm and dropped to 100 mm, and then it increased from 110 to 120 mm at a specified twist of 9°. This shows the superiority of 100-mm chord length over the other chord lengths considered for the analysis.

8.10 Conclusions

CFD analysis is carried out on an industrial centrifugal compressor stage to compare the performance of it with the vaneless and twisted vaned diffuser and to examine the effect of twist angle and a chord length of the twisted vane in a TVD on the performance, as well. Chord lengths are varied from 80 to 120-mm insteps of 10 mm and twist angle from 5° to 11° insteps of 2° at flow coefficients 0.8, 0.9, 1, 1.1, 1.2. The overall performance of the compressor stage is evaluated by means of different performance parameters to arrive at the best results. The study indicated that there is a significant pressure rise in twisted vaned diffusers as compared to VLD. The twisting is provided to the diffuser vanes in the opposite direction of impeller rotation. Among the different twists provided 9° is found to be the best. Lower performance at chord lengths 80 and 90 mm can be attributed to insufficient retardation to the flow and at chord lengths 110 and 120 mm due to higher drag offered. High performance is observed at chord length 100 mm. So, it can be concluded that among different configurations of twisted vaned diffuser examined, the one with chord length 100 mm

and twist 9° operating at design flow rate is found to be the best for the chosen case. For the best configuration of TVD relative to best configuration of VLD, the maximum increase in total-to-static stage efficiency is 07.71%, maximum increase in the static head coefficient is 06.96%, and maximum increase in the static pressure recovery is 25.70%, which clearly shows the significant improvement in the performance of the compressor stage by employing TVD. As the twist angle or chord length changes, there is no considerable effect on the power consumption, but when compared with VLD, the power consumed by the TVD is less.

References

1. Anish, S., Sitaram, N.: Computational investigation of impeller-diffuser interaction in a centrifugal compressor with different types of diffusers. *Proc. Inst. Mech. Eng. J. Power Energ.* **223**, 167 (2009). <https://doi.org/10.1243/09576509jpe662>
2. Engeda, Abraham: Experimental and numerical investigation of the performance of a 240 kw centrifugal compressor with different diffusers. *Exp. Therm. Fluid Sci.* **28**, 55–72 (2003)
3. Galerkin, Y., Soldatov, K., Soloviev, O.: Numerical study of centrifugal compressor stage vaneless diffusers. *IOP Conf. Ser. Mater. Sci. Eng.* **90**, 012048 (2015)
4. Senoo, Y.: Japanese patent application disclosure 119411/78, Oct 1978
5. Senoo, Y., Hayami, H., Ueki, H.: Low-solidity tandem-cascade diffusers for wide-flow-range centrifugal blowers. ASME Paper No. 83-Gt-3 (1983)
6. Yoshinaga, Y., Kaneki, T., Kobayashi, H., Hoshino, M.: A study of performance improvement for high specific speed centrifugal compressors by using diffusers with half guide vanes. *ASME J. Fluids Eng.* **109**, 359–367 (1987)
7. Abdelwahab, A.: On the use of three-dimensional airfoil-shaped vaned diffusers with industrial centrifugal compressors. In: 4th AIAA Theoretical Fluid Mechanics Meeting 6–9 June 2005, Toronto, Ontario Canada
8. Abdelwahab, A., Gordon, G., Baker, R.: Airfoil Diffuser for centrifugal compressor. US Patent Application Disclosure 11/903592, Sept 2007
9. Abdelwahab, A., Gordon, G., Baker, R.: Leaned centrifugal compressor airfoil diffuser. US Patent Application Disclosure 11/199252, Aug 2005
10. Rao, V., Ramana Murty, G.V., Venkata Rao, G.: Analysis of flow through a twisted vaned diffuser V001T01A004. ASME 2014 Gas Turbine India Conference, New Delhi, India (2014). <https://doi.org/10.1115/gtindia2014-8163>, ISBN 978-0-7918-4964-4
11. Rao, V.P., Murty, G.V.R., Venkata Rao, G.: Study on effect of twist direction in a diffuser vane on the performance of a centrifugal compressor stage. In Proceedings of the 6th International and 43rd National Conference on Fluid Mechanics and fluid Power, MNNIT, Allahabad, UP, Dec 15–17, 2016
12. Siva Reddy, TCh., RamanaMurty, G.V., Prasad, M.V.S., Reddy, D.N.: Experimental studies on the effect of impeller width on centrifugal compressor stage performance with low solidity vaned diffusers. *Proc. Instn. Mech. Engrs, Part A: J. Power Energ.* **221**, 519–533 (2007)

Chapter 9

Computational Study on the Effect of Aft-Body Attachments on Base Drag Using Locked Vortex Flow Management Technique



Thippeswamy Sanjitha, Kailas S. Jagtap, Karthik Sundararaj, Prakash S. Kulkarni, Manoj Veetil, Arun Mallappa Bagewadi, Syed Sameer Mujaawar and Kothnur Narayanaswamy Ramyashree

Abstract An attempt to minimize drag has always been a key concern for the expectation of high performance. Bluff bodies are usually dominated by pressure drag which is a result of flow separation, and it accounts for a considerable amount of the total drag. Drag reduction techniques prove to be a major aid in minimizing vortex shedding and wake; this can be applied while building launch vehicles and missiles. Flow over bluff bodies exhibit vortex shedding and produce large wakes which can be countered with the help of passive flow control technique. The modification in the design of the body with the help of attachment of splitter plates for trapping the vortices proves to significantly reduce the base drag, and it is considered as one of the most effective passive control techniques. The paper focuses on the influence of after-body attachments on the base drag and the evaluation of the effectiveness of these attachments. Comparison of variation in base drag is made considering three cases—initial analysis is done on a body without any attachments; further observation of changes in base drag is done with the attachment of a shaft to the base of the body and then with the attachment of single splitter plate to the shaft. Examining the simulation results, it can be observed that with the attached splitter plate design, vortex shedding is suppressed along with the achievement of pressure recovery. The work is a computational study on the effect of aft-body attachments on base drag. Locked vortex method can be considered as an effective method in reducing base

T. Sanjitha (✉) · M. Veetil · A. M. Bagewadi · S. S. Mujaawar · K. N. Ramyashree
IIAEM, Jain University, Bangalore, India
e-mail: sanjitha.soujannya@gmail.com

K. S. Jagtap
K J Somaiya College of Engineering, Mumbai, India

K. Sundararaj
ARK Infosolutions Pvt. Ltd., Bangalore, India

P. S. Kulkarni
IISc, Bangalore, India

© Springer Nature Singapore Pte Ltd. 2020
C. Li et al. (eds.), *Advances in Engineering Design and Simulation*,
Lecture Notes on Multidisciplinary Industrial Engineering,
https://doi.org/10.1007/978-981-13-8468-4_9

drag. Further studies are planned with the attachment of double or triple splitter plates with experimental assessments.

Keywords Base drag · Vortex shedding · Bluff body · Splitter plate · Vortex flow · Wake

Nomenclature

D Diameter of the body
 d Diameter of the shaft
 D_1 Diameter of the splitter plate
 t_1 Thickness of the splitter plate
 x Length of the shaft
 k Turbulent kinetic energy

9.1 Introduction

Drag force acts opposite to the relative motion of any object moving in a fluid and has an effective impact on all kinds of bodies like a bluff body, boat-tailed after-body, and streamlined bodies. While considering the bluff bodies, one can observe that it is dominated by pressure drag, which entirely depends on the cross-sectional area of the body. Pressure drag arises due to the difference in pressure between the front and rear surfaces of the body and is a result of flow separation. Flow separation increases the wake size and causes pressure losses in the wake. Friction between the fluid and the surface over which it is flowing causes frictional drag which is more sensitive to Reynolds number when compared to pressure drag.

Drag due to a base pressure lower than ambient pressure is base drag which forms at the flat base of a body and has a considerable influence on the total drag of the body. The flow over a bluff body results in periodic shedding of vortices formed at the base of the body. Vortex shedding increases the base drag and hence needs to be suppressed to increase the performance of the flying object. Earlier work by Miar, on measurement of drag on a blunt-based body of revolution with addition of several alternative boat-tailed afterbodies has shown that a substantial reduction of drag is obtained with an afterbody consisting of a smooth fairing leading to a conical tail-piece of semi-angle 22° [1]. Another paper by P R Vishwanath discusses about the effectiveness of ventilated cavities, base cavities, locked vortex afterbodies, multistep afterbodies and non-axisymmetric boat-tailing for base, at different speed regimes [2].

Flow control techniques can be implemented to suppress vortex shedding and reduce the base drag. After-body attachments are used to reduce the base drag and are considered as an effective passive control technique. Passive control technique

includes the modifications in the design of the body which helps in pressure recovery and vortex shedding suppression.

Locked vortex drag reduction technique helps in attaining pressure recovery at the base of the body, and with the attachment of single splitter plate, the vortices can be trapped between the base of the body and the plate. In the view of observing the variation in base drag, three different cases are considered. The initial analysis is done on the bluff body without any attachments; further investigation is done by attaching a shaft to the base of the body. And, with the attempt to achieve substantial pressure recovery and a reduction in base drag, a single splitter plate is attached to the connecting shaft.

Many parameters like the Reynolds number, Mach number, and after-body shape have a considerable effect on the drag of the body. The diameter of the shaft, the length of the shaft, and the diameter of the splitter plate also have an important influence on the base drag. The current study is to investigate the effect of after-body attachments on the drag.

9.1.1 Methodology

A simple 2D geometry and the domain surrounding it are developed using ANSYS SpaceClaim tool. ANSYS meshing tool is used to create meshes for the geometries. To set the material properties and boundary conditions, to initiate calculations, and visually examine the flow, ANSYS Fluent is used. The paper written by Miar [3] is used extensively for initial solver validation.

9.1.2 Setup

The total length of the geometry is 457.2 mm, and the diameter is 75.8698 mm. The geometry has a rounded nose, and the angle of attack is 0.2° .

During the studies, the diameter and the length of the rod are varied, and the diameter of the splitter plate is varied to find the best drag reduction model. The simulation is done on these cases to find the accurate results by considering the rectangular cross-sectional domain similar to the wind tunnel which is 4114.8 mm long and 508 mm wide.

All the values are scaled up 5.25 (Tables 9.1 and 9.2).

9.1.3 Mesh

The analysis is done on a simple 2D model, and finding the best mesh settings that provide the ΔC_d value much closer to the experimental value is required. For all the

cases, the maximum layers of inflation given are 5 layers with the first layer height of $2.296e^5$ m.

9.1.4 Grid Independence Test

To obtain improved results, grid independence test is conducted and eight different meshes are created. Meshing is done for two cases: (a) body without splitter plate and (b) body with a splitter plate, to check the variation of ΔC_d value. The simulation is carried out for the three turbulent models (for both simple and coupled schemes), for all the eight meshes of both the cases.

The mesh details for all the eight meshes can be seen from Tables 9.3 and 9.4. Five layers of inflation are given for all mesh cases with a first layer height of $2.296e^5$ m.

Figure 9.1 shows the plot between ΔC_d and mesh; the ΔC_d value is obtained by taking the difference between the drag values obtained for the body with a plate

Table 9.1 Shaft length for different x/D ratios (all dimensions are in mm)

S. no.	x/D	D	x
1	0.2	75.8698	15.17396
2	0.4	75.8698	30.34792
3	0.6	75.8698	45.52188
4	0.8	75.8698	60.69584
5	1.0	75.8698	75.8698
6	1.2	75.8698	91.04376

Table 9.2 Plate diameters for different $D1/D$ ratios

$D1/D$	$D1$	D
0.585	44.384	75.8698
0.795	60.3165	75.8698
0.919	69.7243	75.8698

Table 9.3 Mesh details for the body without splitter plate

Mesh no.	Number of nodes	Number of elements
1	49,031	47,259
2	100,616	97,107
3	155,623	150,357
4	211,313	204,332
5	268,892	260,239
6	326,362	315,998
7	388,075	376,038
8	450,209	436,628

Table 9.4 Mesh details for the body with a splitter plate

Mesh No.	Number of nodes	Number of elements
1	81,636	78,689
2	161,345	155,478
3	240,413	231,723
4	328,609	316,988
5	423,547	409,037
6	473,375	455,913
7	604,890	584,652
8	697,506	674,632

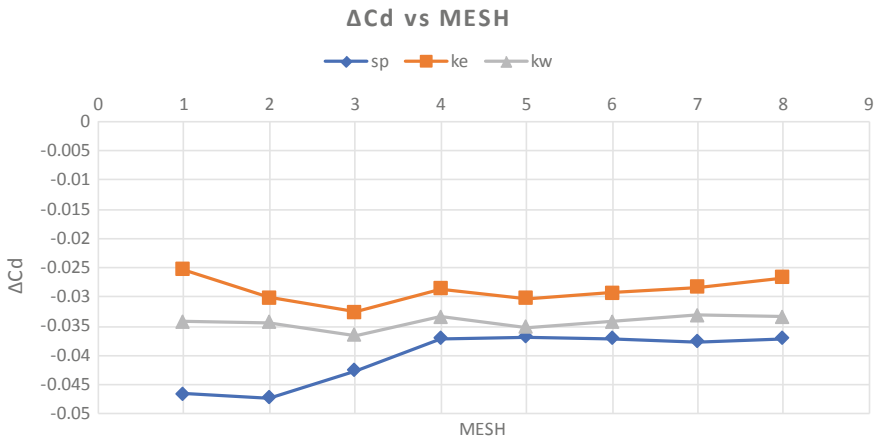


Fig. 9.1 ΔCd versus mesh

(diameter 60.3165 mm) and body without a plate. Out of Spalart–Allmaras, k-epsilon, and k-omega turbulent models, Spalart–Allmaras model with the coupled scheme is chosen for further analysis. Mesh 3 with Spalart–Allmaras model is considered for simulations as its ΔCd value is much closer to the experimental value.

9.1.5 Geometries

Figure 9.2 shows the bluff body considered for initial simulation, with length ‘L’ = 457.2 mm and diameter ‘D’ = 76.8698 mm. The drag value is noted for this geometry as a reference for further simulations with design modifications.

The attachment of the connecting shaft is shown in Fig. 9.3 where ‘d’ refers to the diameter of the shaft and x is the length of the shaft.

Figure 9.4 represents the attachment of a single splitter plate with plate thickness 3.175 mm.

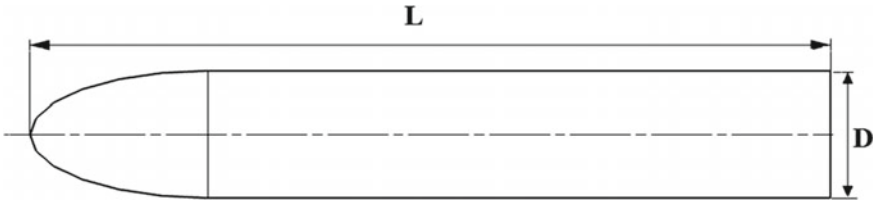


Fig. 9.2 Bluff body [4]

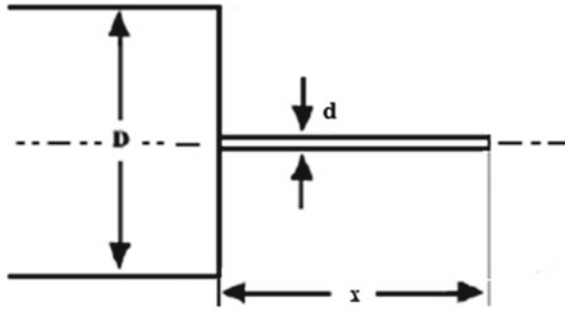


Fig. 9.3 Body with the shaft [4]

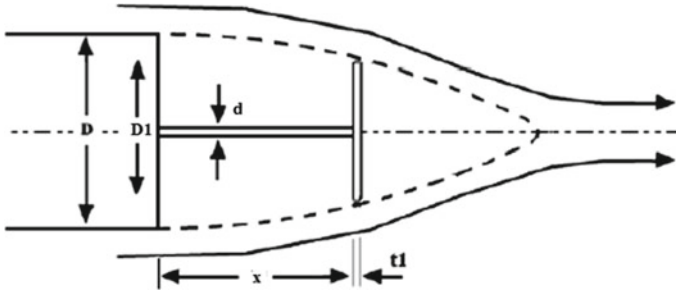


Fig. 9.4 Body with splitter plate [4]

9.1.6 Boundary Conditions

Pressure and velocity play a significant role in the flow over the body. The flow is lower subsonic, and the free flow over the body has an inlet velocity of 30.48 m/s and Reynolds number $6e^5$ with pressure being considered at the outlet. The turbulence intensity considered is 2%.

9.2 Results

9.2.1 Validation Case

Figure 9.5 represents the variation of ΔC_d value from the results of the simulations conducted, and it is compared with results from the reference paper by Miar [3].

ΔC_d value is calculated from the simulation results of the body with the plate and a bluff body, and it is compared with the experimental data of the reference paper. The simulation data plot shows that ΔC_d value decreases as the x/D ratio increases but is valid up to a certain x/D ratio, after which the ΔC_d value increases. The maximum drag reduction is observed between 0.4 and $0.6x/D$ ratio which is similar to the experimental data. The peak between 0.2 and $0.4x/D$ ratio from the experimental data is something which is of unexplainable nature since there is no possibility of such a high increase drag coefficient; this probably could be an error or lapse in data as the experimental work was done many years ago. The numerical analysis provides a clear picture of the variation of drag over different cases in an effective way which seems to be predicting the right physics.

9.2.2 For a Body with Only Shaft

Figure 9.6 represents the ΔC_d values of various cases for the body attached with the shaft. The analysis was done by varying the values of 'x' (the length of the shaft) for a varying diameter of the shaft, and the drag value is noted for each of these x

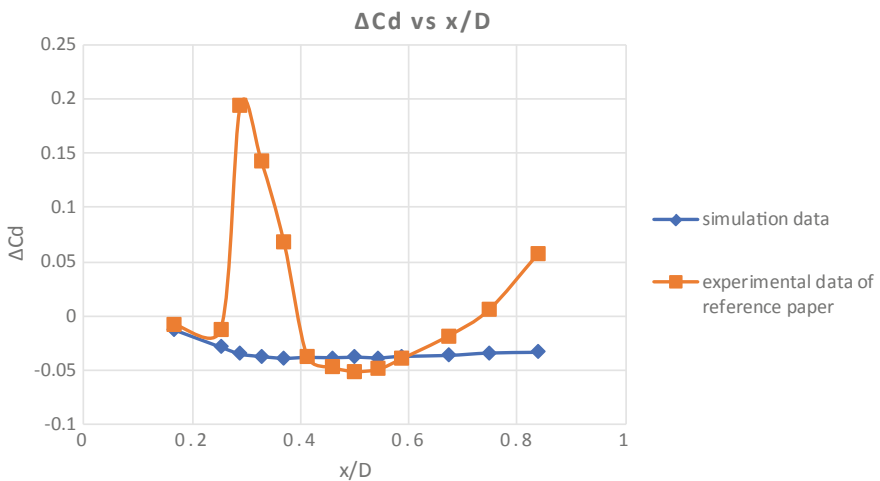


Fig. 9.5 ΔC_d versus x/D [3]

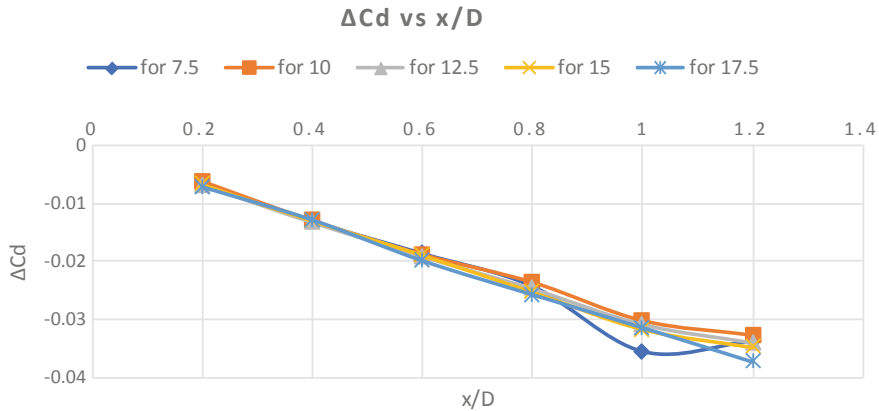


Fig. 9.6 ΔC_d versus x/D

values. The different diameters of the shaft chosen for simulation are ‘7.5, 10, 12.5, 15, 17.5’ mm. It can be observed that the drag is maximum at a smaller value of x and continues to decrease as x increases. There is not much difference in the drag values between various diameters for a similar length.

There is a significant reduction in drag for the bodies attached with the shaft when compared to the drag that is obtained from the body with no attachments. About 30–35 percent of drag reduction can be observed with the attachment of shaft. For further simulation, shaft diameter of 9.523 mm is considered from the literature [3].

9.2.3 For a Body with Plate

To reduce the base drag further, the splitter plate is attached to the connecting shaft. The diameter of the shaft is 9.523 mm, which is kept constant throughout this analysis. Simulation is done by changing the diameter of the plate. Three different diameters are considered, which are calculated from the $D1/D$ ratios—‘0.585, 0.795, and 0.919’. For the first case of $D1/D$ ratio—0.585, keeping the calculated diameter of the plate constant, the distance between the base of the body and the plate (x value) is varied and the changes in drag for each of the x values are observed. In the similar way, the analysis is performed for the other cases of $D1/D$ ratios of 0.795 and 0.919. The difference in the drag value is noted, and ΔC_d value is calculated by comparing obtained drag value with that of the bluff body.

It can be observed from Fig. 9.7 that for the $D1/D$ ratio of 0.585, there is maximum drag reduction corresponding to the x/D ratio of 1. From the curve, it can be seen that as the x/D ratio increases, the drag value reduces up to a certain limit after which it is seen to vary. Around 38–40% of drag reduction is observed for this case.

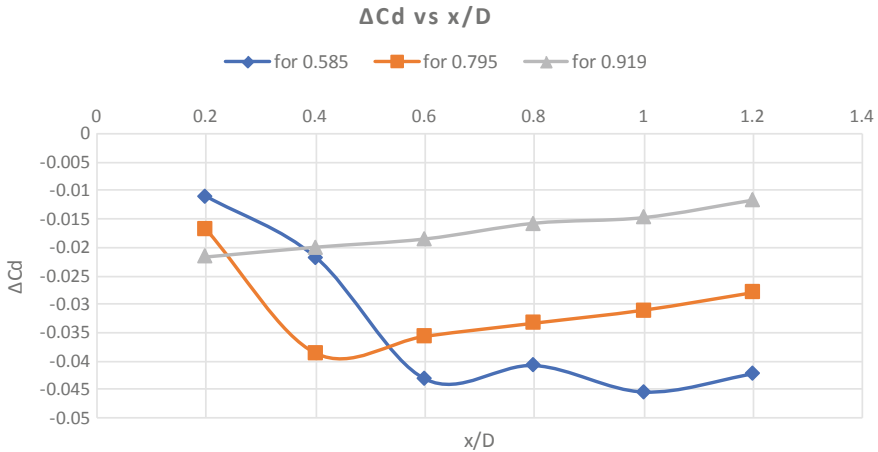


Fig. 9.7 ΔCd versus x/D

And for the ratio of 0.795, there is a substantial drag reduction up to a certain increase in x/D ratio, after which the drag value tends to increase. The best drag reduction for this case is seen for the x/D ratio of 0.4. There is about 32–36% of drag reduction.

But for the case of 0.919, it can be observed that as the x/D ratio increases, the drag value also increases with it. Since the diameter of the plate is large, there is not much drag reduction, and it can be observed that there is less drag at the minimum x/D ratio. Only about 10% of drag is reduced in this case. From Fig. 9.8, it can be noticed that the vortices are trapped between the base of the body and the splitter plate, due to which vortex shedding is suppressed. This reduces the pressure loss at the base which leads to the reduction in base drag.

9.3 Pressure Measurement

Pressure plots convey the information about the distribution of pressure at the base of the body. Line 1 is 0.5331 m from the base; similarly, line 2 and line 3 are at distance of 0.9331 and 1.3331 m from the base of the body, respectively (Figs. 9.9, 9.10 and 9.11).

To observe the evidence of pressure recovery due to attachment of the shaft and plate, the pressure plots are compared with the plot of the bluff body. Also, the plots of the shaft and splitter plate are compared with each other. The attachment of the splitter plate provides more drag reduction and pressure recovery than the shaft. The vortices are locked between the base of the body and the splitter plate. This helps in minimizing the base drag and suppressing the vortex shedding. Substantial pressure recovery can be observed due to the attachment of the splitter plate.

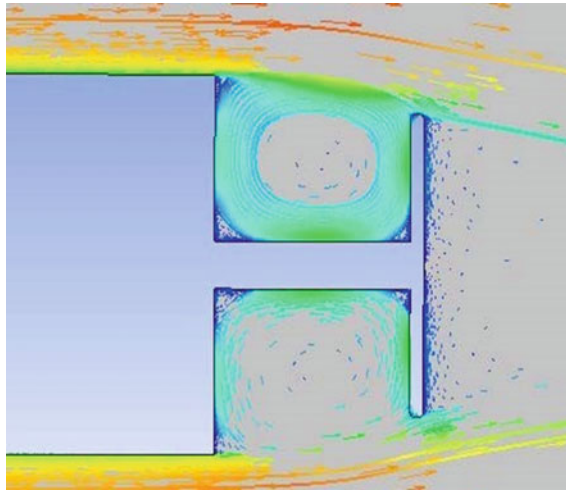


Fig. 9.8 Vortices trapped between the base and the plate [4]

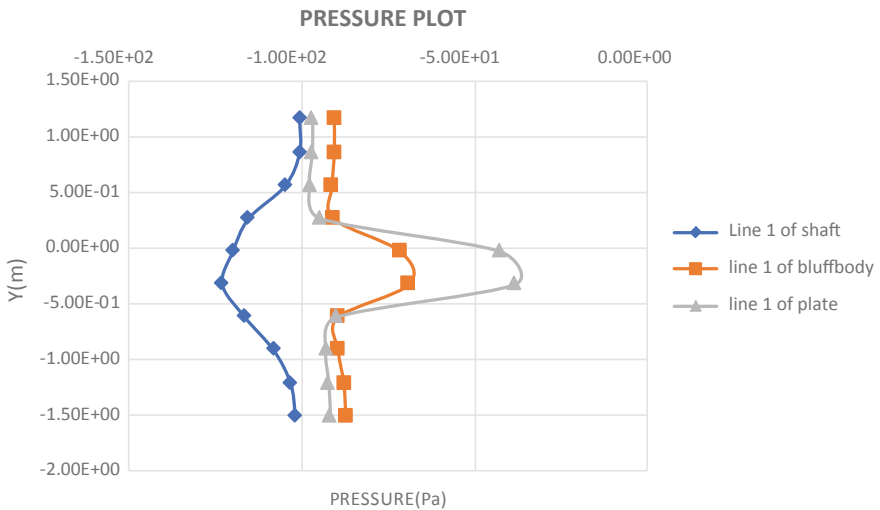


Fig. 9.9 Pressure plot (line 1 is 0.5331 m from the base)

9.4 Conclusion

A bluff body without any attachments is observed to produce more base drag, but with the modifications in the design, the base drag is observed to have reduced. The analysis was performed with the initial objective of observing the effect of attachments on the base drag and to minimize it. The numerical investigation was

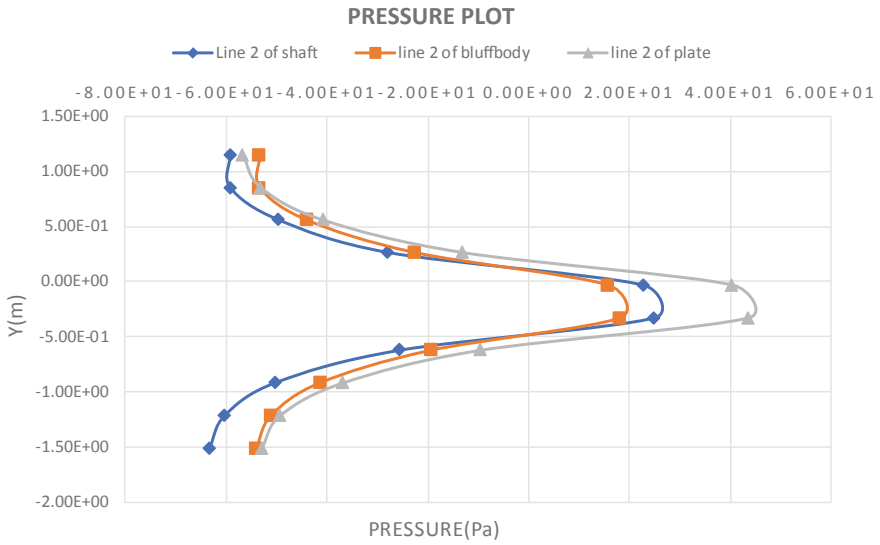


Fig. 9.10 Pressure plot (line 2 is 0.9331 m from the base)

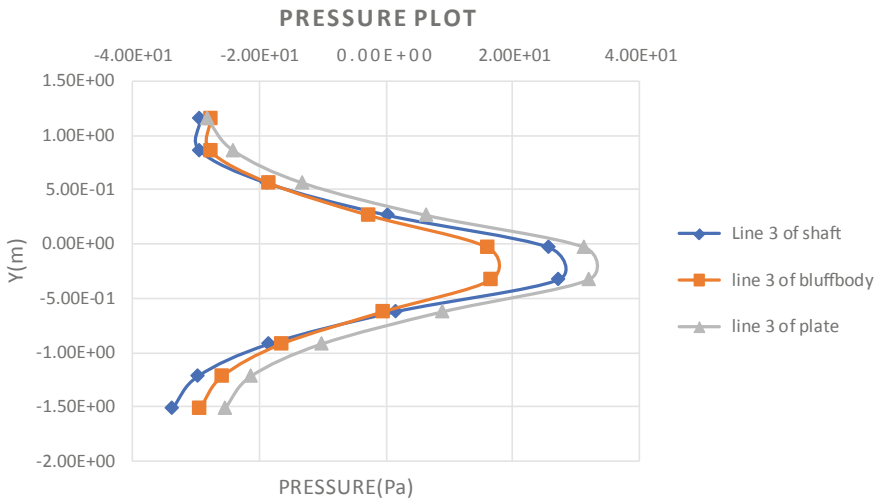


Fig. 9.11 Pressure plot (line 3 is 1.3331 m from the base)

conducted to cater to this objective, and the changes in various parameters were carefully observed.

Due to the attachment of splitter plate, there is substantial pressure recovery at the base of the body and the vortices are trapped between the splitter plate and the base of the body which suppresses vortex shedding. There is a greater reduction in the base drag due to the attachment of splitter plates when compared with the drag values obtained with the attachment of shaft and of the bluff body. There is about 30–35% of drag reduction with the attachment of shaft, but with the attachment of splitter plate, one can observe about 32–40% achievement of a reduction in base drag.

9.5 Future Scope

Further simulation activities are in progress with double and triple splitter plate attachments to the bluff body. Experimental activities have been carried out for all splitter plate configurations at low-speed wind tunnel in Indian Institute of Science, Bangalore.

Acknowledgements We are thankful to IISc, Bangalore, for their continued guidance and support in providing access to the Computational Mechanics Laboratory and to the Low-Speed Wind Tunnel Complex. Our sincere thanks to ANSYS for their support in providing necessary licenses for the successful completion of all simulation activities.

References

1. Miar, W.A., Reduction of base drag by boat-tailed afterbodies in low-speed flow. *Aeronaut. Q.* (1969)
2. Viswanath, P.R.: Flow management techniques for base and afterbody drag reduction. *Aeronaut. Q.* (1995)
3. Miar, W.A.: The effect of a rear-mounted disc on the drag of a blunt-based body of revolution. *Aeronaut. Q.* (1965)
4. Jagtap, K.S., Sundarraj, K., Kumar, N., Rajnarasimha, S., Kulkarni, P.S.: Numerical study of base drag reduction using locked vortex flow management technique for lower subsonic regime. In: ICFMFA, Mumbai (2018)

Chapter 10

Reconstruction of Femur Bone from DICOM Files and FEA on Fractured Human Femur Bone with PEEK Thermoplastic Prosthetic Plate Implantation



S. Kirthana and Mohammed Khaja Nizamuddin

Abstract The longest and strongest bone in the human body is the femur bone also known as the thigh bone supports the maximum weight of the body under loading conditions. Fracture of bones is one of the common issues in the present medical world. One of the methods to treat bone fractures is using prosthetic implants. There are different biomaterials that are used to make these prosthetic plates like metals, polymers, composites, and ceramics. The purpose of this work is to develop the femur bone model from DICOM files and analyze the fractured human femur shaft with PEEK thermoplastic prosthetic plate implant by FEA in static loading conditions. Results are compared with the other biomaterials like SS316L, alumina, and titanium to prove PEEK is also a suitable material for femur shaft fracture prosthetic plate implantation. The femur model is developed using 3D Slicer and Blender softwares. Analysis is done in ANSYS workbench 18.1.

Keywords Femur bone · DICOM files · PEEK · FEA · Prosthetic plate

10.1 Introduction

Fractures in femur bone are caused due to a large force, impact loads, accidents, fall from high altitudes, and disease in the bone. Classifications based on the severity of the fracture are stress fracture, severe impact fracture, partial fracture, and completely displaced fracture. One of the methods to treat bone fractures is using prosthetic implants. The types of prosthetic plates from early stages to the present day of implantation surgeries are compression plate (CP), dynamic compression

S. Kirthana (✉) · M. K. Nizamuddin
Department of Mechanical Engineering, Vasavi College of Engineering, Hyderabad 500031, India
e-mail: kirthana6831@gmail.com

M. K. Nizamuddin
e-mail: nizamohdk@gmail.com

© Springer Nature Singapore Pte Ltd. 2020
C. Li et al. (eds.), *Advances in Engineering Design and Simulation*,
Lecture Notes on Multidisciplinary Industrial Engineering,
https://doi.org/10.1007/978-981-13-8468-4_10

plate (DCP), limited-contact dynamic compression plate (LC-DCP), point contact fixator (PC-Fix), less invasive stabilization system (LISS), locking compression plate (LCP), and precontoured LCP.

10.1.1 Different Materials Available for Manufacturing Prosthetic Plates

There are different biomaterials that are used to make these prosthetic plates like metals, polymers, composites, and ceramics. Stainless steel is mostly used in orthopaedic implants for temporary fixation plates where the plates are removed after the healing process is completed. Otherwise, it leads to allergy and toxic reactions in the body. Titanium alloys are the most usable implantation material as it has extensive mechanical properties, resistance to corrosion, resistance to fatigue corrosion, and low density. It was considered as the better material in implantation when compared with stainless steel. The examples of polymers and composites are polymethyl methacrylate (PMMA), poly lactic acid (PLA), poly glycolic acid (PGA). Alumina and hydroxyapatite (HA) come under the category of bioceramics. But these materials cannot be used directly as implants due to its low mechanical strength and low fracture toughness. But these materials can be used in the form of coatings and mixed ratios with other biomaterials.

The present work can be divided into two main categories. One is the reconstruction of bone from DICOM files and the second one is to do Finite element analysis fractured human femur bone with PEEK thermoplastic prosthetic plate implantation.

10.2 Reconstruction of the Femur Bone from DICOM Images

To develop the 3D models of bones or tissues, CT or MRI data is to be collected. CT or MRI data is saved in the form of DICOM files is used in CAD software to develop the models.

10.2.1 Reconstruction of Bone Using 3D Slicer

The collected DICOM files with the slice thickness of 0.6 mm were imported into this software. By enabling the volume rendering feature, we can observe the visualization of the files on the Slicer window in four views, i.e., axial view, three-dimensional view, sagittal view, and coronal view as shown in Fig. 10.1. A preset selection of CT bones was selected, and it can be observed that in the three-dimensional view, only

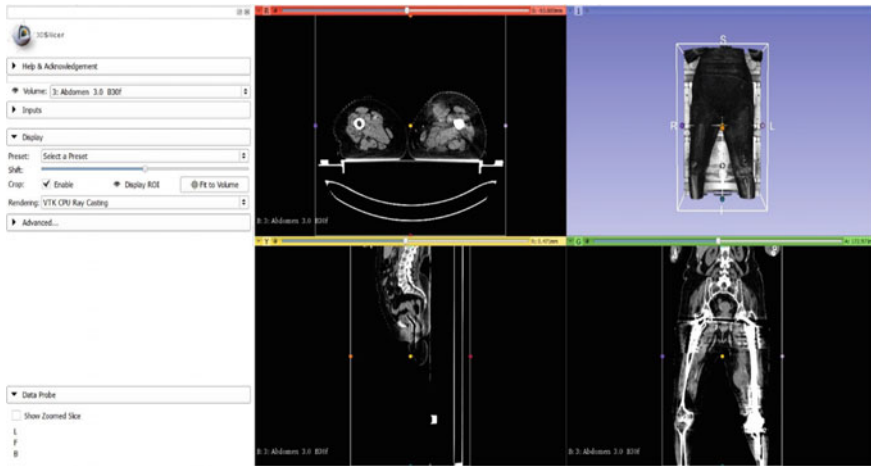


Fig. 10.1 3D Slicer window showing four views

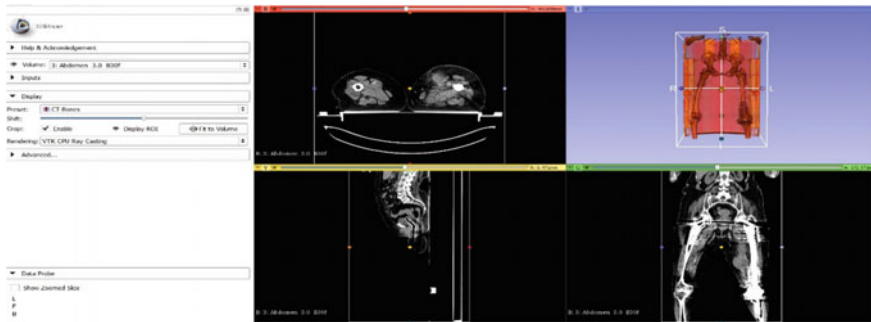


Fig. 10.2 Preset selection

bones were visualized removing all the other unwanted material which is shown in Fig. 10.2.

After this, cropping was done by using the crop volume module. Here the cropping was done to get the right femur bone of the image. The cropped new volume is shown in Fig. 10.3.

From the obtained CAD model, it was observed that the model is with a lot of obstructions, irregularities, and discontinuities as it is already gone for a prosthesis with implantations. So to obtain the best model without any errors, the paint effect was used in the editor module. After using the paint effects, the best 3D cad model of the right femur is as shown in Fig. 10.4 [1, 2]. This obtained model was saved in STL file format as to import the model into the blender. The obtained model was with some errors, and the surface achieved was rough. To remove this, a software called Blender was used.

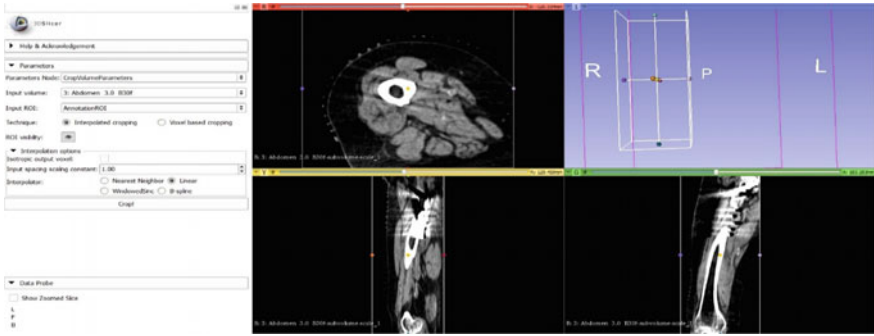
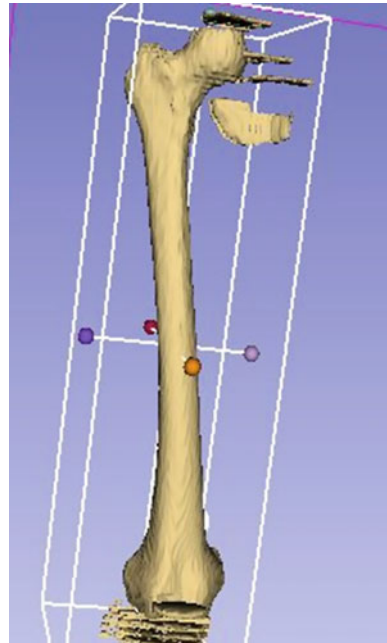


Fig. 10.3 Cropped volume

Fig. 10.4 Showing 3D CAD model of the right femur after using paint effect



10.2.2 Finishing the Femur Model Using Blender

The obtained model from 3D Slicer was imported into Blender to remove the discontinuous shapes and errors and to obtain a good surface finish which is shown in Fig. 10.5 from the selection mode; the continuous and inverted links were selected by vertex selection, and the inverted links were deleted to obtain an error-free femur bone without any obstructions which are shown in Fig. 10.6a, b.

After applying the smoothening option from object modifiers, the final 3D CAD model of the femur with the good surface finish is shown in Fig. 10.6c.

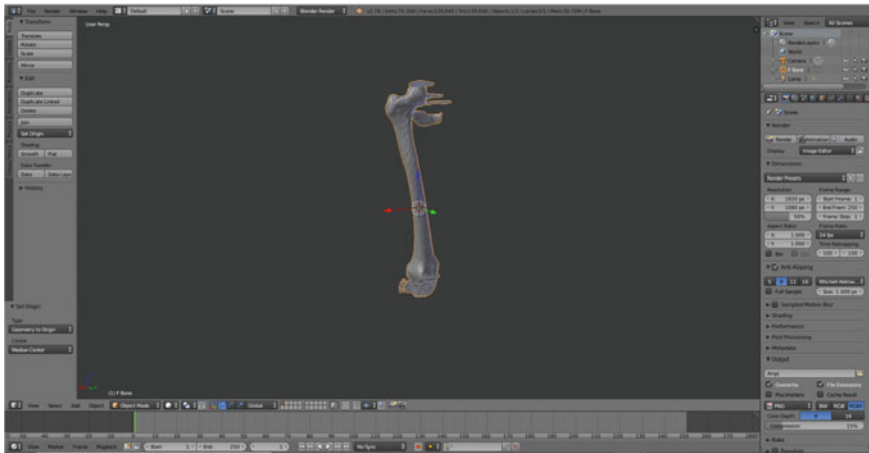


Fig. 10.5 Blender window with imported STL file of the right femur bone

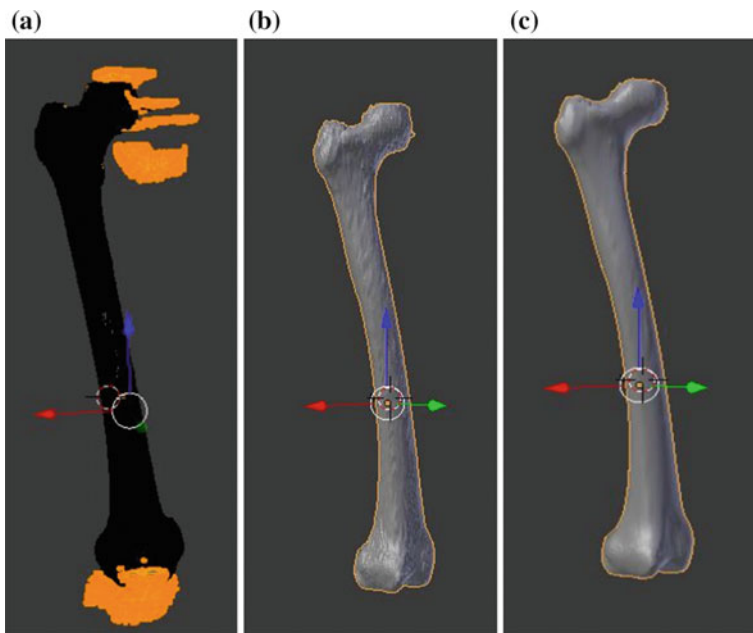
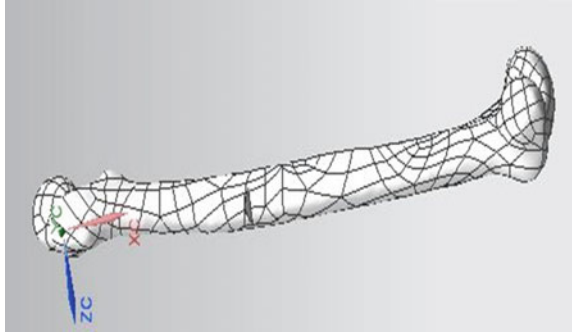


Fig. 10.6 Showing a inverted links b obtained model without errors c final 3D CAD model of the right femur with the good surface finish

Fig. 10.7 Fracture on femur shaft



10.2.3 Initiation of Fracture on Femur Bone

Partial fracture was initiated for further study on analysis of fractured femur bone [3]. The fracture was generated in NX by removing the part material from the shaft of femur bone as shown in Fig. 10.7

10.3 Fractured Femur Bone Analysis

The fractured femur bone was inserted into the static structural module and the material properties of femur bone were assigned from Refs. [4, 5].

10.3.1 Meshing

Meshing of the fractured femur bone was done with element type triangular and element size of 5 mm.

10.3.2 Boundary Conditions

The lower part of the femur bone was fixed, and two forces on the upper part of the femur were assigned [6, 4].

Force 1: 750N, 150, 0 and Force 2: -150N, -50N, 0

Force 1 is the total body weight of the person which is acting downward when the person is standing, and force 2 is the reaction force which is acting in the opposite direction as shown in the Fig. 10.8.

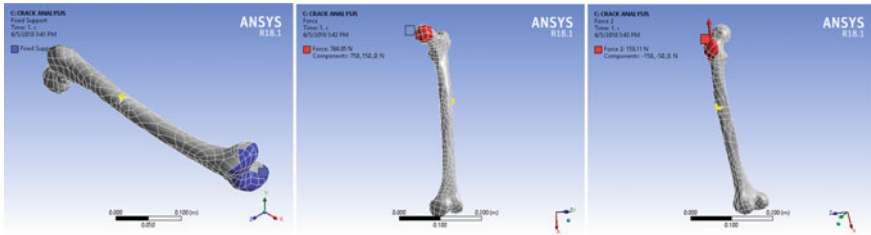


Fig. 10.8 Boundary conditions

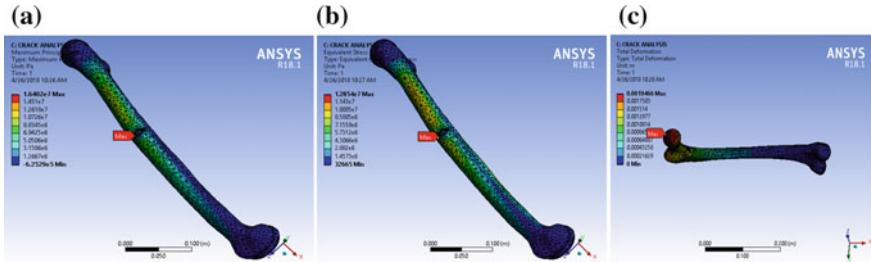


Fig. 10.9 Fractured bone a maximum principal stress b equivalent stress c total deformation

10.3.3 Results of Fractured Bone Analysis

A static structural analysis is carried out, and it was noted that the maximum stresses are acting on the shaft at the initiation of fracture for the boundary conditions that are considered and the total deformation was seen maximum on the head of the femur bone. The results are as shown below Fig. 10.9.

10.4 Assembly for Fractured Bone and Prosthetic Plate

In this work, the prosthetic plate of LCP type is modeled [7] and assembly is done in NX 11.0 assembly module as shown in Fig. 10.10. The meshed assembly of prosthetic plate and femur bone has 29,155 nodes and 16,030 elements. Bonded contact option in ANSYS was used to make sure that plate is in surface contact with the fractured bone.

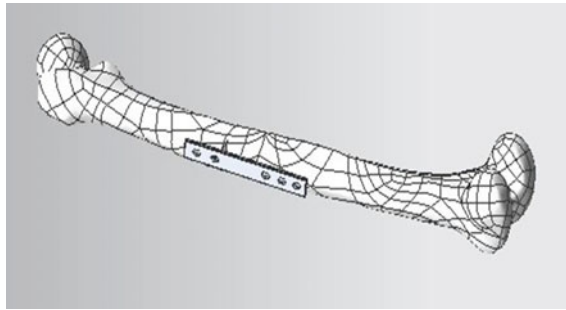


Fig. 10.10 Assembly of femur and prosthetic plate

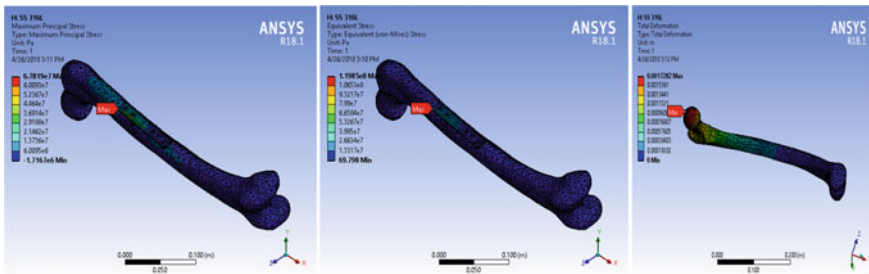


Fig. 10.11 Maximum principal stress, equivalent stress, and total deformation of fractured bone with SS316L plate

10.5 Assembly Analysis

Edge size meshing was generated at the crack by using the same mesh sizing as of fractured bone, and the boundary conditions are kept the same as of fractured bone. Analysis of the assembly was carried out by changing the material properties of prosthetic plates, from Refs. [8–11]. The results of stresses and deformation of prosthetic plate materials SS316L, alumina, titanium, and PEEK are as shown in Figs. 10.11, 10.12, 10.13 and 10.14. The results of maximum principal stress, equivalent stress, and total deformation are consolidated in Table 10.1.

10.5.1 Analysis Results of Fractured Bone with SS316L Prosthetic Plate

See Fig. 10.11.

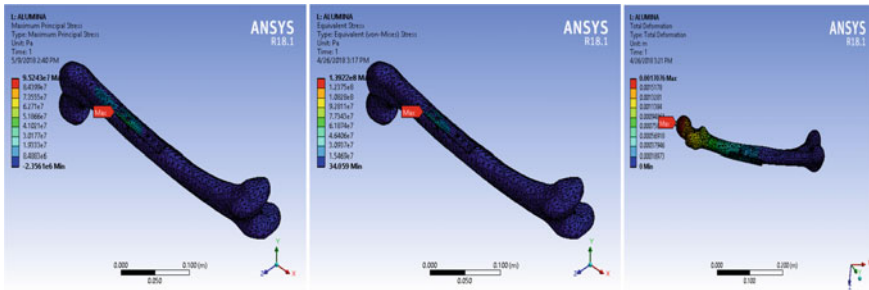


Fig. 10.12 Maximum principal stress, equivalent stress, total deformation of fractured bone with alumina plate

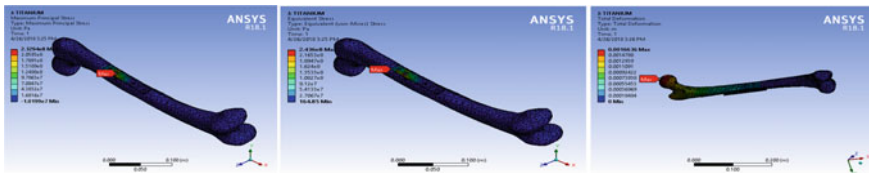


Fig. 10.13 Maximum principal stress, equivalent stress, and total deformation of fractured bone with titanium plate

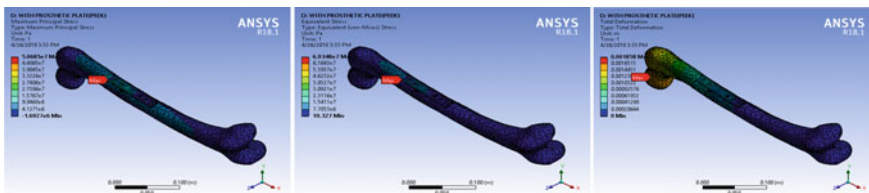


Fig. 10.14 Maximum principal stress, equivalent stress, and total deformation of fractured bone with PEEK plate

Table 10.1 Equivalent stress, maximum principle stress and total deformation of fractured bone and fractured bone with Prosthetic plates of different materials

	Equivalent stress (Pa)	Max principle stress (Pa)	Total deformation (m)
Fractured bone	1.2854e7	1.6402e7	0.0019466
Fractured bone with SS316L plate	1.1985e8	6.7819e7	0.0017282
Fractured bone with alumina plate	1.322e8	9.5243e7	0.0017076
Fractured bone with titanium plate	2.436e8	2.3294e8	0.0016636
Fractured bone with PEEK plate	6.9348e7	5.0685e7	0.001858

10.6 Analysis Results of Fractured Bone with Alumina Prosthetic Plate

See Fig. 10.12.

10.6.1 Analysis Results of a Fractured Bone with Titanium Prosthetic Plate

See Fig. 10.13.

10.6.2 Analysis Results of a Fractured Bone with PEEK Prosthetic Plate

See Fig. 10.14.

10.7 Results and Discussions

It was observed that the stresses are increased, and the deformations are reduced. The maximum stresses were acting on the plate which means that the bone was not taking the load. The decrease in the deformations means that the load-bearing capacity was increased by the plates which are affixed to the bone. The obtained maximum stresses and deformations are tabulated as shown in Table 6.1.

10.8 Conclusions and Future Scope

10.8.1 Conclusions

1. Femur bone was reconstructed successfully by using 3D Slicer and Blender softwares from DICOM files or CT scan data.
2. From the results, it was concluded that the stresses were increased and were acting on the plate, taking the maximum load.
3. It was concluded that deformations were decreased and so that the healing can be obtained with less time duration.
4. It was concluded that the titanium material plate fixation was best suitable material as the values of equivalent stress, maximum principal stress, and total defor-

mation are 2.436e8 Pa, 2.3294e8 Pa, and 0.0016636 m, respectively, showing the best results from other biometals.

5. PEEK can be concluded as compatible materials as the values of equivalent stress, maximum principal stress, and deformations are 6.9348e7 Pa, 5.0685e7 Pa, and 0.001858 m, respectively, and were in approximate range with the other biomaterials.

10.8.2 Future Scope

Fibers and other composite materials can be used as prosthetic plates in future which should be tested clinically [12].

Acknowledgements The authors would like to thank management and Department of mechanical engineering of Vasavi College of engineering for providing resources in successful completion of the project.

The authors would like to thank Dr. Shirish Chandra Gampa, MBBS, MDRT, Radiation Oncologist, KIMS Hospitals, Hyderabad, who helped to complete the project by providing the necessary files.

References

1. Baradeswaran, A., Joshua Selvakumar, L., Padma Priya, R.: Reconstruction of images into 3D models using CAD techniques. *Euro. J. Appl. Eng. Sci. Res.* **3**, 1–8 (2014)
2. Velazquez, E.R., Parmar, C., Jermoumi, M., Mak, R.H., Van Baardwijk, A., Fennessy, F.M., Lewis, J.H., De Ruysscher, D., Kikinis, R., Lambin, P., Aerts, H.J.: Volumetric CT-based segmentation of NSCLC using 3D-Slicer. *Sci. Rep.* **18**(3), 3529 (2013)
3. Reddy, M.V.K., Ganesh, B.K.C., Bharathi, K.C.K., ChittiBabu, P.: Use of finite element analysis to predict type of bone fractures and fracture risks in Femur due to Osteoporosis. *J. Osteopor Phys. Act* **4**(180), 2 (2016)
4. Dhanopia, A., Bhargava, M.: Finite element analysis of human fractured femur bone implantation with PMMA thermoplastic prosthetic plate. *Procedia Eng.* **173**, 1658–1665 (2017)
5. Chiu, W.K., Ong, W.H., Russ, M., Fitzgerald, M.: Simulated vibrational analysis of internally fixated femur to monitor healing at various fracture angles. *Procedia Eng.* **188**, 408–414 (2017)
6. Parashar, S.K., Sharma, J.K.: A review on application of finite element modelling in bone biomechanics. *Perspect. Sci.* **8**, 696–698 (2016)
7. Igna, C., Schuszler, L.: Current concepts of internal plate fixation of fractures. *Bulletin UASVM, Veterinary Medicine* **67**(2), 118–124 (2010). ISSN1843-5270
8. Deokar, N.D., Thakur, A.G.: Design development and analysis of femur bone by using rapid prototyping. *IJEDR* (2016). ISSN: 2321-9939
9. Malekani, J., Schmutz, B., Gu, Y., Schuetz, M., Yarlagadda, P.: Orthopedic bone plates: evolution in Structure, Implementation technique and biomaterial. *GSTF J. Eng. Technol. (JET)* **1**(1) (2017)
10. Nag, S., Banerjee, R.: Fundamentals of medical implant materials. *ASM handbook* **23**, 6–17 (2012)

11. Roeder, R.K., Conrad, T.L.: B.S. Bioactive polyaryletherketone composites. PEEK Biomaterials Handbook (2012). <https://doi.org/10.1016/b978-1-4377-4463-7.10011-9>
12. Basafa, E., Armiger, R.S., Kutzer, M.D., Belkoff, S.M., Mears, S.C., Armand, M.: Patient-specific finite element modeling for femoral bone augmentation. *Med. Eng. Phys.* **35**, 860–865 (2013)

Chapter 11

Numerical Simulation of Electrical Operated Mechanism Considering Impact Force



Abhimanyu Kumar Singh, Parkash Kumar and Mahesh Ranade

Abstract Electrical operated mechanism (EOM) is used to remotely open and close the switching device. This is achieved by electrically actuating a mechanism working against the stored energy of spring. It is required that this switching should happen instantaneously, hence the need for higher spring force resulting in the high-speed mechanism, also necessitating the criticality of impact force assessment at the design stage. EOM under consideration is a compact gear train comprising of the worm—worm wheel, rack and pinion, and planetary gear arrangement of spur and worm gear assembly. All the spur gears and rack are glass-filled plastics which make it critical from strength consideration, particularly in the event of high-speed impact. The mechanism is simulated using a rigid dynamic solver which gives important parameters such as velocity, torque reduction ratio, and impact forces acting on the gear tooth. This data is then used in FEA solver to obtain peak stresses and deformation on all the assembly components and is compared with the allowable strength of each material. The results from rigid dynamic solver aided with FEA are used for design qualification of mechanism, material selection, and in optimizing the performance of EOM. Further to augment the reliability of simulation model, high-speed imaging of mechanism is also performed.

Keywords FEA · MotionSolve · ANSYS · Impact · Gear

11.1 Introduction

A switching device is an automatically operated electrical device designed to protect an electrical circuit from damage caused by fault current. The basic function of a switching device is to detect a fault condition and create a discontinuity in the electrical circuit. Switching devices are made in varying sizes based on the intended appli-

A. K. Singh (✉) · P. Kumar · M. Ranade
Switchgear Design & Development Centre, Electrical & Automation, Larsen & Toubro Ltd.,
Mumbai, India
e-mail: abhimanyukumar.singh@Lntebg.com

© Springer Nature Singapore Pte Ltd. 2020
C. Li et al. (eds.), *Advances in Engineering Design and Simulation*,
Lecture Notes on Multidisciplinary Industrial Engineering,
https://doi.org/10.1007/978-981-13-8468-4_11

cation, from a small device that protects household appliances up to large switchgear designed to protect high voltage network feeding entire region.

The electrical operating mechanism (EOM) is used to remotely open and close the switching device. It consists of spring which is charged with the help of a motor and is equipped with an opening and closing release. Motors generally work at fairly low torque range whereas the forces required to operate a switching device is quite high. Thus, a torque reduction mechanism is designed using compound gear train assembly so that a very small torque is required to charge the EOM spring, and a motor will be able to function at this reduced torque. When the spring is fully charged, the integrated switching device is in ON positions. During remote operation, a signal is fed to operate opening release which enables spring discharge operation and brings the integrated switching device in OFF position.

In order to keep up with the compactness and cost-sensitive market, a compound gear train is designed which consists of a worm–worm wheel, planetary gear, and rack and pinion arrangement. Most of the gear used here are glass-filled plastics which is a cost-effective solution, as well as it reduces the overall weight of the assembly. These plastic gears, as well as other gears, should be designed such that it withstands the high impact forces transmitted through the mechanism assembly during ON and OFF operation.

In this work, we have developed a motor characterization curve which is used as an input during spring charging operation. It was learnt that the impact forces are much higher during spring discharge operation, i.e., switching device OFF operation. A rigid dynamic analysis is performed on MotionSolve which gave important insights such as velocity of gears, torque reduction ratio, and impact forces transmitted during spring charging and discharging operation. Mode superposition technique method has been used to find out the effect of rotation speed on the dynamic stresses and natural frequencies of the gear tooth was obtained to find out the effect of vibration modes on the transient response [1]. The transient dynamic analysis was performed to study the effect of various operations on the contact stress distribution with a change in meshing status and gear modification parameters were also established to reduce transmission noise and gear impact [2]. Some research work has also discussed validation between static and dynamic analysis with experimental data. They obtained the load sharing between planetary gear and pins and also modeled the effect of the dynamic behavior of the gear train [3]. Similar work on dynamic analysis using computer algorithm is discussed in another work [4]. Static and dynamic analysis of gear components and assemblies is a very old topic for academics, and there are several resources which address such simulations.

The prior art of simulation methodologies employed either constraint equations or gear relations to simulate complex gear assembly. The major shortcoming of this approach is that we get force transfer information at the gear axis and not on the gear tooth profile. Another limitation of this approach was the idealization of friction coefficient at a gear axis only which fails to account for the loss of motion/force occurring at the gear tooth during gear engagement and disengagement. In this work, we have simulated gear assembly using the surface-to-surface contacts and the same was validated with the constraint equation model. Friction coefficient, which is a

function of material property and surface conditioning, is explicitly defined at the gear axis and between the surfaces of the gear assembly. Using this approach, we are able to get the forces transmitted across the gear tooth profile while accounting for the impact forces. These parameters are then used to obtain stress and deformation across assembly components using FEA solver and are compared with the allowable strength of a material under consideration. In order to make the simulation model more robust and reliable, high-speed imaging of mechanism is also performed for validation and verification.

11.2 Model Architecture

EOM is operated against the stored energy of spring. Very high force value is required to operate the integrated switching device, resulting in high stiffness of spring for a relatively small stroke length. The electric motor is used to charge this spring using the gear mechanism. Since the operating torque of compact electric motors is low, a very high reduction mechanism is required to achieve this, hence, the design of a compact gear train.

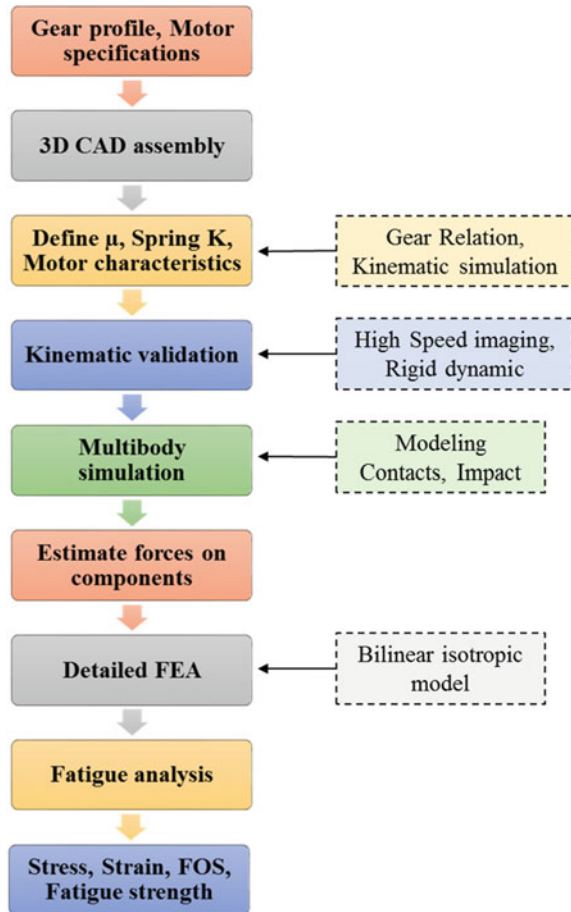
Figure 11.1 shows the solution architecture adopted for this work. We require accurate modeling of the involute profile which is used to model gears, unlike the traditional methods, as the simulation is based on the surface-to-surface contacts. Based on force vs stroke characteristics of the device to be operated using EOM, a motor characteristic curve is developed which will be used as an input to the multibody dynamic solver. Kinematic and dynamic validation is done at this stage to establish friction coefficients, mechanism operating time, torque reduction ratio, and the ratio of force transmission.

Since rigid dynamic solver cannot predict impact forces due to its inherent assumption of treating components as perfectly rigid, a multibody simulation is performed. MotionSolve was able to handle such complex nonlinear surface-to-surface contacts with great ease as the explicit solver is employed for numerical integration. Impact constraints in contact modeling are used to predict impact event and force associated with it. Impact constraints require the definition of local stiffness and local deformation. Based on the mechanical properties of impacting bodies, these parameters can be changed/tuned to get the realistic impact force values. This force is then used in the static analysis to get peak response such as stress, strain, and deformation.

11.2.1 Multibody Simulation

A rigid dynamic analysis is a study of the motion of interconnected bodies in a mechanism with the assumption that all bodies are rigid; i.e., they do not deform under applied forces. A rigid dynamic system is described by the law of kinematics and Newton's second law of motion and basically solves for kinetics and kinematics.

Fig. 11.1 Solution methodology



The solution of rigid dynamic analysis gives us the position, velocity, and acceleration of bodies in a mechanism as a function of time. Whereas in a multibody simulation tool few components can be defined as flexible leaving rest of the components as rigid. This helps in obtaining stress and deformation in the components of interest and saves considerable computation time.

In the traditional simulation, we used the law of gearing equation or constraint equations to transfer motion between gears to account for the inertial forces of all gear mass. One of the limitations of this approach is that we get force transfer information at the gear axis and not on the gear tooth profile. Another limitation of this approach is the idealization of friction coefficient at a gear axis only which fails to account for the loss of motion/force occurring at gear tooth profile during gear engagement and disengagement.

Whereas in this multibody simulation tool, we have used the surface-to-surface contacts across gear assembly to transmit forces, which is much closer to real-world

idealization. Kinetics and kinematics of this were validated with the constraint equation model. Friction coefficient, which is a function of material property and surface conditioning, is explicitly defined at the gear axis and between the surfaces of the gear assembly. With this approach, complemented by impact constraint model, we were able to get the impact forces on gear tooth as a function of time.

11.2.2 Finite Element Analysis (FEA)

Most of the gear used here are glass-filled plastics, and few are metallic. Static structural FEA is performed to study the structural withstand of these materials under impact forces. In this analysis, components are subjected to maximum impact force obtained from multibody simulation, the most severe case was observed in the case of EOM discharge operation. Gears are meshed using 3D tetrahedral elements while ensuring that minimum six layers of elements are modeled at the root of gear tooth for an accurate representation of stress gradient. The nonlinear effect, such as geometry, contacts, and material, are included in the simulation model.

Impact forces thus obtained from multibody dynamic simulation is applied at the pitch circle diameter of gear tooth under consideration, where the force transfer takes place. This is done by applying equivalent pressure on a very small area at the pitch circle diameter to avoid any singularity which will arise due to line load. The results from FEA such as stress and deformation are obtained across assembly components and are then compared with the allowable strength of the material.

In order to make the simulation model more robust and reliable, high-speed imaging of mechanism is also performed for validation and verification.

11.2.3 Assumptions

To reduce the complexity of the simulation, a few assumptions and simplifications are adopted as follows,

- (1) Bilinear isotropic material model is considered for FEA.
- (2) Strain rate effect is not considered here.

11.3 Numerical Model

11.3.1 General Equation of Motion

Full governing equation of motion is:

$$[M]\{\ddot{x}\} + [C]\{\dot{x}\} + [K(x)]\{x\} = \{F(t)\} \quad (11.1)$$

where $[M]$ = structural mass matrix, $[C]$ = structural damping matrix, $[K(x)]$ = structural stiffness matrix, $\{\ddot{x}\}$ = acceleration vector, $\{\dot{x}\}$ = velocity vector, $\{x\}$ = displacement vector, and $\{F(t)\}$ = force vector. This is also the force balance equation where in the first term, second term, and third term on the LHS represents inertial force, damping force, and stiffness force, respectively, and on the RHS is the applied force which is a function of time. For multibody dynamic analysis $[C]$, and $[K]$ is considered only at contacts surfaces to reduce the complexity of the model.

11.3.2 Geometry

CAD Geometry of EOM assembly consists of the spur gear, worm–worm wheel gear, planetary, and rack and pinion arrangement. The involute profile is used to model gear tooth, as shown in Figs. 11.2 and 11.3. The electric motor is mounted on motor gear and loading is idealized as a velocity input curve. Impact forces are investigated primarily at rack pin and across planetary gear assembly.

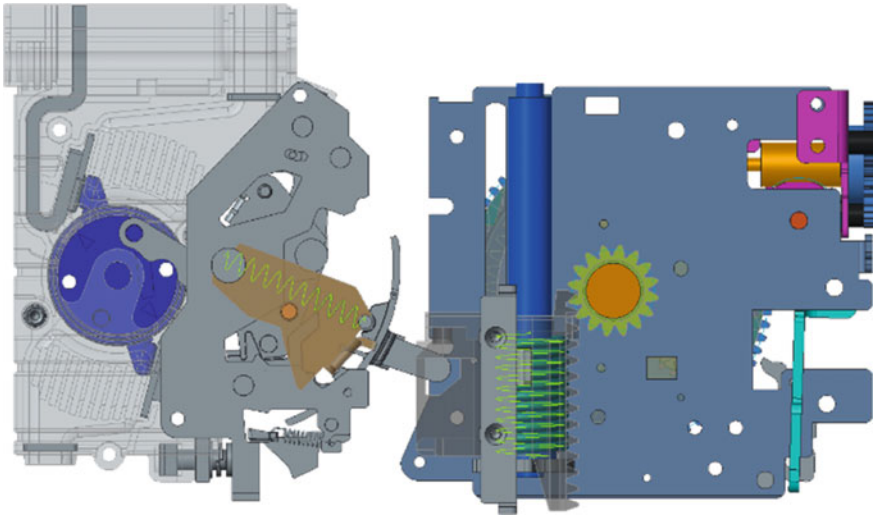


Fig. 11.2 EOM-switching device integrated (ON position)

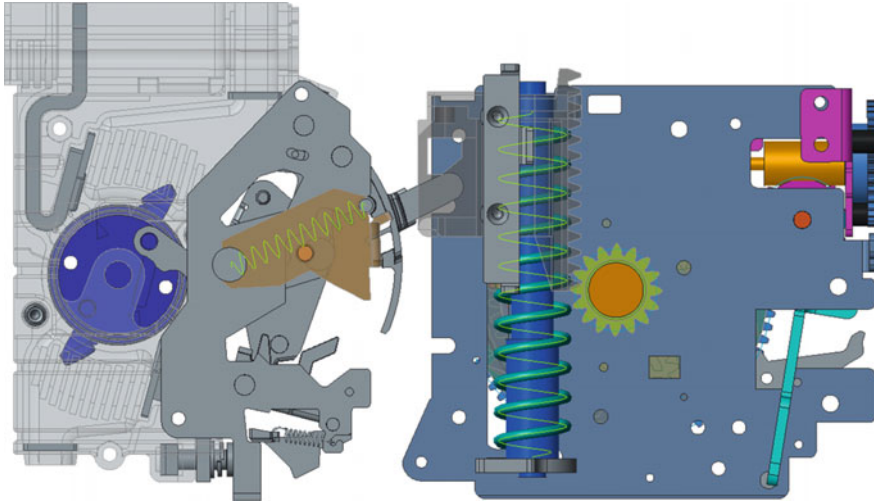


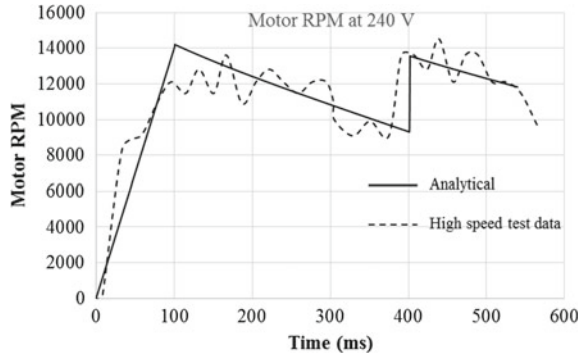
Fig. 11.3 EOM-switching device integrated (OFF position)

11.4 Analysis Set-Up

11.4.1 Dynamic Set-Up

Rigid dynamic analysis of stand-alone EOM and switching device is performed first to establish their kinematics and kinetics before moving on to the simulation of the integrated assembly. Figures 11.2 and 11.3 show the integrated EOM assembly with a switching device. EOM is assembled with a switching device using frictional contact definition between rack assembly of EOM and operating knob of switching device across which force transfer will take place to operate the mechanism. Switching device has a four-bar mechanism to operate which also consists of spring definitions along with linkages. Forces delivered by motor and EOM springs should be high enough to carry out the ON and OFF operation of the switching device (Fig. 11.4).

Fig. 11.4 Motor curve characteristics for simulation input



11.5 Results and Discussion

This section discusses the results obtained from dynamic and FEA static structural simulations.

11.5.1 Multibody Simulation Results

Dynamic analysis of EOM and switching device is performed independently to establish their characteristics. This helped in carrying out the dynamic analysis of EOM integrated with the switching device. Impact forces were estimated at the rack pin which moves in the slotted side plate and represents the most severe impact location. Stress waves travel from this point to the compact gear train including plastics.

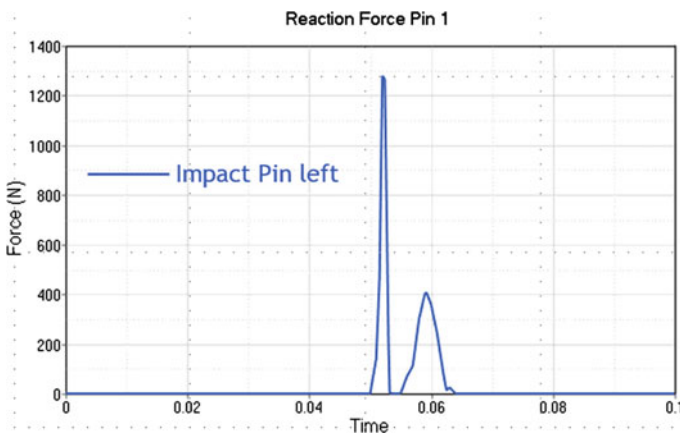


Fig. 11.5 Impact force on rack pin

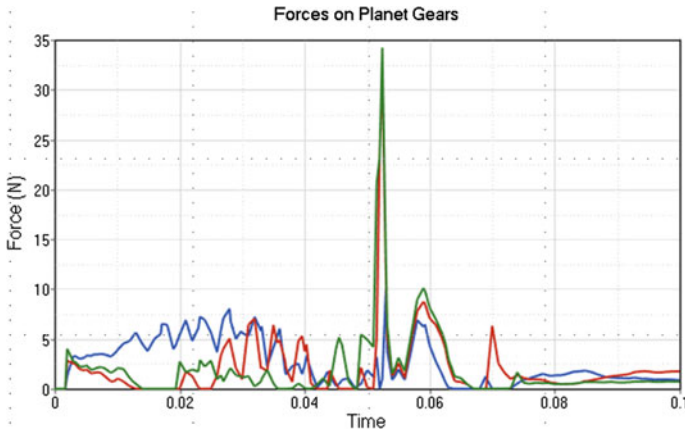


Fig. 11.6 Impact force on planet gears

Table 11.1 Impact factor calculation

Component	Static force	MotionSolve force	Impact factor
Worm wheel	24	100	4.2
Sun gear	25	82	3.4
Internal gear	29	103	3.5
Pinion	255	1280	5
Rack	255	1280	5

Figures 11.5 and 11.6 show the impact force obtained from the simulation. It can be clearly seen that the impact forces are much higher than the static force here, refer to Table 11.1, and thus needs to be accounted for during detailed FEA.

11.5.2 Validation

Kinematics such as velocity, time of operation, and dynamic response such bounce back of the mechanism is validated against the data obtained from high-speed imaging of the mechanism. During spring discharge operation for EOM assembly, the bounce back at rack pin is observed as 4 mm from high-speed imaging, whereas the same comes out to be 3.8 mm from the simulation showing good agreement. The overall time of spring discharge operation is 33 ms from high-speed data, whereas it comes out to be 52.5 ms from simulation, this difference could be attributed to the definition of high of friction coefficients and needs to be fine-tuned further in future simulations.

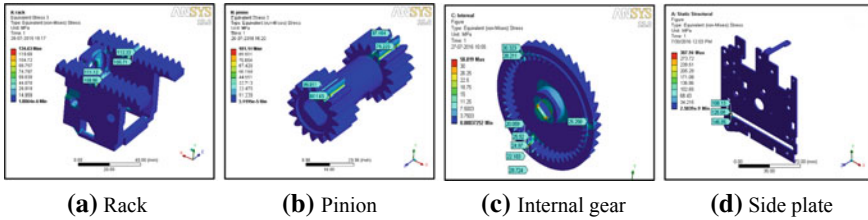


Fig. 11.7 Stresses on EOM mechanism components. **a** rack, **b** pinion, **c** internal gear, **d** side plate

11.5.3 Results from FEA

Maximum impact force obtained from dynamic simulation is used as an input load for static structural analysis. For glass fiber-reinforced plastics, it is assumed that the residual strain appearing above a stress threshold is due to plastic deformation [5]. Since this is a case of non-cyclic loading, a kinematic or isotropic hardening model will produce the same result. Thus, a bilinear isotropic hardening model is used to account for material nonlinearity, and a large deformation is turned on to account for the geometric nonlinearity. Stresses on critical components of EOM assembly are discussed here. As it can be seen from Fig. 11.7, the maximum stress of about 110 MPa is observed on the rack among all gears because of its close proximity to impact location. As we move away from the impact location stresses on gears keeps on decreasing, from 30 MPa on internal gear to 20 MPa on sun gear which is farthest from impact location among all glass filled plastic gears used in the mechanism. Stresses on all plastic and metal gears are well below the allowable limit. These stresses can be further reduced with the help of dampers, and its modeling in the simulation will be taken up in future analysis.

11.6 Conclusion

An improved multibody simulation methodology is established to model high-speed mechanism. Enhancement to include friction between contact surfaces and impact constraint model resulted in the more accurate idealization of real-world situation. Nonlinear FE analysis was carried out for design validation and to estimate the structural withstand of assembly components.

The multibody simulation helped in the visualization of the mechanism working in great details and in the understanding of kinematics and force transfer across the mechanism. This helped in improving the robustness and efficiency of mechanism design. Stress analysis for design validation further augmented the reliability and robustness. Simulation of dampers to reduce impact force transfers will be further investigated in future analysis.

References

Journal Article

1. Hasan, A.R.: Transient stress analysis on medium modules spur gear by using mode super position technique. *Int. J. Mech. Mechatron. Eng.* **3**(5) (2009)
2. Tang, Z.P., Sun, J.P., Yan, L.: Dynamic contact analysis and tooth modification design for EMU traction gear. *Int. J. Sim. Model* **16**(4), 742–753 (2017)
3. Nejkar, H.S., Burande, D.H.: Static and dynamic analysis of epicyclic gear train. *IOSR J. Mech. Civil Eng.* **13**(2), 61–71 (2016)
4. Pennestri, E., Valentine, P.P.: Dynamic analysis of epicyclic gear train by means of computer algebra. *Multibody Sys. Dyn.* **7**, 249–264 (2002)
5. Launay, A., Marco, Y., Maithournam, M.H., Raolt, I., Szmytka, F.: Cyclic behavior of short glass fiber reinforced polyamide for fatigue life prediction of automotive components. *Procedia Eng.* **2**(1), 901–910 (2010)
6. Vijaykumar, M., Shivaraju, M., Srikanth, M.: Vibration analysis of gearbox casing using finite element analysis. *Int. J. Eng. Sci.* **3**(2), 18–36 (2014)
7. Tang, Z., Tang, S., Sun, J., Yan, L.: Multi-condition contact stress analysis of high speed train helical gear. *Periodica Polytech. Transp. Eng.* **44**(4), 193–200 (2016)
8. Sameer Chakravarthy, N.C., Subbaratnam, B.: Finite element analysis and fatigue analysis of spur gear under random loading. *Int. J. Mech. Eng.* **3**(4) (2014)

Book

9. Budynas, R.G., Nisbett, J.K.: Shigley's Mechanical Engineering Design. Ninth editions (2011)

Software Tool

10. Help manual, ANSYS®, Inc. Version 13.0
11. Help manual, Altair® Hyperworks® Version 14.0

Chapter 12

Vibrational Study of Labyrinth Seals for Turbomachines



S. M. Sanjay kumar and C. Suresh

Abstract Turbomachinery is one of the most complex machinery that we have today. They have a variety of applications ranging from aircraft engines to huge industrial machines like power generators and marine propulsion. In this study, dynamic stability aspects are evaluated based on Campbell's criteria. Campbell introduced the concept of traveling waves in his investigations on turbine disk failures. The same concepts are extended to the dynamic stability of Labyrinth seals, which have cylindrical shell-type vibrations. Evaluation of Campbell's criteria involves three main areas—evaluation of frequency versus the nodal diameter (f/N), evaluation of intersection of each frequency line with the per revolution line and evaluation of interaction points for each frequency line with respect to other stationary or rotating component. All these criteria were studied, and it was felt necessary that the process of evaluating by plotting the above graphs needs to be automated to save post-processing time and also to standardize the procedure. The user has to extract the frequencies from a standard FEA package like ANSYS and input them in the marked cells in the Excel-based tool. Standard color-coding like yellow for input fields, blue color for operating speeds, and red color for design margin is used in the tool. Also, a set of clear instructions is provided in one of the worksheets.

Keywords Cylindrical shell · Campbell's criteria · Labyrinth seals · Frequency · Dynamic stability

S. M. Sanjay kumar (✉)
SJB Institute of Technology, Bengaluru 560060, India
e-mail: 1.sanjay20376@gmail.com

C. Suresh
New Horizon College of Engineering, Bengaluru, India

© Springer Nature Singapore Pte Ltd. 2020
C. Li et al. (eds.), *Advances in Engineering Design and Simulation*,
Lecture Notes on Multidisciplinary Industrial Engineering,
https://doi.org/10.1007/978-981-13-8468-4_12

12.1 Introduction

Turbomachinery is one of the most complex machinery that we have today. They have a variety of applications ranging from aircraft engines to huge industrial machines like power generators and marine propulsion. These turbomachines have a large number of rotating components, which are supported by bearings. One of the most important features in the design and manufacture of a jet engine is the elimination of the possibility of vibration occurring at the various natural frequencies of its disk wheels, buckets and various seals.

A Labyrinth seal is a flow restrictor, and in gas turbines, it is used between a rotating and a stationary part or between two independently rotating parts to minimize the leakage flow of air or hot gas. Their design requirements vary extensively depending upon where they are used in the engine. The objective of the designer is to provide a geometry, which presents maximum resistance to flow and maintains the minimum clearance throughout the life of the gas turbine.

The Labyrinth seal can be conceptually shown in Fig. 12.1. It consists of a stationary and a rotating component or in some cases both the components are rotating. The operating clearances are typically around approximately 0.25 mm. Some of the important design parameters are mechanical, thermal and acoustic stability.

A number of papers were studied to understand what has been done so far in the area of axisymmetric vibrations of disks and cylindrical shells. A brief summary of a few important ones is discussed.

Campbell [1] has investigated the reasons for turbine disk wheel failures. He introduces the concept of traveling waves and stationary waves. The definition of Campbell criteria for the design of turbine wheels for axial vibration, which in general can be applied for vibrations in axisymmetric structures evolved from this pioneering work. The concept of standing waves, which is one of the major reasons for turbine disk failures, is discussed in this paper.

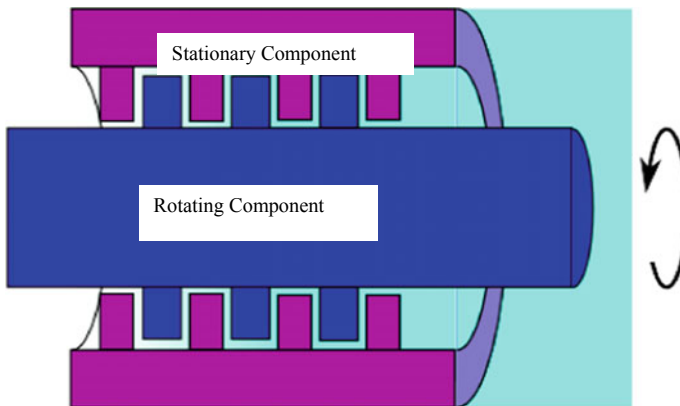


Fig. 12.1 The concept of a Labyrinth seal

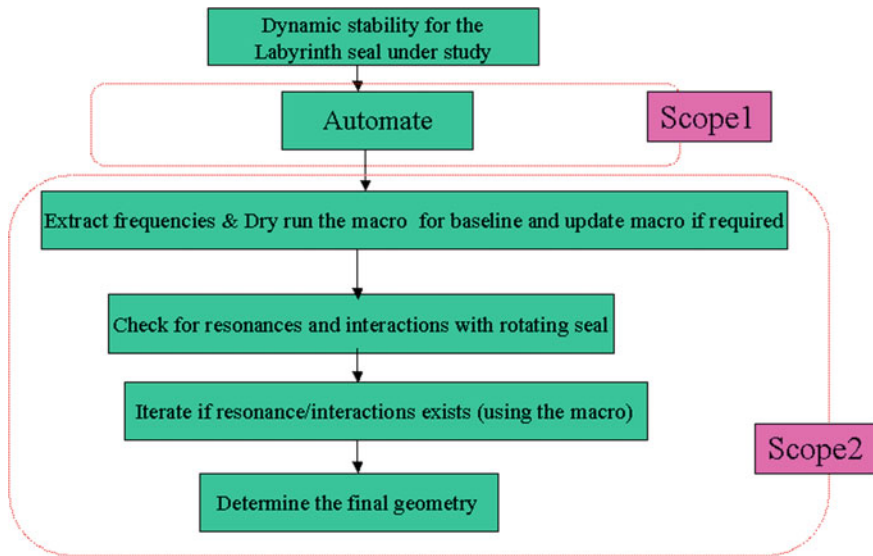


Fig. 12.2 Scope of the project

Heckman and Campbell [2] built the concepts described earlier for tangential vibrations. The condition for exciting a vibration in a rotating member is explained here. It is interesting to note in this work that at critical speeds, the tangential vibrations repeat the same path for each revolution. Any part of it describes a circumferential wave, which is stationary in space, although this is a longitudinal wave while the axial vibration consists of transverse waves. Macke [3] investigated on short compressor casing segments. He explained the motion of a rotating cylindrical shell and the differences in vibrations of disks and cylindrical shells.

Mehdigholi [4] investigated the harmonic excitation of a rotating disk. In both of these vibration interactions, the critical speeds and conditions should be identified and examined in order to take them into consideration in practice. Singh et al. [5] evaluated interferences, and the safe diagram compares not only the frequencies of exciting harmonics with the natural frequencies of blades but also the shape of these harmonics with the normal mode shapes of a completely bladed disk including packet blading.

After studying the design requirements of Labyrinth seals and the importance of dynamic stability using Campbell's criteria, the scope of the project is defined as shown in Fig. 12.2. The scope of the project can be divided into two broad categories:

- Scope 1 To automate the process of evaluating Campbell's criteria with a suitable user-friendly tool.
- Scope 2 The tool developed in scope 1 needs to be tested with several dry runs, and the program needs to be corrected if required. Then the tool needs to be validated with a suitable case study.

12.2 Tool Development

Labyrinth seal design parameters consist of thermal stability, dynamic stability, acoustic coupling, leakage, stress and wear characteristics. Dynamic stability involves evaluation of Campbell's criteria. As shown in Fig. 12.3, evaluation of Campbell's criteria involves three main areas—evaluation of frequency versus nodal diameter (f/N), evaluation of intersection of each frequency line with the per revolution line and evaluation of interaction points for each frequency line with respect to other stationary or rotating component. The manual process of evaluating Campbell's criteria currently used was a cumbersome and time consuming. It involved calculations that could very well be handled by the programed computer-based tool. Figure 12.3 shows the broad level scope of automation in the evaluation of Campbell's criteria.

12.2.1 Objectives of the Tool

The objectives of the tool to evaluate Campbell's criteria for Labyrinth seals are:

1. Plot frequency versus nodal diameter (f/N) curve and check for the trend with respect to the engine baseline speed and 120% margin line.
2. Plot a combined Campbell plot to check for the trend of the resonances within the operating range with respect to the stationary observer.

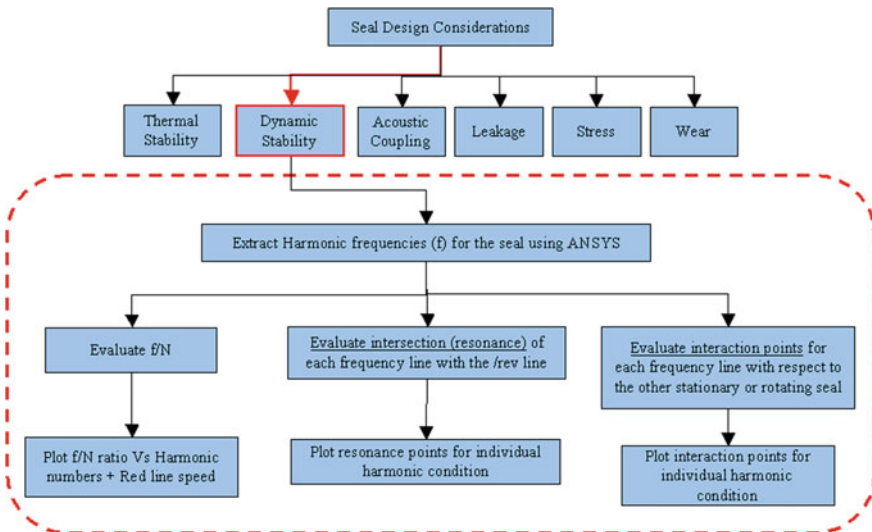


Fig. 12.3 Automation scope for evaluation of Campbell's criteria

3. Evaluate the rpm at which the resonance occurs for individual harmonics and report if within the operating range (Include provision for analyzing stators and rotors with respect to the stationary observer). Report major/minor resonances if any.
4. Plot interactions for stator–rotor conditions and evaluate rpm at which interaction occurs. Report interactions if any within the operating range.
5. The tool must have provision for both disk-type and cylindrical shell-type components.
6. Allow provision for further inclusion of rotor–rotor interaction evaluations.
7. The tool must be user friendly.

12.2.2 Selection of a Host Application

Any application that supports the use of a programming language for applications is called a host application. Microsoft Excel is selected as the host application. Apart from the obvious advantage of being easily available on any PC with windows platform, the other advantages that Excel offers are:

1. Macro generation process is quick.
2. Calculations can be handled using multiple worksheets with one of the worksheets dedicated for user interface and inputs.
3. All the required plots can be generated at the click of a button and also can be stored in a separate directory.
4. Calculations like finding the intersection of per revolution line and the frequency line based on the slope at intersecting points can be easily handled.

12.3 Modal Analysis of Forward Stationary Seal

A section of the forward stationary seal is as shown in Fig. 12.5. The component is axisymmetric except for the 60 oval-shaped holes as shown in Fig. 12.4. A 2D axisymmetric section is shown in Fig. 12.5. The use of an axisymmetric model greatly reduces the modeling and analysis time compared to that of an equivalent three-dimensional model. The region, which has holes, is modeled with orthotropic properties. The analysis is carried out in ANSYS. The objectives of the analysis are to obtain forward stationary seal frequencies and check for the resonance with existing rotating seal frequencies at the rub strip location.

Modify the geometry (forward stationary seal only) if required to eliminate resonance/interaction.

The following assumptions are followed for the analysis as mentioned below:

1. A 2D axisymmetric geometry of the forward stationary seal is used.
2. Appropriate constraining as shown in Fig. 12.5 simulates the bolting of forward stationary seal to Bearing Housing.

Fig. 12.4 Section of UG model

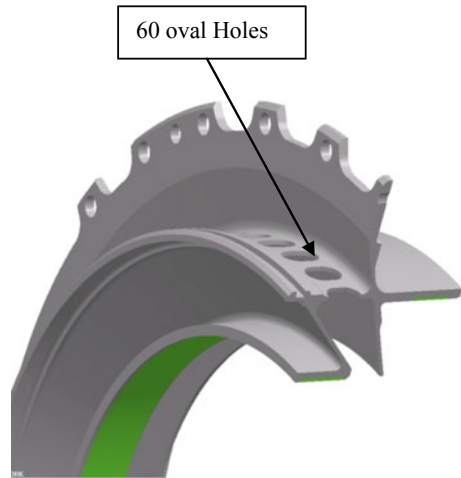
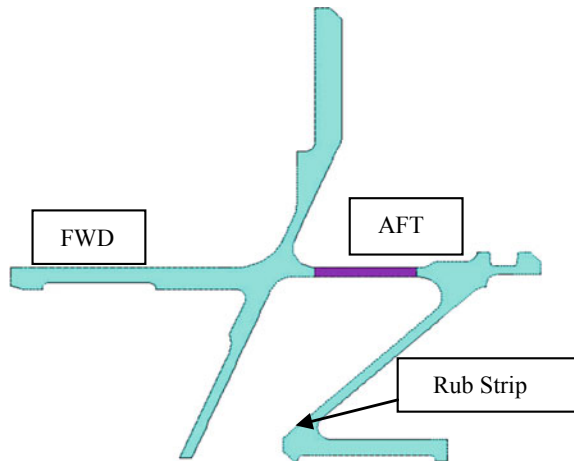


Fig. 12.5 2D cross section



3. Reference temperature of 500 F is used in the analysis.
4. Orthotropic material properties are used for the vent holes in the 2D axisymmetric model.
5. High pressure turbine (HPT) shaft speed is 12,800 rpm and 120% HPT speed 15,360 rpm. (120% maximum exciting frequency is 256 Hz).
6. 2D axisymmetric plane 25 element is used.

The material properties are as listed in Table 12.1.

Table 12.1 Material properties

		Temperature = 260 °C	
Property	Units	Isotropic (material 1)	Vent hole—material 2 (21% material available)
EX	MPa	1.9389E+05	4.07E+04
EY	MPa	1.9389E+05	4.07E+04
EZ	MPa	1.9389E+05	6.89E+00
NUXY		0.3175	0.3175
NUYZ		0.3175	1.00E-03
NUXZ		0.3175	0.3175
DENS	kg/m ³	8248.612	1743.834

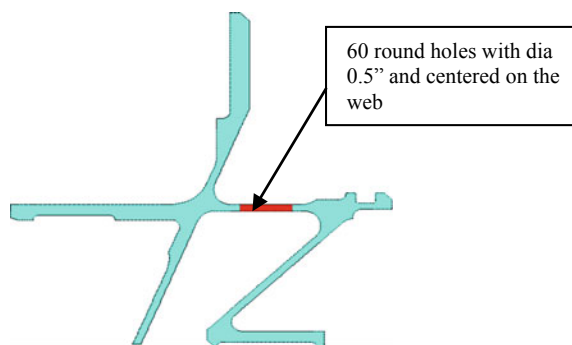
12.3.1 CASE 1: Oval-Shaped Holes Changed to Round Holes

In case 1, the oval-shaped holes are changed to an equal number of round holes in order to shift the frequencies out of the operating envelope which failed to qualify the Campbell criteria and cannot be used in the final design of Labyrinth seal (Fig. 12.6).

Figures 12.7 and 12.8 show the frequency versus nodal diameter (f/N) ratio Campbell diagram for forward stationary seal and forward rotating seal, respectively, which indicates that there is no resonance occurring since the f/N ratio curve lies beyond the operating speed and the red line speed.

Figures 12.9 and 12.10 show the combined Campbell diagram for forward stationary seal and forward rotating seal, respectively, which indicates that there is no resonance occurring since the line joining the intersection of per revolution line and the harmonic frequency lines indicated by the red line lies beyond the operating speed and the red line speed.

Fig. 12.6 Modifications to baseline model (Case 1)



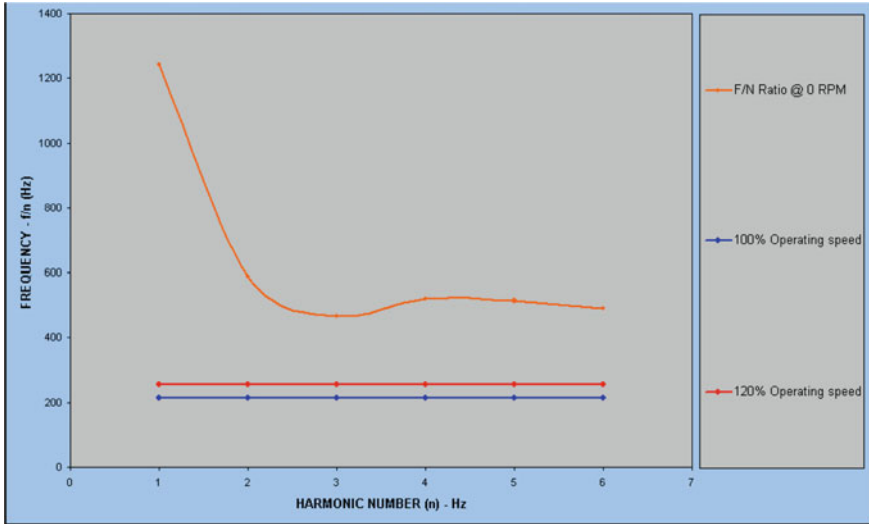


Fig. 12.7 Campbell diagram for forward stationary seal

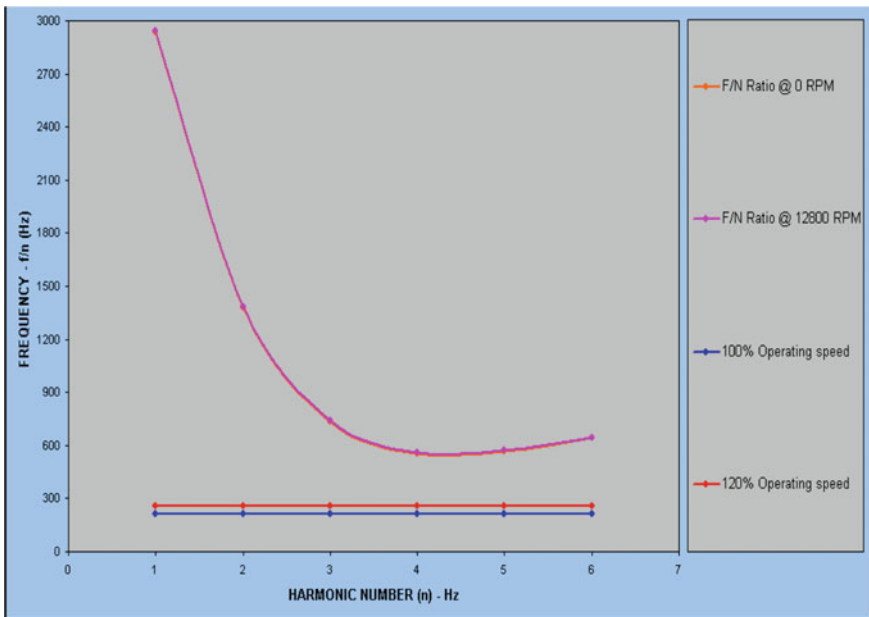


Fig. 12.8 Campbell diagram for forward rotating seal

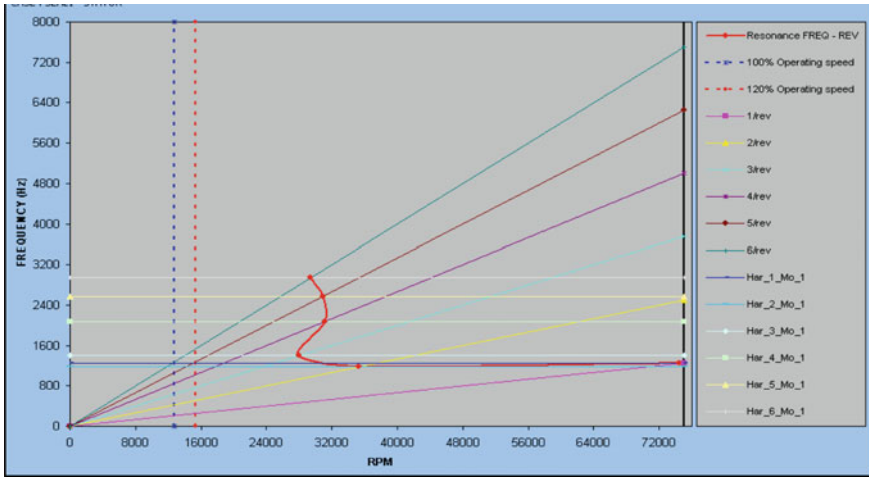


Fig. 12.9 Combined Campbell diagram for forward stationary seal

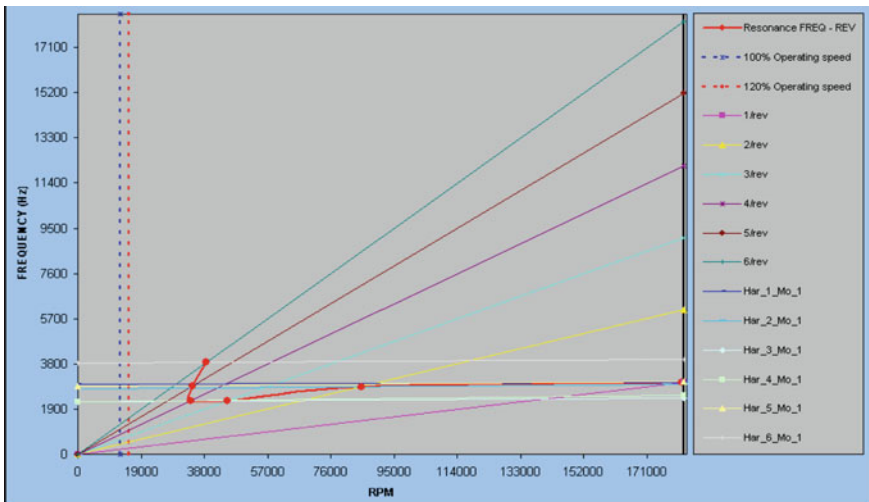


Fig. 12.10 Combined Campbell diagram for forward rotating seal

12.3.2 CASE 2: Addition of Stiffening Shell

These frequencies were input to the tool developed, and Campbell criteria were evaluated as shown in the figures below.

Figures 12.11 and 12.12 show the frequency versus nodal diameter (f/N) ratio Campbell diagram for forward stationary seal and forward rotating seal, respectively,

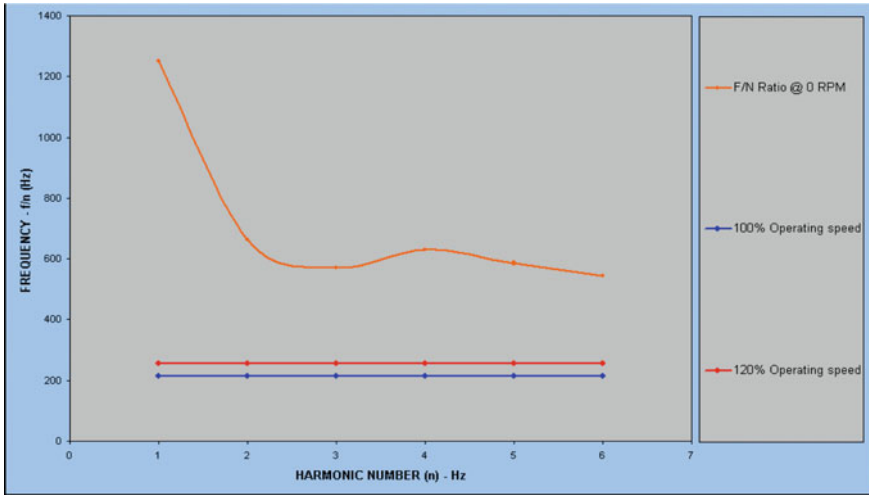


Fig. 12.11 Campbell diagram for forward stationary seal (Case 2)

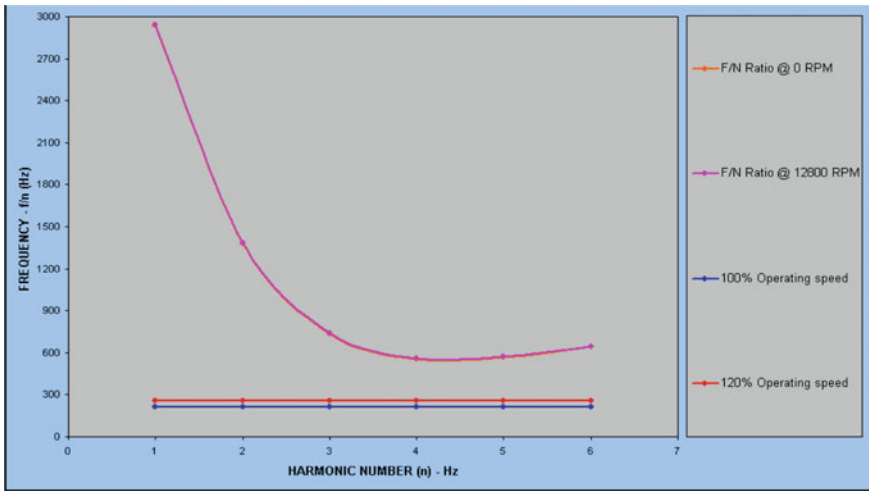


Fig. 12.12 Campbell diagram for forward rotating seal (Case 2)

which indicates that there is no resonance occurring since the f/N ratio curve lies beyond the operating speed and the red line speed.

Figures 12.13 and 12.14 show the combined Campbell diagram for forward stationary seal and forward rotating seal, respectively, which indicates that there is no resonance occurring since the line joining the intersection of per revolution line and the harmonic frequency lines indicated by the red line lies beyond the operating speed and the red line speed.

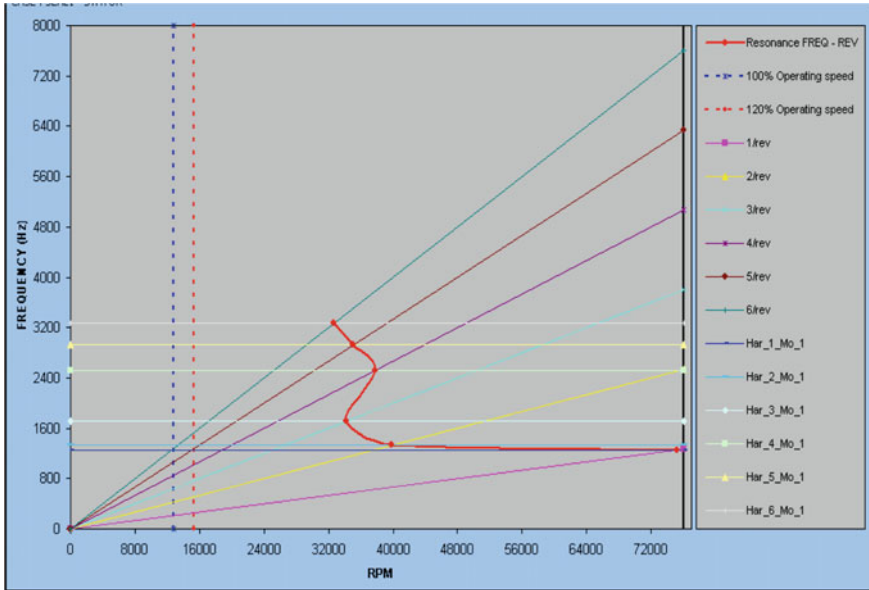


Fig. 12.13 Combined Campbell diagram for Forward stationary seal (Case 2)

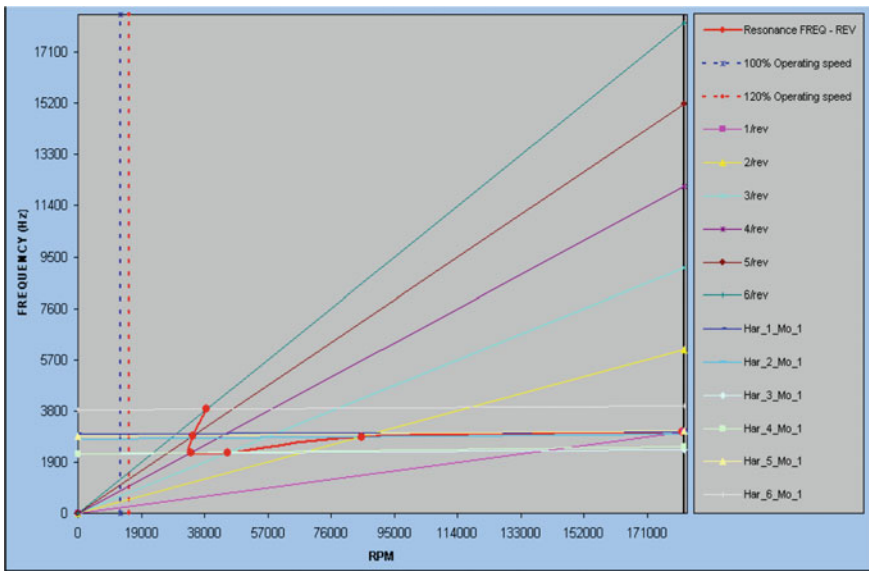


Fig. 12.14 Combined Campbell diagram for forward rotating seal (Case 2)

12.4 Results and Discussion

The various mode shapes obtained from the analysis of the baseline model are as shown in Fig. 12.5. Mode 1 of each harmonic, which is associated with the rub strip, is highlighted in blue color and is important here. The modes that involve the rub strip vibrations which can cause the interactions with the rotating component and hence the frequencies associated with these modes are important.

- By observation of frequency versus nodal diameter (f/N) and combined Campbell plots were obtained; it can be inferred that no resonance was observed with respect to engine rotor speed. The interaction between stator and rotor occurs in harmonic 4 at 3233 rpm, which is within the operating envelope of the engine. Hence, this interaction needs to be eliminated. Stiffening of the rub strip leg to increase the frequency may eliminate interaction. By an observation of frequency versus nodal diameter (f/N) plots shown in Figs. 12.11 and 12.12, and combined Campbell plots shown in Figs. 12.13 and 12.14, it can be inferred that no resonance is observed with respect to engine rotor speed. The interaction between stator and rotor occurs in harmonic 3 at 12,095 rpm and at harmonic 4 at 5052 rpm, which is within the operating envelope of the engine. Hence, these interactions need to be eliminated. Further improvement is needed to shift the frequencies outside the operating envelope.

12.5 Conclusions

This work gives a lot of exposure in the area of dynamic stability of Labyrinth seals using Campbell's criteria. To begin with, the scope of the work was divided into two broad categories and both of them have been successfully completed.

A user-friendly Excel-based tool has been developed. All the requirements of the tool such as plotting of frequency versus nodal diameter curve, the combined Campbell diagram and checking of individual harmonics with the revolution line and also the interaction Campbell diagram are successfully met. This tool was tested with several dry runs for accuracy and user-friendly input and output. The format of the output has been tuned to match the presentation style of the users.

A case study on the design of a stationary Labyrinth seal was also done to show the validity of the tool. The modal analysis was carried out in ANSYS and the tool developed was used to plot the Campbell diagram. By the observation of frequency versus nodal diameter (f/N) plots shown in the respective figures and combined Campbell plots shown in respective figures, it can be inferred that no resonance is observed with respect to engine rotor speed.

The interaction between stator and rotor is also checked and plotted which showed interactions occurring at different frequencies for different cases. The geometry of the stationary part was modified to shift the interacting frequencies within the operating envelope. Thus, this tool significantly reduces the post-processing time and is found to be very user friendly.

References

1. Campbell, W.: The protection of steam—turbine disk wheels from axial vibration. ASME Trans. **46** (1924)
2. Heckman, W.C., Campbell, W.: Tangential vibration of steam turbine buckets. ASME Trans. (1924)
3. Macke, H.J.: Traveling wave vibration of gas turbine engine shells. ASME Trans. (1928)
4. Mehdiholi, H.: Forced Vibration of Rotating Disks and Interaction with Non-Rotating Structures. Imperial College of Science, Technology and Medicine, Dynamics Section, Department of Mechanical Engineering, University of London Imperial College of Science, Technology and Medicine London (April 1991)
5. Singh, M.P., Vargo, J.J., Schiffer, D.M., Dello, J.D.: SAFE diagrams—a design and reliability tool for turbine blading
6. Sarkar, S., Atluri, S.N.: Effects of multiple blade interaction on the containment of blade fragments during a rotor failure. Finite. Elem. Anal. Des. **23** (1996)
7. Prohl, M.A.: A method of calculating vibration frequency and stress of a banded group of turbine buckets. Trans. ASME 56-A-116 (1956)
8. Singh, M., Schiffer, D.: Vibrational Characteristics of Packeted Bladed Discs. ASME Paper No. 82-DET-137 (1982)
9. Singh, M.: SAFE Diagram. Technology Report ST 16. Dresser-Rand Company, Houston (1984)
10. TBDYNE—A Finite Element Based Bladed Disc Program Developed. Dresser-Rand Company, Houston (1987)

Chapter 13

Refrigerant Gas Leakage in ISO Room: A Comparative CFD Study



Sangamesh Hosur, Sachin Kumar Rai and Mahmood Tabaddor

Abstract Much testing research has been funded over the recent years to understand the risks associated with the leakage of combustible refrigerants into confined spaces. The push for more environmentally friendly refrigerants has increased the risk of fire due to the combustibility of this new class of refrigerants. However, the challenge is that a thorough risk assessment would require the understanding of many different scenarios, a very economically expensive endeavor when data is generated by only physical. So, in this paper, we will cover the capabilities of three common (CFD) computational fluid dynamics tools, two freeware and one commercial, to help simulate the gas leakage of refrigerants into confined spaces. The three CFD tools that were selected were Fire Dynamics Simulator (FDS), FLUENT (ANSYS) and OpenFOAM (ESI). We created models for the R32 refrigerant leakage in an ISO 9705 room scenario where testing data was available. Test parameters include inlet location within the room and flow rate of the leaking gas. It is assumed that the refrigerant enters the room in gaseous form and remains in that state throughout the test. For some of the CFD tools, there are many different physics and parameter options. We will present the key physics (turbulence and diffusion sub-models) necessary for the modeling of gaseous refrigerant leakage and compare model results with those from the test conducted in an ISO room.

Keywords Computational fluid dynamics · Turbulence · Refrigerant leakage · Diffusion · Fire safety

S. Hosur (✉) · S. K. Rai
UL India Pvt. Ltd., Kalyani Platina, 3rd Floor, EPIP Zone, Phase II, Whitefield, Bangalore
560066, India
e-mail: sangamesh.hosur@ul.com

S. K. Rai
e-mail: sachin.raai@ul.com

M. Tabaddor
UL LLC, 333 Pflingsten Road, Northbrook, IL 60062, USA
e-mail: mahmood.tabaddor@ul.com

© Springer Nature Singapore Pte Ltd. 2020
C. Li et al. (eds.), *Advances in Engineering Design and Simulation*,
Lecture Notes on Multidisciplinary Industrial Engineering,
https://doi.org/10.1007/978-981-13-8468-4_13

13.1 Introduction

The phase out and restriction of the most common and widely used refrigerants in early 1980s instigated Heat, ventilation, and air conditioning (HVAC) industry to look for alternative refrigerants with lower global warming potential (GWP) and zero ozone depletion potential (ODP). Research on various options found some alternatives; however, these candidate refrigerants present potential fire safety trade-offs in exchange for lower GWP. For example, hydrocarbons are hazardous in many applications due to flammability nature. Whereas, carbon dioxide necessitates a complete and costly system redesign as its properties are so different from fluorocarbons, and its thermodynamic cycle efficiency is lower than that of typical HFCs [1].

ASHRAE standard 34 [1] classifies refrigerants into various classes. Class A2L refrigerants have been identified as a potential replacement for refrigerants currently used in HVAC and refrigeration systems. Safety evaluation of these Class A2L refrigerants requires an understanding of refrigerant flammability in representative scale settings so that equipment can be appropriately designed and installed for safe operation.

A review of previous research on Class A2L refrigerants provided a reference for this investigation relative to measurements, refrigerant release methods and refrigerant build up in different scenarios [1]. The literature review identified a need for additional computational fluid dynamics (CFD) simulations with the intent to validate such models and also to develop insights into refrigerant buildup from leaks into a test room, the safety of the laboratory operations and placement of instrumentation and ignition sources. The CFD simulations performed with three different CFD tools: FLUENT, OpenFOAM and FDS. The results from the different software packages are compared and discussed in some detail.

13.2 Physics

Unlike a physical test, in setting up a model, one must insure that the proper physics of the phenomenon of interest is captured. Based on testing conducted at UL [2] on refrigerant leakage in a test room (Fig. 13.1), there are multiple physical phenomena taking place. First, the refrigerant enters the room as a gas (it could also enter as a liquid but for our study, we only assume gaseous state) with momentum. As it travels down the room due to buoyancy, there is a breakup in the flow due to turbulence. In parallel, concentration gradients lead to diffusion. This diffusion rate may be different from gas to air as compared with air to gas. Finally, there are phase changes that may be occurring that result in thermal energy release or absorption. A decision must be made on how much of the complexity to include without overburdening the model building and solution processes. So, we examine some of the key physics for this type of problem.

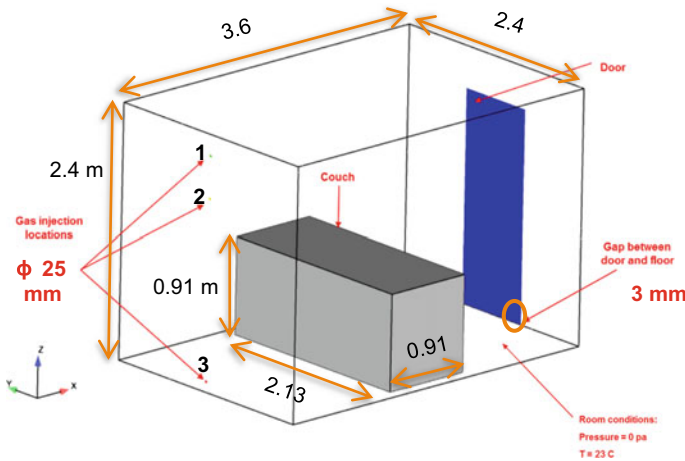


Fig. 13.1 Test room

13.2.1 Species Transport Model

An equation for species transport is shown in Eq. 13.1. This equation narrates the phenomenon of convection and diffusion for the species i under the unsteady condition without reaction [3, 4].

$$\frac{\partial(\rho Y_i)}{\partial t} + \nabla \cdot (\rho U Y_i) = -\nabla \cdot (J_i) + S_i \tag{13.1}$$

ρ , Y_i , U , t , J_i and S_i denotes the density of species i , mass fraction of species i , three-dimensional velocity components, time, diffusion flux of species i and source term of species I , respectively. The convection term $\text{div}(\rho U Y_i)$ is transported material due to the velocity of the fluid. Diffusion $\text{div}(J_i)$ is transported resulting from concentration gradients.

The mass diffusion due to the mixing action of the turbulent velocity fluctuations is given as

$$J_i = -\rho D_i \nabla(Y_i) - (\mu_t/S_{ct})\nabla(Y_i) \tag{13.2}$$

μ_t and S_{ct} denotes the turbulent viscosity and turbulent Schmidt number, respectively. The reaction term is neglected since only air and refrigerant mixing is considered.

Table 13.1 Solver parameter comparison

	OpenFOAM	FLUENT	FDS
Solver type	Compressibility-based transient	Pressure-based transient	Pressure-based transient
Models	Energy equation Viscous— $k-\epsilon$ realizable rhoReactingBuoyantFoam (solver)	Energy equation Viscous— $k-\epsilon$ realizable Species transport	Energy equation Viscous—LES Species transport
Materials	Air, R32	Air, R32	Air, R32
Solution method	PIMPLE limitedLinear	SIMPLE Second-order upwind	Explicit predictor—corrector scheme, second-order accurate in space and time
Solution control	Auto time step	Auto time step	Auto time step

13.2.2 Solver Comparison

A comparison of some key features of OpenFOAM, FLUENT and FDS is shown in Table 13.1.

The transient approach is used for all software, but the OpenFOAM solver methodology is different than FLUENT and FDS. rhoReactingBuoyantFOAM is a solver exists within OpenFOAM which is compressibility based. Compressibility is expressed as the inverse of the product of the temperature and the universal gas constant [5]. In this study, gases were assumed as perfect gases, and the temperature was kept constant. Consequently, the compressibility was essentially constant for rhoReactingBuoyantFOAM simulations. The pressure velocity coupling was managed in different ways by the CFD codes. PIMPLE algorithm is a combination of pressure implicit with splitting of operators (PISO) and semi implicit method for pressure-linked equations (SIMPLE) algorithm [6]. The PIMPLE algorithm switches to PISO mode if the non-orthogonal correction number higher than one [3]. In this simulation, the non-orthogonal correction number is two. Hence, the pressure velocity coupling is operated as the PISO algorithm in OpenFOAM. PISO algorithm operates with an extra correction step compare to the SIMPLE. Hence in this study, OpenFOAM simulations are with an extra correcting than FLUENT simulations [7, 8]. In predictor step of FDS, it estimates species mass density, mass fraction and background density with explicit Euler step. It computes velocity divergence using estimated thermodynamic quantities followed by solving Poisson's equation for pressure term. Toward the end of the predictor step, velocity for the next time step is evaluated. In the corrector step, all the evaluated variables are corrected in the same order as a predictor. In spite of variations in algorithms methodology, solutions should not be influenced.

13.3 Simulation Methodology

13.3.1 Geometry

The general geometry of the test room is shown in Fig. 13.1. The room has three inlets which are located at 0.2, 1.8 and 2.2 m height from the floor. The gap between the door and the floor was also included in the model. There was an obstacle in the room which represents the furniture present in a room.

13.3.2 Meshing

Mesh was created in ANSYS ICEMCFD for OpenFOAM and FLUENT; whereas, mesh for FDS was created within the software. Mesh dependency study carried out with two different meshes one being coarse and another fine which are shown in Fig. 13.2. The mesh refinement studies showed that the difference between the coarse and fine mesh was marginal. Hence, we chose coarser mesh for our studies to save computational time.

13.3.3 Validation

The CFD model developed in OpenFOAM was considered to weakly validate by comparison with the available experimental data obtained from UL testing data. Ideally, a physical test should not simply be designed to answer the specific question that is under investigation but should also gather data needed to help validate a model [9]. The case considered for validation was with 50 gps inlet flow rate from 1.8 m height inlet of 25 mm diameter. The experimental and OpenFOAM results are plotted

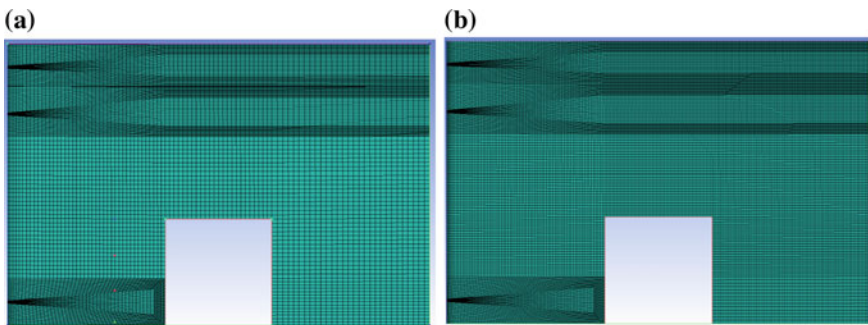


Fig. 13.2 a Coarse mesh with 0.6 million cells, b fine mesh with 1.2 million cells

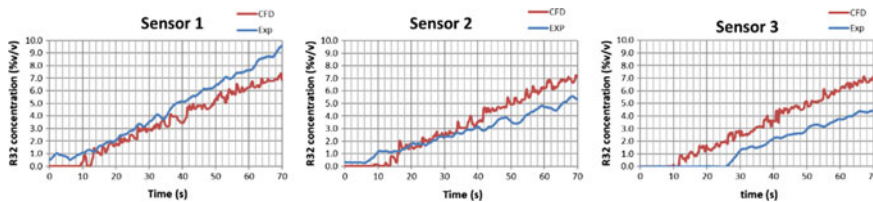


Fig. 13.3 Comparison of CFD results with experimental values

Table 13.2 Solver parameter comparison

S. No.	Inlet mass flow rate (g/s)	Outlet pressure in bars	Walls	Release height (m)/position	Release opening diameter (mm)
1	13.5	1 bar	No slip/adiabatic	2.2/1	25

as shown in Fig. 13.3. From the plot, it was observed that the OpenFOAM results were in good agreement with experiments. OpenFOAM model was considered for future studies to compare other software results.

13.3.4 Boundary and Initial Conditions

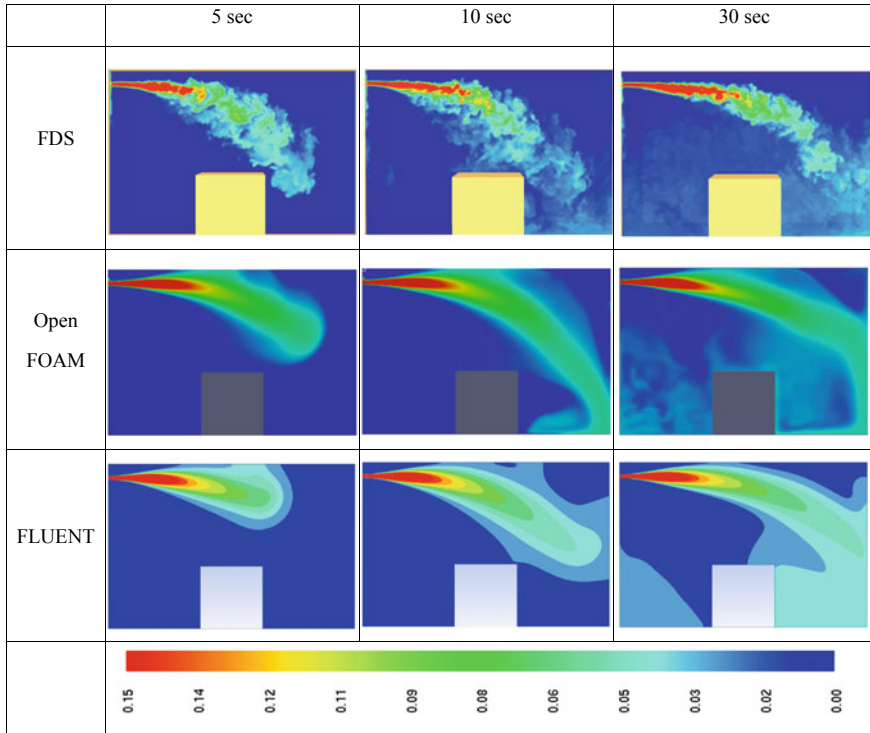
Boundaries are categorized as an inlet, outlet and walls. The conditions for these boundaries are listed in Table 13.2.

Mass flow inlet of 13.5 g/s was defined at the inlet, and outlet is a pressure outlet. The walls were assigned no-slip conditions and adiabatic in nature. The refrigerant was released from a hole of 25 mm diameter at a height of 2.2 m from the floor. The entire room was initialized with air at 1 atm pressure and 25 °C.

13.4 Results

Refrigerant concentration gradient within the room is the key quantity of interest with additional interest in which the concentration levels lie between the lower flammability and upper flammability limits of the refrigerant. If a volume, between the flammability limits, exists near a possible ignition source then that scenario could be an ignition hazard. The concentration contour plots comparison is shown in Table 13.3. These contours were taken at the mid-plane bisecting the inlet of the room. The FDS contour is broken in nature; whereas, OpenFOAM and FLUENT contours are smooth. This difference is basically due to the turbulence model used in

Table 13.3 Comparison of contour plots at mid-plane over time



FDS which has been mentioned earlier. By looking at these plots, it is observed that the models generally appear to be very similar. A more detailed, point comparison of concentration data at four key locations in the test room provides confidence in the model predictions. All four sensors are on the same floor location but at different heights with sensor 1 being nearest to the floor and sensor 4 being the furthest away. The location of the sensor is between the inlet wall and the obstruction offset from the inlet. The concentration plots are shown in Fig. 13.4. The plots show that the concentration predictions from all three CFD codes are very similar and physically realistic.

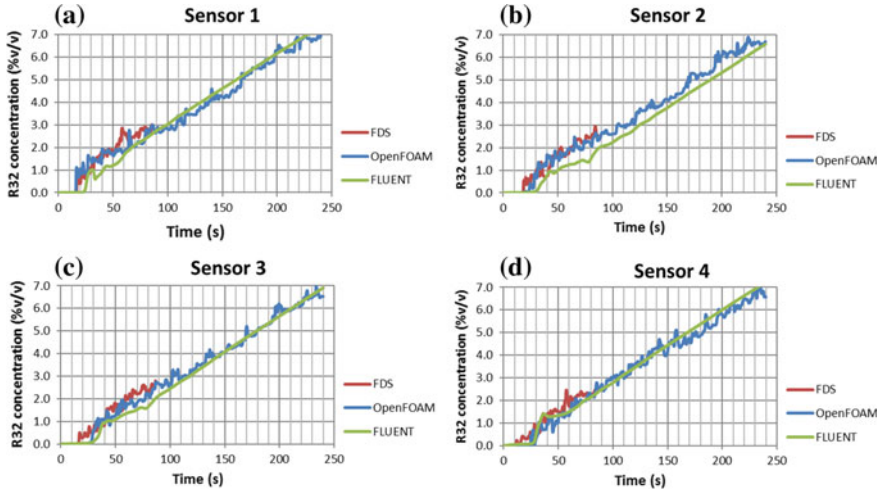


Fig. 13.4 Comparison of numerical values of refrigerant concentration at four sensor locations

13.5 Conclusion

In modeling the leakage of refrigerant gas, three different software packages were studied in order to understand the differences that might exist in some popular CFD codes. Two were freeware, FDS and OpenFOAM, while the third was commercial. The package FDS is specially designed for fire modeling and is designed for ease of use while the other software packages require significant training and have broad CFD capabilities. In modeling a single gas leakage scenario, we found no significant difference in concentration between the three different packages, and where differences exist, they were explained by the differences in the underlying physics and mathematical models. It was found that for modeling the gaseous leakage of refrigerants into a confined space, it is extremely important the turbulent model and the diffusion model are well understood. For our study, a turbulent model that captures well the mixing is necessary, and in this aspect, the LES turbulence model captures small eddies formed due to turbulent diffusion. But the simulation time is much higher in comparison with mean turbulence models. FDS simulation with default LES model requires very fine mesh hence a much longer simulation time in comparison with OpenFOAM and FLUENT with $k-\epsilon$ realizable turbulence model. With all similarities between OpenFOAM and FLUENT models, in our context, OpenFOAM makes faster simulation basically due to the higher number of cores for parallel computation and constraint on core usage with FLUENT. Based on our convenience in use, resource utilization and cost effectiveness, OpenFOAM found to be fit software to be used for future analysis in our organization.

References

Book

1. Standard 15-2016 (packaged w/ Standard 34-2016) “Safety Standard for Refrigeration Systems and Designation and Classification of Refrigerants”
2. UL Research Report, “AHRTI Report No. 9007-01, Benchmarking Risk by Whole Room Scale Leaks and Ignitions Testing of A2L Refrigerants”
3. ANSYS FLUENT 6.3 Documentation, User Guide (2016)
4. Versteeg, H.K., Malalasekera, W.: An Introduction to Computational Fluid Dynamics: The Finite Volume Method, 2nd edn. Pearson Education, Harlow, England (2007)
5. Greenshields, C.J., CFD Direct Ltd.: OpenFOAM, The Open Source CFD Toolbox, User Guide, Version 3.0.1 (2015)

Journal Article

6. Fiates, J., Vianna, S.S.V.: Numerical modelling of gas dispersion using OpenFOAM. *J. Process Saf. Environ. Prot.* **104**, 277–293 (2016)
7. Mack, A., Spruijt, M.P.N.: Validation of OpenFoam for heavy gas dispersion applications. *J. Hazard. Mater.* **262**, 504–516 (2013)
8. Dong, L., Zuo, H., Hu, L., Yang, B., Li, L., Wu, L.: Simulation of heavy gas dispersion in a large indoor space using CFD model. *J. Loss Prev. Process Ind.* **46**, 1e12 (2017)

Conference Article

9. Mahmood Tabaddor, M.: Practical challenges of implementing certification by virtual testing. In: Verification and Validation Symposium 2017, Las Vegas

Chapter 14

Forced Vibration Harmonic Response Analysis of Semi-mobile Crusher Station



Shanmugam Perumal, Raghunathan Swaminathan and Mike Christensen

Abstract The objective of the analysis was to design SMC structure to withstand dynamic loading condition due to crusher operation. A study about forced vibration analysis for Semi-mobile crusher (SMC) using finite element analysis (FEA) was carried out to determine the natural frequencies, mode shapes and forced harmonic frequency response characteristics. Natural frequency analysis and followed by harmonic frequency response analysis were performed using finite element calculations to find out critical frequencies and its corresponding peak displacements and dynamic stresses. The results of the study show the weakest direction and critical frequencies of the structure. Also, the dynamic displacement and stresses were found to be acceptable thereby the structural dynamic integrity of the SMC structure was established.

Keywords Semi-mobile crusher · Modal analysis · Frequency response analysis · Effective mass participation · Critical frequencies

14.1 Introduction

FLSmidth relocatable crushing stations were designed to significantly reduce truck haulage and help realize the many benefits of in-pit crushing and conveying. The result is reduced operating costs and environmental impact. The SMC series of modular crushing stations allows for quick relocations and comes available with a gyratory crusher that can reduce any type of feed material to a conveyable size. To

S. Perumal (✉) · R. Swaminathan
FLSmidth India Private Limited, Chennai, India
e-mail: shanmugam.perumal@flsmidth.com

R. Swaminathan
e-mail: raghunathan.swaminathan@flsmidth.com

M. Christensen
FLSmidth USA Inc, Salt Lake City, USA
e-mail: Mike.Christensen@flsmidth.com

determine the dynamic response of the SMC structure under a steady-state sinusoidal (harmonic) loading due to gyratory crusher at a given frequency, forced vibration harmonic response analysis was carried out.

14.2 Semi-mobile Crusher Station

The semi-mobile crusher (SMC) station was constructed from structural steel and consists of four major sections: the crusher module, two (2) truck bridges and the discharge conveyor. The crusher module was designed to be moved as a single unit except for the truck bridges. The truck bridges were designed to be moved in sections. The discharge conveyor was designed to be moved as a single unit. Figure 14.1 shows the semi-mobile crusher station's description.

The semi-mobile crusher frame was primarily made out of ASTM A36. The property values for this material were listed in Table 14.1.

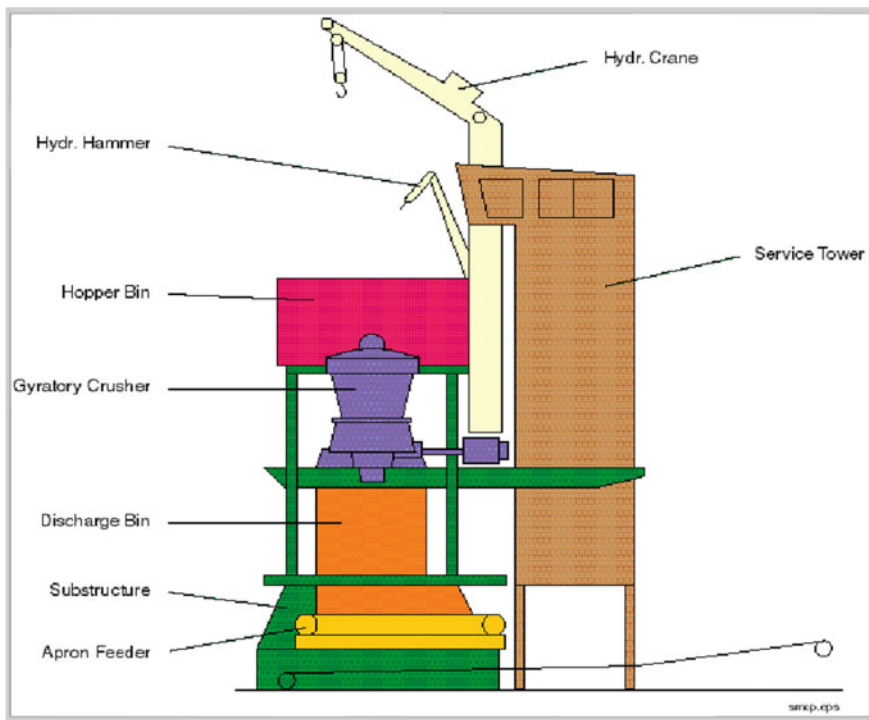


Fig. 14.1 Semi-mobile crusher station description

Table 14.1 Material properties for the Semi-mobile crusher frame

Property	Value
Density (Kg/m ³)	7850
Young's modulus (GPa)	200
Poisson's ratio	0.26
Yield strength (MPa)	250
Endurance strength (MPa)	150

14.3 Assumptions

Material considered was homogeneous. Material considered was linear elastic and isotropic. Nonlinear due to geometry was not considered in the analysis. Overall structural constant damping was assumed as 5%. Welds were modelled as a node to node connectivity at the interface locations. Gyratory crusher, rock breaker, crane, motor and other auxiliary equipment were modelled as point masses and will be connected to the respective mounting points. Mode superposition method was followed for the frequency response analysis.

14.4 Modal Analysis

The mode shapes and frequency directly impact the dynamic response of the system to dynamic inputs such as produced by rotating equipment like the gyratory crusher and motor, wind loads, earthquakes, etc. The modal analysis results of the semi-mobile frame were summarized in the table. The first 50 natural frequencies were reported based on effective mass participation.

14.4.1 Finite Element (FE) Model

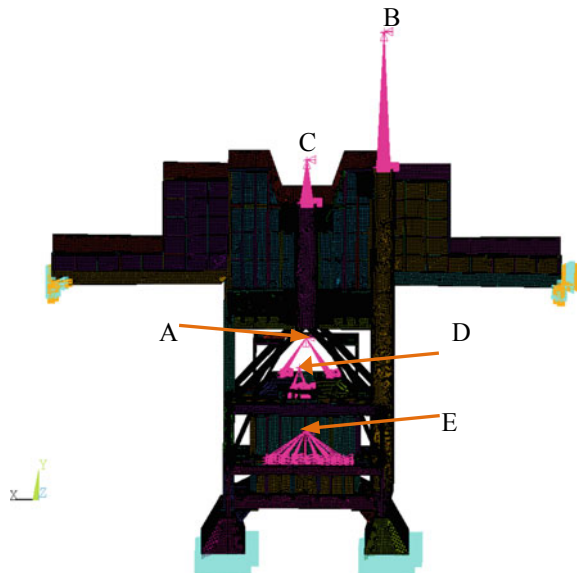
The FE model consists of four noded shell elements. The weld locations were modelled as a node to node connectivity. The total number of nodes 2,283,917 and total number elements was 2,309,721. The mass of the FE model was 943 tonnes.

14.4.2 Loads and Boundary Condition

The crusher, crane, rock breaker, crusher motor, and Lub & Hydraulic Skid and Miscellaneous Equipment were modelled as a lumped point mass at their approximate

Table 14.2 Mass details of different equipment

Location	Assembly/equipment	Mass (T)
A	Crusher	310
B	Crane	41
C	Rock breaker	27
D	Crusher motor	12
E	Lub and Hydraulic skid and Miscellaneous equipment	11
–	Structural steel frame	943
	Total	1344

Fig. 14.2 Semi-mobile crusher—loads and boundary condition

CG locations and connected to their respective mounting locations through rigid connections. Table 14.2 shows the mass details of all equipment/assembly considered.

The bottom faces of the pontoons were constrained in translations in all three directions and rotations were free. Two extreme edges of the truck bridge were constrained with fixed support (All translations and rotations constrained) as shown in Fig. 14.2.

14.5 Significance of Effective Mass Participation

The significance of the vibration mode was represented by effective mass participation. It was a measure of how much energy gets into a mode leading to larger

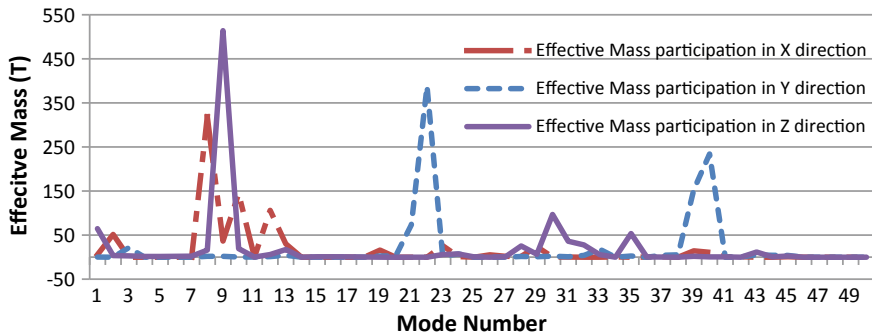


Fig. 14.3 Effective mass participation

Table 14.3 Effective mass participation percentage

Direction	Total mass (T)	Modal effective mass (T)	Percentage
X	1344	801	60
Y	1344	950	71
Z	1344	941	70

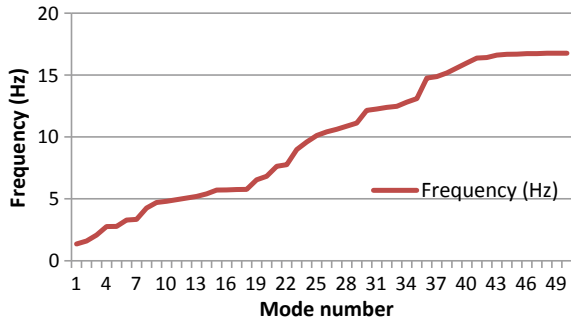
amplitudes. Modes with relatively high effective masses can be readily excited by excitation. On the other hand, modes with low effective masses cannot be readily excited (Fig. 14.3 and Table 14.3).

Effective mass participation in X direction indicates that more effective mass was observed in the first 30 modes. Thereafter, the incremental mass was observed in the remaining modes. Effective mass participation in Y direction indicates that more effective mass was observed between 20th modes and 40th modes. Effective mass participation in Z direction indicates that more effective mass was observed between 1st mode and 15th mode and between 25th mode and 35th mode.

14.6 Natural Frequencies

There were 50 natural frequencies captured based on effective mass participation. The reason behind capturing 50 modes was to capture 80% of the total effective mass. But, even after capturing 100 modes, we could not reach 80% mass participation as after 50th mode only incremental mass captured and it was about less than 5%. Hence it was decided to limit the number of modes into 50 modes to reduce the solution time and without compromising much on the accuracy. Figure 14.4 shows the natural frequencies captured for first 50 modes. The first fundamental natural frequency was 1.36 Hz and there were three natural frequencies lower than 2.3 Hz.

Fig. 14.4 Natural frequencies



14.7 Frequency Response (Harmonic) Analysis

The harmonic analysis was a technique used to determine the steady-state response of a linear structure to loads that vary sinusoidally (harmonically) with time. The idea was to calculate the structure's response at several frequencies and obtain a graph of some response quantity (usually displacements) versus frequency. "Peak" responses were then identified on the graph and stress reviewed at those peak frequencies.

Crusher unbalanced force of 197.9 KN was applied in the X direction to simulate force vibration response on the SMC station structure

14.7.1 Locations Identified for Displacement Measurement Over Frequency Range

To identify critical forcing frequencies—frequencies at which the highest displacements (or stresses) occur at points of interest in the model will be selected—and to then post-process the entire model at these critical forcing frequencies (Fig. 14.5).

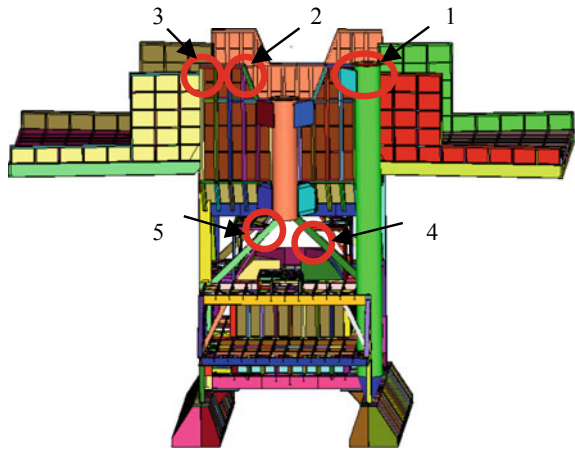
14.7.1.1 Location 1

This location was chosen based on the mode shape 1 where this particular location might deform more as compared to other locations. The node number corresponds to this location was 666,830 in the crane mounting support.

14.7.1.2 Location 2

This location was chosen based on the mode shape 3 where this particular location might deform more as compared to other locations. The node number corresponds to this location was 233,597 in the feed hopper (crane side).

Fig. 14.5 Locations considered for displacement measurement



14.7.1.3 Location 3

This location was chosen based on the mode shape 8. The node number corresponds to this location was 233494 in the feed hopper (crane side).

14.7.1.4 Location 4

This location was chosen based on the mode shape 9, 10, 12 and 13. The node number corresponds to this location was 796,567 in the feed hopper (crane side).

14.7.1.5 Location 5

This location was chosen based on the mode shape 9, 10, 12 and 13. The node number corresponds to this location was 795,948 in the feed hopper (crane side).

14.7.2 *Max Displacement Plots for X Direction Unbalanced Forces*

See Tables [14.4](#), [14.5](#) and [14.6](#).

Table 14.4 Max displacement for X direction unbalanced forces

Location	Displacement in X direction (mm)	Displacement in Y direction (mm)	Displacement in Z direction (mm)
1	2.60	0.11	1.90
2	2.37	0.64	5.20
3	2.37	0.85	6.00
4	26.00	16.85	1.56
5	26.00	16.10	1.78

Table 14.5 Max displacement for Y direction unbalanced forces

Location	Displacement in X direction (mm)	Displacement in Y direction (mm)	Displacement in Z direction (mm)
1	0.21	2.00	0.25
2	0.12	0.12	0.23
3	0.12	0.14	0.50
4	2.03	1.25	1.38
5	2.13	1.30	1.30

Table 14.6 Max displacement for Z direction unbalanced forces

Location	Displacement in X direction (mm)	Displacement in Y direction (mm)	Displacement in Z direction (mm)
1	0.47	0.15	5.40
2	0.58	0.43	5.90
3	0.58	0.28	4.80
4	5.40	2.81	4.40
5	5.30	3.45	4.10

14.7.3 Max Displacement Plots for X Direction Unbalanced Forces

A max displacement of 26 mm was observed in the X direction at locations 4 and 5. In Y direction, max displacement observed was 17 mm at location 4. Max displacement of 6 mm observed in Z direction at location 3 (Figs. 14.6, 14.7 and 14.8).

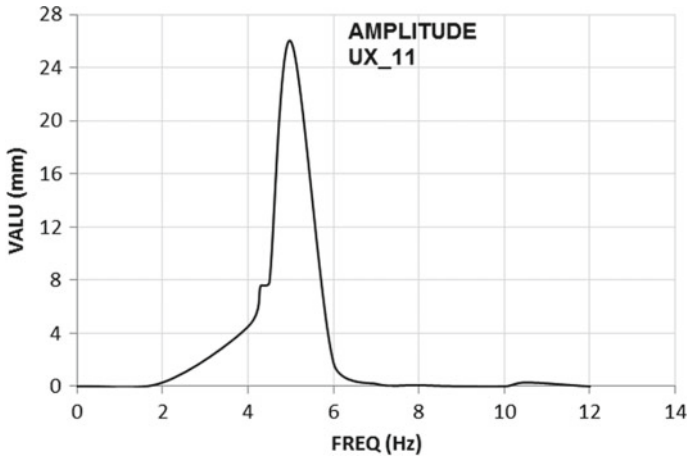


Fig. 14.6 Max X displacement versus frequency

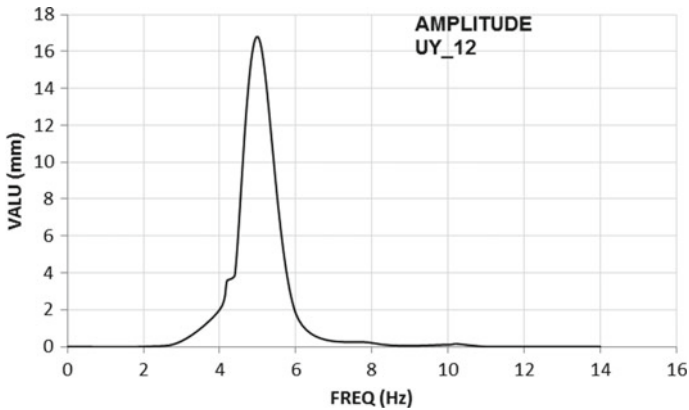


Fig. 14.7 Max Y displacement versus frequency

14.7.4 Max Displacement Plots for Y Direction Unbalanced Forces

A max displacement of 2.13 mm was observed in the X direction at location 5. In Y direction, max displacement observed was 2 mm at location 1. Max displacement of 1.38 mm observed in Z direction at location 4 (Figs. 14.9, 14.10 and 14.11)

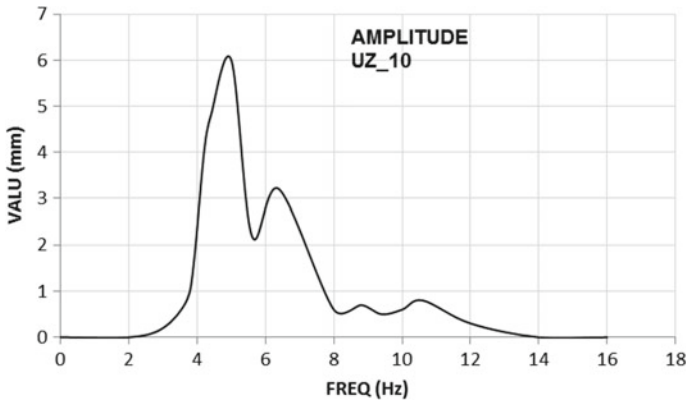


Fig. 14.8 Max Z displacement versus frequency

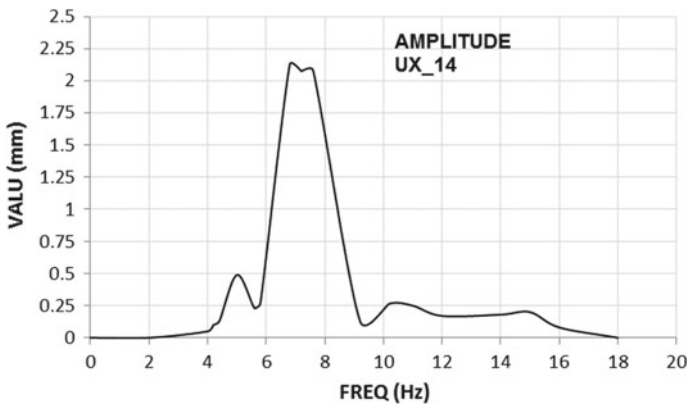


Fig. 14.9 Max X displacement versus frequency

14.7.5 Max Displacement Plots for Z Direction Unbalanced Forces

A max displacement of 5.4 mm was observed in the X direction at location 4. In Y direction, max displacement observed was 3.45 mm at location 5. Max displacement of 5.9 mm observed in Z direction at location 2 (Figs. 14.12, 14.13 and 14.14).

The locations 4 and 5 were experiencing high dynamic displacements. The maximum peak dynamic displacements in X direction was 26 mm. The maximum peak dynamic displacement in Y direction was 17 mm. The X and Y direction peak displacements were observed in the crusher maintenance enclosure.

The maximum Z direction displacement was observed in location 3. The location 3 belongs to feed hopper tip of crane side. The maximum Z direction displacement

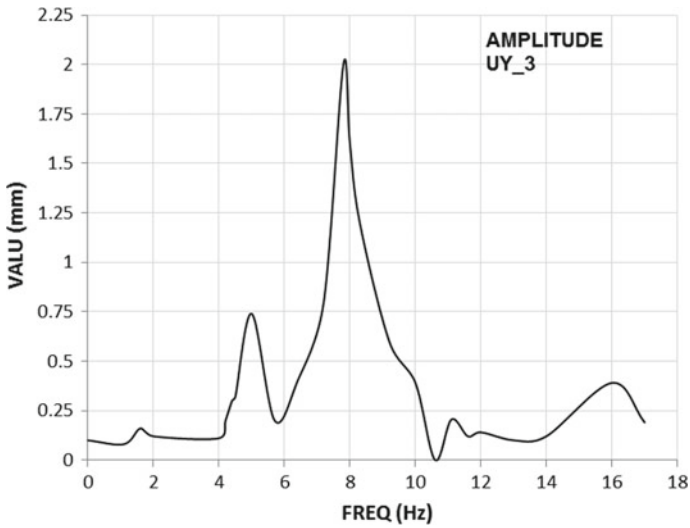


Fig. 14.10 Max Y displacement versus frequency

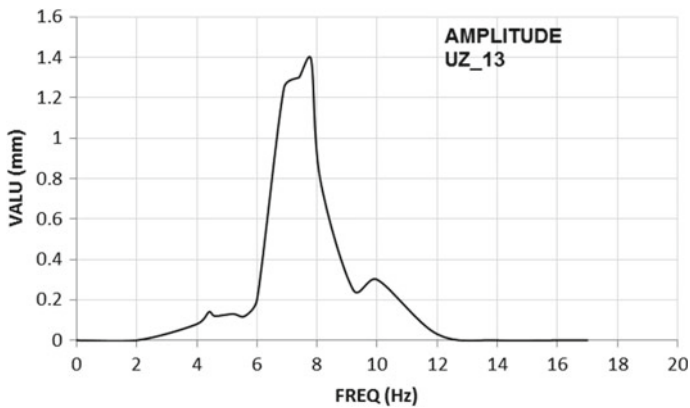


Fig. 14.11 Max Z displacement versus frequency

was 6 mm. Also, the analysis performed by applying the crusher unbalanced loads in the Y and Z direction.

The peak dynamic displacements in all three directions were found to be lesser than the unbalanced load applied in the X direction. The next weaker direction was Z as the displacements and stresses were very low in the case of the unbalanced load applied in the Y direction.

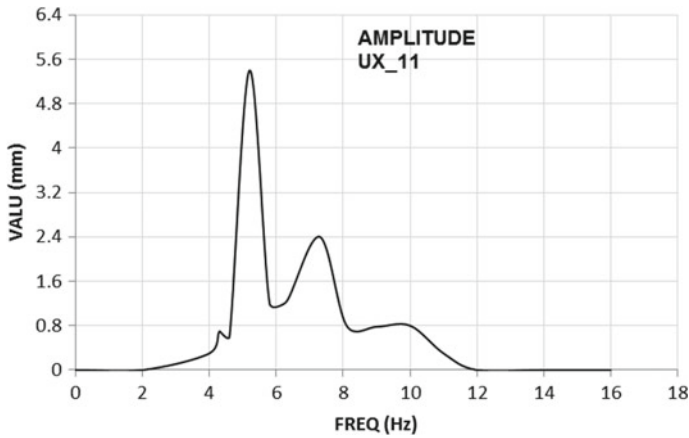


Fig. 14.12 Max X displacement versus frequency

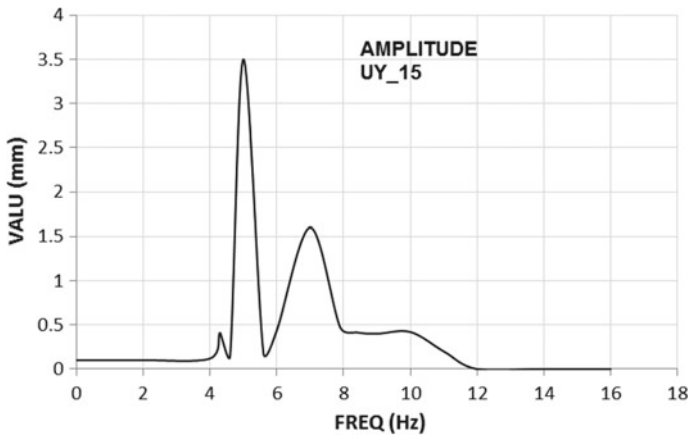


Fig. 14.13 Max Y displacement versus frequency

14.8 Conclusions

Having performed the analysis in all three directions, it was identified that the most critical/weak direction was X when compared to the other two. As expected, Y direction was very stiff when compared to the Z direction.

The X direction frequency response analysis results indicate that the most critical frequencies were 4.7, 4.8, 5.06 and 5.2 Hz. The analysis results indicate that resonance will not happen as the peak displacement was not observed near the excitation frequency of 2.34 Hz.

The critical frequencies observed in the crusher maintenance enclosure. Peak dynamic displacement in X direction was 26 mm observed in the crusher maintenance

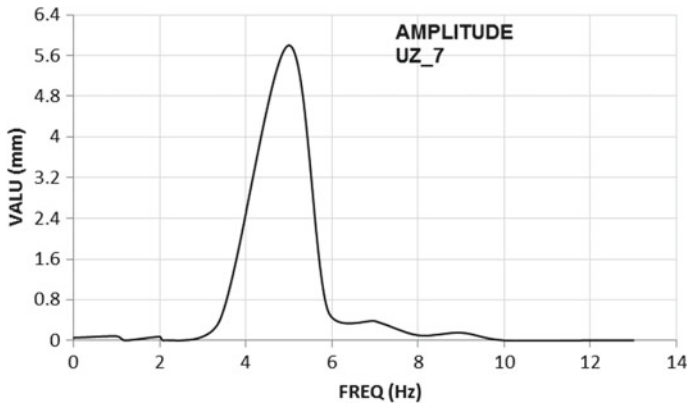


Fig. 14.14 Max Z displacement versus frequency

enclosure. Peak dynamic displacement in Y and Z direction was 17 and 6 mm, respectively, and considered to be acceptable based on L/D ratio and tests results conducted in the similar structure.

The peak dynamic displacement in X direction looks little high. It was suggested to lower the value below 20 mm by providing additional cross stiffeners and column bottom reinforcements. Allowable displacement criteria 20 mm was calculated based on the L/D ratio of the member location and tests results conducted in the similar structure. The hot spot stress observed in the bottom legs of the crusher maintenance enclosure. However, the stresses were lower than the endurance strength (150 MPa) of the material, and hence design was considered to be safe.

References

1. Modal analysis of Linear dynamic systems: Physical interpretation Anil K.Chopra, Member, ASCE
2. Dynamic analysis of structures. Athol J.Carr
3. Dynamic design and analysis method DDAM and Modal effective mass. Tone Abbey
4. He, J., Fu, Z.F.: Modal Analysis, 1st edn, p. 304. Butterworth-Heinemann, Oxford, Boston (2001). 10: 0080511783
5. Rao, S.S.: Mechanical Vibration, 4th edn. Pearson Education Press (2004)
6. Ansys® MAPDL Tutorials

Chapter 15

Comparative Study of Material Approximation Methods for Fatigue Life Prediction of Steels, Aluminum and Titanium



Majnoo M. Gawture and Tanmay Tamhane

Abstract In this study, several methods for approximating strain life parameters for steels, aluminum and titanium alloys are compared. The study was performed on the available strain life data from ASM and SAE database. The comparisons are done on the stress scale using Neuber correction, which is in line with the way approximations are used in simulation and also brings some new insights which are discussed in detail. Statistical measures to capture accuracy, scatter and conservatism were proposed and used for comparison of different methods. Based on this study, ‘modified universal slopes method’ for steels, ‘uniform material law’ for aluminum alloys and ‘Mitchell’s method’ for titanium alloys are suggested as the best methods to approximate strain life parameters of these respective materials. Also, Roessle-Fatemi method for steel is suggested in the absence of %RA data from UTS. Finally, limitations of all the approximation methods for stresses below yield and for materials with a low value of ‘Fatigue Ductility Coefficient’ are discussed.

Keywords Material approximation · Strain-based fatigue · Fatigue life predictions · Monotonic properties · Cyclic properties · Error estimation

15.1 Introduction

Strain life method [1] is emerging as an appropriate approach for evaluating the fatigue life of components having local or gross plastic deformation. For components subjected to elastic loading, strain life method will yield a similar life as predicted by stress life method; however, due to practical measurement limitations, stress life method is preferred under elastic loading conditions. The strain life method is based on the Coffin-Manson relation given by:

M. M. Gawture (✉) · T. Tamhane
Eaton Corporation, Pune, India
e-mail: majnoogawture@eaton.com

© Springer Nature Singapore Pte Ltd. 2020
C. Li et al. (eds.), *Advances in Engineering Design and Simulation*,
Lecture Notes on Multidisciplinary Industrial Engineering,
https://doi.org/10.1007/978-981-13-8468-4_15

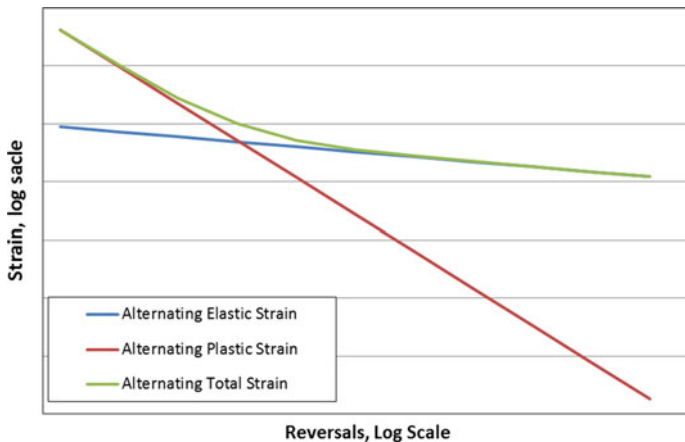


Fig. 15.1 Strain life curve

$$\varepsilon_a = \frac{\Delta\varepsilon_e}{2} + \frac{\Delta\varepsilon_p}{2} = \frac{\sigma'_f}{E} (2N_f)^b + \varepsilon'_f (2N_f)^c \tag{15.1}$$

where ε_a is the alternating component of total strain, $\Delta\varepsilon_e$ is the range of elastic strain, $\Delta\varepsilon_p$ is the range of plastic strain, σ'_f is the fatigue strength coefficient, b is fatigue strength exponent, ε'_f is the fatigue ductility coefficient, c is the fatigue ductility exponent and E is the Young’s modulus.

Equation (15.1) forms the basis of strain life method and is plotted in Fig. 15.1. On a log–log scale, strain life curve is formed by adding the elastic straight line (slope b and intercept σ'_f/E) and a plastic straight line (slope c and intercept ε'_f). The entire strain life curve can be generated if all these four material constants ($\sigma'_f, b, \varepsilon'_f, c$), apart from E , are known.

In the numerical prediction of fatigue life using strain life equation, mathematical modeling of material nonlinear response is needed. This is accomplished using Ramberg-Osgood relation [2] as follows:

$$\varepsilon_t = \varepsilon_e + \varepsilon_p = \frac{\sigma}{E} + \left(\frac{\sigma}{K'}\right)^{\frac{1}{n'}} \tag{15.2}$$

where ε_t is the total strain, ε_e is an elastic strain, ε_p is plastic strain, σ is nonlinear (elasto-plastic) stress, K' is the cyclic strength coefficient and n' is cyclic strength exponent.

Together with four constants of strain life curve, K' and n' , form a complete set of six constants that are required for strain life predictions. Comparing Eqs. (15.1) and (15.2), the following relation can be derived:

$$K' = \frac{\sigma'_f}{(\varepsilon'_f)^{n'}} \quad \text{and} \tag{15.3a}$$

$$n' = \frac{b}{c} \quad (15.3b)$$

Though Eqs. (15.3a) and (15.3b) do not have any physical basis, they can be used as an approximation for strain life calculations (15.1).

There are many situations under which these strain life constants for a given material are not known, like: The material is used in the design for the first time, and detailed strain life testing is not performed; The strain life properties post heat treatment are not known; manufacturing process (like stamping) changes the material strength; in the early stages of design, the material is being evaluated and hence costly strain life testing is not recommended, etc. In such situations, the designer has to make fatigue life predictions in spite of limited material data. In the past few years, there have been several technical literatures, which have tried to approximate the four constants of the strain life Eq. (15.1) using either the monotonic tensile test data or using the material hardness.

A short summary of all these major literature and the basis of their assumptions are listed in Table 15.1. The values in parenthesis are the numerical values to be used in the approximations. All these approximations assume K' and n' as given by Eqs. (15.3a) and (15.3b).

Manson [3] was one of the earliest researchers who attempted an approximation of strain life properties using monotonic tensile properties. Manson [3] studied the material properties of 47 materials, which included steels, aluminum and titanium alloys and proposed two approaches for a material approximation—the universal slopes method and the four-point correction method. In the universal slopes method, Manson assumed that b and c values for all metals can be approximated by -0.12 and -0.6 , respectively. The strain life equation with universal slopes approximation is given by:

$$\varepsilon_a = \frac{1.9\sigma_u}{E}(2N_f)^{-0.12} + 0.76\varepsilon_f^{0.6}(2N_f)^{-0.6} \quad (15.4)$$

The four-point approximation method tries to approximate the strain life curve using separate equations for elastic and plastic lines. The equations of these lines are derived by approximating the strain levels at four different life numbers. The final strain life relation with four-point approximation is given by:

$$\varepsilon_a = A(2N_f)^b + B(2N_f)^c \quad (15.5a)$$

where

$$A = 0.5 * 10^{b \log 2 + \log\left(\frac{2.5\sigma_f}{E}\right)} \quad (15.5b)$$

$$b = \log\left(\frac{2.5\sigma_f}{0.9\sigma_u}\right) / \log[1/(4 * 10^5)] \quad (15.5c)$$

Table 15.1 Material approximation methods

S. No.	Method	Proposed by	Year	Material	σ'_f	b	ϵ'_f	c
1	Universal slopes method [3]	Manson	1965	All	σ_u	(-0.12)	ϵ_f	(-0.6)
2	Four-point method [3]	Manson	1965	All	σ_u, ϵ_f, E	σ_u, ϵ_f, E	σ_u, ϵ_f, E	σ_u, ϵ_f, E
3	Mitchell's method for steels [4]	Socie et al.	1977	Steel	σ_u	σ_u	ϵ_f	(-0.6, -0.5)
4	Modified universal slopes method [5]	Muralidharan, Manson	1988	Steel, Al, Ti	σ_u, E	(-0.09)	σ_u, ϵ_f, E	(-0.56)
5	Uniform material law (UML) [6]	Baumel and Seeger	1990	Unalloyed and low alloy Steels	σ_u	(-0.087)	σ_u, E	(-0.58)
6	Uniform material law (UML) [6]	Baumel and Seeger	1990	Al, Ti	σ_u	(-0.095)	(0.35)	(-0.69)
7	Modified four-point method [7]	Ong	1993	Steels ^a	σ_f	σ_u, σ_f, E	ϵ_f	$\sigma_u, \sigma_f, \epsilon_f, E$
8	Hardness method [8]	Roessle, Fatemi	2000	Steels	HB	(-0.09)	HB, E	(-0.56)
9	Modified Mitchell's method [9]	Park and Song	2003	Al, Ti	σ_u	σ_u	ϵ_f	(-0.664)
10	Medians method (steels) [10]	Meggiolaro, Castro	2004	Steel	σ_u	(-0.09)	(0.45)	(-0.59)
11	Medians method (Al, Ti) [10]	Meggiolaro, Castro	2004	Al, Ti	σ_u	(-0.11)	(0.28)	(-0.66)

Note ^aModified four-point method was originally proposed for steel, but has been found to apply well for aluminum and titanium. Hence, in this paper, we will study its applicability on aluminum and titanium as well

$$c = \frac{1}{3} \log \left[\frac{0.0132 - \Delta \varepsilon_e^@}{1.91} \right] - \frac{1}{3} \log \left[\frac{\varepsilon_f^{3/4}}{4} \right] \quad (15.5d)$$

$$B = 0.5 * 10^{c \log(\frac{1}{20}) + \log \left[\frac{\varepsilon_f^{3/4}}{4} \right]} \quad (15.5e)$$

In Eq. (15.5d), $\Delta \varepsilon_e^@$ is derived assuming that the total strain at 10^4 range cycles is 1% and is given by

$$\Delta \varepsilon_e^@ = 10^{f b \log(4 * 10^4) + \log \left[\frac{2.5 \sigma_u (1 + \varepsilon_f)}{E} \right]} \quad (15.5f)$$

Also, it can be assumed that

$$\sigma_f = \sigma_u (1 + \varepsilon_f) \quad (15.5g)$$

Socie et al. [4] suggested the following approximation for strain life curve for steels

$$\varepsilon_a = \frac{\sigma_u + 345}{E} (2N_f)^b + \varepsilon_f (2N_f)^c \quad (15.6a)$$

where b was approximated assuming that fatigue strength at 10^6 cycles is $0.5 \sigma_u$. Thus,

$$b = \frac{1}{6} \log \left[\frac{0.5 \sigma_u}{\sigma_u + 345} \right] \quad (15.6b)$$

and c was assumed as -0.5 for strong material and -0.6 for a ductile material. This method is popularly referred to as Mitchell's method in the literature.

Muralidharan and Manson [5] modified the original universal slopes method, by using an optimization algorithm and doing least square fit to the coefficients of strain life Eq. (15.1). Their work resulted in the following approximation:

$$\varepsilon_a = \frac{0.623 \sigma_u^{0.823}}{E^{0.832}} (2N_f)^{-0.09} + 0.0196 \varepsilon_f^{0.155} \left[\frac{\sigma_u}{E} \right]^{-0.53} (2N_f)^{-0.56} \quad (15.7)$$

Baumel and Seeger [6] were the first to come up with different approximations for steels, compared to aluminum and titanium alloys. They assumed different slopes b and c for steels and aluminum/titanium. Their approximation for unalloyed and low alloyed steels is:

$$\varepsilon_a = \frac{1.5 \sigma_u}{E} (2N_f)^{-0.087} + 0.59 \alpha (2N_f)^{-0.58} \quad (15.8a)$$

where $\alpha = 1$ for $\frac{\sigma_u}{E} \leq 3E - 3$

$$\alpha = \left(1.375 - 125 \frac{\sigma_u}{E}\right) \text{ for } \frac{\sigma_u}{E} > 3E - 3 \quad (15.8b)$$

Note that the slopes b and c are very close to those arrived in Eq. (15.7). The approximation for aluminum and titanium is

$$\varepsilon_a = \frac{1.67\sigma_u}{E} (2N_f)^{-0.095} + 0.35(2N_f)^{-0.69} \quad (15.9)$$

Note that the slopes b and c in Eq. (15.9) are greater compared to those in Eq. (15.8a). Also, Eqs. (15.8a) and (15.9) require σ_u as the only material constant (apart from E) for approximating strain life curve. This method has emerged as one of the default options in many commercial fatigue tools [11, 12].

Ong [7] suggested a modification to the original four-point correction method for steels. The basis of his approximation was similar to the original four-point method, however, the elastic strain amplitudes at 10^6 cycles were derived using multilinear regression analysis. The fatigue strength coefficient and ductility coefficient were assumed to be σ_f and ε_f , respectively, giving:

$$\varepsilon_a = \frac{\sigma_f}{E} (2N_f)^b + \varepsilon_f (2N_f)^c \quad (15.10a)$$

Where,

$$b = \frac{1}{6} \left\{ \log \left[0.16 \left(\frac{\sigma_u}{E} \right)^{0.81} \right] - \log \left(\frac{\sigma_f}{E} \right) \right\} \quad (15.10b)$$

$$\text{And } c = \frac{1}{4} \log \left[\frac{0.00737 - \Delta\varepsilon_e^*/2}{2.074} \right] - \frac{1}{4} \log(\varepsilon_f) \quad (10c)$$

In Eq. (10c), $\Delta\varepsilon_e^*$ is derived assuming that the total strain amplitude at 10^4 cycles is 0.5% and is given by

$$\frac{\Delta\varepsilon_e^*}{2} = \frac{\sigma_f}{E} \left[10^{\frac{2}{3} \left\{ \log \left[0.16 \left(\frac{\sigma_u}{E} \right)^{0.81} \right] - \log \left(\frac{\sigma_f}{E} \right) \right\}} \right] \quad (15.10d)$$

Roessle and Fatemi [8] tried to approximate the strain life coefficients solely based on the hardness of the material. Their approach did not rely on any other constant from the monotonic tensile test (except E). They used the published literature on 49 steels and tested 20 more steels to derive regression curve fit of strain life parameters plotted against material hardness. They assumed the slopes b and c to be the same as that used in the modified universal slopes method. The Roessle-Fatemi approximation for steels has the following form:

$$\varepsilon_a = \frac{4.25(\text{HB}) + 225}{E} (2N_f)^{-0.09} + \frac{0.32(\text{HB})^2 - 487(\text{HB}) + 191000}{E} (2N_f)^{-0.56} \quad (15.11)$$

It must be noted that Eq. (15.11) may be the only approximation available for some components in which the material strength changes post manufacturing (e.g. stamping). For steels, there is a good correlation between hardness and ultimate strength and hence uniform material law [6] can also be used in such scenarios.

Park and Song [9] have suggested a modification to Mitchell's method, to be used for aluminum and titanium:

$$\varepsilon_a = \frac{\sigma_u + 335}{E} (2N_f)^b + \varepsilon_f (2N_f)^{-0.664} \quad (15.12a)$$

where

$$b = \frac{1}{6} \log \left[\frac{0.446\sigma_u}{\sigma_u + 335} \right] \quad (15.12b)$$

Recently, Meggiolaro and Castro [10] studied material properties for 845 different materials (724 steels, 81 aluminum alloy and 15 titanium alloy). They proposed using the median values of $\frac{\sigma'_f}{\sigma_u}$, ε'_f , b and c for each alloy family. Their method results in the following approximation for steels

$$\varepsilon_a = \frac{1.5\sigma_u}{E} (2N_f)^{-0.09} + 0.45(2N_f)^{-0.59} \quad (15.13)$$

For aluminum and titanium alloys:

$$\varepsilon_a = \frac{1.9\sigma_u}{E} (2N_f)^{-0.11} + 0.28(2N_f)^{-0.66} \quad (15.14)$$

Meggiolaro and Castro [10] also compared the relative prediction capabilities of different methods and concluded that modified universal slopes method, hardness method and uniform material law yield satisfactory results for steels (apart from their proposed medians method). They also suggested that the modified universal slopes method should not be used for aluminum and titanium.

Lee and Song [13] used two approaches to compare the validity of approximation methods. One approach, they referred to as direct hardness method, in which they evaluated Roessle-Fatemi method, uniform materials law and medians method for steels, aluminum and titanium. Another approach, they referred to is the indirect hardness method in which they combined the approximations for strain life parameter (uniform material law and medians Method) with the approximations relating σ_u and hardness, again for steel, aluminum and titanium. They compared the results with those of the priority method—modified universal slopes method for steels and Mitchell's method for aluminum and titanium. For quantitative comparison, they used the error criteria as proposed by Park and Song [14]. Based on their study of 110 steels, 25 aluminum allows and four titanium alloys, they concluded that the modified universal slopes method is the best method for steels. In the absence of fracture ductility ε_f required by this method, Roessle-Fatemi method can be used

for steels. For aluminum alloys, they suggested medians method to be the best. In the absence of ultimate strength σ_u required by this method, they suggested using indirect hardness method with σ_u estimated using Roessle-Fatemi approach (originally for steel) and followed by strain life approximation using uniform material law. For titanium alloys, they suggested modified Mitchell's method to be the best, followed by uniform material law. They also came up with a relationship between σ_u and hardness for titanium alloys.

Basan et al. [15] studied different alloy groups of materials (unalloyed steels, low alloy steels, high alloy steels, aluminum and titanium) and concluded that the strain parameters for different groups of materials differ a lot. Thus, material approximations should cater to a different group of materials separately.

In all the previous literature, no mention is made about the applicability of the said approaches based on the level of stresses/strain (except in the paper by Meggiolaro and Castro [10]). Also, it must be noted that strain-based fatigue approach is preferred over stress-based approach whenever stresses exceed the yield strength of the material [1]. Since the material may cyclically soften or harden, the cyclic yield strength should be used for the above decision. Thus, the decision to use strain-based approach and the corresponding material approximations should be based on the level of stresses and not strains (as used in most of the above-mentioned literature). Though strain-based method theoretically yields similar life estimates as stress-based method for stresses below yield, the validity of material approximation methods below yield is not studied by any of the methods mentioned in Table 15.1 and literature [3–10, 13–15]. Also, for fatigue life predictions using finite element analysis (FEA), results should be populated considering the level of stresses (than strains) as elastic stresses from FEA are usually used for fatigue predictions. Thus, this paper aims to evaluate material approximation methods and their applicability over different stress levels (that might be used in practice).

For relating stresses to strains in plastic zone, Ramberg-Osgood relation (15.2) is used. At notches, local stress and strain can be related by using Neuber approximation [16] given by:

$$\varepsilon\sigma = (K_t S)^2 / E \quad (15.15)$$

Using Eqs. (15.2) and (15.15), we can estimate plastic stress σ and strain ε . The graphical representation of Neuber's rule is shown in Fig. 15.2.

Though Neuber's rule was derived assuming plane stress conditions, it is widely used for plastic stress/strain predictions as it over-estimates the stresses. In fatigue, Neuber's rule is used in conjunction with Massing's hypothesis [17] for estimating stress and strain ranges, as given by:

$$\frac{(\Delta\sigma)^2}{E} + 2\Delta\sigma \left(\frac{\Delta\sigma}{2K'} \right)^{1/n'} = \frac{(K_f \Delta S)^2}{E} \quad (15.16)$$

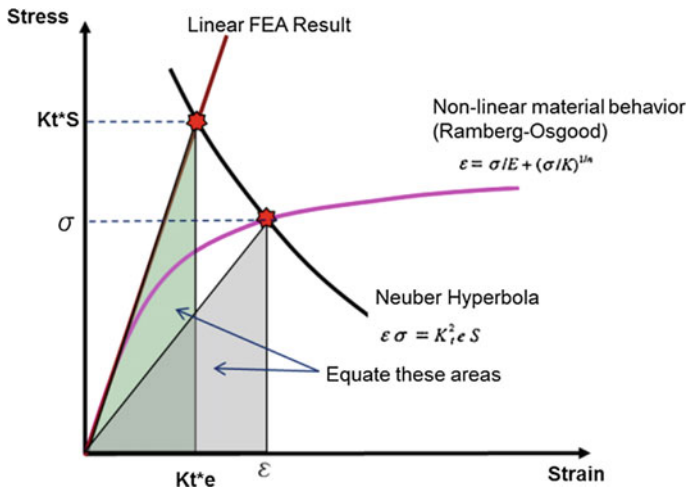


Fig. 15.2 Neuber’s rule

Also, for the multiaxial state of stress, von-Mises stresses and strains can be used in Eqs. (15.15) and (15.16). In this paper, Eq. (15.16) is used for stress and strain range calculation, and Eq. (15.1) is used for fatigue life prediction to compare different material approximations. Comparing the material approximations on the stress scale gives some new insights and conclusions.

15.2 Materials

75 steel, 14 aluminum and 10 titanium materials have been selected from the ASM database [18]. Additionally, 30 steels from SAE J1099 database [19] are selected for this study.

Steel materials have hardness value ranging from 64–670 BHN. Ultimate stress value of 285–2570 MPa and yield stress value of 175–2030 MPa was observed for all steel materials. Percentage area reduction varies between 3 and 90%. All the properties used are at room temperature. Selected grades of steel consist of SAE steels, low alloy steels, carbon steels and stainless steels.

Aluminum selected from ASM database have ultimate stress value of 110–580 MPa and yield stress value of 88–476 MPa. Percentage area reduction varies between 16 and 87.6%. All the properties used are at room temperature.

Titanium selected from ASM database have ultimate stress value of 434–1236 MPa and yield stress value of 303–1188 MPa. Percentage area reduction varies between 22 and 69%. All the properties used are at room temperature.

Figures 15.3 and 15.4 give a visual feel of the range of cyclic stress–strain properties and strain life properties, respectively, that are considered for the current study. The graphs are representative and have been plotted for steel.

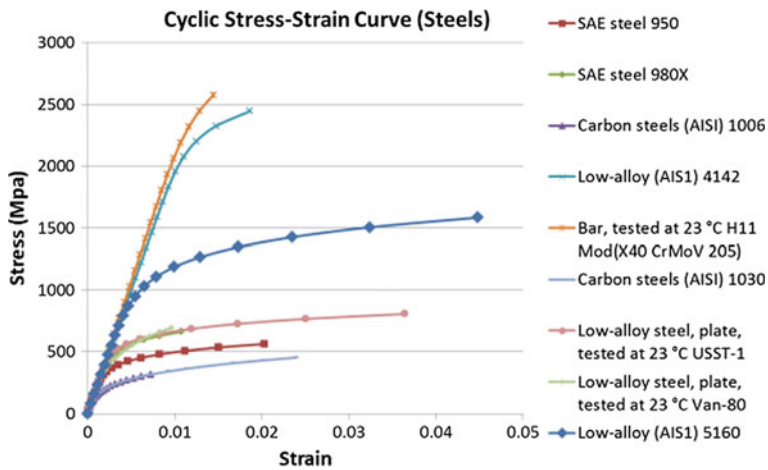


Fig. 15.3 Cyclic stress strain curve (steel)

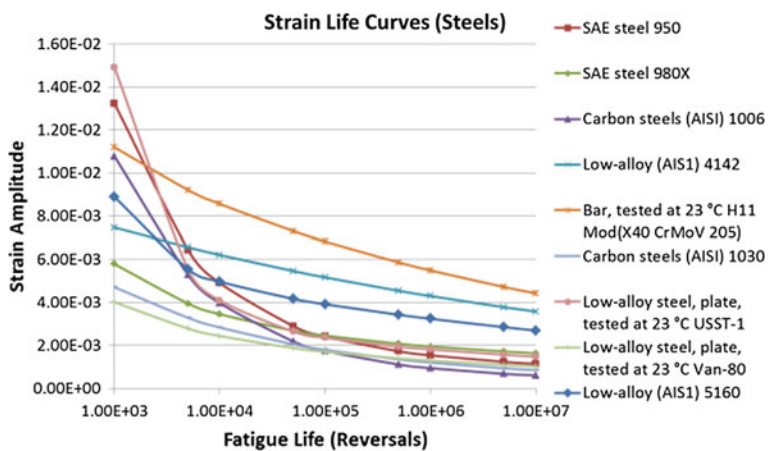
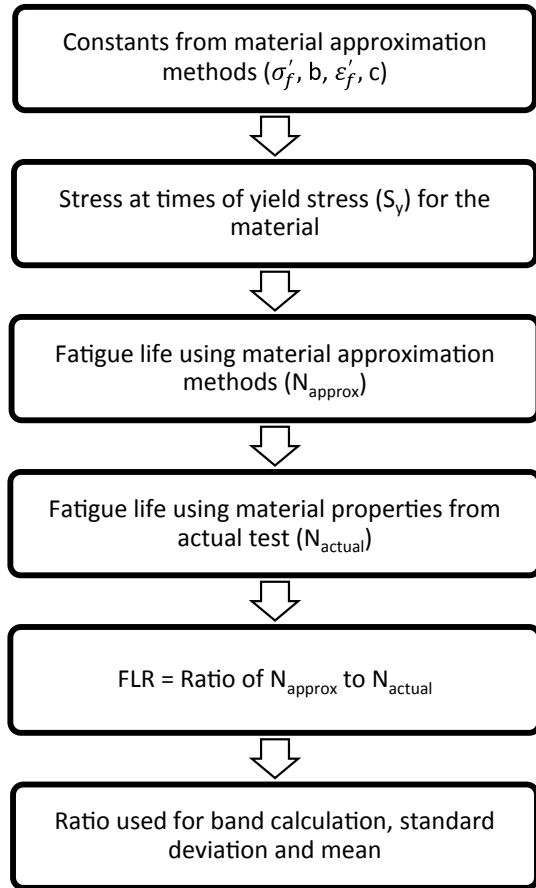


Fig. 15.4 Strain life curves (steel)

Flowchart 15.1 Approach for the current study



15.3 Approach

The following approach would be employed to compare the material approximation methods (Flowchart 15.1):

1. Estimate the strain-based fatigue constants using various approximation methods.
2. Calculate fatigue life of the material between 0.75 times of monotonic yield to four times of monotonic yield.
3. For estimation of strains from the stress levels, Neuber plasticity correction is used with Massings' hypothesis as described above.
4. Fatigue life is also calculated for the prescribed stress range using the actual tested material constants.
5. Fatigue life values obtained from various approximation methods are normalized using fatigue life estimated from actual tested constants.

6. A range of 1/3–3 times of fatigue life from actual properties is selected as a band to ascertain the number of points that are within the limit.
7. The standard deviation of all points is calculated considering a normal distribution of the points.
8. Conservatism is defined as the percentage of FLR values below one. This parameter will be explained in detail in subsequent sections.

The above method is deployed for all materials and the normalized fatigue life numbers are being used in results and discussion.

15.4 Results and Discussion

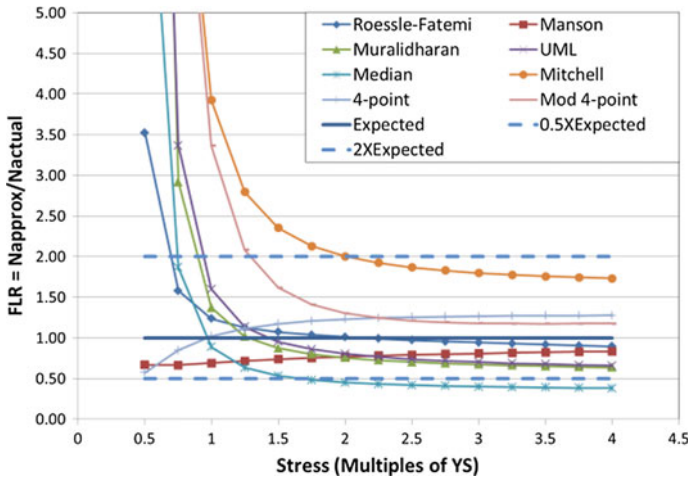
15.4.1 Trend Analysis

As discussed earlier, the applicability of material approximation methods has been studied on materials corresponding to the ASM database as well as SAE J1099 database. The study is performed for several levels of stress ranging from 0.75*YS (0.75 times yield stress) till 4*YS for each material (upper level of 4*YS was selected since, for ductile materials, elastic stresses can be so high). The stress ranges are converted to strain ranges using Neuber plasticity correction and Massing's hypothesis (Eqs. 15.15 and 15.16). The life obtained using different material approximation methods is compared to the life obtained using actual strain life constants. Results for three such representative steels from SAE J1099 are discussed next.

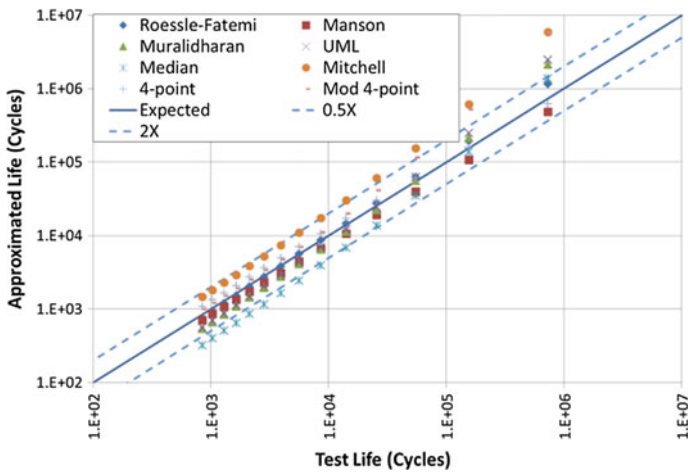
15.4.1.1 SAE 1015 Material (Hot Rolled Sheet—Normalized, Sut 414 MPa)

Figures 15.5a and b show the comparison of N_{approx} calculated using several material approximations and N_{actual} calculated using actual material parameters on stress scale and life scale, respectively. Note that the error band is set to 0.5X to 2X (as opposed to 1/3X to 3X used in statistical calculations), to better differentiate the approximation methods. In Fig. 15.5a, it can be seen that most of the predictions below 1*YS are highly non-conservative for this material. Only Manson's method and original four-point method do a good job in this range. Between 1*YS and 4*YS, most of the predictions fall within the band of 1/2X to 2X (except medians method which falls below 0.5X). Out of all the methods, Roessle-Fatemi (RF) method gives the most accurate prediction for this material. Manson's universal slope method, Muralidharan's modified universal slope method and uniform material law (UML) also show good predictions but are slightly conservative for this material.

Similar conclusions can be derived from Fig. 15.5b, except that the level of stress won't be known.



(a) Stress Scale



(b) Life Scale

Fig. 15.5 Predictions for SAE 1015

15.4.1.2 SAE 15B27 Material (Sut-916 MPa)

For this material, results are shown in Fig. 15.6.

It can be seen that all the methods predict highly conservative life numbers at $0.5 \cdot YS$, but the predictions are better for stresses beyond $0.75 \cdot YS$. Some methods like Mitchell, original four-point method and Manson’s method are highly non-conservative. Most of the other methods predict life within a scatter band of $0.5X$ and $2X$. Roessle-Fatemi method, UML and medians method predict non-conservative life

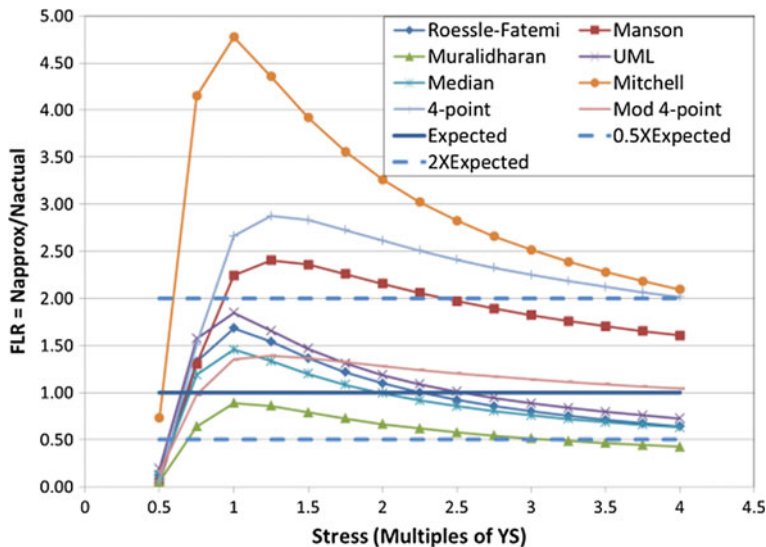


Fig. 15.6 Predictions for SAE 15B27

below $2 \cdot YS$ and conservative life beyond $2.5 \cdot YS$. Modified universal slopes method predicts conservative life over the entire stress range.

15.4.1.3 SAE 4340 Steel (Sut-1468 MPa)

For this material, results are shown in Fig. 15.7.

It can be seen that most of the methods, except Mitchell's, give predictions within the band of 0.5X to 2X. Again for stresses below YS , the predictions fail for some approximation methods. For this material, the original four-point method gives the most accurate result followed by Mitchell's method and medians method. Roessle-Fatemi, Muralidharan's method and UML which worked for other steels discussed earlier predict a very conservative life for this material.

15.4.1.4 ASM Al-7075-T6 (Sut-580 MPa)

Figure 15.8 shows the results for Al-7075-T6 aluminum.

For this aluminum grade, it can be seen that most of the methods, except Manson's universal slopes method, give good predictions. As Manson's universal slopes could not capture b and c values accurately for materials other than steel, it is no surprise that this method has limitations when applied to materials other than steel. Again, for stresses below YS , all the methods fail and highly under-predict fatigue life.

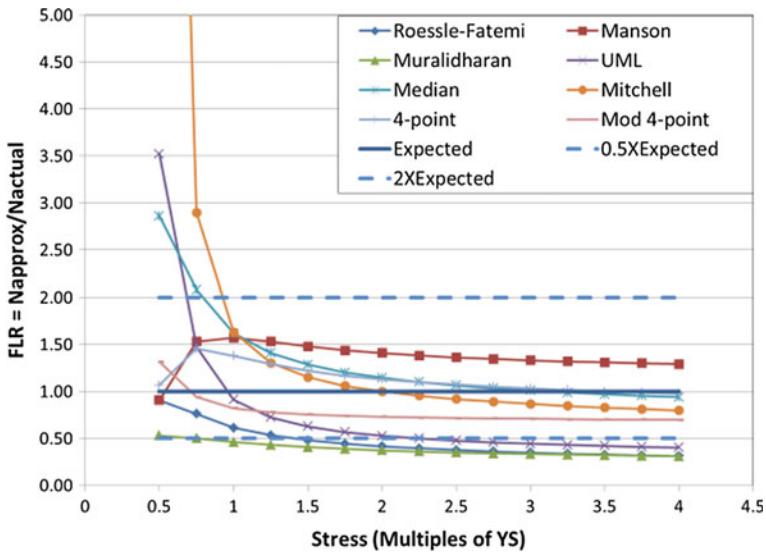


Fig. 15.7 Predictions for SAE 4340

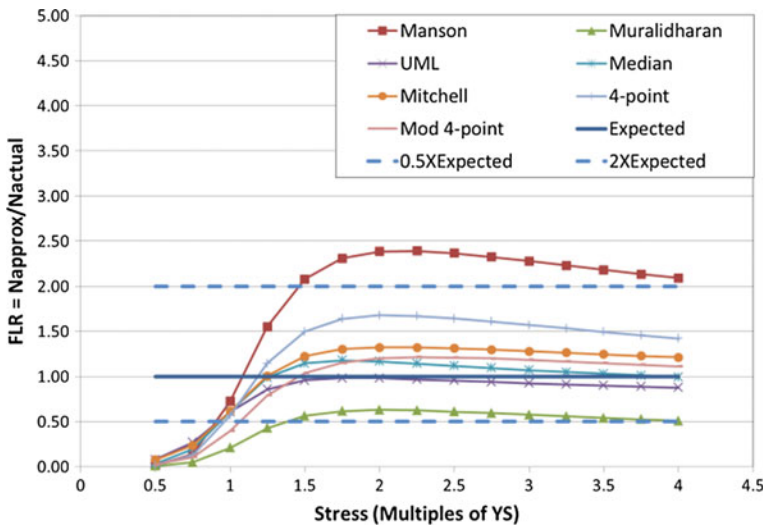


Fig. 15.8 Predictions for Al 7075-T6

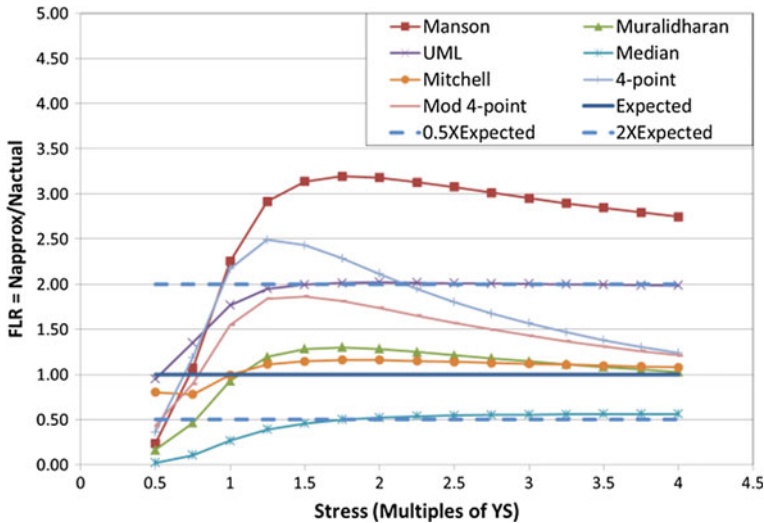


Fig. 15.9 Predictions for Ti-6Al-4 V

Best results are obtained using UML, followed by medians and Mitchell’s method. Muralidharan’s method predicts a very conservative fatigue life.

15.4.1.5 ASM Ti-6Al-4 V (Sut-845 MPa)

Figure 15.9 shows the results for Ti-6Al-4 V titanium alloy.

For this Ti alloy, it can be seen that most of the methods, except Manson’s universal slopes method, predict life within 0.5X to 2X. Again since slopes b and c were derived originally considering steel material, it is no surprise that this method has limitations when applied to materials other than steel. Again, for stresses below YS, some methods fail and highly under-predict fatigue life. Best results are obtained using Mitchell’s method followed by Muralidharan’s method. Medians method is highly conservative for this alloy. Other methods over-predict the fatigue life for this material.

15.5 Summary

Based on the results presented so far, it is clear that different approximation methods work well for different grade of materials. In fact, some of the methods like the universal slopes method (Manson), which were originally proposed to encompass all the materials, work for some materials (steel), but fail for other materials (aluminum and titanium). However, grossly some methods might work well for certain class of

materials like steel. To do this gross comparison of different materials in the same class, statistical techniques as explained in the next section will be used. The methods will be compared on the level of accuracy and the amount of scatter/spread in the FLR data points.

It can also be inferred that based on the level of stresses, the predictions using a particular approximation method might be on a conservative side or non-conservative side. An engineer would prefer to predict fatigue life on the conservative side, to be on safe, hence some statistical measure on conservativeness has to be devised. In the next section, such a measure is proposed and will be used as one of the major criteria for differentiating various approximation methods.

Also, it has been observed that the predictions tend to fail for stresses below YS , more so for stresses below $0.75YS$. This is an important learning and the user has to use these methods with caution for stresses below yield. The authors could think of only two plausible explanations for this:

1. Higher scatter in fatigue life in HCF domain (Stresses below YS)
2. All the approximations are derived to capture the entire range of fatigue predictions (LCF + HCF) and may not be very accurate in HCF alone. For instance, for steels Eq. (15.8a) predicts endurance limit to be 0.42 times S_u ; whereas, literature suggest endurance limit to be 0.5 times S_u .

Finally, it can be added that there are some grades of material on which all or most of these methods might fail badly. Figures 15.10 and 15.11 show the results for 8630 cast steel and 52100 bearing steel. The reason for such a huge error in predicting strain life properties for such steels is related to low ductility of these materials under cyclic loading. This low ductility can be gauged by the value of ϵ'_f for these materials as shown in Table 15.1. It can be seen that ϵ'_f values for these steels is very low in comparison to other steels discussed above.

When we plot strain life curves for all materials in Table 15.2, we obtain Fig. 15.12. It can be seen that the two materials, 8630 and 52100, have very low LCF life owing to the low value of ϵ'_f for these materials and hence these materials show a higher discrepancy in predicted life numbers. Hence, all the approximation methods need to be used with caution whenever ϵ'_f values are low (below ~ 0.25). The authors had a similar experience with aluminum and titanium alloys having low ϵ'_f values.

15.5.1 Error Estimation (for Quantitative Results)

The approach discussed above for different approximation approaches is a visual approach and is qualitative in nature. A robust quantitative approach is necessary as the number of materials under study is large; hence, a statistical approach for comparison of these material approximation methods has been discussed below. A brief discussion of statistical parameters used for comparison is discussed henceforth. The statistical analysis takes into account all the material iterations and material types as stated earlier in the study.

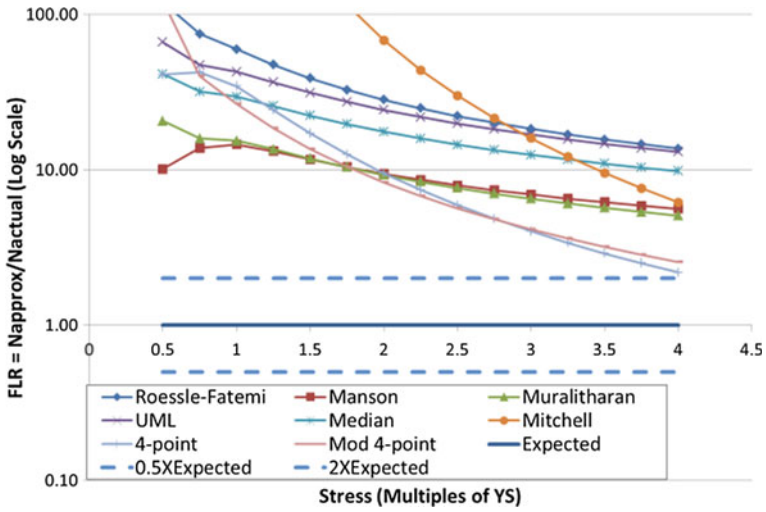


Fig. 15.10 Predictions for 8630 cast steels

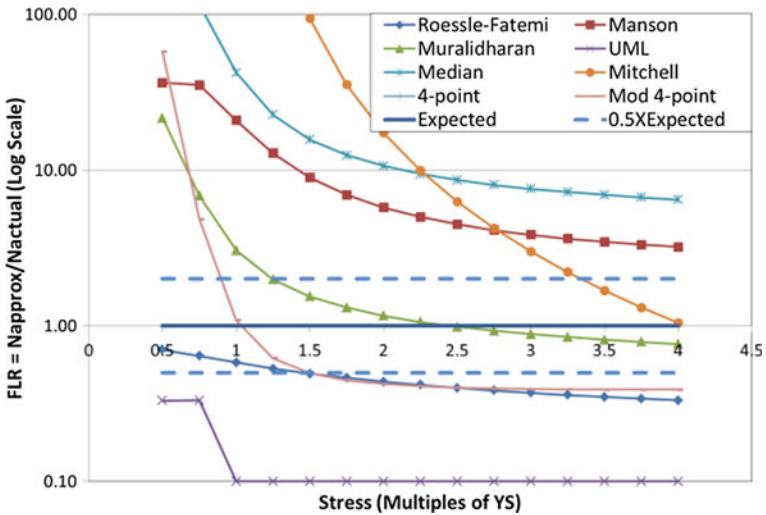


Fig. 15.11 Predictions for 52100 bearing steels

Table 15.2 Strain life properties for various steels

Parameter	1015	15B27	4340	8630	52100
E	207,000	203,000	200,000	199,000	207,000
Y_s	228	854	1371	709	1922
σ'_f	884	1062	1879	1049	2709
b	-0.124	-0.059	-0.0859	-0.11	-0.096
ϵ'_f	0.729	1.575	0.64	0.2	0.243
c	-0.581	-0.782	-0.636	-0.86	-0.642
K'	945	1026	1996	961	3348
n'	0.213	0.075	0.135	0.08	0.15
S_{ut}	414	916	1468	785	2912

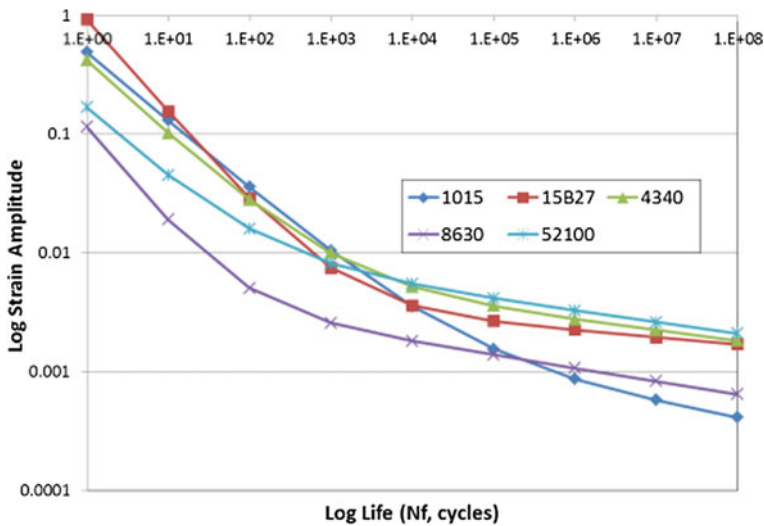


Fig. 15.12 Strain life curves for various steels

Fatigue Life Ratio (FLR): FLR is defined as the ratio of N_{approx} (using material approximation method) to N_{actual} (using actual strain life parameters). An $FLR = 1$ indicates that the predicted fatigue life using material approximation matches with the actual fatigue life.

The percentage in Band is defined as the percentage of FLR values lying within a band of $1/3X$ to $3X$. Since fatigue life is highly sensitive to various input parameters, a wider band of $1/3X$ to $3X$ is acceptable. More the number of points within the band, better is the fatigue prediction using a given approximation method.

Accuracy Level: Accuracy level is defined as the average value of all the FLR values considering all the materials in a given class and all the stress levels. An

accuracy level value close to 1 is desirable as it would indicate that on an average, the values calculated by a given approximation approach are close to the actual fatigue life calculated using tested material properties. A few materials that were studied had an accuracy level exceeding 5, using any approximation method. These materials were ignored from the final statistical analysis as they were considered outliers and would have affected the accuracy level value significantly. Reasons for these values being so high is briefly discussed later in the paper and can be considered a separate topic for future studies.

Root mean square value (RMS Value) is used to quantify the precision of a given approximation method. Average obtained from the FLR for all stress level of a given material are squared and all the squared values of a method are used to obtain mean which is then rooted to obtain the RMS. Lesser the scatter, closer would be the value to 1.

Conservatism: states statistically how many points are estimated below the average value of 1. The distribution of FLR values for a given method for different materials does not have a normal distribution. Hence, all the FLR values are for a given method, and given material are transformed such that they follow a normal distribution. The standard deviation and average from transformation have been used for calculating the area under the bell curve for values below 1. Higher the conservatism (close to 1), better would be the estimation given other conditions/parameters is also satisfactory.

All these statistical measures are used to quantitatively compare different material approximation methods.

15.5.2 Quantitative Results

Tables 15.3, 15.4, 15.5 and 15.6 shows the results for steels from ASM, steels from SAE, aluminum from ASM and titanium from ASM database, respectively, using the above-mentioned error estimates. In each of these tables, different material approximations are compared on the basis of four parameters, namely, percentage in band, accuracy level, conservatism and RMS value, as explained in the previous section.

The acceptable levels of these four parameters are set such that we get top two–three methods for each material database. An approximation method having all the four parameters in the acceptable range can be considered as best for a given material database. It was found that by having the following acceptable values for the four parameters, we get a minimum of two–three methods having all the four parameters in the acceptable range:

- Percentage in band > 0.7 (70% FLR values lying within band of 1/3X to 3X)
- Accuracy level to lie between 0.70 and 1.3 (The accuracy level should be such that an error of 30% on the conservative side and an error of 30% on the non-conservative side is acceptable)
- Conservatism should be a minimum of 50%, meaning that more than 50% of the FLR values should be on the conservative side

Table 15.3 Material approximation methods for ASM steels

Steels ASM					
Methods	% in band	Accuracy level	RMS	Conservatism	Preference
Roessle-Fatemi model for steel	0.75	1.27	1.80	0.56	2
Method of universal slopes (Manson)	0.73	2.66	5.00	0.35	
Method of universal slopes (Muralidharan)	0.70	1.09	1.83	0.70	1
Baumel & Seeger's model for steel	0.66	1.58	2.94	0.58	
Median's method for steel	0.66	3.00	8.83	0.51	
Mitchell's method for steel	0.64	5.40	12.73	0.15	
Original four point correction method	0.74	2.26	3.17	0.29	
Modified four point correction method	0.80	1.81	2.26	0.40	

- RMS value should be below 2 indicating a scatter below 2.

All the values within these acceptable ranges are highlighted in the tables.

Referring to Table 15.3, for steel from ASM database, it is clear that Roessle-Fatemi method, Manson's method Muralidharan's method, Original and modified four-point methods have more than 70% FLR values within 1/3X to 3X prediction accuracy. However, considering accuracy levels, only Roessle-Fatemi method and Muralidharan's method meet the criteria discussed earlier. Moreover, these two methods also satisfy the criteria for conservatism and RMS value, Muralidharan's method being more conservative than Roessle-Fatemi method. Both the methods have the same scatter (precision) as evident by similar RMS values. Considering the higher level of accuracy of Muralidharan's method (accuracy level close to 1) and higher conservatism (70% FLR values on the conservative side), this method is preferred over Roessle-Fatemi method for steels. However, if ε_f value is not available, as required for this method, Roessle-Fatemi method can be a good alternative. It should be noted that UML which is widely used in fatigue software's as the default method, though satisfies the conservatism criterion, does not meet the other criteria on accuracy, percentage in band and RMS value. For steels, there is a good correlation between hardness and ultimate strength and hence, Roessle-Fatemi method which

Table 15.4 Material approximation methods for SAE steels

Steels SAE J1099					
Methods	% in band	Accuracy level	RMS	Convservatism	Preference
Roessle-Fatemi model for steel	0.79	1.00	1.34	0.65	2
Method of universal slopes (Manson)	0.70	2.82	3.92	0.27	
Method of universal slopes (Muralidharan)	0.82	0.82	0.97	0.72	1
Baumel & Seeger's model for steel	0.76	0.91	1.04	0.57	3
Median's method for steel	0.71	2.83	4.97	0.42	
Mitchell's method for steel	0.63	4.21	7.92	0.04	
Original four point correction method	0.73	2.09	2.55	0.25	
Modified four point correction method	0.84	1.51	1.72	0.31	

Table 15.5 Material approximation methods for ASM aluminum

Aluminum ASM					
Methods	% in band	Accuracy level	RMS	Convservatism	Preference
Method of universal slopes (Manson)	0.67	2.18	2.54	0.16	
Method of universal slopes (Muralidharan)	0.73	1.21	1.53	0.53	
Baumel & Seeger's model for AL	0.83	1.09	1.27	0.55	1
Median's method for AL	0.84	1.14	1.35	0.53	
Mitchell's method for AL	0.73	2.04	2.92	0.31	
Original four point correction method	0.65	2.20	2.47	0.20	
Modified four points method	0.72	2.22	2.79	0.26	

Table 15.6 Material approximation methods for ASM titanium

Titanium ASM					
Methods	% in band	Accuracy level	RMS	Conservatism	Preference
Method of universal slopes (Manson)	0.84	1.59	1.80	0.29	
Method of universal slopes (Muralidharan)	0.32	0.46	0.67	0.91	
Baumel & Seeger's model for Ti	0.61	0.83	1.08	0.71	2
Median's method for Ti	0.64	0.64	1.65	0.58	
Mitchell's method for Ti	0.86	1.16	0.84	0.79	1
Original four point correction method	0.89	1.25	1.50	0.47	
Modified four points method	0.79	1.12	1.68	0.62	

requires BHN numbers is preferred over UML which requires ultimate strength as input.

Referring to Table 15.4 for SAE steels, similar conclusions can be derived. Muralidharan's method, Roessle-Fatemi method and UML meet all the criteria. Muralidharan's method is labeled as the first preference, owing to its higher conservatism and more FLR values in the band than all the methods. The second preferred method is Roessle-Fatemi method. It is preferred over UML due to its better conservatism and more number of FLR values in the band.

Thus for steels, it is clear that Muralidharan's method works well compared to all other methods. However, whenever tensile ductility is not known, Roessle-Fatemi method can be used as the second alternative. Especially when tensile properties cannot be derived, such as when manufacturing process alters the material strength (like stamping), Roessle-Fatemi method can be easily applied just by measuring the hardness and using BHN for approximations.

Considering Table 15.5 for aluminum alloys, it can be seen that UML, medians method and Muralidharan's method yield good results for these alloys. It should be noted that Muralidharan's method is very generic and is proposed to be applicable to all materials. It does not have different relations/constants for aluminum v/s steel material. Even with this limitation, the good result with this method is promising. However, the best results for aluminum are obtained using UML, followed by medians method—both of treat aluminum and titanium alloys differently than steel (refer Table 15.1). UML has marginally better accuracy, conservatism and less scatter com-

pared to medians method. Since the same material constant is required by both the methods (σ_u), UML is recommended for use for aluminum alloys.

Considering Table 15.6 for titanium alloys, it can be seen that Mitchell's method and modified four-point method yield good results for these alloys. Both these methods require the same material constants (σ_u, ε_f) for approximation. Mitchell's method is preferred owing to more number of FLR values in the band, higher conservatism and less scatter (RMS Value). For titanium alloys, there are other methods which are also promising, however, they do not meet the criteria on one of the four parameters. For instance, UML has good conservatism, less scatter and descent accuracy but does not meet the criteria on 'Percentage in Band.' Muralidharan's method applied to this material yield highly conservative results with more than 90% FLR values yielding conservative fatigue results. However, only 32% FLR values fall within 1/3X to 3X accuracy level, indicating that the method is overly conservative for these alloys. Whenever data on ε_f is not available, UML can be used as an alternative for Mitchell's method for titanium alloys.

In summary, Muralidharan's method for steels, UML for aluminum and Mitchell's method for titanium alloys are preferred methods. In the absence of ε_f data, Roessle-Fatemi method for steel and UML for titanium alloys can be used as an alternative.

15.6 Conclusions

In the present paper, the authors have compared various material approximation methods for fatigue life prediction for steel, aluminum and titanium. For the first time, we have done this comparison on a stress scale (and not strain scale as done by earlier literature). The Neuber correction method has been used for conversion from strain to stress scale. Also, the material approximation methods have been compared on four statistical parameters, namely, average FLR values in the band, accuracy (accuracy level), conservatism and scatter (RMS value). Since fatigue life estimates will always have some scatter, conservatism parameter was included as one of the basic criteria for selecting one method over the other.

Based on the outcomes of this study, the following conclusions can be derived:

1. For steels, Muralidharan's method yields the best results compared to other methods. In case, ε_f value is not available, the Roessle-Fatemi method can be used for approximation. Since this method relies on hardness alone (apart from E), it can be also used when tensile testing is not feasible as in the case of stamped components.
2. For aluminum alloys, UML yields the best results. This method just requires the ultimate strength of the material for predictions.
3. For titanium alloys, Mitchell's method is recommended for material approximation. Again, if ε_f value is not available, UML can be used as a second preferred method for titanium alloys.

4. Material approximation methods sometimes yield erroneous results for stresses below the yield stress of materials.
5. These approximation methods might yield very inaccurate results for some materials, especially for materials with a low value of ϵ'_f (below 0.2 for steels). This aspect of material approximation methods can be studied further to derive more quantitative and meaningful conclusions.
6. Even for Stresses up to $4*YS$, strain-based fatigue life prediction using material approximation methods and Neuber correction/Massing's hypotheses yields reasonable results.

Finally, it becomes imperative to mention that these material approximation methods should only be used in the initial phases of design and these cannot replace the actual material testing once the design is finalized.

Acknowledgements The authors like to thank EATON Corporation and Modeling & Simulation CoE Leadership team for providing the motivation and required support to perform the studies documented in present work. Special thanks to Steve McCutcheon and Dale Doddington who provided the technical guidance for the work.

References

1. Stephens, R.I., Fatemi, A., Stephens Robert, R. Fuchs, H.O.: Metal Fatigue in Engineering, second edn., p. 69. Wiley (2001). ISBN 0-471-51059-9
2. Ramberg, W., Osgood, W.R.: Description of Stress-Strain Curves by Three Parameters. National Advisory Committee for Aeronautics, Washington DC (1943)
3. Manson, S.S.: Fatigue: a complex subject—some simple approximations. *Exp. Mech.* SESA 5(7), 193–226 (1965)
4. Socie, D.F., Mitchell, M.R., Caulfield, E.M.: Fundamentals of Modern Fatigue Analysis—FCP Report. University of Illinois, Urbana (1977)
5. Muralidharan, U., Manson, S.S.: A modified universal slopes equation for estimation of fatigue characteristics of metals. *J. Eng. Mater. Technol.* **110**, 55–58 (1988)
6. Bäuml, A., Seeger, T.: Materials Data for Cyclic Loading—Supplement 1. Elsevier, Amsterdam (1990)
7. Ong, J.H.: An improved technique for the prediction of axial fatigue life from tensile data. *Int. J. Fatigue* **15**, 213–219 (1993)
8. Roessle, M.L., Fatemi, A.: Strain-controlled fatigue properties of steels and some simple approximations. *Int. J. Fatigue* **22**, 495–511 (2000)
9. Park, J.H., Song, J.H.: New estimation method of fatigue properties of aluminum alloys. *Trans. ASME* **125**, 208–214 (2003)
10. Meggiolaro, M.A., Castro, J.T.P.: Statistical evaluation of strain-life fatigue crack initiation predictions. *Int. J. Fatigue* **26**, 463–476 (2004)
11. nCode—DesignLife Theory Guide
12. fe-safe6—User Manual
13. Lee, K.S., Song, J.H.: Estimation methods for strain life fatigue properties from hardness. *Int. J. Fatigue* **28**, 386–400 (2006)
14. Park, J.H., Song, J.H.: Detailed evaluation of methods for estimation of fatigue properties. *Int. J. Fatigue* **17**(5), 365–373 (1995)
15. Basan, R., Franulović, M., Prebil, I., Črnjarić-Žic, N.: Analysis of strain-life fatigue parameters and behaviour of different groups of metallic materials. *Int. J. Fatigue* **33**, 484–491 (2011)

16. Neuber, H.: Theory of stress concentration for shear-strained prismatical bodies with arbitrary nonlinear stress-strain law. *J. Appl. Mech.* **28**(4), 544–550 (1961)
17. Massing, G.: Proceedings of 2nd International Congress for Applied Mechanics, Zurich (1926)
18. ASM International Handbook Committee: ASM Handbook, Volume 19—Fatigue and Fracture. ASM International, Section 8 (1996)
19. SAE J1099—Technical Report on Low Cycle Fatigue Properties Ferrous and Non-ferrous Materials: A novel approach to the estimation of strain life fatigue parameters (2002)

Chapter 16

Recurrence Perspective of Forces Generated by Flapping Wing Under Different Frontal Inflow Conditions



M. De Manabendra, J. S. Mathur and S. Vengadesan

Abstract Qualitative and quantitative recurrence paradigms have been frequently used to study the stability of dynamic systems. In the present work, Global Recurrence Plots (GRPs) and Windowed Recurrence Quantification Analysis (WRQA) were employed to analyse the force patterns of a flapping wing in 3D reference frame for $Re = 150$. The wing followed a canonical form of asymmetric 1DoF flapping. Force patterns were numerically estimated for four different frontal inflow conditions viz. uniform inflow profile, shear inflow profile, temporally oscillating uniform inflow profile and spatiotemporally varying inflow profile. User-defined functions (UDFs) were developed to specify these frontal inflow conditions. The flapping kinematics of wing was simulated by dynamic meshing technique and UDFs. 3D unsteady Navier–Stokes equations were solved using finite volume formulation, assuming incompressible and laminar flow. Mass and momentum equations were solved in a fixed inertial reference frame by the Arbitrary Lagrangian–Eulerian (ALE) formulation. Spatial discretization was second-order upwind and temporal discretization was second-order implicit. PISO scheme was used for pressure–velocity coupling. The finite volume formulation based commercial CFD code ANSYS Fluent was used. Force patterns were qualitatively evaluated using GRPs and quantitatively by evaluating the WRQA of eight parameters viz. recurrence rate (RR), determinism (DET), laminarity (LAM), trapping time (TT), ratio (RATIO), entropy (ENTR), maximum line (L_{max}) and trend (TREND). From these recurrence studies, it was observed that shear inflow condition influenced the forces and moment pattern more than the other primary inflow conditions for the chosen wing kinematics.

M. De Manabendra (✉)

CSIR-National Aerospace Laboratories, CSMST, Bengaluru, India
e-mail: manav@nal.res.in

J. S. Mathur

CSIR-National Aerospace Laboratories, CTFD, Bengaluru, India
e-mail: mathur@nal.res.in

S. Vengadesan

Department of Applied Mechanics, Indian Institute of Technology Madras, Chennai, India
e-mail: vengades@iitm.ac.in

© Springer Nature Singapore Pte Ltd. 2020

C. Li et al. (eds.), *Advances in Engineering Design and Simulation*,
Lecture Notes on Multidisciplinary Industrial Engineering,
https://doi.org/10.1007/978-981-13-8468-4_16

Keywords 1DoF asymmetric flapping · Frontal inflow · Gust · Global recurrence plot · Windowed recurrence quantification analysis

Nomenclature

c	Wing chord length, m
f_g	Gust frequency, Hz
f_w	Wing flapping frequency, Hz
l	Diagonal line
l_{\min}	Minimum threshold diagonal line
m	Dimensional phase space trajectory
t	Time, sec
v	Length of vertical structures in recurrence plot
v_{\min}	Minimum threshold vertical line
\vec{u}	Flow velocity, m/s
\vec{u}_g	Velocity of the moving mesh, m/s
C_H	Coefficient of horizontal force
C_M	Coefficient of moment
C_V	Coefficient of vertical force
L_{\max}	Maximum diagonal structure of the recurrence plot
N	Length of data series
$P^\varepsilon(l)$	Frequency distribution of the diagonal lengths l
$P^\varepsilon(v)$	Frequency distribution of vertical length, v
$R_{i,j}^{m,\varepsilon}$	Recurrence matrix of an m -dimensional phase space trajectory and a neighbourhoods radius ε
Re	Reynolds number
S_ϕ	Source term
T	Period of flapping, sec
T_g	Period of gust, sec
U_g	Gust amplitude, m/s
U_w	Root mean square average flapping velocity at the tip of the wing, m/s
U_G	Gust velocity, m/s
U_∞	Mean free stream velocity, m/s
V	Arbitrary control volume

Greek symbols

Υ	Elliptical flow domain around the wing
ε	Threshold distance
ϕ	Any scalar quantity
ρ	Fluid density, kg/m ³
Γ	Diffusion coefficient

16.1 Introduction

Flapping wing micro, nano and pico aerial vehicles (MAVs/NAVs/PAVs) are popular areas of research, both in academic and industrial circles, across the globe. Various aspects like the aerodynamics of flapping wing under different modes of flight (hover, ascending, descending, forward flight and manoeuvres), flow physics of single and tandem wings with different wing-to-wing positions and kinematics, aero-elastic studies of flexible flapping wings and corrugated wings have been extensively studied by researchers. Ground effects on the forces generated by the flapping wings and swarm dynamics have also been deliberated. MAVs, NAVs and PAVs have good manoeuvrability and stealth characteristics. However, due to less mass (0.5–20 g) and small size (50–150 mm), they are sensitive to the frontal inflow profile. Hence, a thorough appreciation of the aerodynamics of flapping wings subjected to various frontal inflow conditions is imperative.

Earlier attempt to explain the effect of the gusty frontal inflow on stationary and plunging airfoil for chord-based $Re = 2 \times 10^4$ in 2D was numerically made by Lian and Shyy [1]. Wan and Huang [2] carried out a 2D numerical simulation of flapping wings under gust wind condition using ANSYS Fluent. Lian [3] studied the aerodynamics of flapping airfoil in various gusty inflow conditions using a novel algebraic moving grid technique to handle the dynamic airfoil motion. Viswanath and Tafti [4] assessed the effect of a frontal gust on a forward flapping flight of rigid wing in a 3D reference frame using an in-house LES code with sub-grid stress model. Prater and Lian [5] numerically investigated the 2D flight characteristics of stationary and flapping single and tandem wing configuration, under sinusoidal velocity inflow condition. Sarkar et al. [6] studied the effect of zero mean gusts on pure and sinusoidal hovering flight in the 2D reference frame. Zhu et al. [7] numerically studied the flow physics in the vicinity of a variable camber plunge airfoil under temporally varying inflow conditions in the 2D reference frame. Jones and Yamaleev [8] studied the effect of lateral, downward and frontal oscillatory inflow profile on force generation pattern of the horizontally flapping wing in the 3D reference frame. Zhan et al. [9] numerically investigated of a semi-activated flapping foil in unsteady inflow from the point of view of power extraction application using ANSYS Fluent in 2D reference frame.

While few of these efforts focused on studying either thrust or lift patterns, other attempts confined kinematics to symmetric flapping. Majority of these studies considered only temporally varying gusty inflow profiles with zero mean velocity. In the light of these literature, the present study aimed at investigating forces generated by asymmetrically flapping wings with semi-elliptical wing planform under different frontal inflow conditions with non-zero mean velocity. The findings were analysed using qualitative and quantitative recurrence paradigms viz. global recurrence plots and windowed recurrence quantification analysis, respectively.

16.2 Numerical Formulations, Wing Kinematics and Domain Details

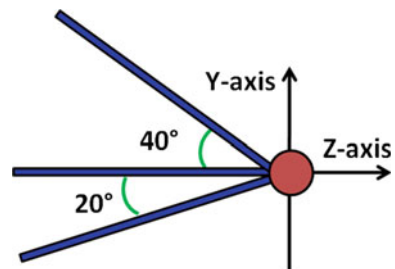
Three-dimensional unsteady Navier–Stokes equations were solved using the finite volume formulation approach by assuming incompressible and laminar flow for simulation $Re = 150$. Mass and momentum equations were solved in a fixed inertial reference frame by the formulation proposed by Ferziger and Peric [10]. The generic integral form of the conservation equation for a scalar quantity ϕ in an arbitrary control volume, V , with moving boundaries inside it is shown in Eq. (16.1).

$$\frac{d}{dt} \int_V \rho \phi dV + \int_{\partial V} \rho \phi (\vec{u} - \vec{u}_g) \cdot d\vec{A} = \int_{\partial V} \Gamma \Delta \phi \cdot d\vec{A} + \int_V S_\phi dV \quad (16.1)$$

Here ρ is the fluid density, \vec{u} is the flow velocity vector, \vec{u}_g is the mesh velocity of the moving mesh, Γ is the diffusion coefficient and S_ϕ is the source term of ϕ .

Spatial discretization was second-order upwind and temporal discretization was second-order implicit. PISO scheme, proposed by Issa [11], was used for pressure–velocity coupling. The convergence of the iterative method was considered to be satisfied when mass and momentum residues decreased below $O(10^{-6})$ in magnitude. The finite volume formulation-based commercial CFD code ANSYS Fluent was used to solve the 3D time-dependent unsteady Reynolds averaged Navier–Stokes equations. Asymmetric wing kinematics, when viewed from upstream (face ABCE), is shown in Fig. 16.1. Domain details and boundary conditions are shown in Fig. 16.2. The wing was bounded by a non-deforming spherical flow domain. This domain moved with the wing. The non-deforming domain was bounded by a cubical deforming flow domain. The finite volumes in this domain deformed and re-gridded to adjust their shapes and sizes as the wing with the non-deforming domain marched in time and moved as per the prescribed flapping kinematics. Face ABCD (in YZ plane) was attributed with velocity inlet condition. Different frontal inflow boundary conditions were specified at this face. Face EFGH (in YZ plane) was attributed with pressure outlet boundary condition. Faces ABFE (in XY plane), BCGF (in XZ plane), CGHD (in XY plane) and HEAD (in XZ plane) were attributed with symmetric boundary condition to avoid the effect of their existence on the solutions inside

Fig. 16.1 Wing kinematics (looking from downstream)



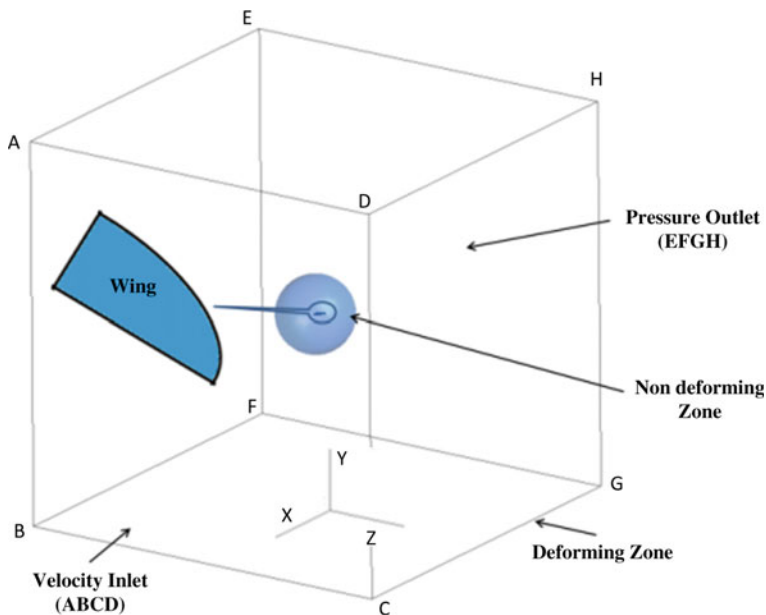


Fig. 16.2 Domain details

the domain. Wing planform was semi-elliptical in shape with an aspect ratio of 4, wing half-span of 155 mm and thickness of 0.3 mm. The flapping axis coincided with the X -axis.

16.3 Methodology

1 DoF simple flapping wing kinematics, similar to that documented by Fejtek and Nehera [12], was chosen for verification and validation studies. User-defined function (UDF) for simulating the prescribed kinematics of the wing in the 3D reference frame was developed. Domain, grid and time-step independency studies were carried out and reasonable domain size, grid resolution, and time step were derived. Validation studies were carried out for the benchmark simulation documented by Fejtek and Nehera [12]. Numerical predictions by the present methodology were found to be similar to the experimental observation. Comparison of the cycle-averaged force coefficients is shown in Table 16.1.

Subsequently, UDF for specifying a uniform inflow profile ($U_{\text{inlet}} = U_{\infty}$), shear inflow profile ($U_{\text{inlet}} = U_{\infty} + V_{\text{grad}} \cdot y$), temporally oscillating uniform inflow profile ($U_{\text{inlet}} = U_{\infty} + U_g \sin(2\pi f_g t)$) and spatiotemporally varying inflow profile ($U_{\text{inlet}} = U_{\infty} + U_g \sin(2\pi f_g t) + V_{\text{grad}} \cdot y$) were coded. Here, U_{inlet} is the inlet velocity, U_{∞} is mean free stream velocity, U_g is gust amplitude, V_{grad} is the spatial velocity

Table 16.1 Flapping cycle-averaged vertical and horizontal force coefficients

	Vertical force coefficient	Horizontal force coefficient
Fejtek and Nehera [12]	0.412	-0.02864
Present (ANSYS Fluent)	0.419	-0.02711

gradient per unit length along Y -axis, y is the spatial location along Y -axis, f_g is gust frequency in Hz and t is a time in second. The velocity terms in the gust equation were normalized by dividing them with the root mean square wingtip velocity, U_w and frequencies were non-dimensionalized by flapping frequency, f_w . For the simulation reported in this paper, the ratios of U_g to U_w and f_g to f_w were considered as 1.0 and 0.1 and spatial velocity gradient, which was represented by the ratio of V_{grad} to U_w , was considered as 10. U_∞ was chosen in a manner such that it maintained the root-chord-based Re as 150.

The findings were compared in terms of instantaneous vertical and horizontal force coefficients and aerodynamic moment about the flapping pivot, 3D phase plots of vertical and horizontal force coefficients and the aerodynamic moment about the flapping pivot, global recurrence plots and windowed recurrence quantification analysis. The latter two approaches are computationally inexpensive, as compared to the conventional approach of numerical flow visualization.

16.4 Results and Discussion

The findings of various studies are discussed in the following subsections.

16.4.1 Effect of Variations in Inflow Condition on Instantaneous Force and Moment Coefficients

Temporal variation of instantaneous force coefficients and aerodynamic moment are shown in Fig. 16.3a–c, respectively.

The temporal and spatiotemporal variations had a gust frequency element, f_g , which was an order of magnitude lower than the wing flapping frequency, f_w . 30 flapping cycles were simulated. Effect of transients during the initial stage of the simulation was observed during the first five cycles. Hence, first 10 flapping cycles were not considered while analysing the data. It was observed that variation in the force patterns between 10th and 20th flapping cycles were similar to that between 20th and 30th flapping cycle. Hence, the values of force coefficients from 10th to 30th flapping cycles were considered for computing the average values. Here, T_g is the period of gust for the present simulation and covered 10 flapping cycles. It was observed from Fig. 16.3a–c that changes in the inflow conditions affected the ver-

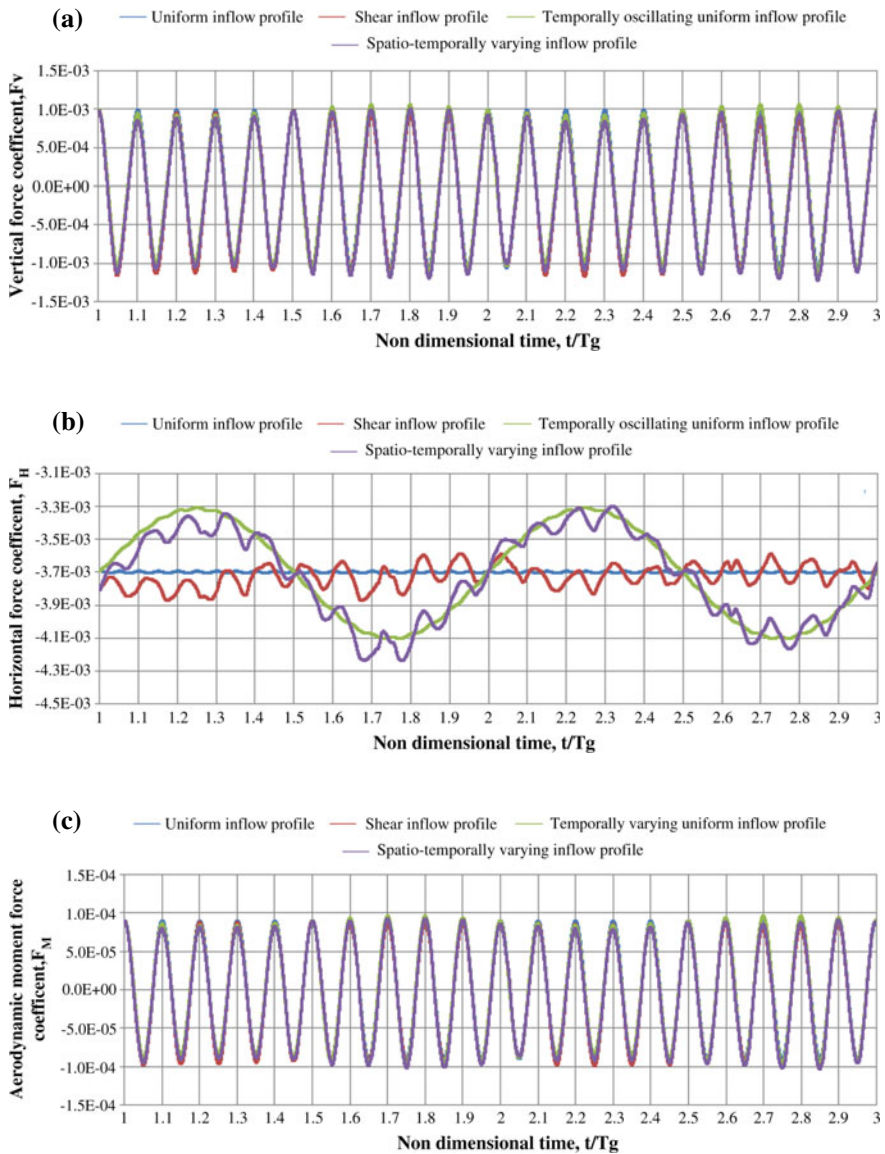


Fig. 16.3 a Temporal variation of instantaneous vertical force coefficient. b Temporal variation of instantaneous horizontal force coefficient. c Temporal variation of instantaneous aerodynamic moment coefficient

tical force coefficients and aerodynamic moments during pronation and supination. Horizontal force coefficient, on the other hand, varied throughout the 20 cycles for different inflow conditions.

16.4.2 3D Phase Plots

3D phase plots of force coefficients with aerodynamic moment about flapping pivot point for uniform inflow, shear inflow, temporally varying inflow and spatiotemporally varying inflow profile are shown in Fig. 16.4a–d. It was observed that the pattern of the phase plot was repetitive for the uniform inflow condition. This indicated that the variations in the force and moment strongly correlated with each other. As for the shear inflow condition, the patterns changed and became disorganized. For a temporally varying inflow condition, even though the patterns were relatively similar, they were not strongly correlated with each other, as in the case with a constant inflow condition. The interrelationship pattern between the forces and moment for a spatiotemporally varying inflow condition was a combination of the previous two inflow conditions.

16.4.3 Global Recurrence Plots (GRPs) [13]

GRP is an X – Y plot of the times at which a phase space trajectory visits the same area in the phase plot at a given moment in time. They describe the distances of every point $x(i)$ to all the other points $x(j)$ in the phase space diagram. The plot is represented by Eq. (16.2).

$$\text{Dist}(i, j) = \vartheta(x(i) - x(j)) \quad (16.2)$$

Here, i and $j = 1, 2, 3, \dots, N$, and $\vartheta(\cdot)$ is the colour code operator that maps the distance to a colour scale. The colour scale in the present work was varied from blue to red colour. The blue colour in the GRP indicated that the points in the phase plots were located close to each other and the red colour indicated that the points were located farther apart in the phase space plot. GRPs based on the vertical and horizontal force coefficient and aerodynamic moment generated by the flapping wing with different inflow conditions are shown in Figs. 16.5, 16.6 and 16.7. GRP patterns of the vertical force patterns and the aerodynamic moments exhibited a regular checkerboard pattern for all the inflow conditions. This indicated that their variation was periodic and homogeneous in nature. For the horizontal force coefficient based GRPs, the pattern for the shear inflow condition was different and showed uneven blurred patterns. This was an indication that the evolution of states was similar at different times but with reverse times. GRPs for temporally varying

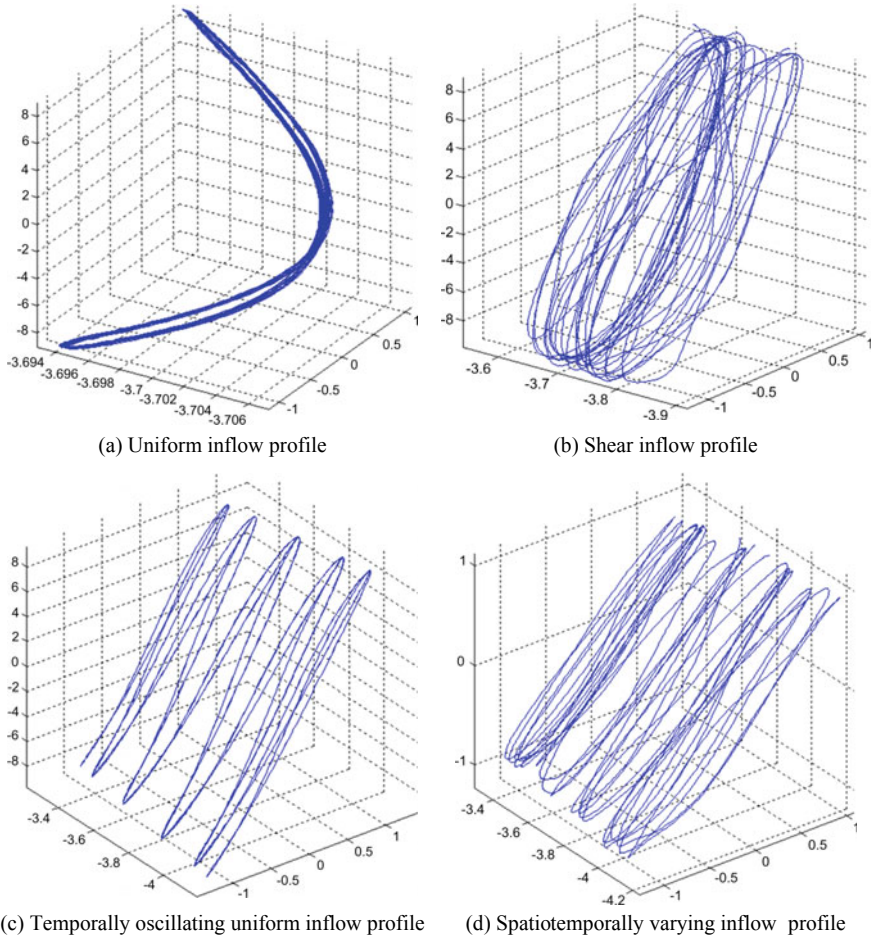


Fig. 16.4 3D phase plots of force and moment coefficients

uniform inflow conditions showed secondary checkerboard patterns apart from the primary patterns. This was due to the periodic cycle-to-cycle temporal change in the force pattern due to the presence of gust frequency, f_g .

16.4.4 *Windowed Recurrence Quantification Analysis [14, 15]*

The textures of GRPs primarily gave a qualitative insight into the behaviour of a dynamic system. However, they did not distinctly confirm the inferences in a

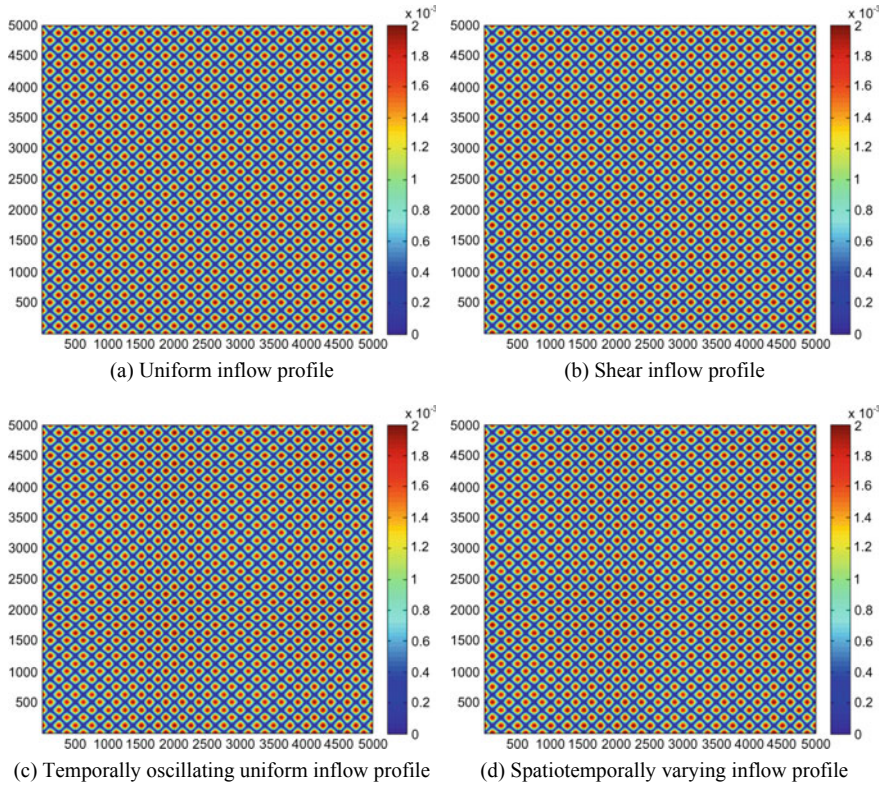


Fig. 16.5 GRPs of vertical force coefficient

quantitative manner. This subjectivity was addressed by carrying out WRQA of the predicted force and moment patterns. WRQA helped to quantitatively assess any event and precisely judge the possibility of an onset of a system’s unstable behaviour. In the present study, recurrence rate (RR), determinism (DET), laminarity (LAM), trapping time (TT), the ratio (RATIO), entropy (ENTR), maximum line (L_{MAX}) and trend (TREND) were employed. The time period of one flapping cycle was considered as one window period width. This choice was based on the reasoning that gust caused variation in the inflow conditions between two consecutive flapping cycles. It was envisaged to assess whether due to the difference in the inflow conditions, the recurrence variables exhibited uneven fluctuations. A noticeable uneven fluctuation in the recurrence variable series would indicate an onset of instability. Standard deviations of these recurrence variable series were calculated to ascertain uncertainty, i.e. the uneven fluctuation of the series. Force pattern variations between 10th and 30th flapping cycles were considered in computing the recurrence variable series. The threshold for computing the recurrence variables was chosen as five times the standard deviation to avoid the effect of noise in the signals. All variables were calculated for a

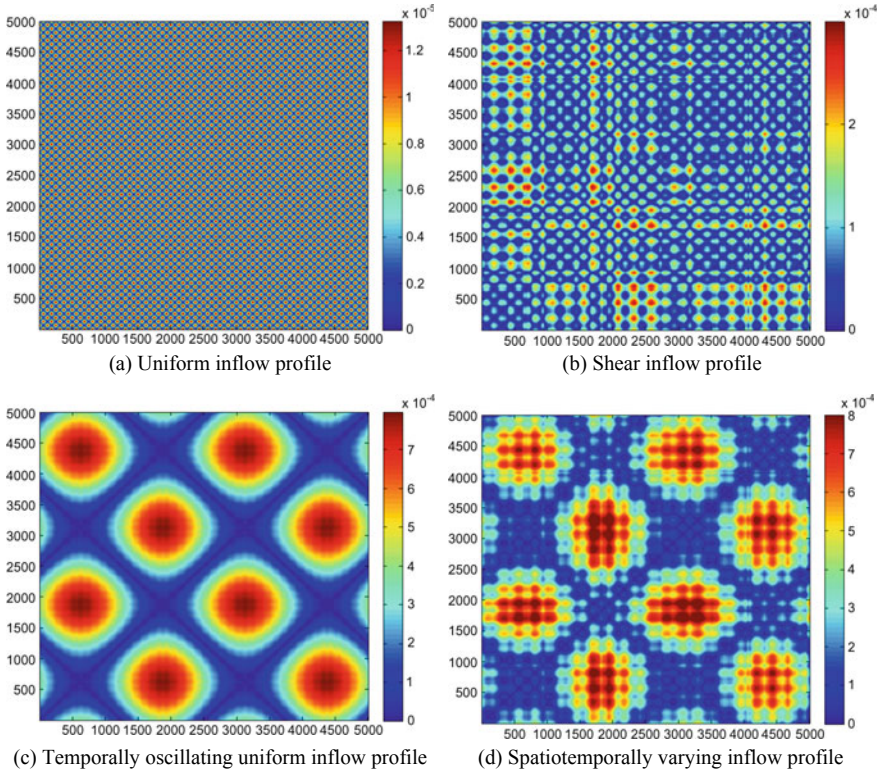


Fig. 16.6 GRPs of horizontal force coefficient

dimension of 1. Euclidean norm was used while defining the neighbourhood radius. The next portion of this section deals with the mathematical description and the computation of the eight variables used for the WRQA.

Recurrence Rate (RR) Recurrence rate is the measure of the density of recurrence points in a recurrence plot and is calculated using Eq. (16.3).

$$RR = \frac{1}{N^2} \sum_{i,j=1}^N R_{i,j}^{m,\varepsilon} \times 100 \tag{16.3}$$

Here, N is the length of the data series and $R_{i,j}^{m,\varepsilon}$ is the recurrence matrix of an m -dimensional phase space trajectory and a neighbourhood radius ε . In the present case, m was chosen as 1. RR series for force coefficients and moment coefficient are shown in Fig. 16.8a–c.

Determinism (DET) Determinism (aka predictability) is the ratio of recurrence points that form a diagonal line of length l_{\min} to all the recurrence points in a recur-

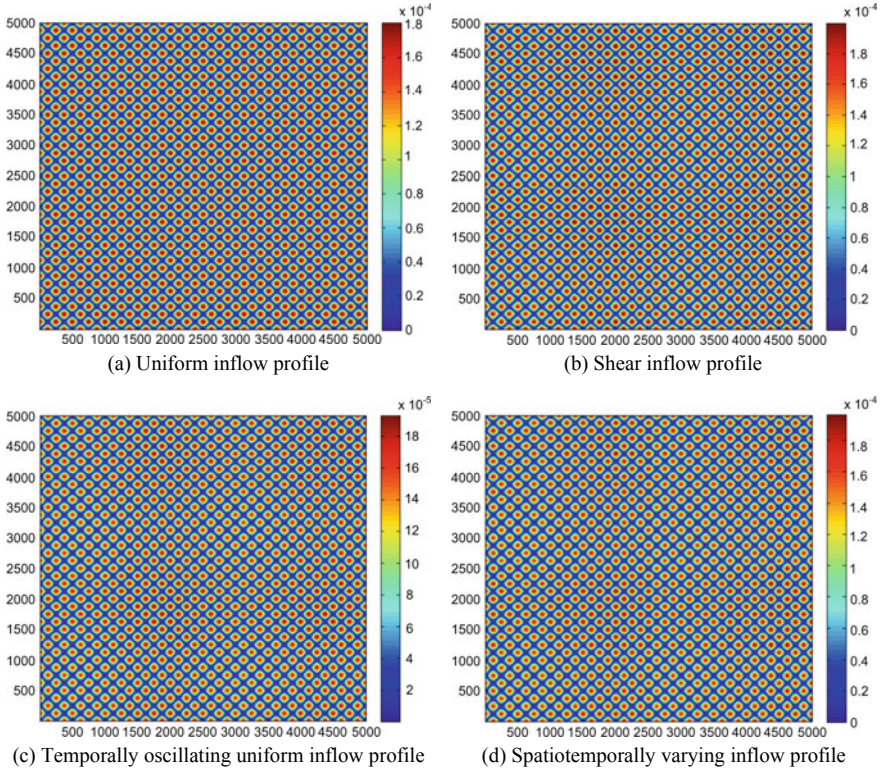


Fig. 16.7 GRPs of aerodynamic moment coefficients

rence plot. For systems with stochastic nature, DET has smaller value and for systems with periodic behaviour, DET has larger values. It is calculated using Eq. (16.4).

$$DET = \frac{\sum_{l=l_{\min}}^N \min IP^\epsilon(l)}{\sum_{i,j}^N R_{i,j}^{m,\epsilon}} \times 100 \tag{16.4}$$

Here, $P^\epsilon(l)$ is the frequency distribution of the lengths l of the diagonal structures in the recurrence plot with a neighbourhood radius ϵ and l_{\min} is the minimum threshold diagonal line. For the present studies, $l_{\min} = 2$ was considered. DET series for force coefficients and moment coefficient are shown in Fig. 16.9a–c.

Laminarity (LAM) Laminarity is the ratio of recurrence points that form a vertical line of length v_{\min} to all the recurrence points in a recurrence plot. It is the measure of the number of vertical structures in the whole recurrence plot and represents the occurrence of a laminar state in the system without describing the length of these laminar phases. LAM generally decreases if the occurrence of single recurrence

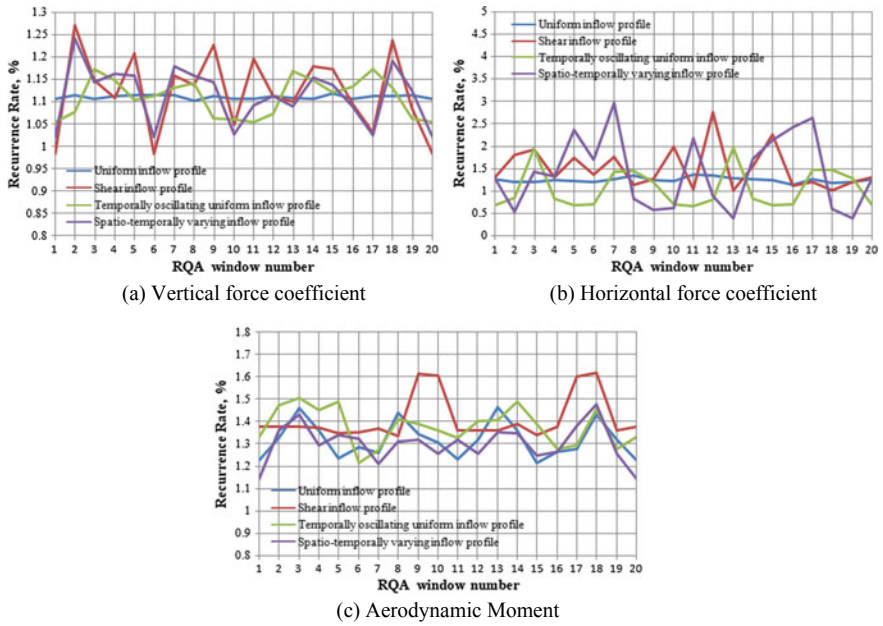


Fig. 16.8 Recurrence rate series

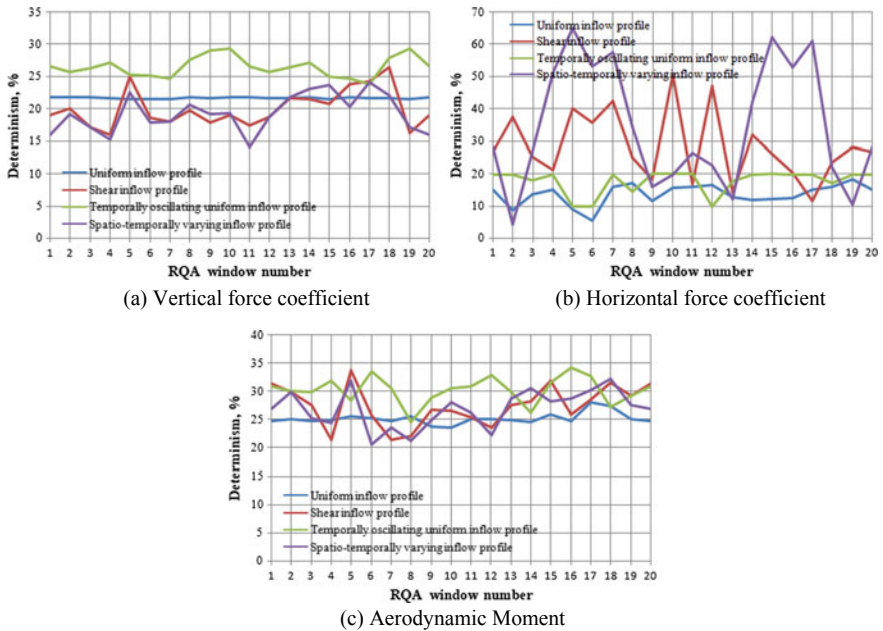


Fig. 16.9 Determinism series

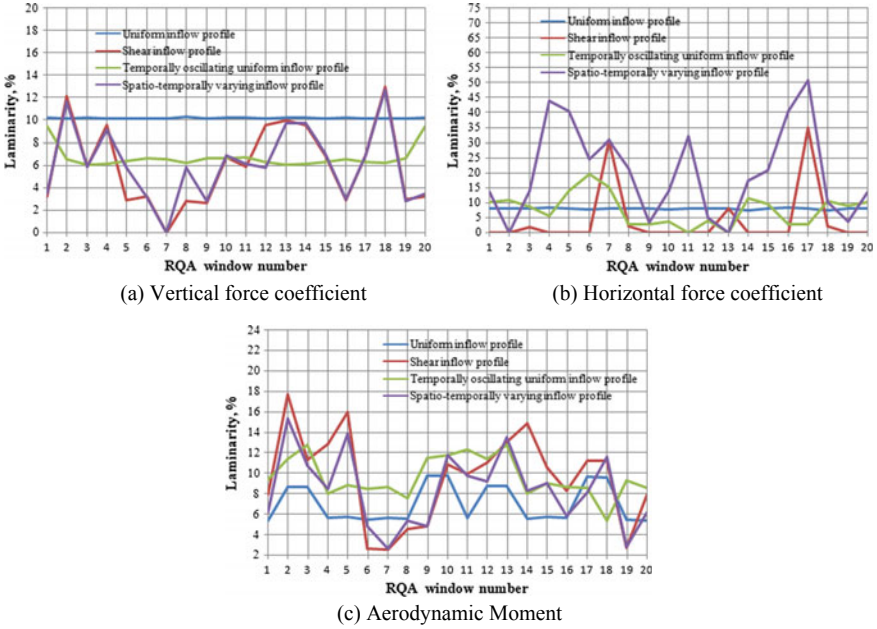


Fig. 16.10 Laminarity series

points is more than the vertical structures. Mathematical expression to compute LAM is shown in Eq. (16.5).

$$LAM = \frac{\sum_{v=v_{\min}}^N v P^\epsilon(v)}{\sum_{i,j}^N R_{i,j}^{m,\epsilon}} \times 100 \tag{16.5}$$

Here $P^\epsilon(v)$ is the frequency distribution of the lengths v of the vertical structures in the recurrence plot with a neighbourhood radius ϵ and v_{\min} is the minimum threshold vertical line. For the present studies, $v_{\min} = 2$ was considered. LAM series for force coefficients and moment coefficient are shown in Fig. 16.10a–c.

Trapping Time (TT) Trapping Time is computed from the vertical structures of the recurrence plots. It represents information about the amount and length of the vertical structures in the recurrence plots. It measures the mean time that the system will be trapped in a specific state. TT is computed using Eq. (16.6).

$$TT = \frac{\sum_{v=v_{\min}}^N v P^\epsilon(v)}{\sum_{v=v_{\min}}^N P^\epsilon(v)} \tag{16.6}$$

TT series for force coefficients and moment coefficient are shown in Fig. 16.11a–c.

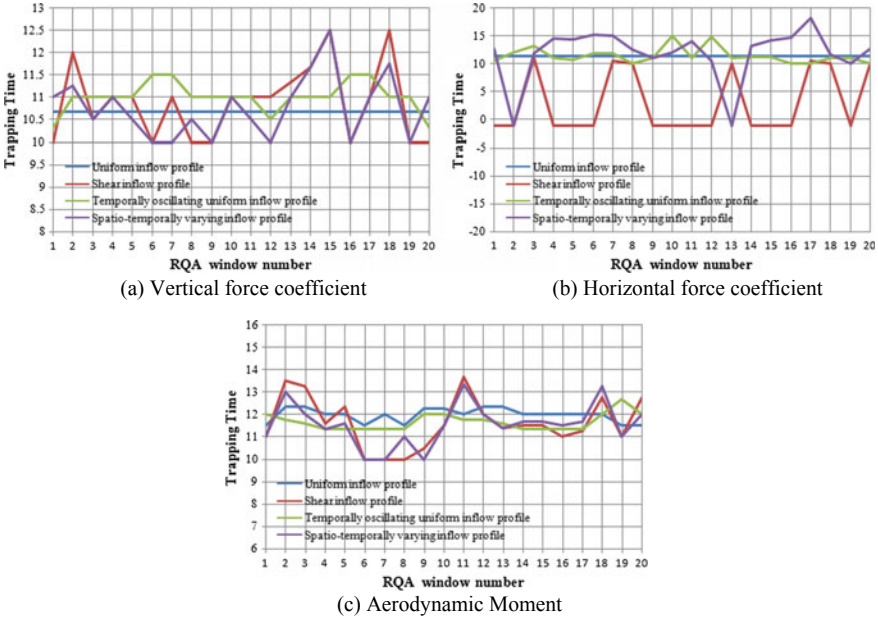


Fig. 16.11 Trapping time series

Ratio (RATIO) Ratio is defined as the ratio between DET and RR. It is used to discover transitions in the behaviour of a dynamic system subjected to the fact that during certain types of transitions, RR decrease, whereas DET does not change at the same time. RATIO is computed using Eq. (16.7).

$$RATIO = N^2 \frac{\sum_{l=l_{\min}}^N 1P^\epsilon(l)}{\left(\sum_{i,j}^N R_{i,j}^{m,\epsilon}\right)^2} \tag{16.7}$$

RATIO series for force coefficients and moment coefficient are shown in Fig. 16.12a–c.

Entropy (ENTR) Entropy refers to the Shannon entropy of the frequency distribution of diagonal line length. It reflects the complexity of the deterministic structures in a dynamic system. ENTR is calculated using Eq. (16.8).

$$ENTR = - \sum_{l=l_{\min}}^N p(l) \ln p(l); p(l) = \frac{P^\epsilon(l)}{\sum_{l=l_{\min}}^N P^\epsilon(l)}; \tag{16.8}$$

Here, $l_{\min} = 2$ was considered. ENTR series for force coefficients and moment coefficient are shown in Fig. 16.13a–c.

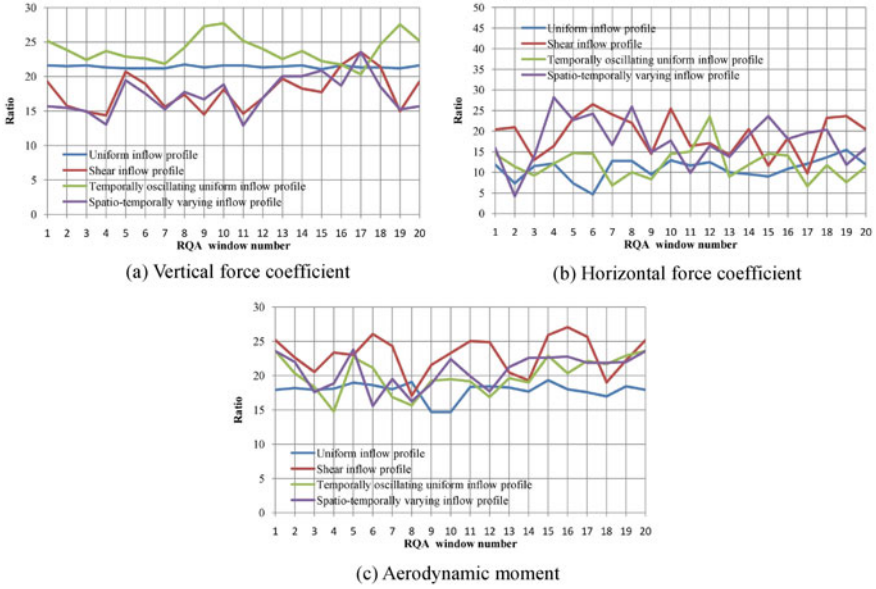


Fig. 16.12 Ratio series

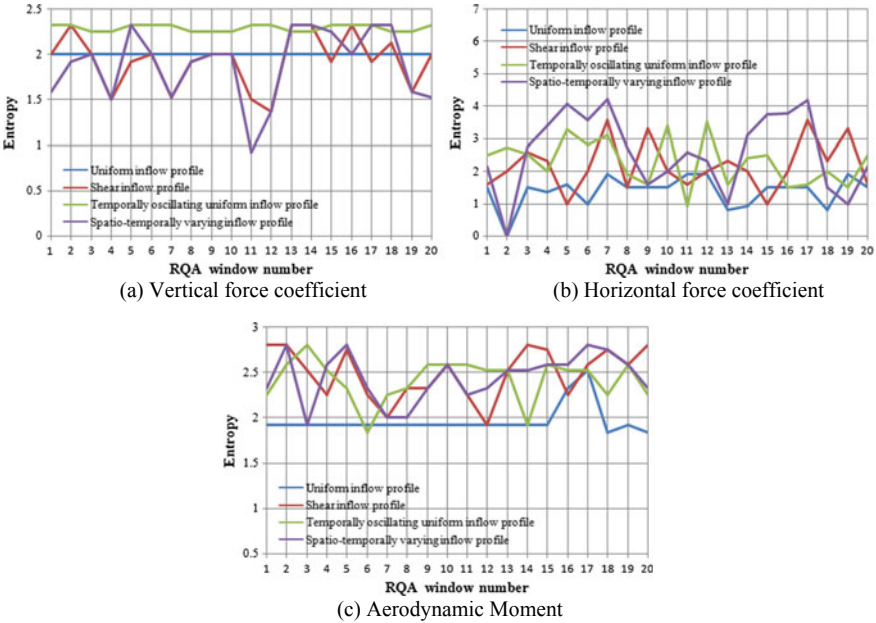


Fig. 16.13 Entropy series

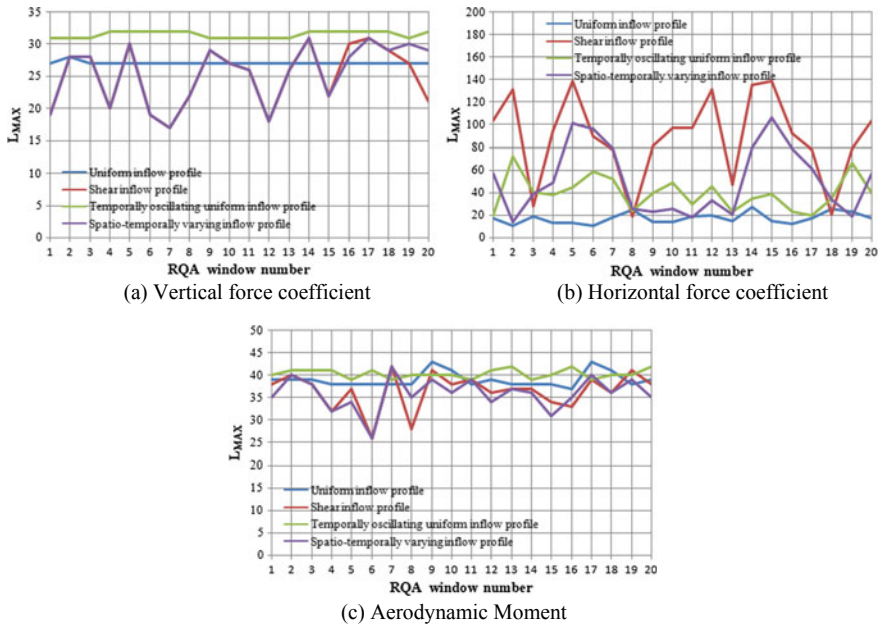


Fig. 16.14 Maximum line series

Maximum Line (L_{max}) This variable deals with the divergence of the trajectory segment. It gives information about the range in which a segment of the trajectory is close to one another at a different time. Length of the diagonal lines is related to the largest positive Lyapunov exponent and characterizes the rate of separation of the infinitesimally closed trajectories in the phase space diagram. L_{max} is computed using Eq. (16.9).

$$L_{max} = \max(\{l_i; i = 1 \dots N\}) \tag{16.9}$$

L_{max} series for force coefficients and moment coefficient are shown in Fig. 16.14a–c.

Trend (TREND) Trend is a linear regression coefficient over the recurrence point density of the diagonal lines parallel to the line of identity (LoI). It is a function of the time distance between diagonals and LoI. It gives information about the non-stationary nature in the process like a drift. It is computed using Eq. (16.10).

$$TREND = \frac{\sum_{i=1}^N \left(i - \frac{N}{2}\right) (RR_i - \langle RR_i \rangle)}{\sum_{i=1}^N \left(i - \frac{N}{2}\right)^2} \tag{16.10}$$

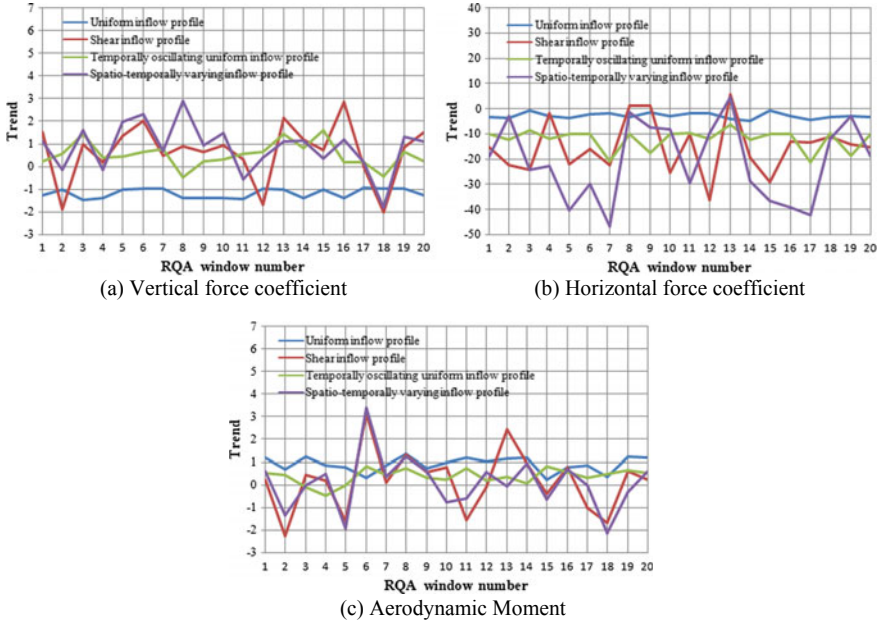


Fig. 16.15 Trend series

Here, $\langle RR_i \rangle$ is the average recurrence rate of the i th diagonal line. TREND series for force coefficients and moment coefficient are shown in Fig. 16.15a–c.

Standard deviations of all the recurrence variables series based on forces and moment coefficients were computed and are tabulated in Tables 16.2, 16.3 and 16.4.

It was observed from the collective plots (Figs. 16.8, 16.9, 16.10, 16.11, 16.12, 16.13, 16.14 and 16.15) of the WRQA series for all the eight parameters that the fluctuation of the windowed series was more for the shear inflow profile. This was prominently brought out in the tables of the standard deviation, wherein the values of the standard deviation of the WRQA parameters for the shear inflow profile were relatively higher as compared to that for the other two primary inflow profiles viz. uniform inflow and temporally oscillating uniform inflow profile. The higher values of standard deviation were indications of higher fluctuation in the force and moment patterns and thus a possible onset of instability in the behaviour of the system.

16.5 Conclusions

The findings of the numerical investigation of a semi-elliptical-shaped wing undergoing a 1 DoF asymmetric flapping kinematics under the influence of different frontal inflow profiles were reported in this paper. Quantitative and qualitative assessments

Table 16.2 Standard deviation based on vertical force coefficient

Inflow conditions	Recurrence Rate	Determinism	Laminarity	Trapping Time	Ratio	Entropy	L_{MAX}	Trend
Uniform inflow profile	0.00	0.11	0.05	0.00	0.19	0.00	0.22	0.21
Shear inflow profile	0.09	2.95	3.63	0.83	2.70	0.29	4.74	1.29
Temporally oscillating uniform inflow profile	0.04	1.58	0.97	0.34	2.00	0.04	0.51	0.53
Spatiotemporally varying inflow profile	0.06	2.93	3.27	0.69	2.69	0.39	4.74	1.05

Table 16.3 Standard deviation based on horizontal force coefficient

Inflow Conditions	Recurrence Rate	Determinism	Laminarity	Trapping Time	Ratio	Entropy	L_{\max}	Trend
Uniform inflow profile	0.05	3.19	0.20	0.00	2.51	0.47	4.88	1.10
Shear inflow profile	0.47	10.76	10.04	5.54	4.78	0.77	37.47	10.72
Temporally oscillating uniform inflow profile	0.44	3.61	5.34	1.44	3.89	0.72	14.76	4.12
Spatiotemporally varying inflow profile	0.82	19.19	15.33	4.79	5.70	1.19	30.18	15.48

Table 16.4 Standard deviation based on aerodynamic moment coefficient

Inflow Conditions	Recurrence Rate	Determinism	Laminarity	Trapping Time	Ratio	Entropy	L_{\max}	Trend
Uniform inflow profile	0.08	1.05	1.86	0.31	1.21	0.16	1.69	0.32
Shear inflow profile	0.10	3.58	4.41	1.13	2.72	0.28	4.15	1.34
Temporally oscillating uniform inflow profile	0.08	2.40	1.99	0.37	2.62	0.24	1.03	0.33
Spatiotemporally varying inflow profile	0.08	3.36	3.62	0.95	2.52	0.27	3.65	1.20

were presented by the plots of instantaneous vertical and horizontal force coefficients and aerodynamic moment and the 3D phase plots, respectively. Subsequently, GRPs were plotted and windowed recurrence quantification analysis was carried out to have more insight into the effect of different inflow profiles on the forces and moment patterns of the flapping wing. It was observed that the influence of shear inflow profile on the forces and moments generated by the flapping wing was more as compared to the other two primary inflow profiles that were considered. The influence of the spatiotemporally varying inflow profile was a combination of the effects that the two primary inflow profiles induced on the forces and moment patterns. Since the present case of flapping was a simple canonical 1 DoF asymmetric flapping, it is envisaged to simulate higher degree of freedom flapping kinematics and assess the effect of the different inflow profiles and for a range of variation in their fundamental parameters in future.

References

1. Lian, Y., Shyy, W.: Aerodynamics of low Reynolds number plunging airfoil under gusty environment. In: 45th AIAA Aerospace Sciences Meeting and Exhibit, AIAA Paper 2007-70 (2007)
2. Wan, T., Huang C.: Numerical simulation of flapping wing aerodynamic performance under gust wind conditions. In: 26th International Congress of the Aeronautical Sciences, ICAS 2006-3.5 (ST 1) (2008)
3. Lian, Y.: Numerical study of a flapping airfoil in gusty environments. In: 27th AIAA Applied Aerodynamics Conference, AIAA Paper 2009-3952 (2009)
4. Viswanath, K., Tafti, D.K.: Effect of frontal gusts on forward flapping flight. *AIAA J.* **48**(9), 2049–2062 (2010)
5. Prater, R., Lian, Y.: Aerodynamic response of stationary and flapping wings in oscillatory low Reynolds number flows. In: 50th AIAA Aerospace Science Meeting including the New Horizons Forum and Aerospace Exposition, AIAA Paper 2012-0418 (2012)
6. Sarkar, S., Chajjed, S., Krishnan, A.: Study of asymmetric hovering in flapping flight. *Eur J Mech. B/Fluids* **37**, 72–89 (2013)
7. Zhu, J., Jiang, L., Zhao, H., Tao, B., Lei, B.: Numerical study of a variable camber plunge airfoil under wind gust condition. *J. Mech. Sci. Technol.* **29**(11), 4681–4690 (2015)
8. Jones, M., Yamaleev, N.K.: Effect of lateral, downward and frontal gusts on flapping wing performance. *Comput. Fluids* **140**, 175–190 (2016)
9. Zhan, J., Xu, B., Wu, J., Wu, J.: Power extraction performance of a semi-activated flapping foil in gusty flow. *J. Bionic Eng.* **14**, 99–110 (2017)
10. Ferziger, J.H., Peric, M.: *Computational Methods for Fluid Dynamics*, 3rd edn. Springer, Berlin, Heidelberg, New York (2002)
11. Issa, R.I.: Solution of the implicitly discretized fluid flow equations by operator-splitting. *J. Comput. Phys.* **65**, 40–65 (1985)
12. Fejtek, I., Nehera, J.: Experimental study of flapping wing lift and propulsion. *Aeronaut. J.* **84**, 28–33 (1980)
13. Sipers, A., Borm, P., Peeters, R.: Robust reconstruction of a signal from its unthresholded recurrence plot subject to disturbances. *Phys. Lett. A* **381**–6, 604–615 (2017)
14. Chen, Y., Yang, H.: Multi-scale recurrence analysis of long-term nonlinear and non-stationary time series. *Chaos, Solitons Fractals* **45**–7, 978–987 (2012)
15. Webber Jr., C.L., Marwan, N.: *Recurrence Quantification Analysis: Theory and Best Practices*. Springer, Switzerland (2015)

Chapter 17

Convergence Studies in the Finite Element Analysis of CFRP Shaft Under Torsion Using Shell281, Shell181, and Comparison with Analytical Results



Akshay Kumar and H. K. Rangavittal

Abstract In this paper, convergence studies of displacement, stress and failure index of the composite drive shaft model using shell281 and shell181 elements in ANSYS Mechanical is carried out, since the mesh plays a major role in giving the proper result which is close to real-life model. These results are compared with the analytical results of classical laminate theory (CLT), third-order shear deformation theory (TSDT), and classical shell theory (CST). It was found that shell181 without initial curvature with four nodes had a very slow convergence rate compared to the shell181 with initial curvature which has four nodes and shell281 which has eight nodes, and the CLT, TSDT, and CST results are in very close accordance with the shell281 element and the shell181 with the initial curvature result. Also, see that the shell181 without initial curvature requires a very fine mesh leading to a large number of elements to match the shell281 and the shell181 with initial curvature.

Keywords Composite · Drive shaft · Mesh · ANSYS · Classical laminate theory · Third-order shear deformation theory · Classical shell theory

17.1 Introduction

The composite materials are now one of the highly researched areas since industries want Materials and methods to make the structure stronger and lighter, which can be done by tailoring the composite material in an appropriate way as a designer. Composite materials can be designed to be both strong and light. Hence, it is widely applicable in the field of automobile parts design, aerospace, marine, and other, one of them is the composite material drive shaft.

Around the 1970s, it was found that composite material is a potential candidate for the drive shaft, and the most important development was seen in aerospace [1] and automotive industry [2]. Other applications are the use of composite in aircraft

A. Kumar (✉) · H. K. Rangavittal
Department of Mechanical Engineering, BMS College of Engineering, Bengaluru 560019, India
e-mail: akshaykumar00325@gmail.com

© Springer Nature Singapore Pte Ltd. 2020
C. Li et al. (eds.), *Advances in Engineering Design and Simulation*,
Lecture Notes on Multidisciplinary Industrial Engineering,
https://doi.org/10.1007/978-981-13-8468-4_17

generator shaft [3], an aircraft power take-off shaft [4], quill shaft [5], naval propulsion systems [6], and a shaft for cooling tower [7]. Design methodology for the complete design of the composite drive shaft and its advantages, which is then used for replacing a two-piece metallic automotive drive shaft by single-piece composite shaft is discussed in [8, 9].

Finite element analysis has been widely used for designing because of their power to work with the complex model and near to a real-world system. Some of the recent work in FEA includes the comparison of the experimental result of shaft subjected to combined torsional and tension/compression [10, 11], failure of E-glass/epoxy cruciform specimen under static load [12], and GFRP woven composites under combined tension-bending loading [13]; these results are correlated with theoretical analysis and finite element model, and they show a very good match with the experimental data. Other works include analysis of high strength carbon/epoxy shaft [14] and E-glass/epoxy resin hollow composite drive shaft [15]. As the weight of the shaft increases, it prompts more consumption of fuel, and by substituting the composite drive shaft in place of the steel, shaft resulted in a reduction of its weight by 72% [16].

For finding solution of laminated composite which is 2D plate and shells, there are analytical methods like classic laminate theory (CLT) and classical shell theory (CST) which have been derived, but they are an approximates of the real system, and hence there have been a lot of research on refining the theory so as to get a better approximation. This resulted with methods like first-order shear deformation theory (FSDT) and higher-order shear deformation theory (HSDT).

One of them is a simple first-order shear deformation theory by Huu-Tai Thai et al. [17] which involves only four unknowns instead of five unknowns like classical first-order shear deformation theory, and also this has similarity to classical plate theory in many ways such as the equations of kinematics, boundary conditions, and expressions of stress resultant.

The most popular simple higher-order displacements were proposed by Levinson [18] and Murthy [19]. Based on the kinematics given by Levinson, Bickford [20] came up with a variational consistent higher-order beam theory, and later J. N. Reddy [21] presented the variational consistent equilibrium equations for plates. And Rohwer did a comprehensive numerical investigation of the accuracy of various higher-order shear deformation theories; it showed that the Reddy's and Murthy's theories are the best options for higher-order shear deformation theory. Also, the Reddy's third-order shear deformation theory is still considered as the most popular and most simple higher-order shear deformation theory, which will be used in this work.

The aim of this work is to show the convergence studies on finite element model of composite drive shaft using two different element type shell181 and shell281 from Mechanical APDL, and comparison of results with the analytical method approach of plate and shell such as classical laminate theory [22], third-order shear deformation theory [21], and classical shell theory [23].

The remaining segment of the paper is arranged as follows. In Sect. 17.2, a clear description of the problem and concept is explained. In Sect. 17.3, the method of

Table 17.1 Specification of the shaft

Specification	Length in mm	Inner diameter in mm	Outer diameter in mm	Ply thickness in mm	Total number of ply	Orientation of the ply
Shaft	380	43	49	0.2	15	45/−45

approach is discussed. In Sect. 17.4, the results of the various methods are tabulated and compared. And the conclusion is discussed in Sect. 17.5.

17.2 Description

17.2.1 Problem Statement

A thin shaft with a uniform, circular cross-section is applied with the torque of 1000 Nm and the specification is given in Table 17.1.

The material properties of the carbon fiber-reinforced polymer (CFRP) with 70% volume fraction of graphite fiber are given in Tables 17.2 and 17.3.

In this study, the $\pm 45_3/45/-45$ laminate is taken, since at the 45-degree ply orientation, the rigidity modulus is maximum.

17.3 Approach

17.3.1 Numerical Method

Finite element modeling is a very powerful numerical analysis tool which can be used for analyzing composite material structures with complex boundary. And depending on the number of elements used, the accuracy of the result and time taken for analysis varies.

Mechanical ANSYS Parametric Design Language (APDL) is highly used for the research as it gives good control and exploitation of FEM variables like element type, mesh type, mesh size, etc., and hence it is opted for numerical analysis in this study. Some of the element types for 2D thin composite analysis is shell281—(eight-node element), shell181—(four-node without initial curvature effects), shell181—(four-node with initial curvature effects), the model is a simple tube with inner diameter 43 mm and length 380 mm is created as shown in Fig. 17.1a, quadrilateral mesh is used whose edge size is varied for the convergence study.

The layer stacking sequence is as shown the Fig. 17.1b, and the boundary conditions being one end of the shaft are completely fixed for all degrees of freedom,

Table 17.2 Material stiffness properties [22]

Material	Volume fraction	Density	E_1 in GPa	E_2 in GPa	γ_{12}	γ_{23}	γ_{13}	G_{12} in GPa	G_{23} in GPa	G_{31} in GPa
CFRP	0.7	1620	181	10.3	0.28	0.6	0.27	7.17	3	7

Table 17.3 Material strength properties [22]

Material	$(\sigma'_1)_{ult}$ in Mpa	$(\sigma'_2)_{ult}$ in MPa	$(\sigma^c_1)_{ult}$ in MPa	$(\sigma^c_2)_{ult}$ in MPa	$(\tau_{12})_{ult}$ in MPa
CFRP	1500	40	1500	246	68

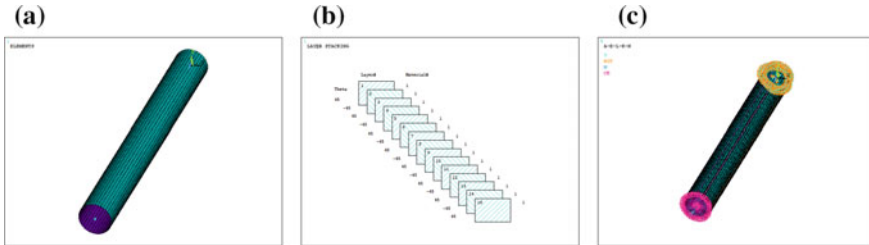


Fig. 17.1 **a** Meshed shaft with 4 mm element size. **b** Laminate sequence. **c** Boundary condition of the shaft

another end is applied with a moment of 1000 Nm about the shaft axis. The notation in Fig. 17.1c refers to *M*—moment, *U*—displacement constraint, ROT—rotational constraints, and CE—coupling element.

17.3.2 Analytical Methods

(a) Classical Laminate Theory [22]

Classical laminate plate theory (CLT) assumes that any point in a system is a plate and finds the strains and curvature of the midplane of the plate based on the loading condition as shown in Fig. 17.2a, and the strain at any other height varies linearly as a function of midplane strain and curvature. From the strains, the stress can be found.

This theory overestimates the displacement in most cases.

$$\epsilon_{(k)} = \epsilon^o + z_{(k)} \times k^o \tag{17.1}$$

where ϵ^o is the midplane strain, k^o is the midplane curvature, and (k) is the layer number, and $z_{(k)}$ will give the distance of layer (k) from the midplane as shown in Fig. 17.2b.

(b) Third-order Shear Deformation Theory [21]

In the case of higher-order shear deformation theory, the widely used, as well as simple one, is Reddy’s third-order shear deformation theory (TSDT). Since CLT overestimated the displacements, the TSDT is a better approximation to the plate under any loading condition as shown in Fig. 17.3. Similar to the CLT the midplane

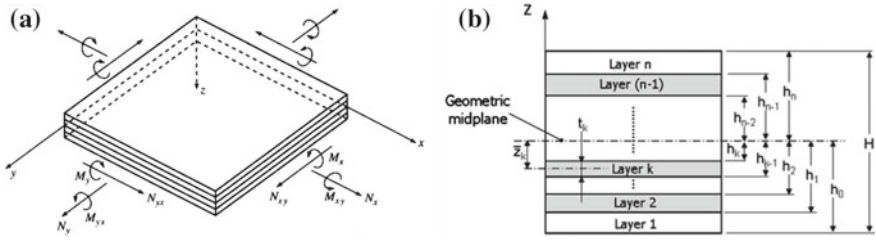


Fig. 17.2 a Loading on a laminated plate. b Coordinate location of the plies in a laminate

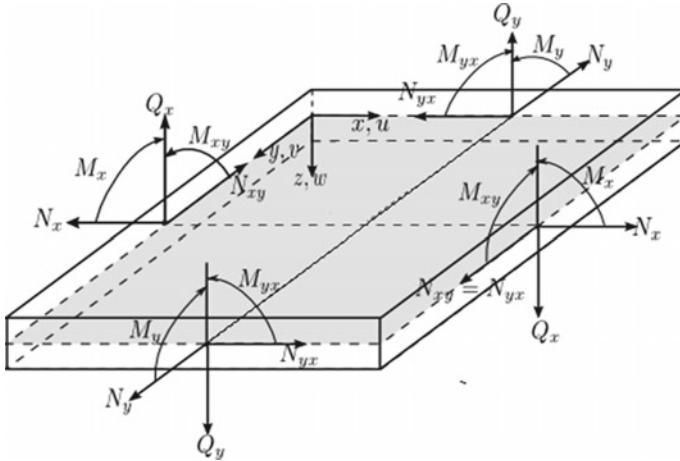


Fig. 17.3 Loading on laminated plate under TSDT

strains, curvatures is found. And the strain at any other height which varies quadratically as a function of midplane strain and curvature can be calculated. From the strains, the stress can be found.

$$\epsilon_{(k)} = \epsilon^o + z_{(k)} \times k^o + z_{(k)}^2 \times k^2 \tag{17.2}$$

where ϵ^o is the midplane strain, k^o is the midplane curvature, k^2 is the midplane constant, and (k) is the layer number, and $z_{(k)}$ will give the distance of k th layer from the midplane of stack.

(c) Classical Shell Theory [23]

The classical shell theory is very similar to the CLT except for the point that the shell has an initial curvature which changes the relationship of load to the stress as shown below.

$$(N_x, N_{xy}) = \int_{-h/2}^{h/2} (\sigma_x, \tau_{xy}) \times \left(1 + \frac{\zeta}{R_2}\right) d\zeta \tag{17.3}$$

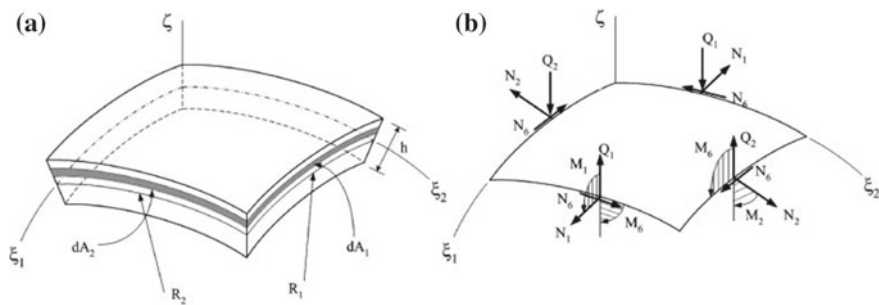


Fig. 17.4 a Geometry of the shell. b Loading on the shell structure

$$(N_y, N_{yx}) = \int_{-h/2}^{h/2} (\sigma_y, \tau_{yx}) \times \left(1 + \frac{\xi}{R_1}\right) d\xi \tag{17.4}$$

$$(M_x, M_{xy}) = \int_{-h/2}^{h/2} (\sigma_x, \tau_{xy}) \times \left(1 + \frac{\xi}{R_2}\right) \times \xi \times d\xi \tag{17.5}$$

$$(M_y, M_{yx}) = \int_{-h/2}^{h/2} (\sigma_y, \tau_{yx}) \times \left(1 + \frac{\xi}{R_1}\right) \times \xi \times d\xi \tag{17.6}$$

Referring to the Fig. 17.4a, since the cylinder is a single-curved shell, the $R_1 = \text{Inf}$ and R_2 is the mean radius of the cylinder.

Similar to the CLT, the midplane strains and curvatures are found due to the loads N_x, N_y, N_{xy}, N_{yx} and M_x, M_y, M_{xy}, M_{yx} . The strain at any other height from the midplane varies linearly as a function of midplane strain and curvature. From the strains, the stress can be found.

$$\epsilon_{(k)} = \epsilon^o + z_{(k)} \times k^o \tag{7}$$

where ϵ^o is the midplane strain, k^o is the midplane curvature, and (k) is the layer number, and $z_{(k)}$ will give the distance of layer (k) from the midplane similar to the laminate coordinate of CLT.

17.4 Results

17.4.1 Numerical Method

In ANSYS Mechanical, the axial stress on the shaft is in the Z-direction— S_z , the lateral stress on the shaft is Y-direction— S_y , the shear stress in YZ plane— S_{yz} , in the cylindrical coordinate system (Fig. 17.5).

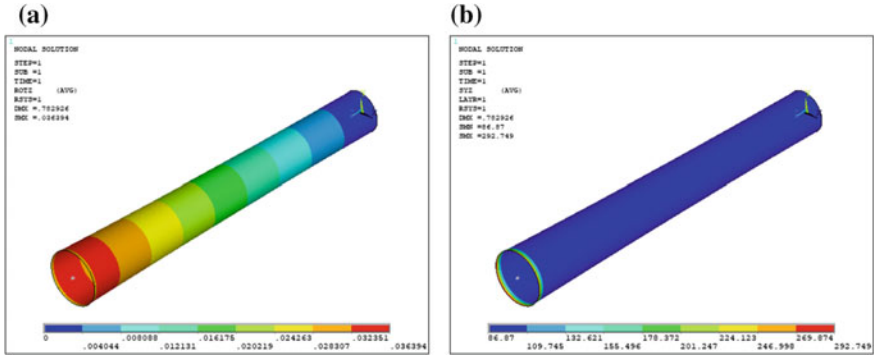


Fig. 17.5 a Axial rotational displacement in radians. b Shear stress on layer 1

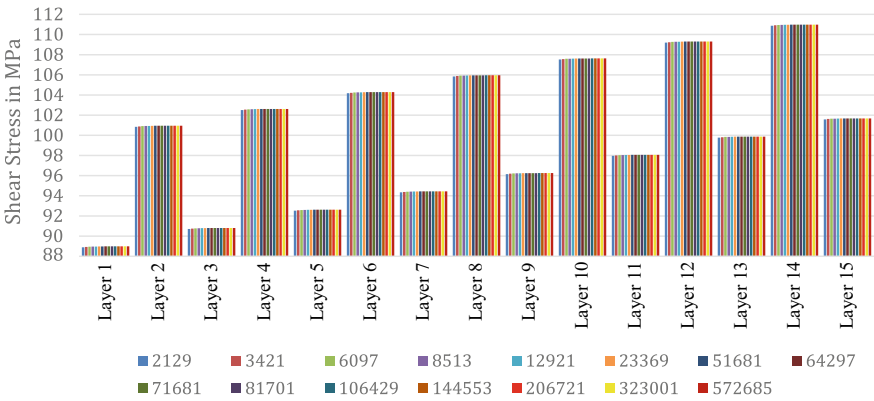


Fig. 17.6 Shear stress on each layer for different number of elements with shell281

The value at fixed and loaded end form singularity which could be seen in Fig. 17.5b, hence neglected.

(a) Shell281 Element Results (Fig. 17.6)

The legend represents the number of elements in the shaft mesh model, and shear stress is plotted for different layer number. The shear stress increases from the inner to the outer layer, with odd and even number layer having different stresses. For a smaller number of elements, the stress is slightly underestimated.

Similarly, the Tsai Wu failure index variation was seen, and the index is slightly larger on outer layers, and there is not much variation of the index with a change in a number of elements. Same is seen with the axial stress of the shaft. Also, the shear strain increases with the laminate thickness, but the change is very small.

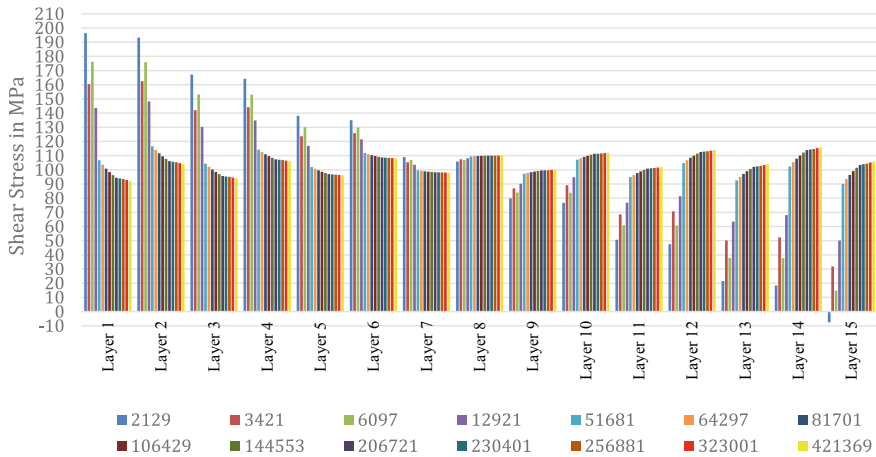


Fig. 17.7 Shear stress on each layer for different number of elements with shell181 without initial curvature

(b) Shell181 Element Without Initial Curvature

The shear stress is different in each layer for different mesh and the highly overpredicts for a smaller number of elements (Fig. 17.7).

Similarly, the Tsai Wu failure index, shear strain, and axial stress behave with a change in element number.

(c) Shell181 with Initial Curvature

The variation of the shear stress in this element is much similar to the 281 but slightly overestimating the stress for a small number of elements.

The same trend can be seen with the Tsai Wu failure index, shear strain, and axial stress, i.e., a small number of elements lead to results higher than a large number of the element (Fig. 17.8).

Now, when we compare the different element types together, it was found that the shell281 and shell181 with initial curvature have good agreement with regard to the shear stress (Fig. 17.9), axial stress (Fig. 17.10), rotational displacement (Fig. 17.11), and Tsai Wu failure index.

The shell181 without curvature does not show any agreement with the shell281 element type unless the number of elements in the model is more than 400,000.

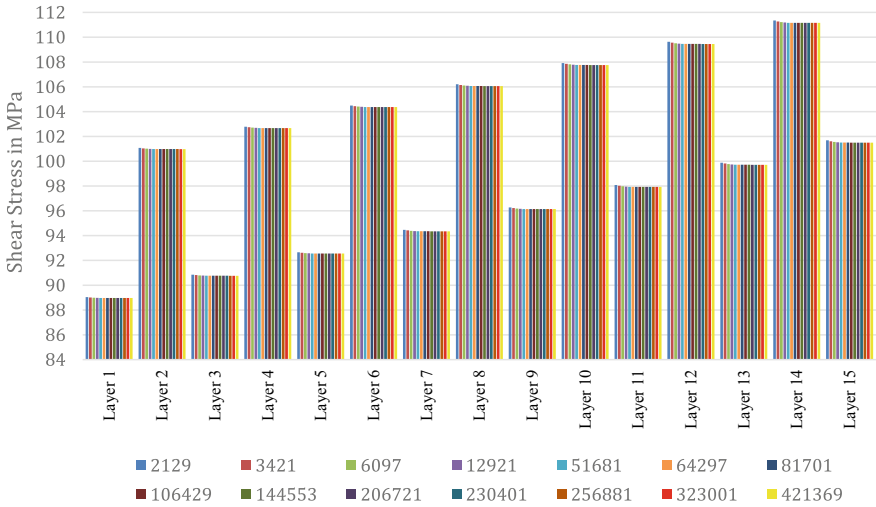


Fig. 17.8 Shear stress on each layer for different number of elements with shell181 with initial curvature

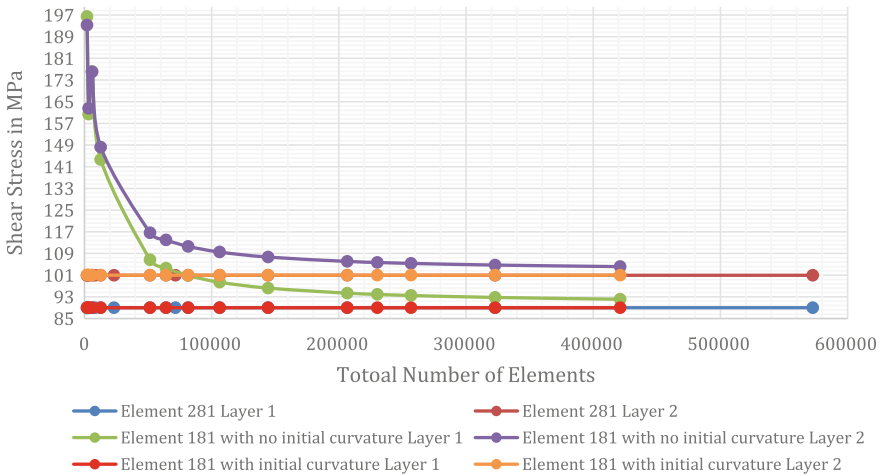


Fig. 17.9 Shear stress on layers 1 and 2 for different number of element and element type

17.4.2 Analytical Results

(a) Classical Laminate Theory and Third-order Shear Deformation Theory

Due to the application of only N_{xy} load on the plate, the curvature effect will be very small and thus, the results of CLT and TSDT are similar (Fig. 17.12).

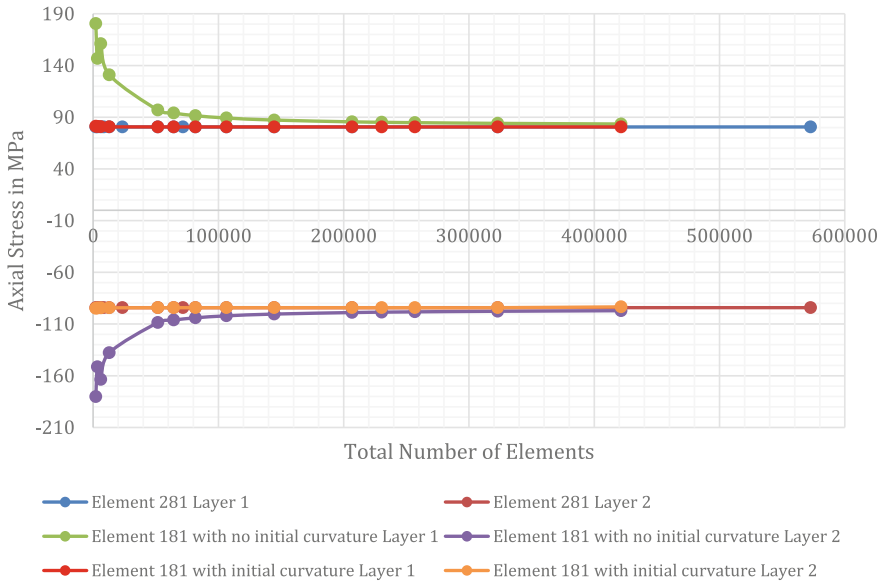


Fig. 17.10 Axial stress on layers 1 and 2 for different number of element and element type

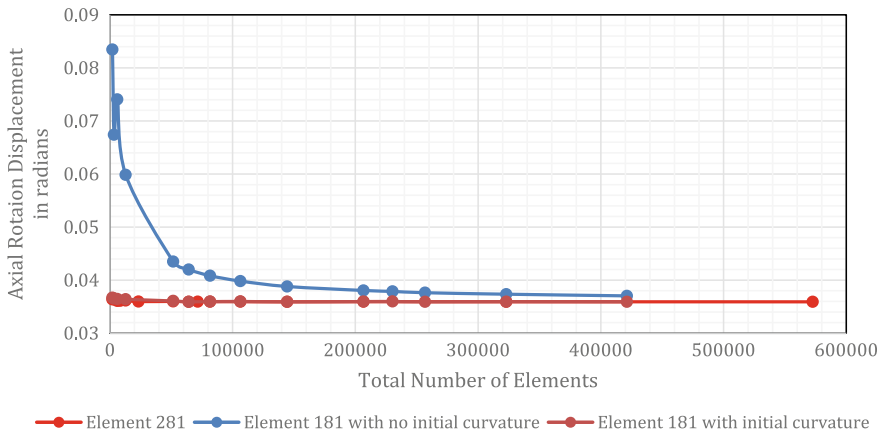


Fig. 17.11 Axial rotation displacement (twist) for different number of element and element type

The variation of shear stress over the laminate thickness remains constant in odd and even lamina, as well as shear strain over the whole length. And the axial stress is positive for 45 angles and negative for -45 angles.

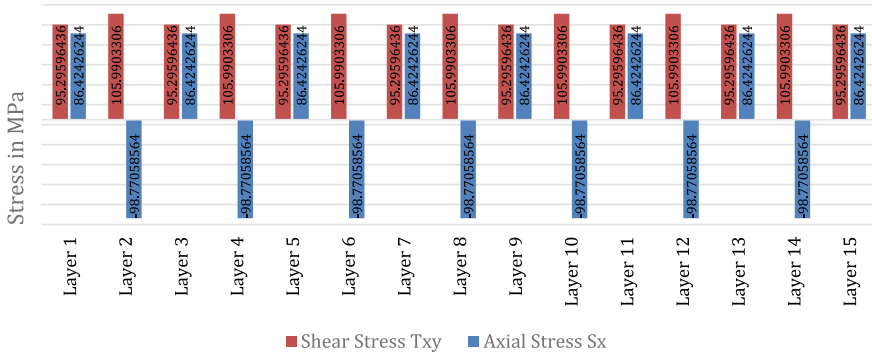


Fig. 17.12 Shear stress and axial normal stress of the shaft in each layer

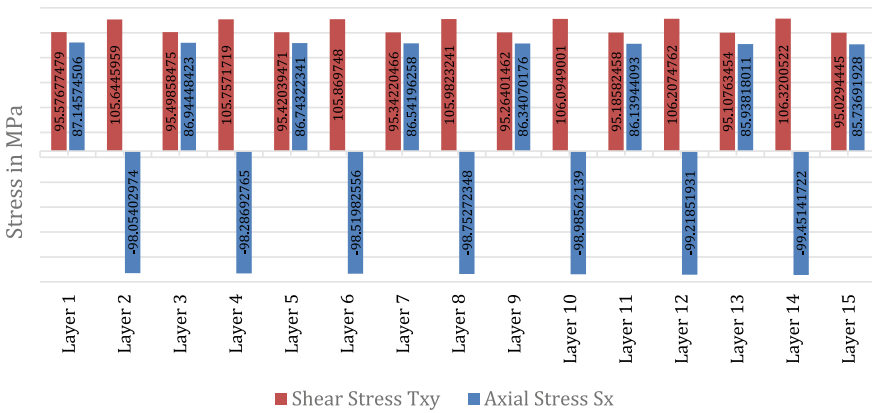


Fig. 17.13 Shear stress and axial normal stress of the shaft in each layer

(b) Classical Shell Theory

The variation of shear stress increases over the laminate thickness, the axial direction stress is positive for 45 angle and negative for -45 angles, slightly decreasing over the length of the laminate (Fig. 17.13).

17.4.3 Comparison of the Two Approaches

(i) Shear Stress

The fine mesh result of different element types is compared with analytical methods in Fig. 17.14. The shell181 without initial curvature overpredicts the stress, and analytical methods seem to be large for inner layers compared to numerical results and small for outer layers.

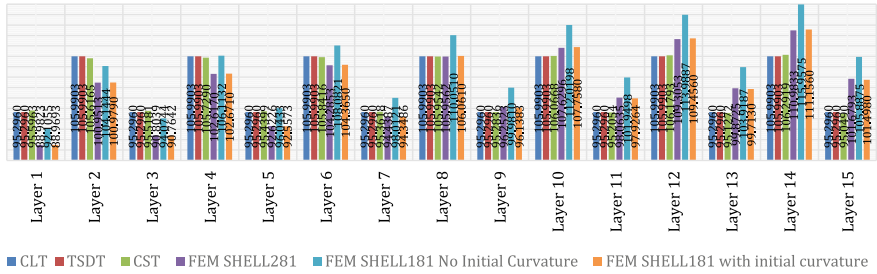


Fig. 17.14 Shear stress of the shaft in each layer with different approaches

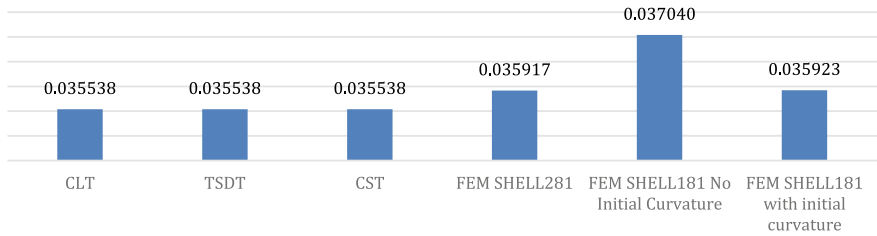


Fig. 17.15 Axial rotation displacement of the shaft in each layer with different approaches

The same effect can be seen with Tsai Wu index and shear strain.

(ii) Axial Rotation Displacement (Twist)

The rotation about the axis of rotation is compared between these approaches in radians. Except for Shell181 without initial curvature, other element type shows good correlation with the analytical result (Fig. 17.15).

17.5 Conclusion

In this paper, a comprehensive study of the change in mesh size with different element types is conducted on CFRP shaft and the results were compared against the analytical method of plate and shells. It was found that the shell281 2D element with eight nodes and shell181 2D element four nodes with initial curvature had good agreement with the CLT, TSDT, and CST for more than 12,921 elements, as well as the convergence of the stress and strains takes place faster. Shell181 without any initial curvature converges to the stress and strain only for more than 2lakh element, then also there is still a small difference between the converged value and the result from the analytical approach and other element types. In such simple case, the analytical method will be computationally more efficient than finite element analysis of shafts.

References

1. Kraus, R.E., Darlow, M.S.: Design and experimental studies of composite power transmission shafting. In: American Helicopter Society, 43rd Annual Forum, vol. 2, pp. 733–738 (1987)
2. Belingardi, G., Calderale, P.M., Rosetto, M.: Design of composite material drive shafts for vehicular applications. *Int. J. Veh. Des.* **11**(6) (1990)
3. Raghava, R.S., Hammond, R.S.: Development of a filament wound composite shaft for an aircraft generator. In: Technical Sessions, 39th Annual Conference on Reinforced Plastic Institution, pp. 1–24 (1984)
4. Garguilo, D.J.: Design and development of a power takeoff shaft. *J. Aircr.* **23**(12), 876–880 (1986)
5. Spencer, B.E.: Advances in power transmission using filament wound composites. In: 34th International SAMPE Symposium and Exhibition, vol. 34, pp. 1109–1117 (1989)
6. Wilhelmi, G.F., Appleman, W.M., Loo, F.T.C.: Composite shafting for naval propulsion system. *Nav. Eng. J.* **98**(4), 129–136 (1986)
7. Berg, K.R.: Composite driveshafts in cooling towers. *J. Cool. Tower Inst.* **10**(1), 36–37 (1989)
8. Spencer, B., McGee, J.: Design methodology for a composite driveshaft. In: Proceedings of Conference Advanced Composites, pp. 69–82 (1985)
9. Pollard, A.: Polymer Matrix Composites in Driveline Applications. In: 3rd International Conference on Materials for Lean weight Vehicles at Warwick. GKN Tech, UK. <http://www.spinning-composites.com/images/CompositesInDriveline.PDF> (1999)
10. Antoniou, A.E., Kensche, C., Philippidis, T.P.: Mechanical behavior of glass/epoxy tubes under combined static loading. Part I: Experimental. *Compos. Sci. Technol.* **69**(13), 2241–2247 (2009)
11. Antoniou, A.E., Kensche, C., Philippidis, T.P.: Mechanical behavior of glass/epoxy tubes under combined static loading. Part II: Validation of FEA progressive damage model. *Compos. Sci. Technol.* **69**(13), 2248–2255 (2009)
12. Antoniou, A.E., Van Hemelrijck, D., Philippidis, T.P.: Failure prediction for a glass/epoxy cruciform specimen under static biaxial loading. *Compos. Sci. Technol.* **70**(8), 1232–1241 (2010)
13. Khosbakhht, M., Chowdhury, S.J., Seif, M.A., Khashaba, U.A.: Failure of woven composites under combined tension-bending loading. *Compos. Struct.* **90**(3), 279–286 (2009)
14. Ravi, A.: Design, comparison and analysis of a composite drive shaft for an automobile. *Int. Rev. Appl. Eng. Res.* **4**(1), 21–28 (2007)
15. Gireesh, B., Shrishail, S., Satwik, V.N.: Finite element & experimental investigation of composite torsion shaft. *Int. J. Eng. Res. Appl.* **3**(2), 1510–1517 (2013)
16. Khoshnavan, M.R., Paykani, A.: Design of a composite drive shaft and its coupling for automotive application. *J. Appl. Res. Technol.* **10**(6), 826–834 (2012)
17. Thai, H.T., Choi, D.H.: A simple first-order shear deformation theory for laminated composite plates. *Compos. Struct.* **106**, 754–763 (2013)
18. Levinson, M.: An accurate, simple theory of the statics and dynamics of elastic plates. *Mech. Res. Commun.* **7**(6), 343–350 (1980)
19. Murthy, V.V.M.: An improved transverse shear deformation theory for laminated anisotropic plates. *NASA Tech. Pap.* **1903**, 1–37 (1981)
20. Bickford, W.B.: A consistent higher-order beam theory. *Dev. Theor. Appl. Mech.* **11** (1982)
21. Reddy, J.N.: A simple higher-order theory for laminated composite plates. *J. Appl. Mech.* **51**(4), 745 (1984)
22. Kaw, A.K.: *Mechanics of Composite Materials*. CRC Press, New York (2005). ISBN 9780429125393. <https://doi.org/10.1201/9781420058291>.
23. Reddy, J.N.: *Mechanics of Laminated Composite Plates and Shells: Theory and Analysis*, 2nd edn, CRC Press, New York (2003). ISBN 9780849315923

Chapter 18

Testing a Fire Door Through Simulation



Amita Tripathi, Chenthil Kumar, Thomas Grinnaert and Anil Kumar

Abstract Fire doors are usually tested in laboratory experiments and subjected to a standard heat load to assess their degree of resistance. However, once the fire door is in place, such experiments cannot take place anymore while it might still be necessary to check if they can withstand a realistic fire with similar performances to a standard fire scenario. In the case study presented here, the fire door in place on an industrial site was certified for standard fire curves lasting one hour. However, it became necessary to check if the fire door design was enough to keep its functions for one hour and a half in case an electrical cabinet located in front of the door was burning. Since the door could not be dismantled and tested again in the laboratory, a numerical simulation had to be performed. The numerical tool used here is fluidyn-VENTFIRE, a multiphysics tool based on the numerical platform fluidyn-MP and combining the finite volume approach for CFD, simulating the fire reaction, tracking the smoke propagation and calculating the convective and radiative part of the heat load with the finite element approach for FEM, simulating the conduction inside the door and the subsequent thermal stresses to determine the possible deformations or failures of the door. The three major functions of the fire door were then verified: maintaining its structural integrity while preventing heat levels and smoke to propagate to adjacent rooms.

Keywords CFD · Fire modeling · Fire door · Structural integrity · Deformation · Smoke propagation · Radiation

A. Tripathi (✉) · T. Grinnaert
FLUIDYN France, Saint-Denis, France
e-mail: amita.tripathi@fluidyn.com

C. Kumar · A. Kumar
FLUIDYN India, Bengaluru, India

© Springer Nature Singapore Pte Ltd. 2020
C. Li et al. (eds.), *Advances in Engineering Design and Simulation*,
Lecture Notes on Multidisciplinary Industrial Engineering,
https://doi.org/10.1007/978-981-13-8468-4_18

18.1 Introduction

A passive fire protection system such as a fire door needs to fulfill several functions during a given period of time to be certified for use in an industrial or nuclear context: it needs to be fire-resistant (no collapse due to the heat load), it needs to prevent the spread of smoke (i.e., no deformation that would allow fumes to expand to the entire building) and it needs to insulate the fire (i.e., cut-off the heat behind it) [1–3]. These three functions are usually tested in laboratory experiments for the period of time defined by the needs for intervention and/or evacuation and this before the fire door is mounted. However, the laboratory tests are usually performed using a standard fire curve and do not account for the real conditions of the mounted fire door [4–9]. Moreover, once it has been certified for a given duration and mounted, its validity for a longer duration cannot be checked without dismounting and changing it.

Multiphysics simulation coupling CFD with FEM is used in the present case to alleviate these two restrictions [10–15]. A fire door already in place can be tested against a real fire scenario and the duration for which it could fulfill its duties in real condition directly evaluated.

In the case presented in this paper, the fire door is isolating an electrical cabinet, inside a room, called the BT room, from the rest of the industrial site. The scenario studied here is about the cables inside the cabinet catching fire with the cabinet door open. Upon detection (at maximum 4 min after the fire outbreak), the ventilation emergency system kicks in and stops completely the ventilation inside the room. The three functions of the fire door described above are tested numerically by estimating the temperature of the door and the resulting stresses; the door deformation; the temperatures and heat radiated behind the door in the neighboring room as described by the ISO 834 norm: specifically, the temperature on the face not exposed to fire must be on average less than 140 °C and must not exceed in any point 180 °C.

In addition, the analysis also includes the thermal radiation experienced by the cable tray located outside the room:

- About 2 m above the door of the BT room.
- On the wall in front of the door of the BT room at a height of about 4 m above the floor.
- On the free zone within a radius of 2 m around the door of the BT.

The radiative field obtained on these points is compared over time to the thermal radiation thresholds for effects on humans and structures (thresholds of 3, 5 and 8 kW/m²). These results will validate or not the functioning of the fire door on the requested duration of 1 h and 30 min.

18.2 Software Used

The multiphysics software used here is fluidyn-VENTFIRE, a dedicated module of the fluidyn-MP platform (version 6.0.2). This platform combines in a strong coupling

a finite volume CFD solver with a finite element solver [10, 11], allowing for a precise description of the behavior of coupled systems (heat transfers, fluid-structure interaction, etc.) [12–15].

Inside fluidyn-VENTFIRE, the finite volume solver is tailor-made to solve Navier–Stokes equations for turbulent, compressible and reacting flows employing structured or unstructured meshes for unsteady as well as steady state cases.

Coupling VENTFIRE with a suitable FEM solver allows for a coupled resolution of thermal conduction inside the door material and the thermal strains and stresses developed due to the temperature gradient through automatic exchange of boundary conditions between temperature and stresses at every time step.

18.3 Case Description

18.3.1 Simulation Domain

The simulation domain is described in Fig. 18.1.

The fire is supposed to take place inside the electrical cabinet in front of the door (Fig. 18.2). The doors of the electrical cabinet are open, which means that the fire is in full view of the door. The ventilation system is working initially and it stops once the fire has been detected (4 min after the beginning of the fire in a conservative approach). Thus, all the choices have been made in order to ensure that this configuration is the worst-case scenario. Turbulence is modeled using the standard k - ϵ turbulence model [16]. The computational time step of 0.2 s is used for fire studies. In this study, the typical mesh size was based on other studies [17].

18.3.2 Ventilation

The injection of fresh air is located on the right wall, while two extraction grids are located above the fire door (green lines on Fig. 18.1). The air velocity at the inlet is 3.0 m/s and a static pressure condition has been applied to the extraction grids. The air inlet is stopped after 4 min after the fire beginning and the conditions are then changed to wall conditions.

18.3.3 Firedoor

The fire door is made up of three different materials in five layers: zinc (a layer of 1.5 mm of thickness), rockwool (30 mm of thickness), the air in between (28 mm of thickness) and again rockwool and zinc. The structure is maintained by supports

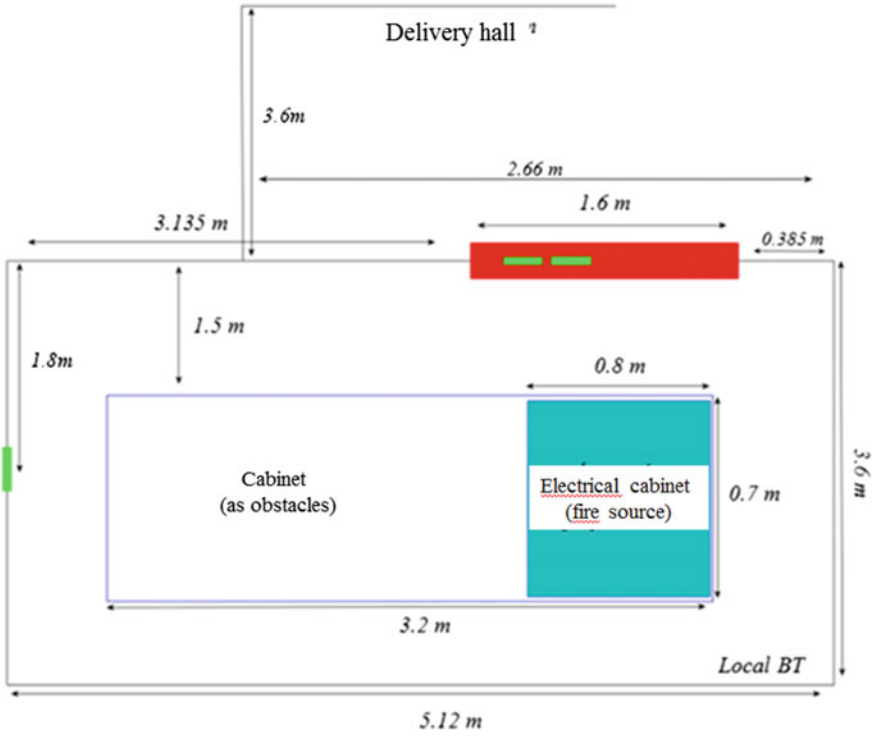


Fig. 18.1 Domain of simulation (top view): in red the fire door; in green the ventilation extraction and blowing; in blue the electrical cabinet

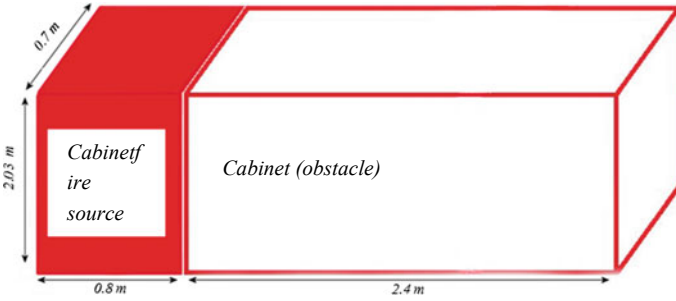


Fig. 18.2 Dimensions of the cabinets: in red the cabinet catching fire

Table 18.1 Material properties (from Engineeringtoolbox.com)

Material	Density	Young modulus	Poisson coefficient	Thermal dilatation coefficient	Thermal conductivity	Specific heat
	Kg/m ³	GPa		K ⁻¹	W/mK	
Zinc sheet	7135	82.7	0.25	29.7e-6	116	390
Supports						
Bottom						
PPF	160	14	0.43	7.10e-06	0.04	840

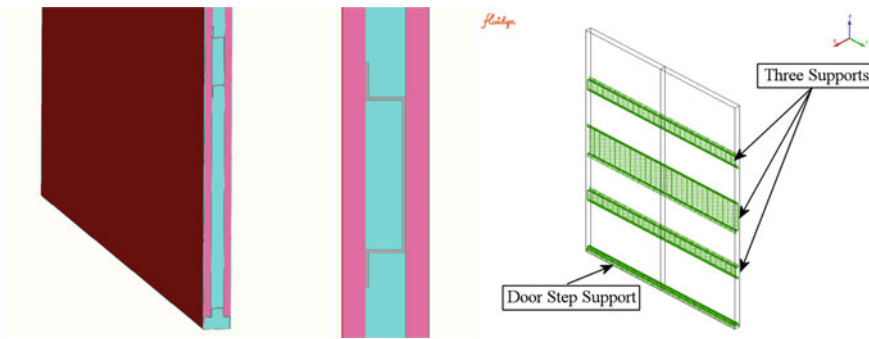


Fig. 18.3 Door composition (lower part of the door, zoom on supports, the position of supports in the door)

in the air layer. The zinc layers are maintained by rivets doors (except at the bottom where the layers are welded). Rivets are 5 mm in diameter and spaced by 250 mm. Finally, hinges are located at the top and bottom on the door panels.

In Fig. 18.3, the zinc layers are in brown, PPF layers in pink, the air in blue and supports in green.

The material properties used are given in the (Table 18.1 and Fig. 18.3).

18.3.4 Fire Description

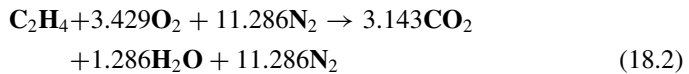
The cables inside the cabinet are made of 50% of polyethylene (C₂H₄ or PE), and 50% of polyvinyl chloride (C₂H₃Cl or PVC). The release combustion products and heat energy in the proportion defined by stoichiometry (Table 18. 2).

The PVC and the PE stoichiometric equations in terms of mass are provided below.



Table 18.2 Chemical and combustion properties of PE and PVC

	Density	Emissivity	Heat of combustion	Ideal specific burning rate	HRR
	kg/m ³		MJ/kg	kg/sm ²	kW/m ²
PVC	1380	0.88	16.4	0.016	92
PE	929	0.92	43.6	0.026	993



The power released by the fire depending on time is obtained from the experimental test [3]. The HRR (heat release rate) curve is comprised of three parts:

- Increasing part, given by this equation

$$\text{HRR} = \text{HRR}_{\text{peak}} * \left(\frac{t}{\tau}\right)^2 \quad (18.3)$$

where total time for reaching the $\text{HRR}_{\text{peak}} = \tau$

- Constant part: $\text{HRR} = \text{HRR}_{\text{peak}}$
- Decreasing part: Straight line until zero.

The HRR_{peak} and the heat of combustion are calculated as the average of the HRR_{peak} of both types of fuel. The duration of each part is defined by the following two criteria:

- The time of the increasing and the decreasing part are chosen from an experimental test, test ST11 of [3]
- The time of the constant part depends on the availability of the fuel.

The curves of HRR and power released obtained are shown in the following Fig. 18.4.

The peak oxygen consumption rate and peak total product generation rate are calculated from the mass stoichiometric equation using calculated peak fuel consumption of 0.077 kg/s.

The total power released by the fire is split into 80% convective power and 20% radiative power.

The data obtained and used in the simulation are summarized (Table 18.3).

The geometry of the flame is evaluated from experimental test reports [6] in similar configurations: equivalent electrical cabinet and open doors. The experimental flame, however, is constantly ventilated to ensure good combustion. The flame height is estimated at 2 m. It does not reach the fire door; therefore, its direct action on the

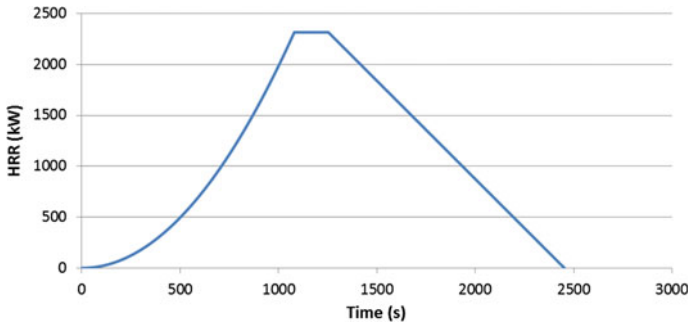


Fig. 18.4 Heat release rate

Table 18.3 Summary of fire data

Maximal power fire (MW)	3.5
Maximal convective power (MW)	2.8
Maximal radiative power (MW)	0.7
Maximal burning rate (kg/s)	0.2
Total mass of smoke (kg)	293
Maximal energy available (Heat Comb x Mass) (MJ)	3637
Total convective energy (MJ)	2910
Total radiative energy (MJ)	727

door does not need to be taken into account. The geometry of the flame is kept the same with and without ventilation. This positioning of the flame is penalizing insofar as, after 4 min, the fire modeled here becomes under-ventilated.

In Fig. 18.5, the zone in orange defines the region in which the flames are fully developed. The heat and combustion gas sources are imposed on this zone.

18.4 Numerical Model

18.4.1 Mesh

The mesh combines the mesh for the fluid domain and the mesh for the structural part (fire door). The two sub-domain meshes are non-matching mesh (boundary elements between fluid and structure are not matching). The mesh size is detailed in the Table 18.4.

Figure 18.6 shows fluid mesh (in red) and the structured mesh (in black). Figure 18.7 zooms in on the finite element mesh used for the various materials comprising the fire door.

Fig. 18.5 Geometry of the flame

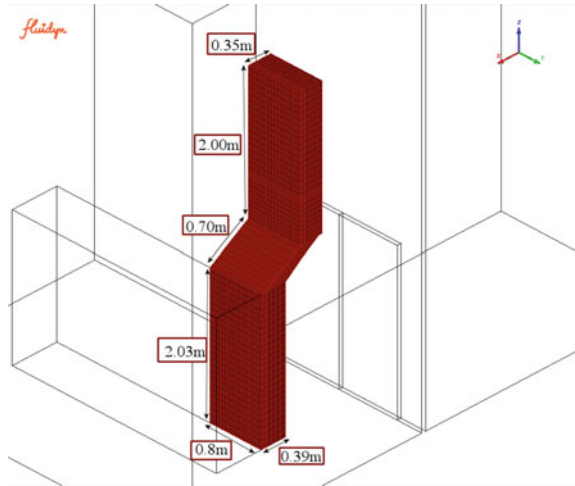


Table 18.4 Mesh properties

	Elements		Total Bface	Total faces fluid/structure interface	Nodes
	Type	Number			
Fluid	Hexahedral	292,098	37,300	2368	311,044
Structure	Hexahedral	49,140	14,892	7560	56,896



Fig. 18.6 Mesh in 3D view

18.4.2 Solver Parameters

The fluid solver used here is a transient Euler implicit solver. The turbulence model is a k -epsilon model and the radiation model is a discrete ordinate method (DOM) model. The gravity is modeled through a buoyancy term.

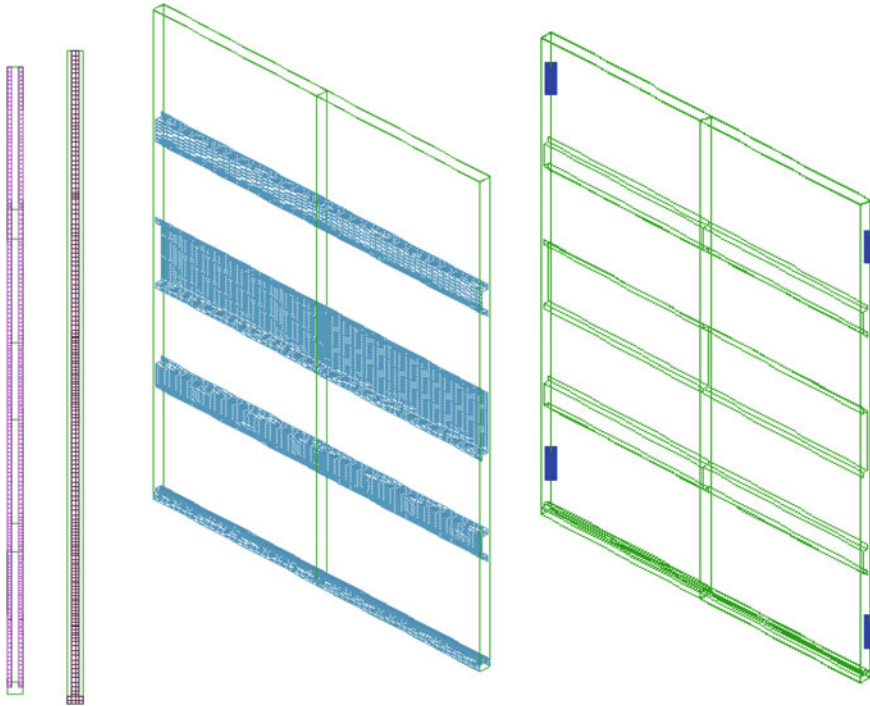


Fig. 18.7 Rockwool layers, air, supports and hinges (from left to right)

18.4.3 Coupling Methodology

The heat exchange at the door is done by the convective and radiative modes. The heat exchange coefficient on the door is imposed from analytical laws (engineering techniques—flow on a flat surface). Indeed, the calculation of the thermal coefficient by the simulation can require a mesh in the very thin boundary layer and possibly incompatible with the dimensions of the room. The DOM model is used here for calculating radiation to fluids and structures. For the calculation of the absorption coefficient of radiation by gases, Planck’s law was used considering a variation of absorption with pressure, temperature and gas concentration. The conduction through the door and through the walls is done by the finite element method (coupled with the finite volume method, used for convection).

The coupling between the two modules is achieved thanks to an exchange of boundary conditions at the interface between the fluid and the structure. The coupling problem is reduced to the interface algorithm between the two. The following sections describe the procedure of this exchange.

1. Fluid field resolution

- a. The limiting condition applied for the interface temperature is the Dirichlet boundary condition.
 - b. The heat flux is obtained at the fluid-structure interface.
2. Transfer of information from the fluid to the structure. The boundary condition of convection (from fluid to structure).
 - a. The method of exchange of boundary conditions applied is the exchange of fluid temperature, T^{fluid} , and heat transfer coefficients (*film coefficients, h*) at the interface.

$$q = h \cdot (T^{\text{fluid}} - T^{\text{structure}}) \quad (18.4)$$

With:

q: Heat flux, h: heat transfer coefficient; T^{fluid} and $T^{\text{structure}}$: fluid and structure temperatures at the interface

- b. Transfer of the values **het** T^{fluid} from fluid to the structure.
3. Structure field resolution.
 - a. The boundary condition applied for the interface temperature is the Neumann boundary condition.
 - b. The temperature at the wall of the structure is obtained.
 4. Transfer of information from the structure to the fluid. Isothermal boundary condition (from structure to fluid).

$$T^{\text{structure}} = T^{\text{fluid}}$$

5. $T^{\text{structure}}$ at the interface is transmitted to the fluid (boundary condition).

18.5 Results

18.5.1 Impact of Fire on the Flow Field

The fire directly impacts the flow in the BT room. The following Fig. 18.8 details the evolution of the flow in the room before the fire starts, at the beginning of the fire (with the ventilation still activated), at the end of the fire (once the ventilation has been deactivated) and after the end of the fire. The images are presented with the scale adapted to the maximum value and in a view perpendicular to the fire door.

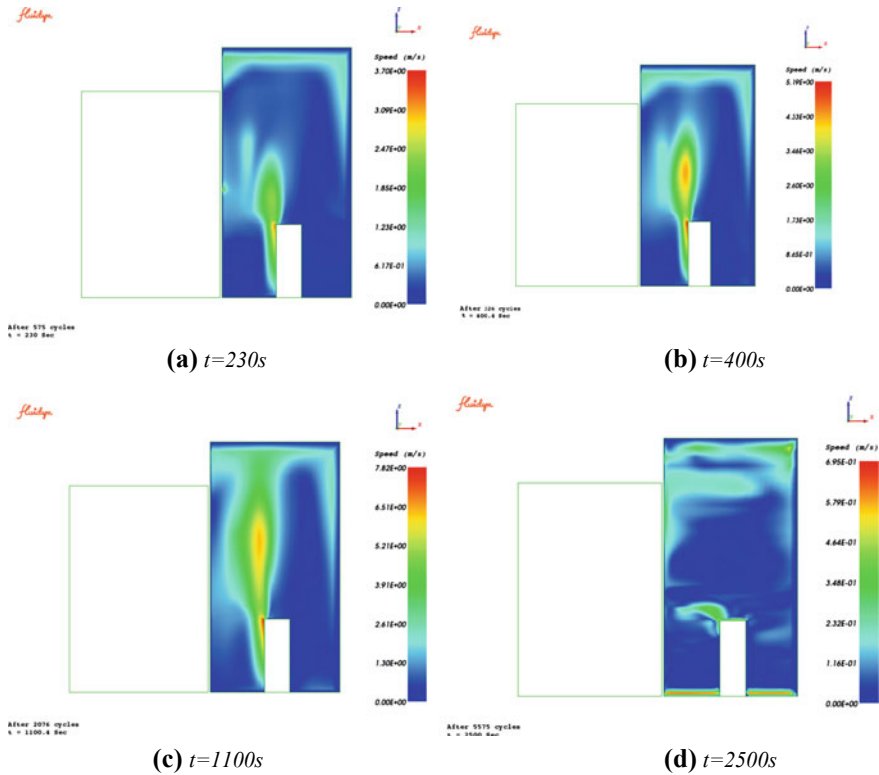


Fig. 18.8 Evolution of the flow field (velocity contours) (maximum of the scale at 0.547)

18.5.2 Temperature Inside the Room

The following Fig. 18.9 presents the evolution of the average temperature in the room.

The following Fig. 18.10 shows some iso-temperature contours at 900 °C to visualize the presence of the flame.

The following Fig. 18.11 details the evolution of the temperature in the room after the fire starts. The images are presented with the scale adapted to the maximum value and in a view perpendicular to the fire door.

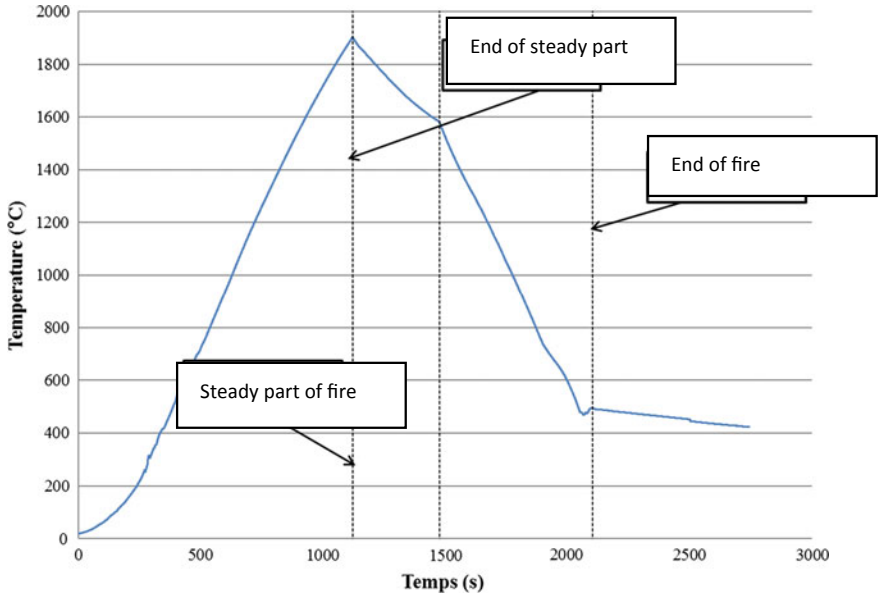


Fig. 18.9 Evolution of the temperature inside the room

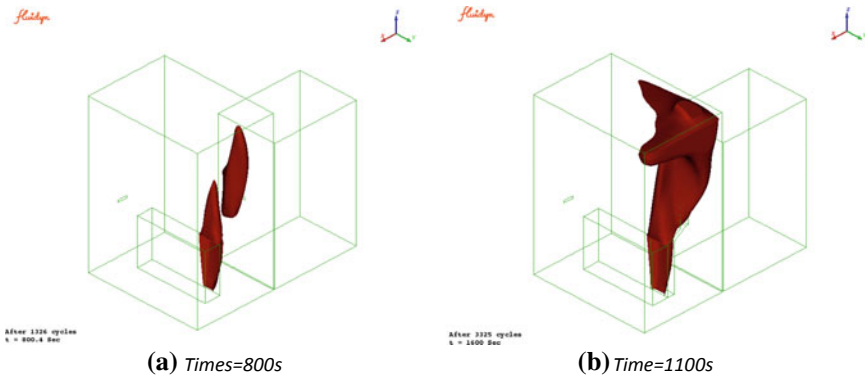


Fig. 18.10 Temperature isocontours 900 °C—Isometric view

18.5.3 Behavior of the Door

The following Figs. 18.12 and 18.13 show respectively the temperatures, the max von Mises stresses, as well as maximum deformations on the face of the door not exposed to the fire at the maximum.

A focus on the deformations of the door layers and the doorstep is shown in Fig. 18.14.

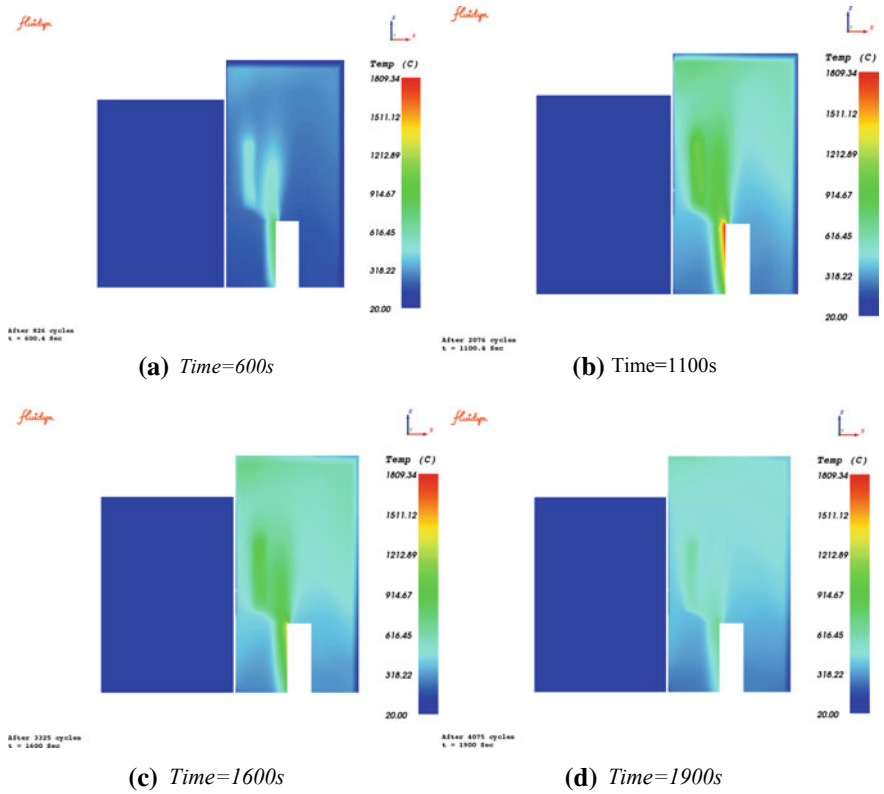
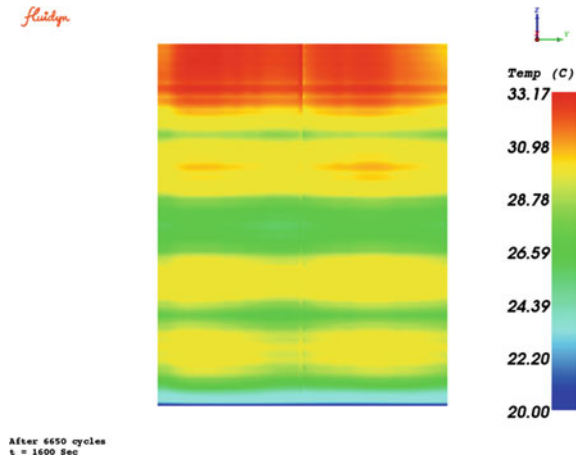


Fig. 18.11 Evolution of the temperature inside the room (scale maximum at 1810 °C)

Fig. 18.12 Temperature contours at the maximum on the non-exposed door face



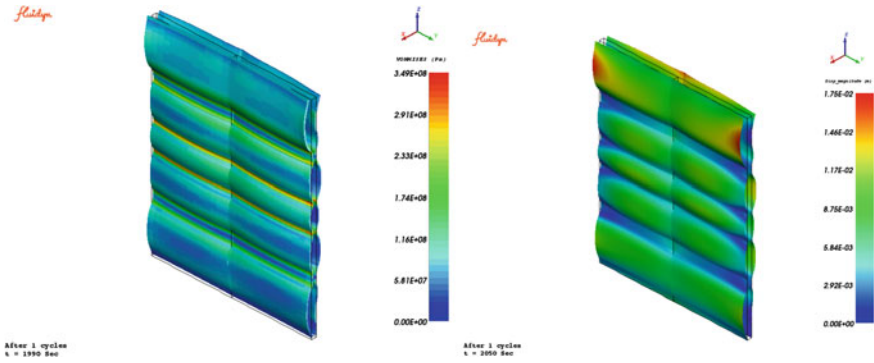


Fig. 18.13 Stress contours at the maximum on the non-exposed door face (left)—Maximum door deformation (right)

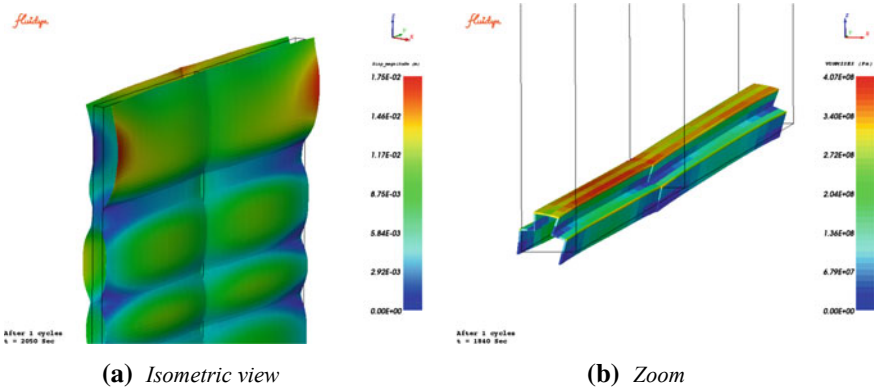


Fig. 18.14 Deformation of the door layers (left) and the doorstep (right)

18.5.4 Heat Transfer Behind the Door

The following Fig. 18.15 presents the radiative flux experienced by the adjacent room behind the fire door.

18.6 Conclusion

This study proposes to simulate and analyze the behavior of a fire door designed to withstand a one-hour fire subjected to a realistic cable fire of one hour and a half an industrial unit containing an electrical cabinet. The parameters of the fire (power output and duration) were set up according to the quantity of cables available in the cabinet and in agreement with the literature. The simulation was performed

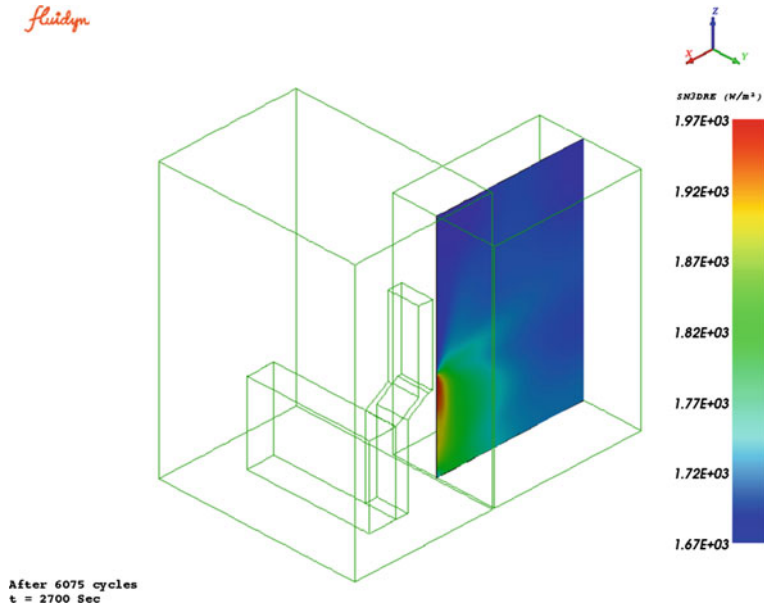


Fig. 18.15 Radiative flux in a vertical section in the adjacent room

using a multiphysics tool, with a strong coupling between finite volume CFD and finite element CSM, fluidyn-VENTFIRE. The behavior of the door is checked for the following criteria:

- The maximum radiation value in the delivery hall does not exceed 2 kW/m^2 , which is well below the limit of 15 kW/m^2 .
- The average temperature of the unexposed surface of the door does not exceed $140 \text{ }^\circ\text{C}$ (maximum average temperature of $39 \text{ }^\circ\text{C}$).
- The temperature of the unexposed surface does not exceed $180 \text{ }^\circ\text{C}$ (maximum temperature of $49 \text{ }^\circ\text{C}$).

The present simulation shows that even in the absence of data on a full-scale testing, the fire door may withstand a realistic fire situation.

References

1. PN ISI.: Caractérisation des foyers—4 janvier (2011)
2. SFPE Handbook of Fire Protection, 5th edn. Springer
3. Fire PRA Methodology for Nuclear Power Facilities, vol. 2. NUREG/CR-6850
4. Dumont, F.: Essais de résistance au feu. Université de Liège, Belgique
5. EN 1634–1.: Fire resistance test for door and shutter assemblies—Part 1: fire doors and shutters. Danish Institute of Fire and Security

6. Coutin, M., Such, J.M., Piller, M.: Etude expérimentale du rayonnement thermique induit par un feu d'armoire électrique. IRSN (2007)
7. Beji, T.: Modélisation CFD d'un incendie en milieu ouvert généré par des câbles disposés dans des chemins de câbles horizontaux. Université de Gand, Belgique
8. Zavaleta P., Hanouzet, R.: Evaluation simplifiée de la puissance d'un feu de chemins de câbles électriques. IRSN (2016)
9. McGrattan, K.S.: Bareham, Heat Release Rates of Electrical Enclosure Fires (HELEN-FIRE). U.S.NRC (2016)
10. Jasak, H.: Error analysis and estimation for the finite volume method with applications to fluid flows. Ph.D. Thesis, Dept. of Mechanical Eng., Imperial College of Science, Technology & Medicine, London (1996, June)
11. Anderson, W.K., Thomas, J.L., van Leer B.: Comparison of finite volume flux vector splitting for the euler equations. AIAA J. **24**(9) (1986, September)
12. Kennedy, J.M., Belytschko, T., Lin. J.T.: Recent developments in explicit Finite Element techniques and their application to Reactor Structures. Nuclear Eng. Design **97** 1–24 (1986)
13. Cebal, J.R., Lohner, R.: Conservative load projection and tracking for fluid-structure interaction problems. AIAA J. **35**(4), 687–692 (1997)
14. Felippa, C.A., Park, K.C., Farhat, C.: Partitioned analysis of coupled mechanical systems. Comput. Methods Appl. Mech. Eng. **190**, 3247–3270 (2001)
15. Barone, M.F., Payne, J.L.: Methods for simulation-based analysis of fluid-structure interaction. Sandia Report, SAND2005-6573 (2005, October)
16. Chen, Y.S., Kim, S.W.: Computation of Turbulent flows using an extended k- ϵ turbulence closure models. NASA CR-179204(1987)
17. Chenthil Kumar, K., Anil Kumar. K.R., Amita T.: A unified 3D CFD model for jet and pool fires. Hazards 25, 2017 Conference (2017)

Chapter 19

Modeling of Aircraft Arresting Gear System by Multibody Dynamics Approach and Co-Simulation of Multibody Dynamics With Hydraulic System Using Adams and Easy5



S. Mohan Raju, H. G. Manjunath, Naveen Narayan and C. Ganga Reddy

Abstract Arresting gear system is a system used to decelerate and arrest the aircraft as it lands on the aircraft carrier. Aircraft with a mass of 10–11 tons traveling at a speed of 250–260 km/hr has to come to rest within a span of 90 m as it lands on the aircraft carriers flight deck. The tail hook of the aircraft landing on the deck of aircraft carrier engages on one of the four deck pendants. The force developed due to the forward motion of the aircraft landing on the deck is transferred to the aircraft recovery equipment or the hydraulic system under the deck through the purchase cable, which is used to absorb the kinetic energy developed by landing the aircraft. The arresting gear system above the deck of cable and pulley arrangement is modeled using cable module of MSC ADAMS. Aircraft recovery equipment below the deck is modeled with a hydraulic system using EASY5. Co-simulation of ADAMS and EASY5 is performed to obtain the characteristics of the arresting gear system. The aircraft deceleration or arrestment occurs mainly from the arresting engine placed below the deck. The coupling between the arresting engine below the aircraft carrier deck and arresting cable above the deck was a challenging task. The coupling of arresting cable and hydraulics control systems modeled using multibody dynamics and system-level design is achieved by co-simulation of both the systems using multibody dynamics tool (ADAMS) and hydraulics tool (EASY5—system-level control design).

S. Mohan Raju (✉) · H. G. Manjunath · N. Narayan · C. Ganga Reddy
HCL Technologies, Bangalore, India
e-mail: Rajus.m@hcl.com

H. G. Manjunath
e-mail: manjunatha_h@hcl.com

N. Narayan
e-mail: naveen.narayan@hcl.com

C. Ganga Reddy
e-mail: Gangareddy.C@hcl.com

Keywords Aircraft arresting gear system · Aircraft recovery equipment · ADAMS · EASY5 · Co-simulation of ADAMS and EASY5 · Multibody dynamics · Hydraulic simulation

19.1 Introduction

To land the aircraft on an aircraft carrier, the aircraft has to be stopped within a span of 100 m after contacting the deck, which is achieved by the use of aircraft recovery equipment called as the hydraulic arresting engine placed below the deck. The hydraulic engine absorbs the kinetic energy developed by the landing aircraft. It is commonly used in both CATOBAR and STOBAR aircraft carriers.

When the aircraft lands on the aircraft carriers deck, the aircraft's tail hook opens up and engages any one of the four deck pendants. If the tail hook does not engage any one of the four deck pendants/rope, it has to take off, hence the aircraft travels at the same thrust which is required to take off. Once the aircrafts tail hook engages the rope, the kinetic energy is transferred to the hydraulic actuator in the arresting engine through the cable. Thus, the absorption of kinetic energy by the hydraulic system will decelerate the aircraft.

19.1.1 Arresting Gear System

Arresting gear system consists of hydraulic system called the arresting engine, which is placed below the aircraft carrier deck, and the cable system wrapped around a set of pulleys, which is connected to the arresting engine through a moveable sheave. The subunits of arresting engine assembly consist of an engine system (piston cylinder connected to a cam valve unit), the accumulator system a damper sheave system, and an anchor damper system [3].

While an aircraft landing on the carrier's deck, the tail hook of the aircraft engages on any one of the four ropes of the cable system placed above the deck. As the aircraft moves forward at high speed, force is developed due to the tail hook and rope/cable engagement. This force from the tail hook and rope contact is transferred to the arresting cable, which is wound around the movable sheave (crosshead) and fixed sheave assembly.

The arresting engine is located below the aircraft carrier's deck and the moveable sheave of the arresting cable is connected to the engine or piston ram assembly below the flight deck. When the cable or rope called as receiving cable is dragged out on the flight deck due to the force exerted by the aircraft tail hook and rope engagement, the moveable crosshead moves toward the fixed sheaves, which are attached to the engine frame at the opposite end of the arresting engine from the crosshead. As the crosshead moves toward the fixed sheaves, the piston ram connected to the crosshead moves forward, thereby forcing the hydraulic fluid out of the piston cylinder and eventually

the fluid passes through a variable orifice called as a control valve and finally to the accumulator. The purpose of the control valve is to achieve a smooth and controlled aircraft arrestment, which works as a variable flow orifice by controlling the fluid flow from the piston; henceforth, the movement of piston ram (position) in the piston cylinder is governed by control valve which creates a pre-calculated pressure in the cylinder by closing the orifice, thereby exerting retarding force to the moveable crosshead and finally to the aircraft.

Once the aircraft comes to rest, the aircraft tail hook is disengaged from the cable and the cable gets back to its original position by the action of a retracting control lever [1–3].

Zhu et al. explain in Ref. [4] that CROV valve can be designed to stop any type of aircraft variants such as aircraft with different mass and varying speed in the same amount of stopping distance on the carrier's deck, and the constant run out valve is the heart of the hydraulic engine. It controls the amount of hydraulic fluid flow from the piston cylinder and the actuator. It is possible to arrest any aircraft with different weight or speed by controlling the CROV valve opening area, thereby developing pressure inside the actuator system which resists the motion of movable sheave and finally decelerating the aircraft on the carrier deck within the specified distance of 100 m [4].

While arresting the aircraft, the hydraulic fluid is forced out of the engine cylinder (actuator) and passes through the constant run-out valve to reach the accumulator. The initial air pressure of 400ψ in the accumulator gets increased up to 600ψ during arresting. This increased pressure pushes the fluid out of the accumulator and to the fluid cooler [4] (Fig. 19.1 and 19.2).

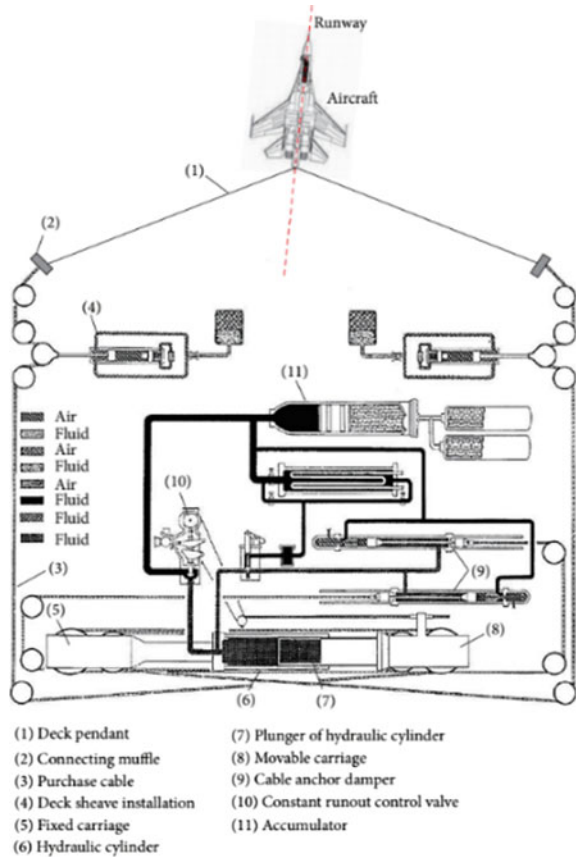
The volume in the accumulator varies with the displacement of fluid from the main engine cylinder. Since it is not an exact function, i.e., varies with piston area and ram stroke, it was necessary to interpolate from the known initial and final conditions to determine how this volume varies. It is known for most aircraft arrestments, which the pressure in the accumulator varies between 400 and 650ψ over a complete ram stroke [1].

Mikhailuk et al. [2] have studied the efficient arrestment of deck-fighters of masses 10 – 25 tons with a landing speed of 240 km/hr. using LS Dyna and Delphi code makes multiple restarts during the simulation for continuous changes in stiffness and damping curves.

19.2 Methodology

The tail hook of the landing aircraft engages the cable (rope) and while moving forward due to higher velocity, the force from the cable is transferred to arresting equipment (hydraulic engine placed below the deck) through the cable and pulley arrangement; therefore, the whole aircraft arresting gear system is modeled and developed by multibody dynamics approach in two steps.

Fig. 19.1 Principle of operation (arresting engine) [3]



The arresting gear system above and below the deck consists of cable and pulley arrangement is modeled using a cable module of MSC ADAMS detailed in Sect. 19.2.1

Aircraft recovery equipment/arresting engine below the deck is modeled with a hydraulic system using EASY5 detailed in 19.2.2.

Hydraulic system or the arresting engine below the deck is modeled in such a way that it can be used to arrest any type of aircraft variants, such as aircraft traveling or approaching the deck at higher speed, various aircraft with different weights, etc. The resistance developed by the hydraulic cylinder depends on the velocity of aircraft/cable end connected to piston—which in turn depends on the resistance—thus, it is a coupled system—which requires a co-simulation approach for the integration of hydraulic system behavior (Easy5) with that in ADAMS as real-time simulation of the motion of aircraft after latching on to the cable.

Co-simulation of multibody dynamics/cable module (ADAMS) and system-level controls/hydraulic system (EASY5) is performed to obtain the dynamics of arresting

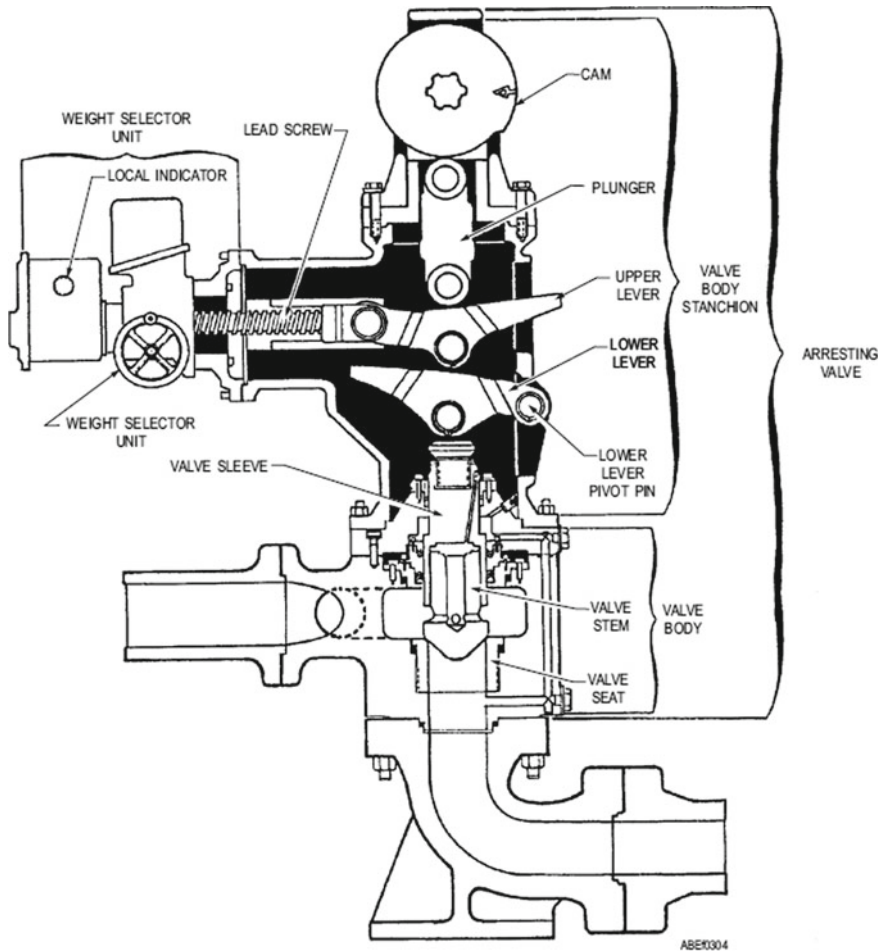


Fig. 19.2 CROV valve [5]

gear system, wherein ADAMS and EASY5 communicate each other to solve different states referenced with time till the aircraft gets arrested as shown in the schematic Fig. 19.6 through Fig. 19.9.

19.2.1 The Arresting Gear System Is Modeled by Multibody Dynamics Approach

Arresting gear system consists of pulley and cable arrangement modeled using MSC ADAMS is shown in Fig. 19.3. The geometrical parameters of cable/rope are listed

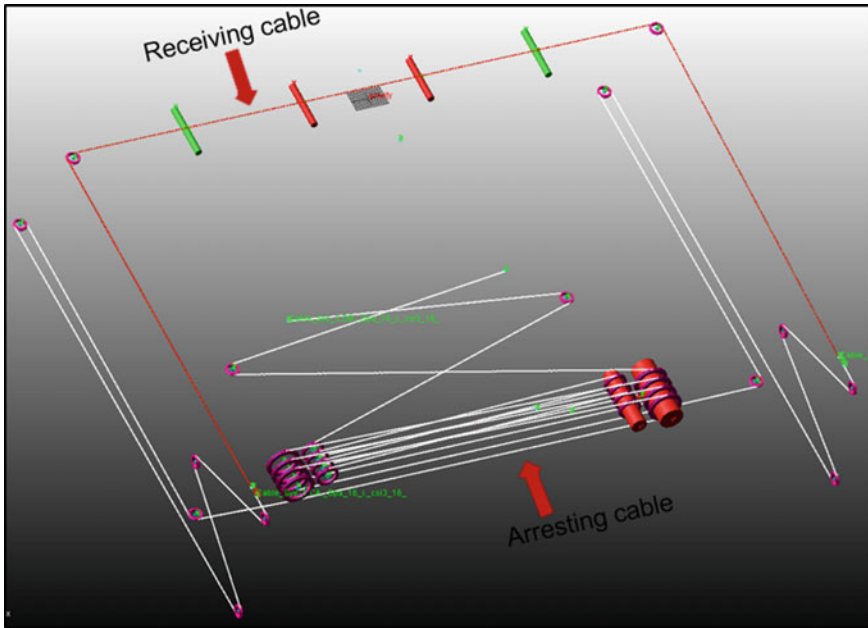


Fig. 19.3 ADAMS model showing cable and pulley arrangement above and below the deck

in Table 19.1. Cable/rope system is modeled using two types of cables connecting each other. Aircraft hook which engages the cable is called receiving cable and the one which passes along the set of pulleys and sheaves is called the arresting cable. The receiving cable is modeled using discretized (mesh) cable which acts as a solid rigid body henceforth obtaining a dynamic contact between aircraft hook and the cable. The arresting cable is modeled using a simplified cable which behaves as a one-dimensional linear spring which is very simple and efficient in studying the mechanism. Thus, by considering both discretized and simplified cable, solution run time can be reduced to an hour. If we consider only discretized cable all along the sheaves and pulleys, simulation run time will be high enough, since our model is built for 695 m (330 + 365 m) of cable and the contact dynamics will be changing for each element contact (based on number of mesh) for each time step, henceforth increasing the background calculation time (Fig. 19.3).

The receiving cable of the arresting gear system is modeled in such a way that the tail hook can get underneath to catch it, i.e., the cable is placed in the air above the deck for a few inch with the help of a leaf plate as shown in Fig. 19.4, allowing the tail hook to engage the cable.

Boundary conditions such as aircraft mass of 11 tons and an initial speed of 260 km/hr. is applied on aircraft geometry, translation joint in the negative X -direction is applied to the set of pulleys on the right (arresting cables) which is defined as a movable sheave. Once the boundary conditions and initial velocity to the aircraft is

Table 19.1 Dimensions of the cable system

Sl. no.	Cable/rope parameters		Description	Unit
1	Diameter of receiving cable and arresting cable	Dr	$36.5 + 2$	mm
2	Receiving cable length	Lr	27 ± 0.05	m
3	Arresting cable lengths	L1	330	m
		L2	365	m

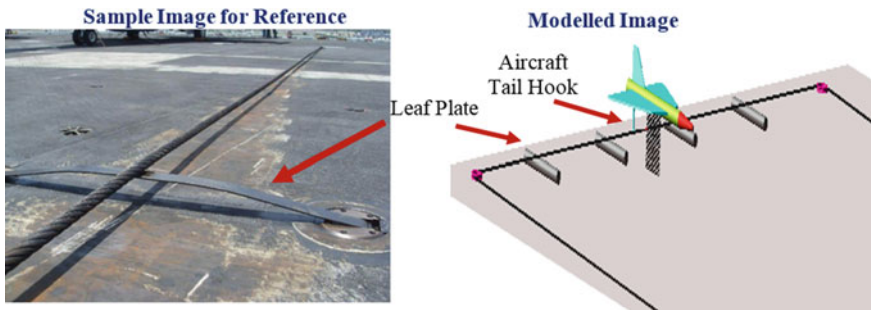


Fig. 19.4 Create cable and pulley using cable module of ADAMS machinery

provided and simulation is done in Msc Adams, which shows that the arresting hook of incoming aircraft due to the initial speed of 260 km/hr engages the cable and the force due to the forward motion of aircraft is transferred to movable sheave through the cable. Moveable sheave (set of the large and small pulley in the arresting side) is considered to move up to 4 m. This force from the movable sheave is transferred to piston of a single-chamber actuator modeled in EASY5 through ADAMS EASY5 co-simulation (Fig. 19.5 and 19.6).

19.2.2 Arresting Engine Below the Aircraft Carrier’s Deck Is Modeled Using EASY5

The arresting engine below the Carrier’s deck is modeled using hydraulics library of EASY5, and the modelled block-based circuit of the hydraulic system is shown in Fig. 19.7 which consists of an actuator, a fixed orifice, a variable orifice, and an accumulator. Ethylene glycol 60/40 is used as the hydraulic fluid in arresting engine system.

Co-simulation between ADAMS and EASY5 is performed, and in ADAMS, the tail hook of the landing aircraft engages the cable and force due to the forward motion

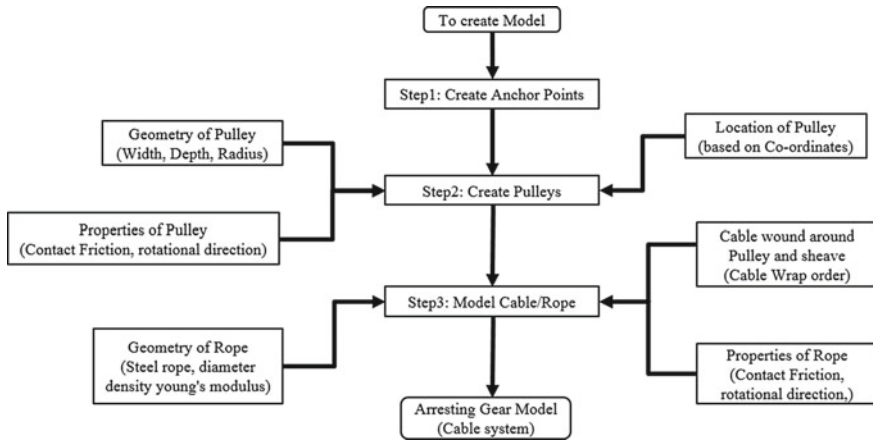


Fig. 19.5 Create cable and pulley using cable module of ADAMS machinery

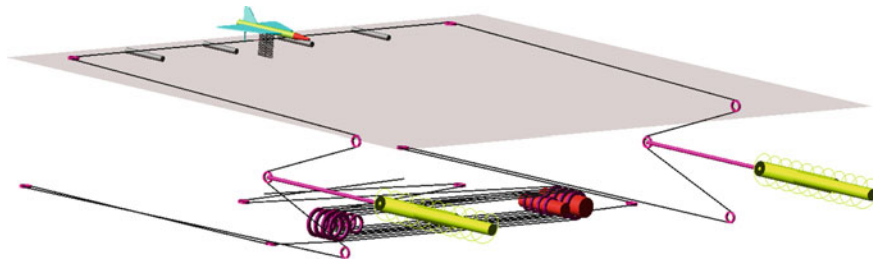


Fig. 19.6 ADAMS model while co-simulation, tail hook engaging the cable

of aircraft is transferred to the movable sheave through the cable. The force from the movable sheave is applied on the piston of a single-chamber actuator modeled in EASY5 through ADAMS interface.

Principle of Operation

Due to the applied force on the actuator, the piston moves in positive direction creating pressure in the extended chamber due to which the fluid flows out of the actuator and passes through the fixed orifice, variable orifice, and intern to the accumulator, where the fluid gets accumulated.

CROV Valve/Variable Orifice: The variable orifice is modeled to behave as a CROV valve, wherein the orifice area is reduced as the actuator piston moves forward, i.e., variable orifice creates pressure by reducing the area of orifice based on the position of the piston in actuator shown in Fig. 19.14. This fluid pressure created in variable orifice (CROV valve) and single-chamber actuator will apply a resisting force on the movable sheave in ADAMS through ADAMS interface, thereby absorbing the energy created by aircraft and henceforth bringing the aircraft to rest.

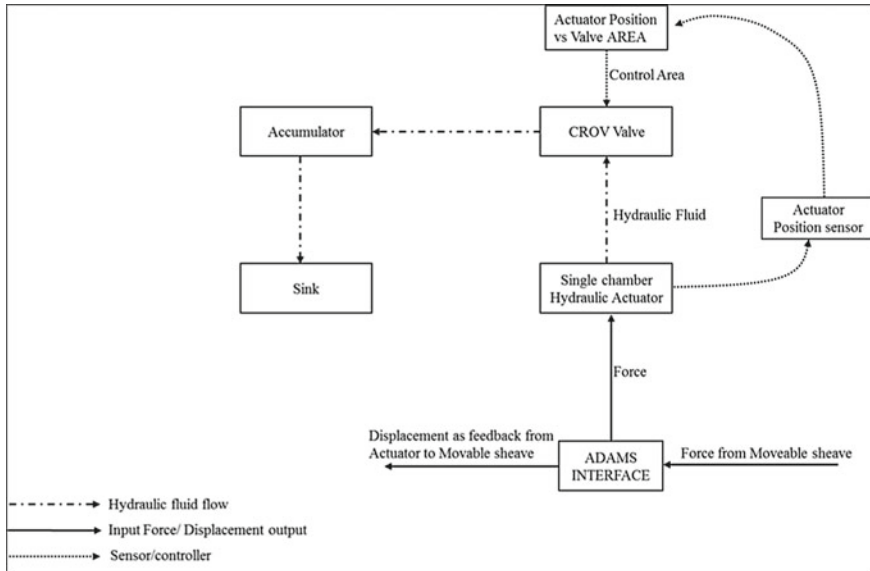


Fig. 19.7 Integrated arresting gear hydraulic schematic (Easy5)

Being velocity dependent, the behavior of the hydraulic system is not representable directly in ADAMS and so the co-simulation with Easy5 is required for accurate prediction of the stopping distance, force encountered, etc., for various masses and velocities of the aircraft. So, co-simulation has been found to be a better option to evaluate the arresting gear system before any experiments/tests are held (Figs. 19.8 and 19.9).

19.3 Results and Discussion

It can be concluded from observations of co-simulation results that aircraft gets arrested at 2 s. Figure 19.10 through Fig. 19.14 shows the velocity of aircraft, displacement of aircraft on the flight deck in meters, displacement of the piston (piston position observed in EASY5), displacement of movable sheave (from ADAMS), and area of variable orifice based on piston position. Figure 19.15 shows the summary of all results, and it is over a plot of aircraft velocity and displacement curves.

Figures 19.10 and 19.11 follow the observations similar to the deceleration curves shown in Ref. [2]; henceforth, it is clear that aircraft gets arrested before it reaches 90 m within a time of 2 s. Figure 19.12 shows the displacement of piston and Fig. 19.13 shows the displacement of movable sheave following the same path as the displacement of the piston, which indicates movable sheave and piston move in tan-

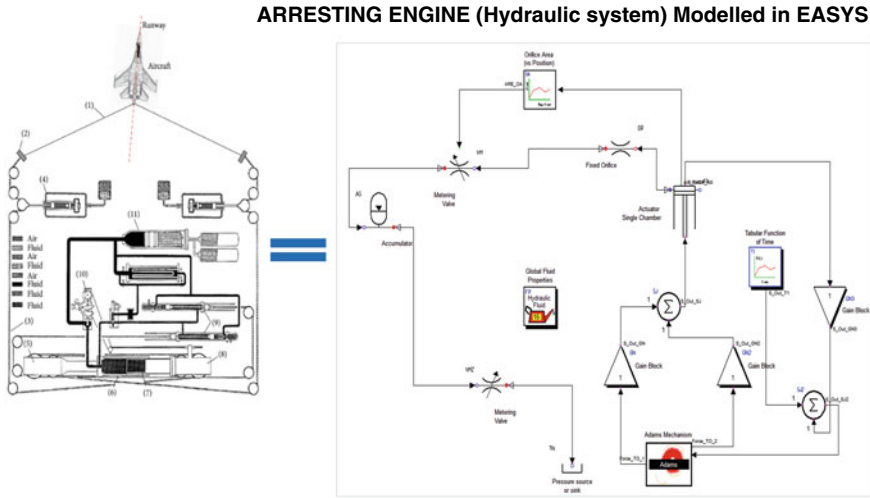


Fig. 19.8 A sample image showing the model of arresting engine

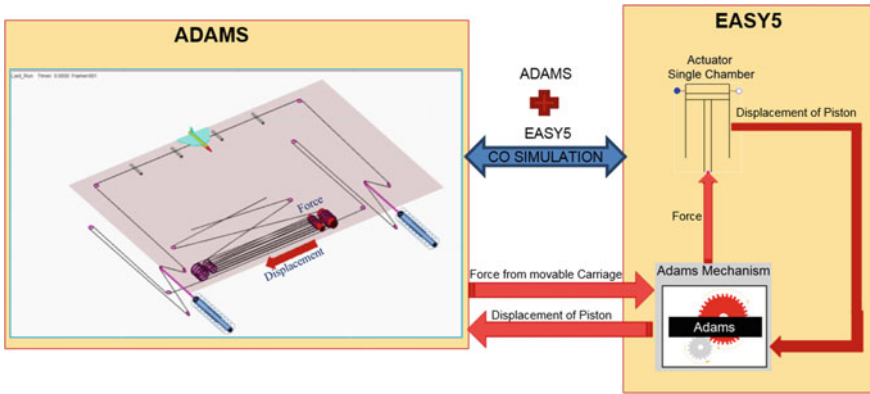


Fig. 19.9 Co-simulation of ADAMS and EASY5, showing the motion of aircraft after the engagement of the cable and aircraft hook

dem, thereby confirming that the co-simulation occurs and data exchange between ADAMS and EASY5 occurs in each time step provided (Figs. 19.14 and 19.15).

19.4 Conclusion

In this study, arresting gear system was developed in ADAMS and hydraulic arresting engine in EASY5 and performed co-simulation to obtain the characteristic curves

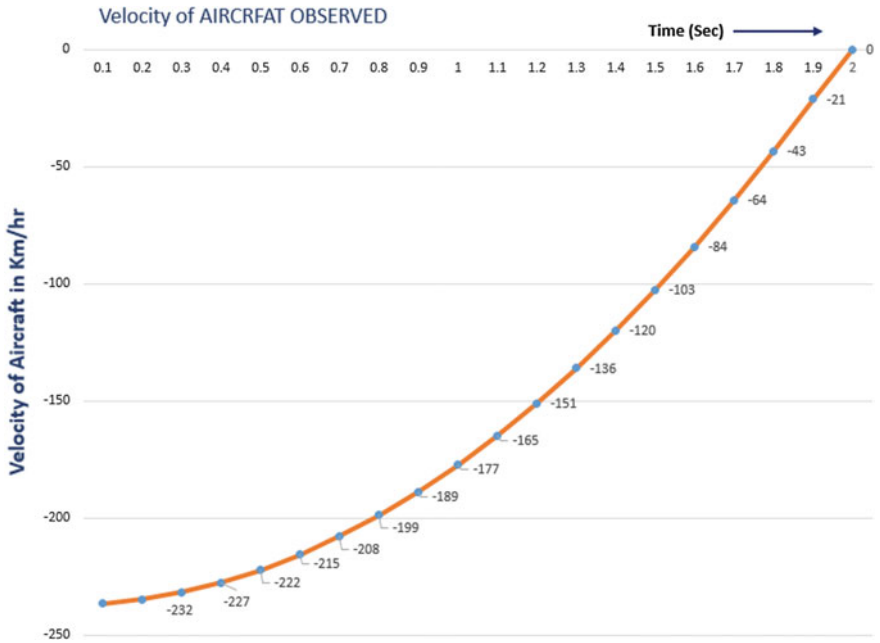


Fig. 19.10 Velocity of aircraft (Km/hr.)

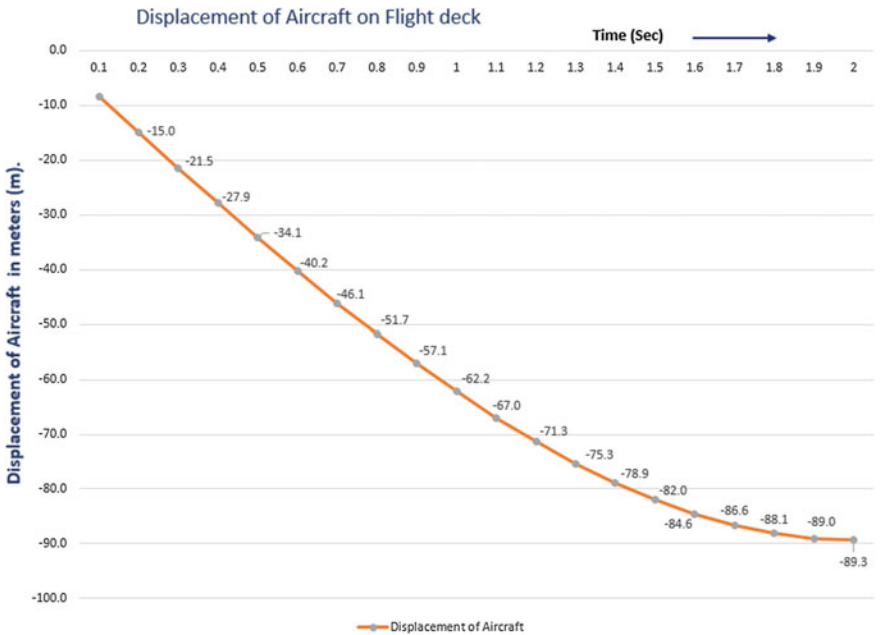


Fig. 19.11 Displacement of aircraft in “Y” direction

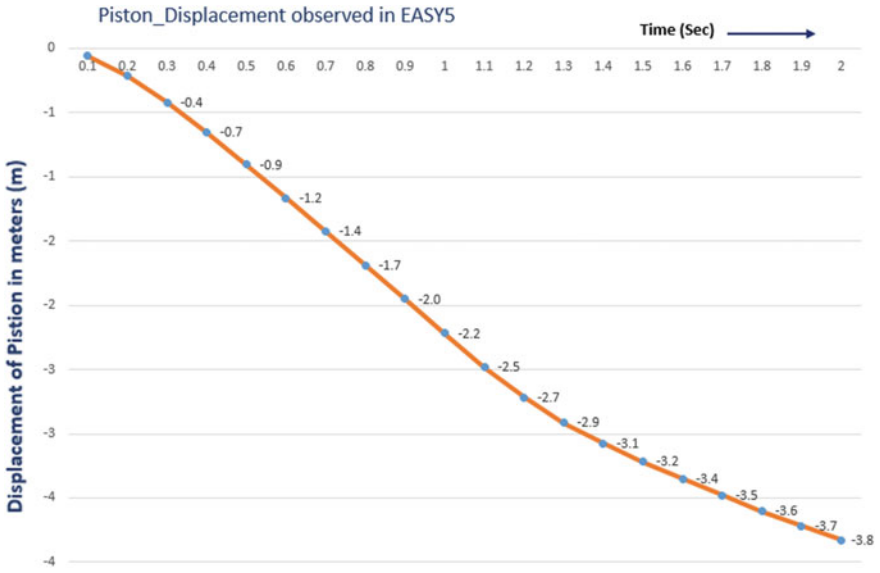


Fig. 19.12 Displacement of piston (m) in arresting engine (below the aircraft carriers deck) observed in EASY5 (hydraulics)

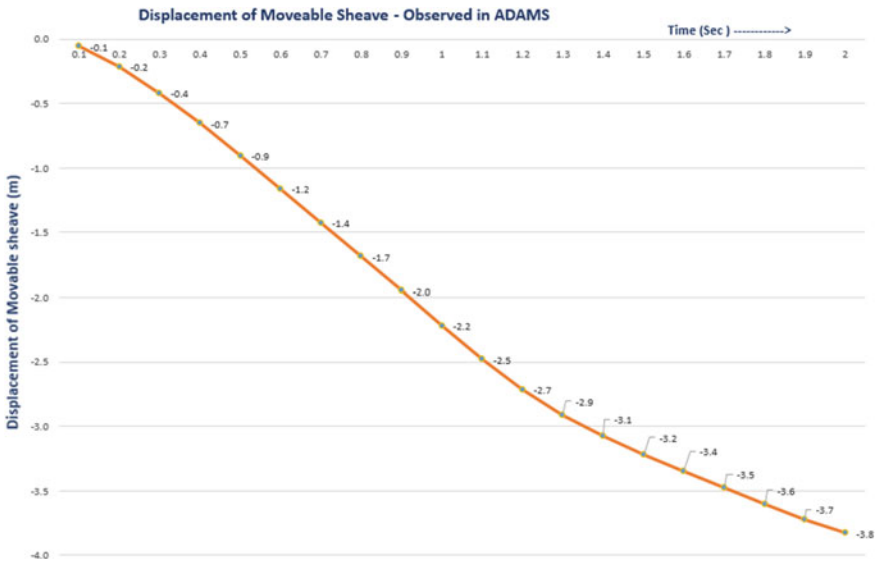


Fig. 19.13 Displacement of movable sheave in ADAMS (m)

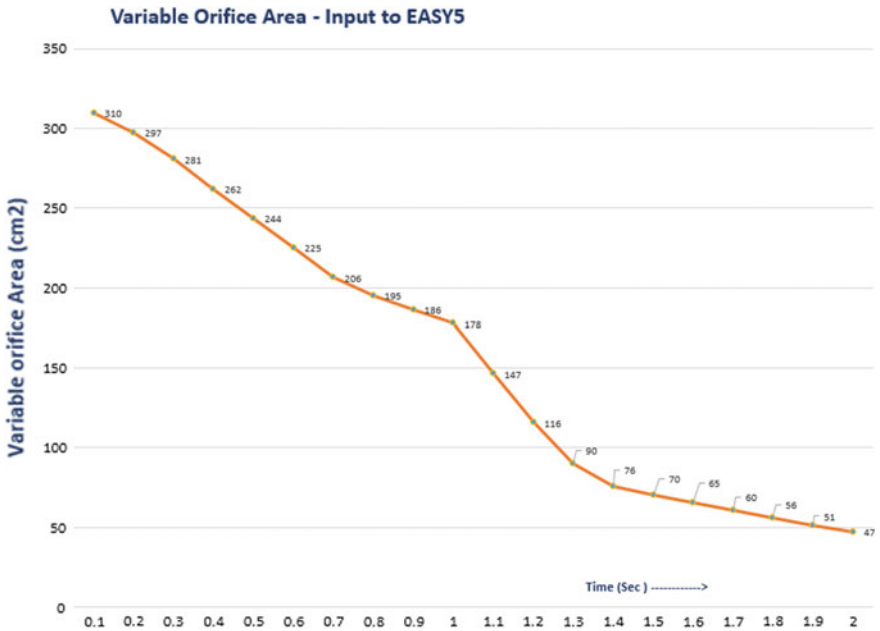


Fig. 19.14 Area of variable orifice based on piston position (closed loop detailed in Fig. 19.7)

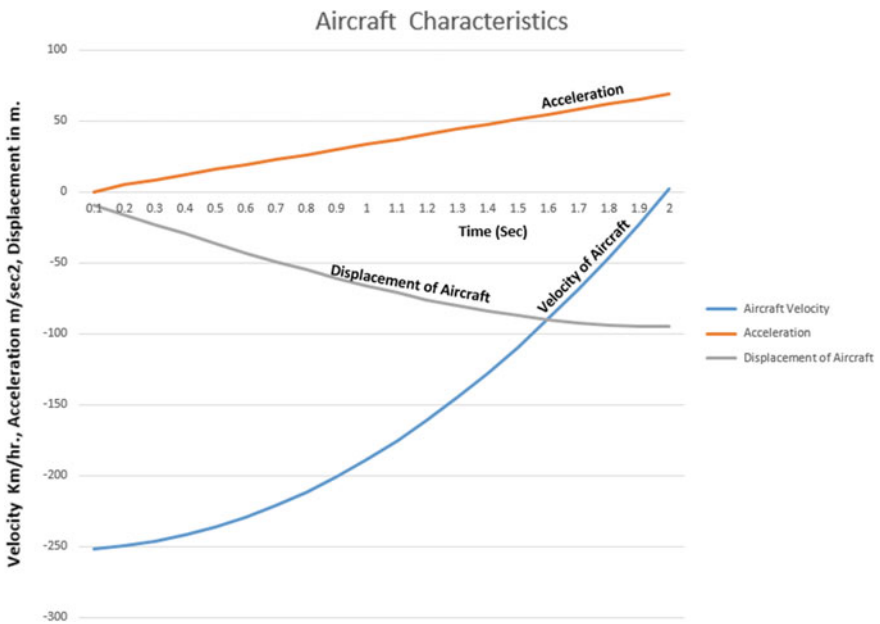


Fig. 19.15 A summary showing the over plot results of aircraft velocity, its acceleration and displacement

which illustrate the behavior of aircraft and the hydraulic system placed below the deck.

The investigation reveals that the aircraft landing at a speed of 250–260 km/hr can be arrested within a span of 90 m by controlling CROV valve based on the ram position.

CROV valve can be designed based on the aircraft weight/speed to arrest the aircraft within 90 m. From results plotted above aircraft, speed goes on decelerating with respect to time and comes to rest at 2 s.

It has been learned that ADAMS and EASY5 offer a benefit of investigating the dynamics of complex mechanisms and transfer of loads/forces across the systems.

This system-level design validation improves efficiency and reduces development cost.

References

Book

1. Naval Air Engineering Center.: Report NAEC-91-7927. A study of the effect of different cam designs on Mk7 Mod 1 arresting gear performance. Commander, Naval Air Systems Command AIR-5372 Washington, D.C. 20361 (1978, August 2)

Conference

2. Mikhailuk, D., Voinov, I., Borovkov, A.: Mechanics and control process Dept. of St. Petersburg State Polytechnical University. Finite element modeling of arresting gear and simulation of the aircraft deck landing dynamics. In: ENOC-2008, Saint Petersburg, Russia, June 30–July 4 (2008)
3. Zhu, Q., Wen, Z., Zhang, Z., Yu, Y.: College of Automation, Harbin Engineering University, Harbin 150001, P. R. China. Shipboard aircraft arresting system modeling and simulation. In: 2012 Second International Conference on Instrumentation & Measurement, Computer, Communication and Control, 2012 IEEE, China (2012)
4. Zhu, Q., Li, X., Lv, K.: Department of Automation, Harbin Engineering University, Harbin 150001, P. R. China. Modeling and simulation for arrested landing of carrier-based aircraft. In: Proceedings of the 2011 IEEE International Conference on Mechatronics and Automation, August 7–10, Beijing, China (2011)
5. Zhu, Q, Li, X., Lv, K.: College of Automation, Harbin Engineering University, Harbin 150001, P. R. China. Mathematical model and simulation of a hydraulic arresting gear system. In: Proceedings of the 30th Chinese Control Conference, July 22–24, Yantai, China (2011)

Chapter 20

Design and Optimization of Knuckle of an All-Terrain Vehicle



Aditya Kulkarni, Aditi Bang, Akanksha Hundekari, B. G. Akshata, Arun Y. Patil and B. B. Kotturshettar

Abstract This study aims at designing, optimizing, and performing static analysis on front steering knuckle of a rear driven single seater. All-Terrain Vehicle (ATV). Weight reduction was carried while retaining satisfactory Factor of Safety (FOS) and structural strength. In the first step, the component was modeled using a licensed version of SOLIDWORKS® 2016 and was initially analyzed with two different materials—aluminum and EN8. The knuckle was designed as per constraints set by suspension, steering, and wheel assemblies. In the next step, the analysis was carried out in licensed finite element software of ANSYS® WORKBENCH™ by applying constraints and loads such as braking moment, cornering force, bump force, steering effort, lateral and longitudinal load transfer. Automated meshing with the sphere of influence at stress-prone areas was used for precise analysis. Second-order hex-dominant mesh type was employed for computation and convergence graph was plotted. The feasible material was chosen out of the two based on results and shape optimization was performed for two designs by adding material to sites that are subjected to higher stress than safety factor permits and removing material from low stress areas. Results were compared based on von Mises stress analysis and total deformation. A comparative study was carried out with analytical and simulation results and percentage of error was extracted from interpretation. A 3D printed

A. Kulkarni · A. Bang · A. Hundekari · B. G. Akshata · A. Y. Patil (✉) · B. B. Kotturshettar
KLE Technological University, Hubballi, India
e-mail: Patilarun7@gmail.com

A. Kulkarni
e-mail: kulkamiaditya666@gmail.com

A. Bang
e-mail: aditibang11@gmail.com

A. Hundekari
e-mail: akanksha811.aa@gmail.com

B. G. Akshata
e-mail: akshatabg104@gmail.com

B. B. Kotturshettar
e-mail: bbkshettar@gmail.com

model was also created in order to interpret the component's physicality on the vehicle. Overall endorsement for the viability of design and fabricated component was provided by testing it on the vehicle.

Keywords Steering knuckle · Finite element analysis (FEA) · Weight reduction · Optimization

20.1 Introduction

BAJA SAE, the ATV design event provides a platform for undergraduate students to apply the principles of engineering science to expose their proficiency in the automotive world. The object of the competition is to simulate real-world engineering design projects and their related challenges. The event is organized by SAEINDIA and Mahindra & Mahindra every year.

Steering knuckle also known as upright is classified into spindle type and hub type. For the study, knuckle with spindle has been chosen. Knuckle is an important component which connects the wheel assembly to the chassis of the vehicle through the steering and suspension system. The design process started with a preliminary study on the existing steering knuckle used for the previous ATV including. The design also needs to follow the criteria and regulations drawn by BAJA organizer, mainly depends on suspension as well as steering geometry [8]. The vehicle wheel is connected to the exterior part of the knuckle with the help of spindle. The knuckle takes the load from wheels and transfers these forces to the suspension system. The vehicle encounters rough terrain which imparts heavy loads to the wheel assembly. Knuckle plays an important role in transferring the active loads to the designed suspension system. Further, the brake calipers and mounting of tie rod of the steering sub system also affects the design of the knuckle. In the present study, the design of a durable and reliable steering knuckle for an ATV is being the ultimate aim to be achieved. Hence, the knuckle being an integral part was designed and optimized.

20.2 Methodology

This section deals with analytical calculation [1, 2], finite element method used, loading conditions on component and material selection procedures. Also, the justification for the choice of meshing has been stipulated.

20.2.1 Analytical Calculations

- Steering force

Steering axis inclination (λ) = 6.74°

Caster angle (μ) = 2.6°

Scrub radius (d) = 60.4 mm

Inner angle (δ) = 50.27°

$$\begin{aligned} \text{Moment to overcome SAI axis} &= (FZR + FZL) \times d \times \sin \lambda \times \sin \delta \\ &= 80,159.50 \text{ N-mm} \end{aligned} \quad (20.1a)$$

$$\begin{aligned} \text{Moment to overcome offset of caster trail} &= (FZR - FZL) \times d \times \sin \mu \times \cos \delta \\ &= 821.38 \text{ N-mm} \end{aligned} \quad (20.1b)$$

$$\begin{aligned} M_T &= 8019.50 + 821.38 \\ M_T &= 8840.88 \text{ N-mm} \end{aligned} \quad (20.1c)$$

$$\begin{aligned} \text{Aligning torque - friction couple } (M_f) &= \text{Centrifugal force} \times d/2 \times \sin \mu \times \sin \delta \\ M_{\text{eff}} &= M_f + M_T \\ &= 47,862.03 + 8840.88 \\ &= 56,702.91 \text{ N-mm} \end{aligned} \quad (20.1d)$$

The tangential force across the pinion is given by

$$M_{\text{eff}} = F_T \times \text{steering arm} \quad (20.1e)$$

Steering arm length = 115 mm

$F_T = 493.06 \text{ N-mm}$

For accurate mounting and moderate shocks:

$$P_{\text{eff}} = (K_a \times k_m) \times F_T \times K_v \text{ (from design data book)} \quad (20.1f)$$

$P_{\text{eff}} = 318.5 \text{ N}$

Steering force = **318 N**

- Braking moment

Force on the push rod

$$\begin{aligned} F_1 &= F_a \times h \\ &= 250 \times 5 = 12,500 \text{ N} \end{aligned} \quad (20.2)$$

Pressure on the master cylinder

$$\begin{aligned}
 P_{mc} &= F_1/A_1 \\
 &= 1250/2.85 \times 10^{-4} = 4.38 \text{ MPa}
 \end{aligned}
 \tag{20.2a}$$

Force calculated for caliper

$$\begin{aligned}
 F_c &= P_{mc} \times A_{\text{calliper}} \\
 &= 4.38 \times 10^6 \times 12.3 \times 10^{-4} \\
 &= 5387.4 \text{ N}
 \end{aligned}
 \tag{20.2b}$$

$$\begin{aligned}
 F_{\text{clamp}} &= 2 \times F_c \\
 &= 2 \times 5387.4 = 10,774.8 \text{ N}
 \end{aligned}
 \tag{20.2c}$$

$$\begin{aligned}
 F_{\text{brake pad}} &= F_{\text{clamp}} \times \mu_{BP} \\
 &= 10,774.8 \times 0.4 = 4309.92 \text{ N} \\
 \text{Torque on the rotor} &= F_{\text{brake pad}} \times R_{\text{eff}} = \mathbf{215 \text{ Nm}}
 \end{aligned}
 \tag{20.2d}$$

- Bump force

$$\begin{aligned}
 &= \frac{(\text{mass} \times \text{weight distribution})/2 \times \text{velocity}^2}{\text{bump radius}} \\
 &= \frac{\frac{380 \times 0.4}{2} \times 100}{0.5} \\
 &= \mathbf{1846.66 \text{ N}}
 \end{aligned}
 \tag{20.3}$$

- Lateral load transfer

$$\begin{aligned}
 &= \frac{\text{acceleration} \times C G \text{ height} \times \text{mass} \times \text{weight distribution}}{g \times \text{track width}} \\
 &= \frac{1.66 \times 0.490 \times 380 \times 0.4}{9.81 \times 1.219} \\
 &= \mathbf{530.66 \text{ N}}
 \end{aligned}
 \tag{20.4}$$

- Longitudinal load transfer

$$\begin{aligned}
 &= \frac{\text{acceleration} \times C G \text{ height} \times \text{mass}}{\text{wheelbase} \times 2} \\
 &= \frac{1.66 \times 0.490 \times 380}{1.560 \times 2} \\
 &= \mathbf{752 \text{ N}}
 \end{aligned}
 \tag{20.5}$$

- Cornering force

$$\begin{aligned}
 &= \frac{\text{mass} \times \text{velocity}^2}{\text{radius}} \\
 &= \frac{0.4 \times 49}{1.8} \\
 &= \mathbf{461.32\text{ N}}
 \end{aligned}
 \tag{20.6}$$

20.2.2 Finite Element Method

For the FEA of existing and modified knuckle, the 3D model was created in a licensed version of SOLIDWORKS® 2016 and imported to the licensed version of ANSYS® Workbench™. Material selection was done on the basis of weight to strength ratio, availability, and feasibility. The finite element analysis of knuckle has been carried out for the set of above-calculated loads using different mesh size and element type. It was then analyzed for stress and deformation as per mechanical property of the chosen material. The component was analyzed exercising amalgamation of both *H*-type and *P*-type.

20.2.2.1 Material Selection

A wide range of materials from gray cast iron to the composite matrix are employed for knuckle manufacturing. Though these materials have high yield strength, they also have high density or cost or both. For a race car, this is a luxury. Hence, choice of material should be such that it should be cost-effective and also have satisfying yield strength [3]. To aid this, many materials were considered prior to narrowing down to the following materials (Table 20.1).

Since yield strength of above materials is almost similar, we can conclude that for the same volume of the component, the mass of component manufactured with Al

Table 20.1 Material properties

Property	Unit	Al 6061 T-6	EN-8
Density	kg/m ³	2700	7850
Yield strength	MPa	276	280
Ultimate strength	MPa	310	550
Young’s modulus	GPa	68.9	200
Poisson ratio	–	0.3	0.33
Elongation	%	13	16

Table 20.2 Chemical composition of Al 6061 T-6 in (wt%) and Al 95.85–98.56 in (wt%)

Si	Fe	Cu	Mn	Mg	Cr	Zn
0.4–0.8	Max. 0.7	0.15–0.4	Max. 0.15	0.8–1.2	0.04–0.35	Max. 0.25

6061 T-6 as the material will be light in weight and also have similar FOS. Hence, Al 6061 T-6 was used as a material for analysis and simulation (Table 20.2).

20.2.2.2 Geometry of the Component

- (1) A arm mount
- (2) Brake caliper mount
- (3) Steering arm mount
- (4) Stub axle (Fig. 20.1).

The control arm mounts have eye-to-eye distance of 6 inches as simulated from the Lotus Shark software. The caliper mounts were designed corresponding to the caliper placement on the knuckle. The stub diameter is in accordance with the internal diameter of the bearing used. The length of the stub axle was set according to results obtained from the suspension simulation software (Table 20.3).

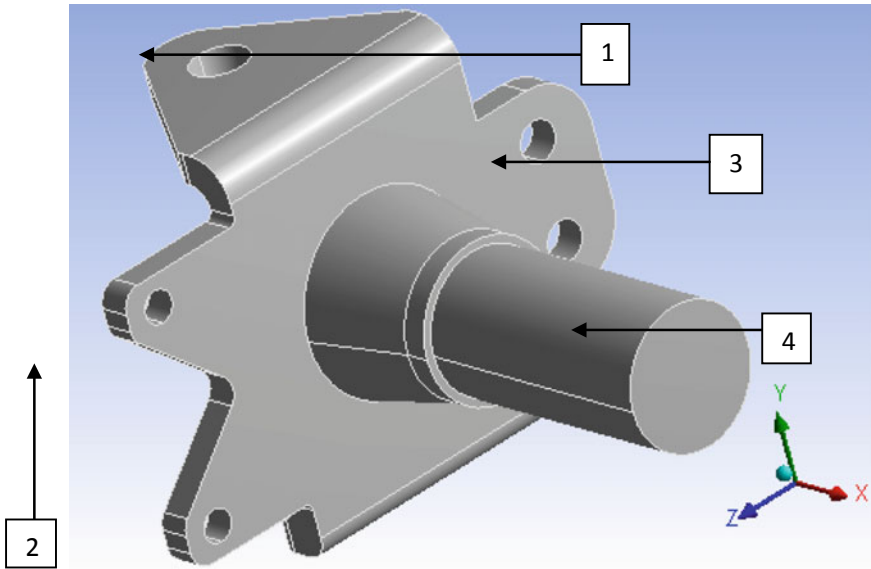


Fig. 20.1 Geometry of the component

Table 20.3 Suspension parameters and vehicle dimensions

Parameters	Values
King pin inclination (KPI)	6.74°
Caster	2.6°
Scrub radius	0.058 m
Weight of the vehicle	3433.5 N
Weight distribution	40:60
Track width	1.32 m
Wheelbase	1.70 m

20.2.2.3 Loading Conditions

The analysis was carried out on the component by fixing the pivot points of knuckle, i.e., where the control arms are attached to it. The component is subjected to the following loads [1, 2, 7];

- **Braking moment:**
Induced due to clamping force of brake calipers on the disk when brakes are applied. It is applied on the brake caliper mounts provided on the knuckle.
- **Steering forces:**
Induced due to KPI offset, castor trail offset, and friction couple generated during cornering. Applied on the mount provided for the steering arm.
- **Longitudinal load transfer:**
Induced during pitching of the vehicle, i.e., either while accelerating or braking in a straight line or applied on the stub axle in a downward direction.
- **Lateral load transfer:**
Induced during the roll of the vehicle and applied on the stub axle in the lateral direction.
- **Bump forces:**
Generated while the vehicle encounters an obstacle in its motion. It was applied on stub axle in an upward direction.
- **Cornering forces:**
Induced due to centrifugal forces while cornering of the vehicle. It was applied on stub axle in the lateral direction (Fig. 20.2).

20.2.2.4 Meshing-Element Size and Type

The purpose of meshing was to meet the exact size of the element to a great extent in order to obtain the optimum result. Hence, under the umbrella of *H*-type, the component was iterated for 1, 2, 3, 5, and 10 mm element size. Similarly, under *P*-type it, was iterated for first-order hexagonal (08 node) and second-order Tetrahedron (10 node), and hex-dominant (20 node). It is to be noted that first-order tetragonal (4 node) was not considered for analysis as it would behave like a stiff member (due to

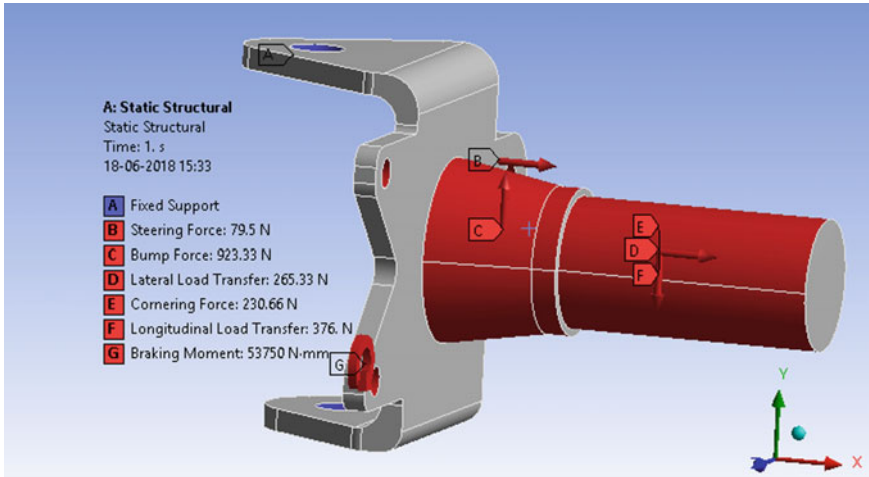
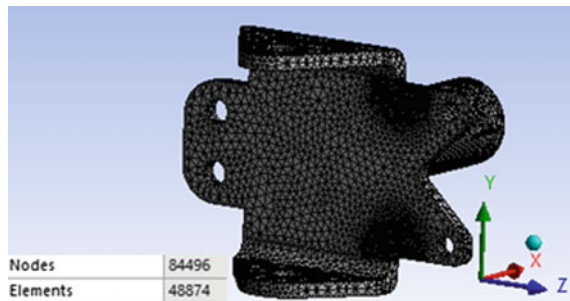


Fig. 20.2 Forces on the knuckle

Fig. 20.3 Meshing on the knuckle

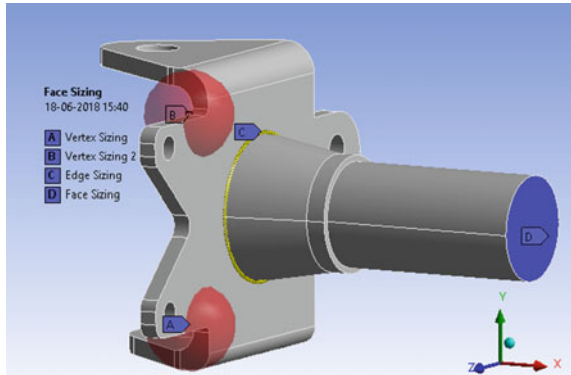


less number of nodes) and would not be subjected to bending or deformation. As a result, accuracy would not be achieved.

Sphere of influence was employed in the process of analysis to extract the highest possible enhanced results [6]. It was used in places where stress concentration was found to be high. Element size of 1 mm was employed for 2 mm overall element size, 1.5 mm for 3 mm overall element size, and similarly 2 mm for 5 mm and 3 mm for 10 mm. The “radius of the sphere of influence” was considered to be of 15 mm throughout, as the geometry of component does not change. This was carried out for all the element types under *P*-type.

Following pictures provide a pictorial idea for the sphere of influence (Figs. 20.3 and 20.4);

Fig. 20.4 Areas subjected to sphere of influence



20.3 Initial Model

20.3.1 Stress and Deformation Graphs for Initial Model

It is recommended that at least four to five iterations have to be conducted in order to arrive at the convergence of solution [5]. The component was analyzed for stress and deformation, whose graphs have been plotted below. Number of iterations carried out in order to check the convergence of the results, hence obtained. The above-stipulated meshing criteria were employed for analysis.

From the above stress graphs, we infer that stress behavior is similar and decreases as the element size increases in case of hexagonal and hex-dominant element type while in case of a tetrahedron, stress increases as element size increases from 1 to 2 mm and then decreases with increase in element size. Figure 20.5 was plotted in order to depict the converging nature of stress-based graph for the three element types. From the above deformation graphs, we infer that the deformation follows a similar pattern for the three types of elements. The deformation remains almost constant up to 5 mm element size and shows a sudden increase for 10 mm element size. Figure 20.6 shows the deformation values in case of tetrahedron and hex-dominant are nearly same (Table 20.4).

20.4 Shape Optimization

The factor of safety for all the iterations ranged from 3.4 to 5 which are comparatively higher than a required factor of safety range of 1.1 to 2. Thus, shape optimization was carried out in order to reduce the weight of the component without compromising on safety. The material was removed from the areas that will not affect the functionalities or safety of the component [4]. The thickness of the C section was reduced by 2 mm to further optimize the model (Fig. 20.7).

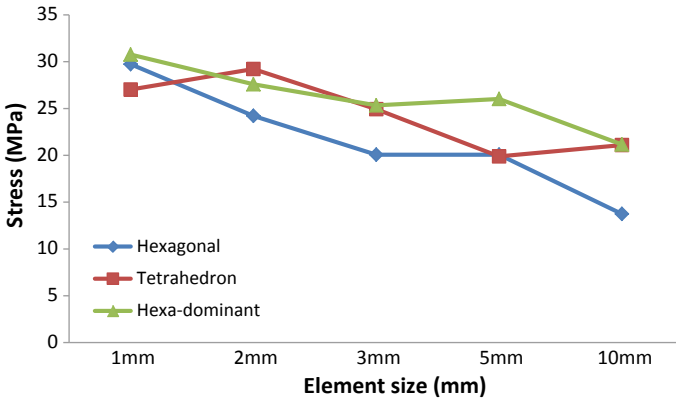


Fig. 20.5 Stress versus element size

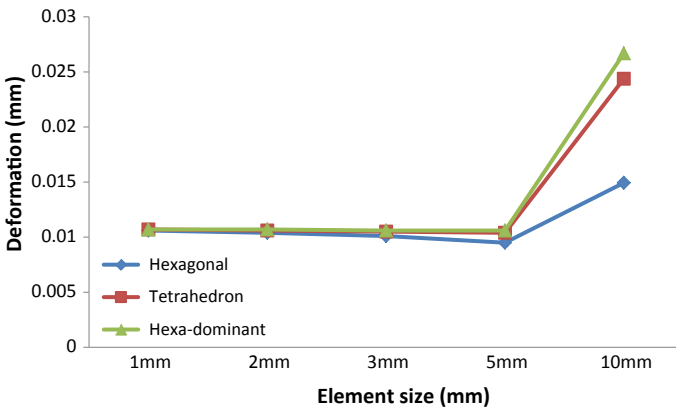


Fig. 20.6 Deformation versus element size

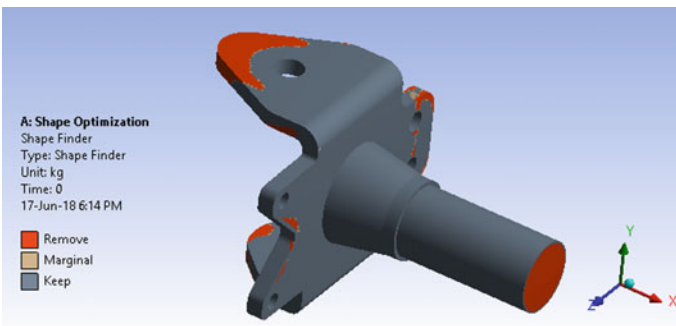


Fig. 20.7 Shape optimization of the knuckle

Table 20.4 Stress and deformation values for initial model

<i>P</i> -type (mm)	<i>H</i> -type	Stress (MPa)	Deformation (mm)
1	Hexagonal	29.739	0.0106
	Tetrahedron	27.033	0.0107
	Hex-dominant	30.763	0.0107
2	Hexagonal	24.216	0.0104
	Tetrahedron	29.217	0.0106
	Hex-dominant	27.590	0.0107
3	Hexagonal	20.069	0.0101
	Tetrahedron	24.933	0.0105
	Hex-dominant	25.337	0.0106
5	Hexagonal	20.063	0.0095
	Tetrahedron	19.889	0.0104
	Hex-dominant	26.022	0.0106
10	Hexagonal	13.740	0.0149
	Tetrahedron	21.093	0.0243
	Hex-dominant	21.150	0.0266

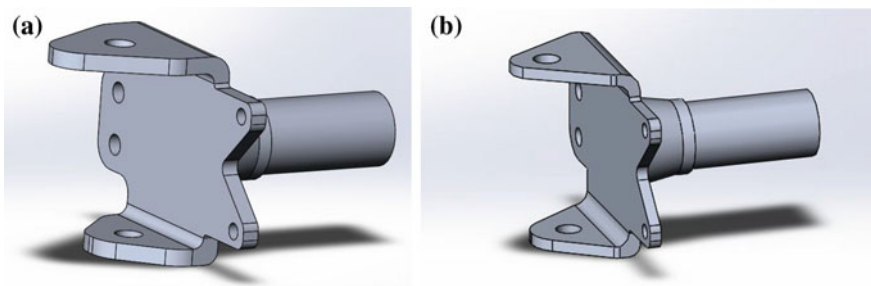


Fig. 20.8 **a** Initial CAD model and **b** CAD model after optimization

The mass of the initial model was 0.6963 kg, while that of the optimized model was 0.5217 kg. A weight reduction of 25.07% was achieved. Considering a complete vehicle with four knuckles, a total weight reduction of 0.6984 kg was achieved. The cost of Al 6061 T-6 is approximately Rs.550/- per kg. As per these statistics, the cost reduction for material came to be Rs.384/- per vehicle (Fig. 20.8).

20.5 Results and Discussion

The optimized component was also analyzed for stress and deformation and the graphs were plotted. The same meshing criteria were employed for the optimized model as well.

From the above stress graphs, we infer that for hexagonal, stress goes on decreasing with the increase in element size. In the case of a tetrahedron, the behavior is irregular, whereas for hex-dominant, the stress decreases and remains almost constant. Figure 20.9 depicts the converging nature of stress with the increase in element size for the tetrahedron and hex-dominant element type. The stress increases after 5 mm element size which depicts the diverging nature of the graph. Hence, the element size for analysis should fall within 5 mm. From the above deformation graphs, for hexagonal, the deformation decreases with the increase in element size. In the case of tetragonal, the deformation increases and then decreases while in case of hex dominant, it increases and almost remains constant. Figure 20.10 depicts the converging nature of the graph for hexagonal and hex-dominant with the increase in element size (Table 20.5).

Hexagonal—stress and deformation for 1 mm element size

Tetrahedron—stress and deformation for 1 mm element size

Hex-dominant—stress and deformation for 1 mm element size.

Following section entails figures and tables corresponding to 1 mm P -type with hexagonal, tetrahedron, and hex-dominant as H -type (Table 20.6).

The above figures depict the stress and deformation of the component for hexagonal, tetrahedron, and hex-dominant element type. From Figs. 20.11, 20.12, 20.13, 20.14, and 20.15, we infer that the stresses fall in the range of 43–50 MPa which is less

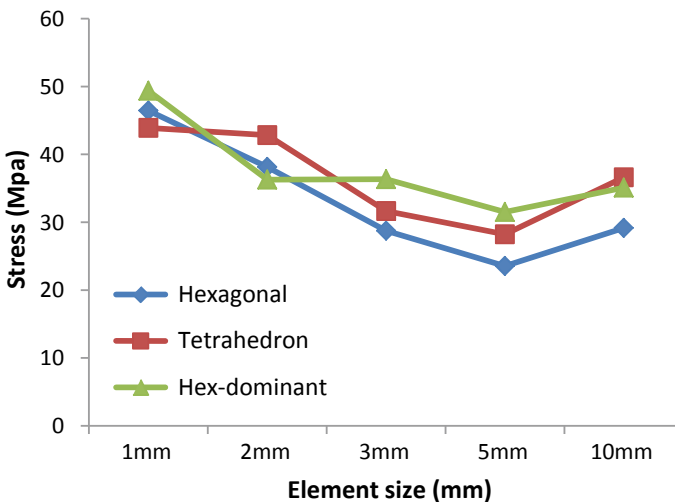


Fig. 20.9 Stress versus element size

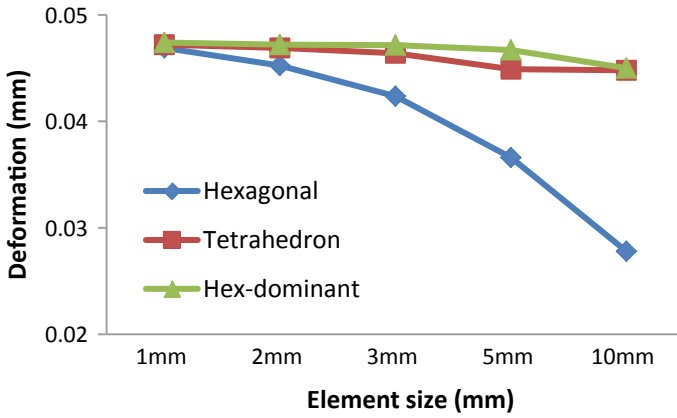


Fig. 20.10 Deformation versus element size

Table 20.5 Stress and deformation values for optimized model

<i>P</i> -type (mm)	<i>H</i> -type	Stress (MPa)	Deformation (mm)
1	Hexagonal	46.43	0.0469
	Tetrahedron	43.90	0.0472
	Hex-dominant	49.36	0.0474
2	Hexagonal	38.14	0.0452
	Tetrahedron	42.84	0.0469
	Hex-dominant	36.27	0.0472
3	Hexagonal	28.75	0.0423
	Tetrahedron	31.64	0.0464
	Hex-dominant	36.34	0.0471
5	Hexagonal	23.55	0.0366
	Tetrahedron	28.21	0.0449
	Hex-dominant	31.52	0.0467
10	Hexagonal	29.21	0.0278
	Tetrahedron	36.69	0.0448
	Hex-dominant	35.09	0.0450

Table 20.6 Meshing values for 1 mm element size

H-type (element type)	Number of elements	Number of nodes
Hexagonal	332,067	288,103
Tetrahedron	155,781	260,640
Hex-dominant	326,661	1,186,470

Fig. 20.11 Total deformation

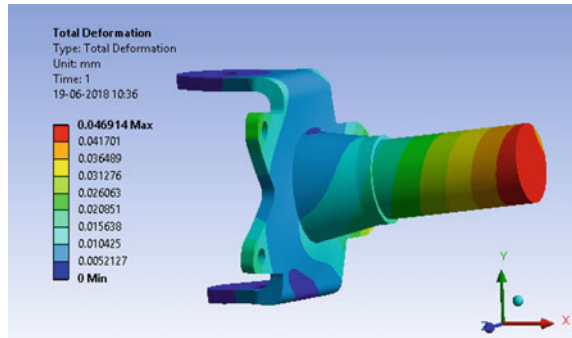
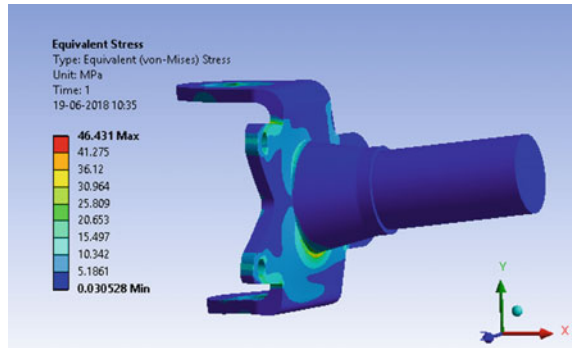


Fig. 20.12 Von-mises stress



than the yield strength of aluminum 6061-T6. Figures 20.12, 20.14, and 20.16 depict the deformation for the three element types. The maximum deformation obtained is 0.0474 mm. The stress and deformation results obtained prove to be safe for our design considerations (Fig. 20.17).

20.6 3D Printing

The CAD model component was 3D printed in “Cube Pro3D” printer. The material used was acrylonitrile butadiene styrene (ABS). The method used in 3D printing was fuse deposition modeling (FDM). This was incorporated as a final step to check the physicality and tolerances prior to integrating it on the vehicle (Fig. 20.18).

Fig. 20.13 Von-mises stress

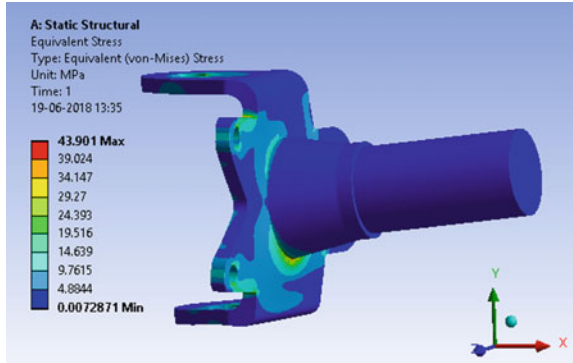


Fig. 20.14 Total deformation

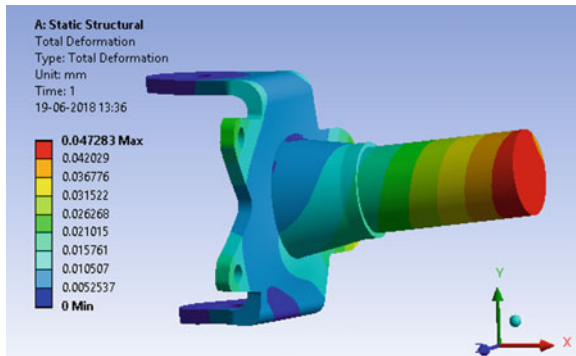


Fig. 20.15 Von-mises stress

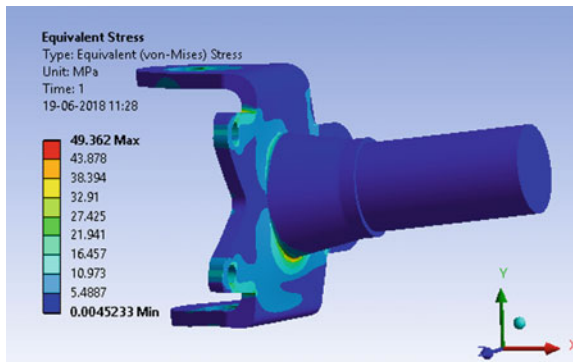


Fig. 20.16 Total deformation

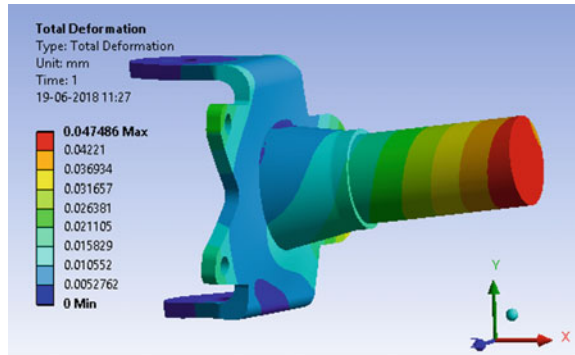


Fig. 20.17 Assembly of component on vehicle for validation

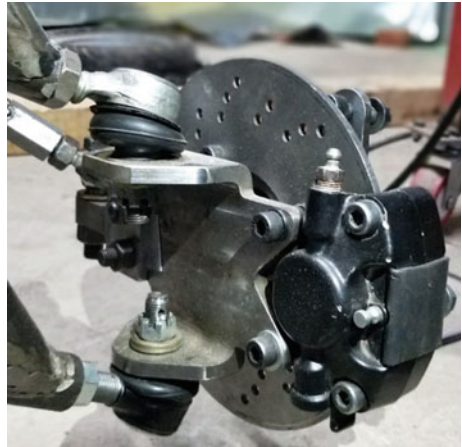
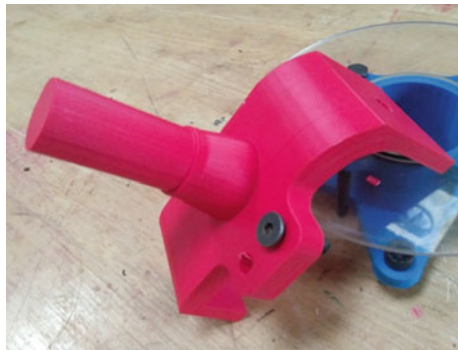


Fig. 20.18 3D printed model (in red color)



20.7 Conclusions

The initial model was optimized in the best possible way using appropriate *P*-type and *H*-type meshing. As various amalgamations were exercised, the best suited meshing criteria were found to be 1 mm (as *P*-type) with hex-dominant (as *H*-type). This was concluded after analyzing all the stress and deformation graphs plotted above and had a converging nature. Also, as hex-dominant element type has 20 nodes, it is more flexible and adaptive to the model's geometry. Thereby, it is ought to yield accurate results. Moreover, it was noted that the sphere of influence was not employed for 1 mm element size (*P*-type) as the available software version was constrained to this range. Although, results were not compromised as the element size used under the sphere of influence in our study was not more than 1 mm.

The weight reduction objective was realized by using a shape optimization module in ANSYS® Workbench™ and also reducing 3 mm thickness from the knuckle. This resulted in a reduction of weight and cost while maintaining the required FOS, hence maintaining strength.

The component which was subjected to analysis was put to test on the vehicle and no signs of damage, bending or any sort of mechanical failure gave the validation for our design.

Acknowledgements We would like to express our sincere gratitude to Dr. P. G. Tewari, Principal, KLETECH, Hubballi and Dr. Ashok Shettar, Vice chancellor, KLETECH, Hubballi for providing all sorts of help and support during the course of the work.

References

Journal Paper

1. International Journal of Engineering Research and Technology (IJERT): Design and analysis of upright of an FIA regulated cruiser class solar electric vehicle. **3**(10) (2014); ISSN: 2278-0181
2. International Journal of Scientific and Research Publications: Designing of all terrain vehicle (ATV) **4**(12) (2014); ISSN 2250-3153
3. Imperial International Journal of Eco Friendly Technologies (IJET): Design and optimization of passenger ATV knuckle **1**(1) (2016), 183–187
4. International Journal of Mechanical Production Engineering: FEA and optimization of steering Knuckle of ATV **3**(12) (2015); ISSN 2320-2092
5. Patil AY, Umbrajkar Hrishikesh N, Basavaraj GD, Chalageri GR, Kodancha KG: Influence of bio-degradable natural fiber embedded in polymer matrix, IMME17, Mater. Proc. **5**(2), 7532–7540 (2018); Part 2

Web URL

6. <https://altairuniversity.com/wp-content/uploads/2014/02/meshing.pdf>

Conference Paper

7. IOP Conf. Series: Analysis of steering knuckle of an ATV using finite element analysis. Mater. Sci. Eng. **149**, 012133 (2016). <https://doi.org/10.1088/1757-899x/149/1/012133>
8. IOP Conference Series: Materials Science and Engineering, Analysis of Steering Knuckle of All Terrain Vehicles (ATV) Using Finite Element Analysis, S V Dusane et al 2016 IOP Conf. Ser.: Mater. Sci. Eng. **149**, 012133

Chapter 21

Modeling and Analysis of ATV Roll Cage



A. S. Shridhar, Abhilash Tukkar, Akshay Vernekar, Vinod Badderu,
Arun Y. Patil and Basavaraj B. Kotturshettar

Abstract Driver safety is the main concern in any motorsport event, and evaluating the fatalities, it was observed that most of the fatalities were due to head on collision. SAE Baja competition expects the student teams to build an ATV vehicle from scratch, pertaining to the rules specified by the governing bodies. The work focuses on the safety of vehicle at the student level. The model of the roll cage was prepared according to the rule book in SOLIDWORKS 2016. The calculations necessary for the forces to be applied on the roll cage include basic mechanical formulae like bending moment, force calculations, and mass-energy conversions. The model was analyzed for two materials, namely AISI 4130 and AISI 1018 using static structural in the ANSYS Workbench. The main parameters considered for analysis were mesh sizes, mesh type, and the order of element, and various iterations were made considering these parameters. The model was further optimized for weight reduction. The simulation results were compared with analytical results, and a convergence graph was obtained to justify the design.

Keywords ATV · Roll cage · SAE · Bending moment · Mass-energy conversion · Static structural · Fatigue

A. S. Shridhar · A. Tukkar · A. Vernekar · V. Badderu · A. Y. Patil (✉) · B. B. Kotturshettar
School of Mechanical Engineering, K.L.E Technological University, Hubballi, India
e-mail: Patilarun7@gmail.com

A. S. Shridhar
e-mail: shridhar.as1997@gmail.com

A. Tukkar
e-mail: tukkarabhilash@gmail.com

A. Vernekar
e-mail: akshayv007.av@gmail.com

V. Badderu
e-mail: badderurvinod9497@gmail.com

B. B. Kotturshettar
e-mail: bbkshettar@gmail.com

21.1 Introduction

SAE BAJA is an intercollegiate design competition run by Society of Automotive Engineers (SAE). Teams from various colleges build an all-terrain vehicle (ATV) and run it in the competition held at NATRAX facility, Pithampur, Indore. An ATV is a typical mini off-road vehicle powered by a 10 HP gasoline engine. The roll cage of the ATV must be equally strong and lightweight. Since the vehicle's terrain is off-road, the chances of mishaps and accidents are more, so proper analysis of the roll cage needs to be done in every aspect.

The roll cage (chassis) is the main body of a vehicle which gives support to the vehicle, protects the driver, and is the housing for all other subsystems like suspension, braking, power train, etc. The roll cage is made up of circular hollow cross section consisting of primary and secondary members. The difference between them is wall thickness, bending strength, and bending stiffness. The criteria for assigning of the member as primary and secondary are its placement in a roll cage and its severity during crashes. Front impact, side impact, rear impact, and rollover analysis are carried out in static structural function in ANSYS Workbench.

21.2 Design of Roll Cage

The design is made according to the rules of SAE Baja rule book in SOLIDWORKS 2016 [1]. The roll cage is made of tubular steel frame, which is joined together by the welding process. As per the rules, the material for roll cage must contain a minimum of 0.18% of carbon and has a particular minimum bending strength and bending stiffness. The materials shortlisted from these criteria for the roll cage were AISI 1018 and AISI 4130. The vehicle is designed as to accommodate one person 1.95 m tall weighing 113 kg (i.e., 95 percentile male) according to the rule book specification. The dimensions of the roll cage are 1.82 m length 0.9 m width and 1.2 m height (Figs. 21.1 and 21.2).

21.3 Material Selection

The material properties of AISI 4130 and AISI 1018 are as mentioned below in the table [2]. Chemical properties of the material are also listed below. The material was finalized depending on the highest bending strength with a maximum outer diameter of 1.25 inch and a maximum thickness of 2 mm as mentioned in the rule book. The material satisfying all these properties was AISI 4130 (Tables 21.1, 21.2, 21.3, 21.4 and 21.5).

Fig. 21.1 Isometric view of the roll cage

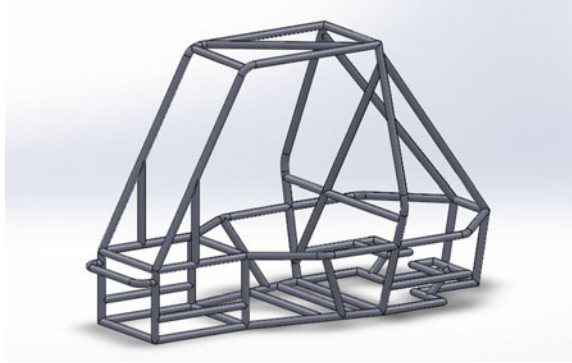


Fig. 21.2 Side view of the designed roll cage

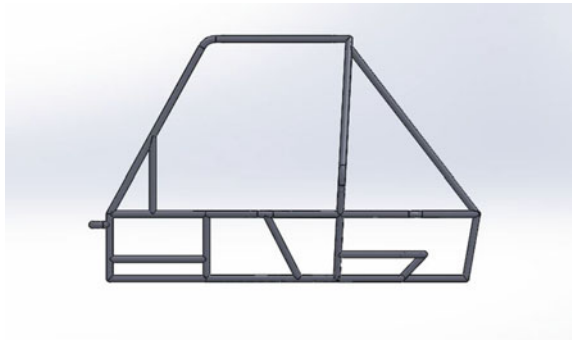


Table 21.1 Mechanical properties of AISI4130

Property	Values
Density	7.85 g/cm ³
Yield strength	460 MPa
Poisson's ratio	0.28
Young's modulus	210 GPa

Table 21.2 Mechanical properties of AISI 1018

Property	Values
Density	7.87 g/cm ³
Yield strength	370 MPa
Poisson's ratio	0.29
Young's modulus	205 GPa

Table 21.3 Chemical composition of AISI4130

Element	Content (%)
Iron (Fe)	97.03–98.22
Chromium (Cr)	0.80–1.10
Manganese (Mn)	0.40–0.60
Carbon (Fe)	0.280–0.330
Silicon (Si)	0.15–0.30
Molybdenum (Mo)	0.15–0.25
Sulfur (S)	0.040
Phosphorous (P)	0.035

Table 21.4 Chemical composition of AISI 1018

Element	Content (%)
Carbon (C)	0.14–0.20
Iron (Fe)	98.81–99.26
Manganese (Mn)	0.60–0.90
Phosphorous (P)	≤0.040
Sulfur (S)	≤0.050

Table 21.5 Tabular column of physical quantities

Physical quantity	Front impact	Rear impact	Side impact	Rollover analysis
Mass of the vehicle (kg)	300	300	300	300
Final velocity (m/s)	0	0	0	0
Initial velocity (m/s)	11.11	11.11	11.11	11.11
Height (m)	0	0	0	3.04
Impact time (s)	0.3	0.15	0.15	0.15
Work done	18,514.8 N-m	18,514.8 N-m	9257.4 N-m	8969.89
Displacement (m)	1.44	3.33	3.33	1.005
Force (N)	12,857.5	5560	5560	8925.26

21.4 Analytical Calculation [3]

Formulae:

1. Work done $W = 0.5 \cdot m \cdot (v_f^2 - v_i^2)$
2. Displacement, $S = t \cdot v$
3. Force, $F = W/S$
4. Velocity, $v = \text{sqrt}(2gh)$

Table 21.6 Front impact results

Element size	Stress	Deformation
6 mm	371.20	14.7580
8 mm	359.92	7.7553
10 mm	282.02	7.5000

21.5 Analysis

The design of roll cage is finalized considering all the constraints of all the subsystem and analyzed for front impact, rear impact, side impact, and rollover analysis in ANSYS Workbench, and various iterations are carried out to increase factor of safety and rigidity without undergoing much deformation. The meshing was done for element sizes of 6, 8, and 10 mm with first-order tetrahedron and hexahedron elements, and also various functions such as the sphere of relevance and edge sizing were used where the complexity of the model arises leading to stress concentrations. Tetrahedral elements can fit better complex geometry. Since there are curved paths, acute angles in our roll cage, we decided to go with tetrahedral elements. Thus, meshing was done for three element sizes with the least size of the element being 6 mm and first-order tetrahedrons being the element type [4]. The element size was finalized from the stress versus element size graph after the convergence was achieved from the graph. The assumptions made are: (1) Weight is considered to be 300 kg; (2) maximum velocity of the buggy is 40 kmph; and (3) the material used for the roll cage is ductile and von Mises theory is considered for the analysis.

21.5.1 Front Impact

In this scenario, a buggy is considered to be moving with a speed of 40 kmph and colliding with a stationary rock or tree. Here, the rear suspension pickup points are fixed and force is applied on the front hitch members (hitch point) of the vehicle which are the ones experiencing a force as they come in contact first [5]. The force applied is 12,857.50 N. The stress induced is 358.86 MPa and deformation is 6.44 mm. The factor of safety is 1.28. Numbers of nodes are 903,185 and numbers of elements are 455,660 for 6 mm element size (Table 21.6; Figs. 21.3 and 21.4).

21.5.2 Rear Impact

In this scenario, the buggy is considered to be at rest and another buggy is considered to come and collide at the rear end of the buggy at 40 kmph. Here, force is applied on the rearmost member and the front suspension pickup points are fixed as the buggy

Fig. 21.3 Equivalent stress

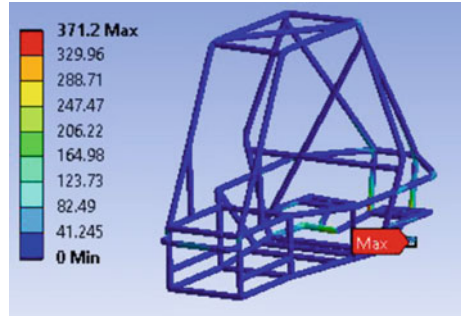


Fig. 21.4 Deformation

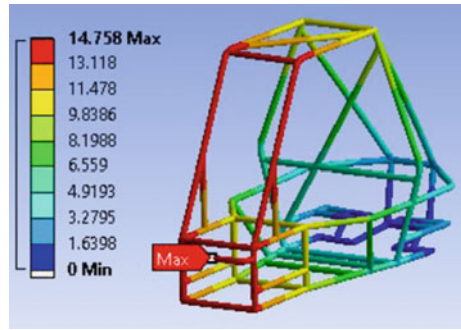


Table 21.7 Rear impact results

Element size	Stress	Deformation
6 mm	288.77	1.1895
8 mm	254.03	1.1706
10 mm	185.23	1.0107

would be hit at the rearmost member first. The force applied is 5560 N. The stress induced is 288.77 MPa and deformation is 1.19 mm. The factor of safety is 1.59. The numbers of nodes are 828,310 and the numbers of elements are 420,201 for 6 mm element size (Table 21.7; Figs. 21.5 and 21.6).

21.5.3 Side Impact

In this scenario, the buggy is considered to be at rest while another buggy hit the earlier buggy from the side. Thus, experience of force exerted on the side impact members and the constrain, i.e. fixed points are the opposite side suspension pickup points as they are in contact with the ground. The force applied is 5560 N. The stress induced is 333.08 MPa and deformation is 4.0077 mm. The factor of safety is 1.38.

Fig. 21.5 Equivalent stress

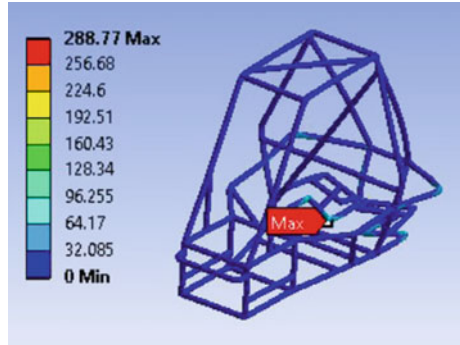


Fig. 21.6 Deformation

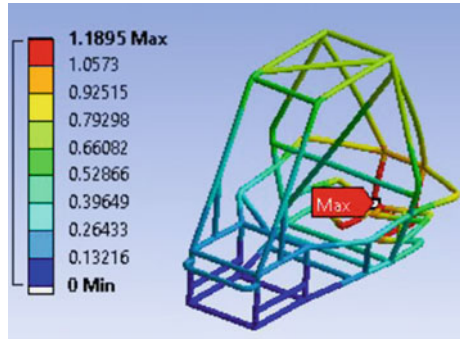
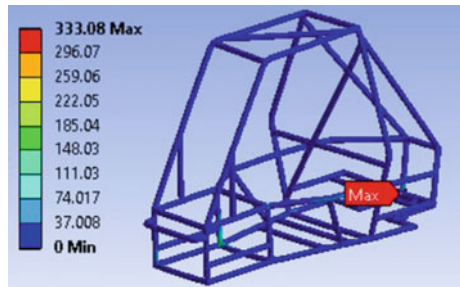


Table 21.8 Front impact results

Element size	Stress	Deformation
6 mm	333.08	4.0077
8 mm	324.21	3.9335
10 mm	279.81	3.8477

Fig. 21.7 Equivalent stress



The numbers of nodes are 829,121 and the numbers of elements are 420,653 for 6 mm element size (Table 21.8; Figs. 21.7 and 21.8).

Fig. 21.8 Deformation

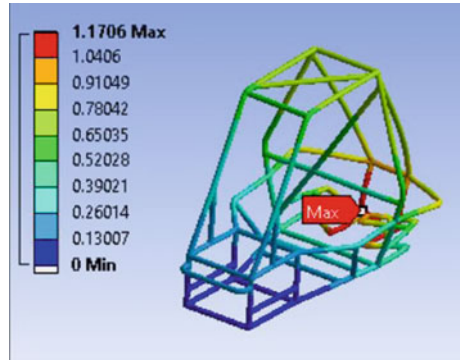
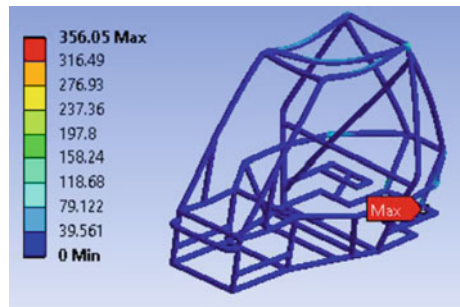


Table 21.9 Rollover analysis result

Element size	Stress	Deformation
6 mm	356.05	1.9855
8 mm	234.38	1.9257
10 mm	206.65	1.8565

Fig. 21.9 Equivalent stress



21.5.4 RollOver Analysis

In this analysis, it is considered that the roll cage is assumed to be dropped from a height of 10 feet and to fall upside down. All four suspensions pickup points are fixed, and force is applied to the overhead members as they come in contact first. The force applied is 8969.69 N. The stress induced is 356.05 MPa and deformation is 1.9855 mm. The factor of safety is 1.29. The numbers of nodes are 829,340 and the numbers of elements are 420,574 for 6 mm element size (Table 21.9; Figs. 21.9 and 21.10).

Fig. 21.10 Deformation

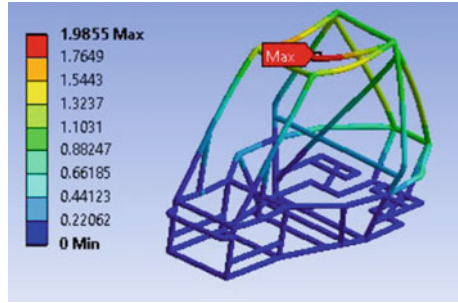


Fig. 21.11 Deformation

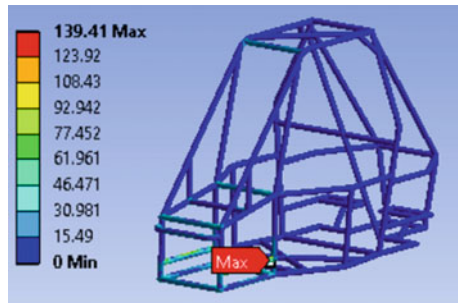
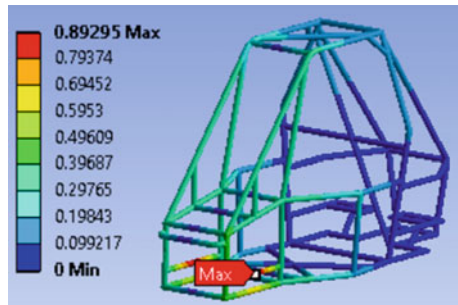


Fig. 21.12 Equivalent stress



21.5.5 Torsional Analysis

In this analysis, the roll cage is expected to undergo torsion due to bumps and the spring forces acting in conduction. The force is calculated according to it. The rear suspension pickup points are fixed, and force is applied on the front suspension pickup points applying force in the clockwise direction on the left suspension pickup point while anticlockwise on the right suspension pickup point. The force applied is 8969.69 N. The stress induced is 139.41 MPa and deformation is 0.8929 mm. The factor of safety is 3.22. The numbers of nodes are 159,618 and the numbers of elements are 28,124 for 6 mm element size (Figs. 21.11 and 21.12).

Fig. 21.13 Deformation

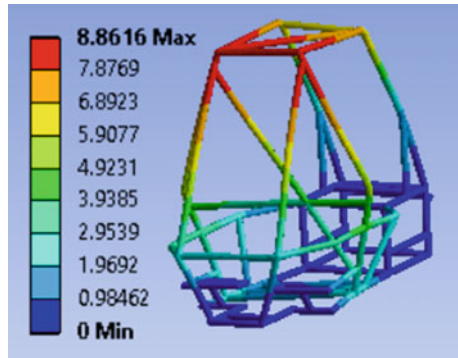


Fig. 21.14 Frequency

	Mode	<input checked="" type="checkbox"/> Frequency [Hz]
1	1.	44.785
2	2.	63.926
3	3.	81.098
4	4.	101.04
5	5.	105.68
6	6.	129.41

21.5.6 Modal Analysis

Considering six major modes of vibrations for the frequency chart, it was found that there is no resonance as the frequency of any other subsystem does not match with the six frequency modes obtained in the analysis. The maximum deformation observed was 8.68 mm and the maximum frequency observed was 129.41 at the sixth mode (Figs. 21.13 and 21.14).

21.6 Result and Discussion

It is recommended that at least four to five iterations have to be conducted in order to arrive at the convergence of solution [7]. The roll cage was analyzed for front impact, rear impact, side impact, rollover analysis, modal analysis, and torsional analysis which are the most expected scenarios at the competition site, and the factor of safety yielded was above 1.2 in all the cases which is the primary threshold limit of the roll cage. It was also seen that resonance with all other subsystem was avoided. The yield stress of the material is 460 MPa, and equivalent stress is less than yield

Fig. 21.15 Stress versus element size

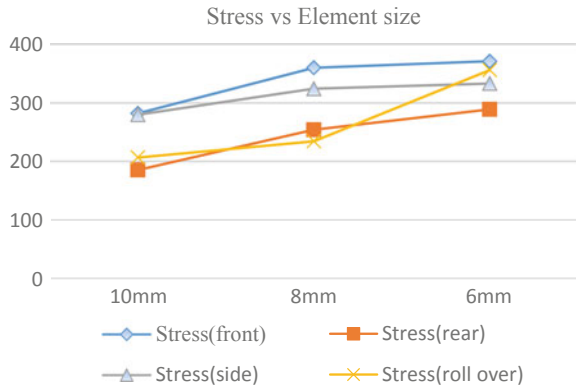


Fig. 21.16 Deformation versus element size



stress in all the above conditions. Hence, it can be concluded that roll cage is safe in all the conditions. The graphs of stress versus element size and stress versus deformation are plotted for all the four cases, namely front impact, side impact, rear impact, and rollover [6] (Figs. 21.15 and 21.16).

21.7 Conclusion

In this paper, the design and analysis of the roll cage were completed using the finite element method. The study of analysis explores the static analysis selection of mesh size and element size. The front impact, side impact, roll over analysis, rear impact, torsional analysis, and modal analysis were carried out in this paper. The main objective of the study was to obtain an optimum factor of safety for the roll cage to ensure the safe condition of the driver in all conditions of the crash while also trying to cut down on mass for a better power to weight ratio figure. It was observed that the roll cage stresses were well within the yield limits, and hence, there was no

need of addition of gussets at any of the regions. AISI 4130 was the most suitable material for our study.

References

Book

1. Rulebook BAJA SAE International (2018)

Journal Paper

2. Aru, S., Jadhav, V., Kumar, A., Angane, P.: 'Design Analysis and Optimization of a Multi_Tubular Space Frame'. (IJMPERD). ISSN(P): 2249-6890; ISSN(E): 2249-8001. **4**(4) (2014), 37_48[©] TJPRC Pvt. Ltd
3. Harshit, R.: Design and Analysis of the Roll Cage of an ATV. Int. J. Eng. Res. Technol. (IJERT). ISSN: 2278-0181 **6**(09) (2017)
4. Noorbasha, N.: Computational analysis for improved design of an SAE BAJA frame structure. UNLV Thesis, Disserations, Professional Papers, and Capstones Paper 736, 12 (2010)
5. Raina, D., Gupta, R.D., Phanden, R.K.: Design and Int. J. Technol. Res. Eng. (IJTRE) **2**(7). ISSN: 2347-4718 (2015)
6. Sati, B.K., Upreti, P., Tripathi, A., Batra, S.: Static and dynamic analysis of the roll cage for an All-Terrain vehicle. Imperial J. Interdisciplinary Res (IJIR) **2**(6). ISSN: 2454-1362 (2016)
7. Patil, A.Y., Hrishikesh, N.U., Basavaraj, G.D., Chalageri, G.R., Kodancha, K.G.: Influence of bio-degradable natural fiber embedded in polymer matrix, IMME17. Mater. Proc. **5**(2), 7532–7540, Part 2 (2018)

Chapter 22

Computational Flow Analysis of a Blade Wedge Duct



K. R. Deepthi and S. Shankar

Abstract The paper presents a computational analysis of solid wedge duct of the trailing edge of the turbine blade for flow and convective heat transfer coefficient characteristics for elliptical in-line pin fins. The k- ϵ turbulent model coupled with the Reynolds-averaged Navier–Stokes equation is considered and hence analyzed. Low Reynolds numbers (Re) of 10,000, 20,000, 30,000, 40,000, and 50,000 were considered in order to attain the variation of flow parameter on pressure drop and rate of convective heat transfer. Scrutiny study for circular and elliptical inline pinfin variation at the end wall and area averaged Nusselt number with the variation in the Reynolds numbers was obtained and validated with the experimental data. The equivalence in results shows an elliptical pin fins with the case, where air coolant at 26 K temperature deviation agrees well the experimental results and a better rate of convective heat transfer coefficient than that of temperature difference of 50 K. Area-averaged Nusselt numbers at the end wall for case (1) of air coolant increase with different Reynolds numbers. Conclusively, compared with two cases of coolants for two different pin fin shapes, case (2) of elliptical pin fins gives a lower friction coefficient and higher thermal performance factor, significantly improving the rate of heat transfer of pin–fins arrayed in solid wedge duct.

Keywords Pin fins · Convective heat transfer · In-line · Air · Wedge duct

22.1 Introduction

A rotary mechanical device called Turbine extracts the energy from a flow and converts it into useful work. In jet engines, the turbine work produced is used for the generation of the electrical power when coupled with a generator and produces thrust

K. R. Deepthi (✉)
Cambridge Institute of Technology, Bengaluru, India
e-mail: deepthiramesh89@gmail.com

S. Shankar
Mechanical Department, Cambridge Institute of Technology, Bengaluru, India

© Springer Nature Singapore Pte Ltd. 2020
C. Li et al. (eds.), *Advances in Engineering Design and Simulation*,
Lecture Notes on Multidisciplinary Industrial Engineering,
https://doi.org/10.1007/978-981-13-8468-4_22

to propel the aircraft forward. The inlet temperature of the turbine is the most effective factor in the turbine blade of the gas turbine, and the inlet turbine temperature should be high. The turbine inlet temperature for the aero-engines reaches up to 1500 K and has been closed to 2000 K, respectively, that is higher than melting point of the blade material of the turbine. So, it is necessary to remove the heat for the safe mode operation of the turbine.

For the safest mode operation of the turbine, turbine blade should be cooled with different cooling techniques. As it will minimize the high temperature on the turbine blade. Mostly, the leading edge of the turbine blades experiences a very high temperature because the hot air from the combustion chamber enters into leading end of the turbine blade. For the leading edge, most commonly used cooling is film cooling; impingement cooling is used to cool the intermediate portion of turbine blade; further, trailing end is cooled by pin-fin cooling, respectively.

Pin-fin is an external cooling method. It also serves an additional purpose of providing structural support. It is an arrangement of holes and of different design shapes; preferable shape is circular or cylindrical fins which arranged in an in-line type, staggered type or any other desired type. The turbine blade trailing edge has a very thin surface; so, the wedge shape is installed at the trailing end of the blade for structural support. This pin-fin cooling can enhance the performance of the heat transfer [1].

These are installed at the trailing edge; it connects the upper end wall and lower end wall of the duct, and it effectively intensifies the rate of heat transfer and improves the blade strength, respectively. Computational fluid dynamics (CFD) and more specifically conjugate heat transfer (CHT) analysis can accurately predict heat transfer by simultaneously solving all the relevant solid and flow field heat transfer processes.

Various investigators such as Sparrow and Ramsey [2], Lau et al. [3], Li et al. [4], Li et al. [5], and Deng [6] investigated factors influencing the heat transfer and pressure drop characteristics of cooling duct with pin-fins. Parametric studies outlined about pin-fins tip clearance, cross-sectional shapes, H/D , and SX . La et al. [3], Li et al. [4] found that unlike the cross-flow heat changer ($H/D > 8$, where the end wall heat transfer is negligible) and the plate-fin-and-tube compact heat exchangers ($H/D < 0.25$, in which the tube heat transfer is relatively small), the heat transfer from pin-fins and end walls contributes to the overall heat transfer effect for short pin-fins ($0.5 < H/D < 4$).

Sparrow and Ramsey [7], BabusHaq et al. [8], Tahat et al. [9], Hwang and Lui [10], and Jeng et al. [11], studied the heat transfer coefficient and pressure drop characteristics of cooling duct with in-line and staggered arrays. The studies verified that a staggered pin-fin array gives higher end wall heat transfer enhancement and more pressure drop penalty compared to in-line array.

22.2 Numerical Analysis

22.2.1 Geometric Modeling

In current studies, the solid wedge model configuration is used from Ref. [12]. The solid wedge duct model consists of inlet, outlet, wall, upper end wall, lower end wall, and five rows with 25 pin fins for circular [13] and elliptical pin fins, respectively. The pin–fin height-to-diameter ratio H/D ranges from about 1.3–3.6. Figure 22.1 shows the solid wedge duct model for elliptical pin fins and the structured grid generated in ANSYS ICEM-CFD 13.0. Around the pin–fins, an O-grid is used and at the end walls, grid refinement was carried out. To obtain the resolution of near end wall (y^+ is less than 1) which meets the requirement of ANSYS CFX 13.0 solver.

22.2.2 Boundary Conditions

The domain with coolant as air for two different temperature conditions is considered with total energy turbulence model of $K-\epsilon$ model. At inlet, magnitude and the direction of the normal speed and static temperature are specified, and at outlet, relative pressure is defined. For the wall, no slip boundary condition is defined and heat transfer is adiabatic and also for the upper and lower end wall, no slip condition along with wall temperature is considered (Table 22.1).

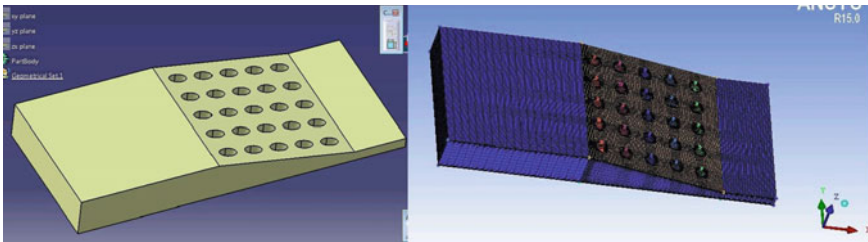


Fig. 22.1 Elliptical design model and solid meshed model

Table 22.1 Two cases of coolants-boundary conditions

Cases	Fluid	T_1°	T_w°
Case 1	Air	65	39
Case 2	Air	100	150

22.2.3 Formula Used

Two different Reynolds numbers are considered based on the mean velocity (U) and equivalent hydraulic diameter (D_h) at the entrance, namely “duct Reynolds number,” defined as:

$$Re = (\rho U D_h) / \mu \quad [\text{Duct Reynolds number}] \quad (22.1)$$

The other is minimum cross-sectional average velocity (U_{\max}) of each pin-fin row and pin diameter (D), namely [1] “pin Reynolds number,” expressed as:

$$Re_d = (\rho U_{\max} D) / \mu \quad [\text{Pin Reynolds number}] \quad (22.2)$$

The non-dimensional pressure drop throughout the computed domain is represented by friction coefficient as:

$$f = (2\Delta P) / \rho N (V_{\max})^2 \quad (22.3)$$

$$Nu_{\infty} = 0.023 Re^{0.8} Pr^{0.4} \quad [\text{Dittus–Boelter correlation}] \quad (22.4)$$

$$f_{\infty} = 0.0791 Re^{0.25} \quad [\text{Blasius–equation}] \quad (22.5)$$

$$\eta = (Nu / Nu_{\infty}) / (f / f_{\infty})^{0.333} \quad [\text{Thermal performance factor}] \quad (22.6)$$

where Pr is Prandtl number. The values of pr for air is 0.7.

The fitting formulas of Nu and Re for air is

$$Nu = 0.06 Re^{0.78294} \quad (22.7)$$

22.3 Results and Discussion

A conjugate heat transfer analysis is carried out on wedge shaped duct of circular and elliptical pin fin configuration. Five different low Reynolds numbers are studied to determine the effect of flow, on the pressure drop and the convective heat transfer for circular pin fin wedge duct [13] and the elliptical pin fin wedge duct severally. Finally, the wedge duct with elliptical pin fin gives the better results than circular pin fin wedge duct.

To increase the accuracy of the numerical analysis, grid independent study was done to ensure that the results obtained has no influence on grid size and a grid of size 5,69,502 elements was chosen for further studies in the current work when the number is greater than 1, 58,922 elements.

The wedge duct with 25 circular pin fins is carried out for two cases of coolants (air) [13]. Case (1) has the lowest thermal efficiency when compared to the case (2). So, the case (2) condition is suitable for the better thermal efficiency. Case (1) condition significantly satisfies the experimental results Ref. [1].

22.3.1 Effect of Heat Transfer Coefficient on Elliptical Pin Fin Design

To investigate the effect of two different coolant cases on elliptical pin fins in the wedge duct, a two-equation turbulence model k-epsilon which is a Reynolds-averaged Navier–Stokes was used to capture the flow physics and heat transfer characteristics. Case (1) and case (2) of elliptical pin fin model give higher efficiency than the circular pin fin [13], with the conditions similar to that of the experiment Ref. [1], have been investigated numerically, and the results are compared with the circular pin fins results [13]. On the bottom end wall, the rate of heat transfer coefficient distributions in the wedge duct is shown for different Reynolds Numbers.

In the circular pin fin [13], the heat transfer coefficient of case (2) has better value than the case (1). For case (2) $Re = 50,000$ ROW 5 having the highest HTC = 284.51 (W/m²k). For the circular pin fin, the friction coefficient for case (2) is less when compared to the case (1). The Reynolds number 50,000 for case (2) gives the lowest $f = 0.263$ when compared to other four Reynolds number, respectively. For the circular pin fin, the thermal performance factor (η) for case (2) is higher than that of case (1). The $Re = 10,000$ of case (2) having the highest thermal performance factor, i.e., $\eta = 79\%$, respectively. In the elliptical pin fin for the case (2), the pin Reynolds number and the pin Nusselt number are increased when compared to the case (1) of elliptical design, the case (2) pin Reynolds number for $Re = 50,000$, the ROW 2 having the highest value than the other four Reynolds number, i.e., $Re_d = 9.67E + 03$ (Figs. 22.2, 22.3, 22.4, 22.5 and 22.6).

22.3.2 Variation in Pressure Drop and Thermal Performance Factor for Elliptical Pin Fin Design

The variation of dimensionless friction coefficient with Reynolds number is shown in Table 22.3 for the case (1) and case (2) for the elliptical pin fin design. The density of case (1) air is greater than that of case (2) when the temperature is at 100 °C and the air velocity is the lowest. The pressure drop for case (1) is lower when compared to case (2), and the thermal performance factor is high in case (2) condition when compared to case (1).

The temperature difference is an absolute value of the difference between the temperature at inlet and the wall temperature, represented as below:

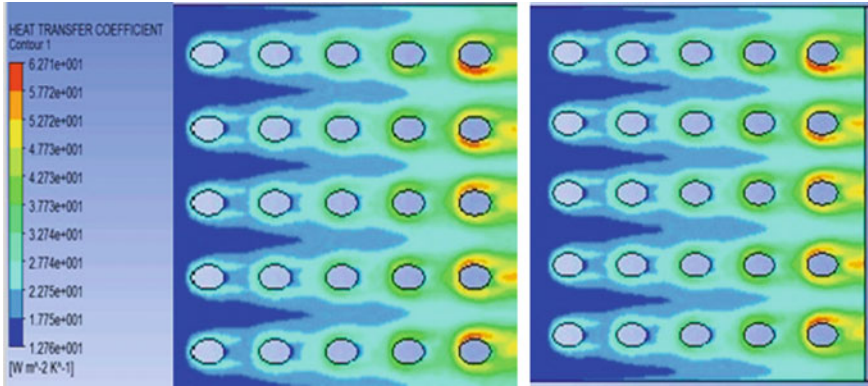


Fig. 22.2 $Re = 10,000$ Case 1 and Case 2 for lower end wall (elliptical pin-fin)

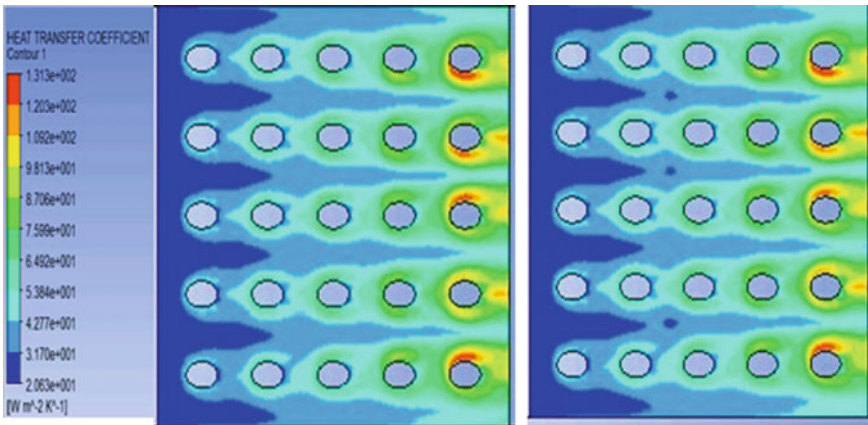


Fig. 22.3 $Re = 20,000$ Case 1 and Case 2 for lower end wall (elliptical pin-fin)

$$\Delta T = T_1 - T_w$$

By definition, ΔT of Case 1 = 26 K and Case 2 = 50 K, case (2) of elliptical pin fin design gives higher thermal efficiency than the circular pin fin design [13].

In the case of elliptical pin fin, the coefficient of friction for case (2) is less compared to the case (1). At Reynolds number 50,000 for case (2) gives the lowest $f = 0.230$ when compared to other four Reynolds number respectively. In the elliptical pin fin, the thermal performance factor (η) at case (2) is higher than case (1). At 10,000 Reynolds number, case (2) has the highest thermal performance factor, i.e., $\eta = 83\%$, respectively (Table 22.2; Graph 22.1).

Thermal performance factor for case (1) is lower when compared to the case (2) thermal performance factor; from the Graph 22.1, its observed that case (1) maximum efficiency is 82% but the case (2) maximum efficiency is 83%, respectively.

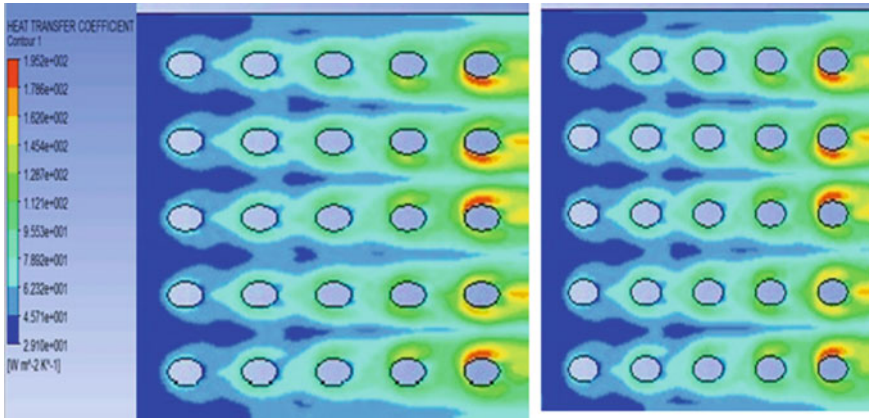


Fig. 22.4 $Re = 30,000$ Case 1 and Case 2 for lower end wall (elliptical pin-fin)

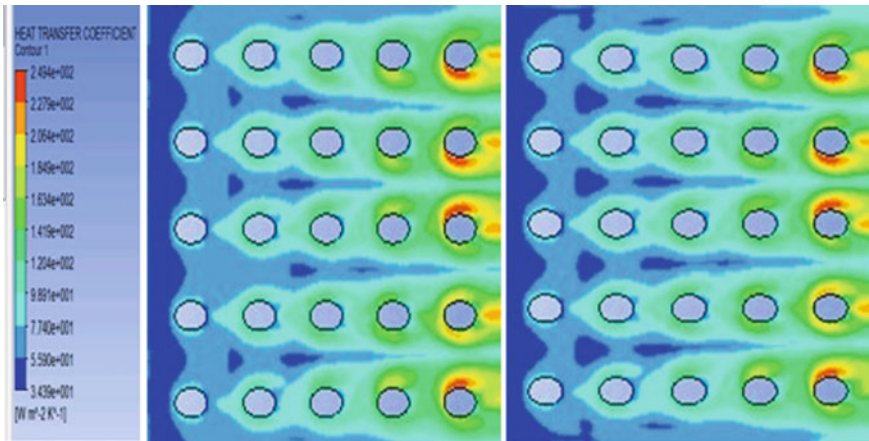


Fig. 22.5 $Re = 40,000$ Case 1 and Case 2 for lower end wall (elliptical pin-fin)

Table 22.2 Case (1) and case (2) thermal performance factor for circular [13] and elliptical pin fin design

TPF (efficiency)	$Re. no$	TPF (efficiency)	$Re. no$
0.826556	10,000	0.822142	10,000
0.776075	20,000	0.772489	20,000
0.744595	30,000	0.741467	30,000
0.725725	40,000	0.722883	40,000
0.711123	50,000	0.708933	50,000

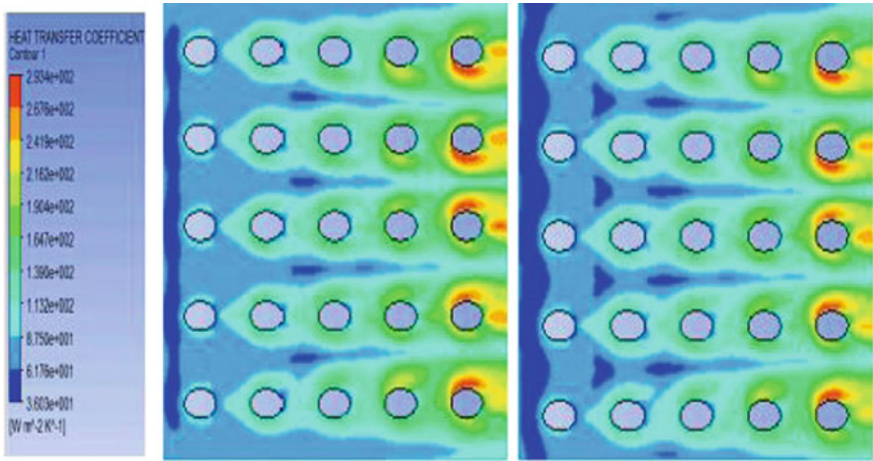
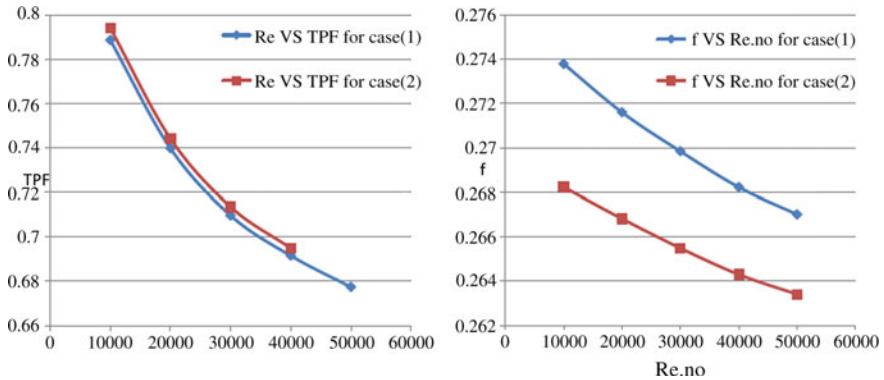
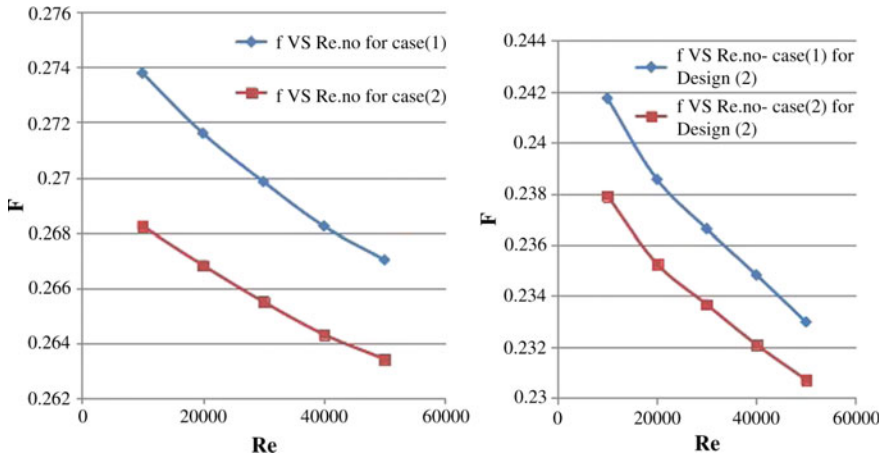


Fig. 22.6 At $Re = 50,000,000$ Case 1 and Case 2 for lower end wall (elliptical pin-fin)



Graph 22.1 Re versus TPF for case (1) experimental results and case (2) for circle [13] and elliptical pin-fin

For the elliptical pin fin, the pressure drop is high in case (2) than the case (1); the Reynolds number of 50,000 for case (2) gives the higher pressure drop ($P_2 = 1352.182 P$). For the elliptical pin fin, the heat transfer coefficient of case (1) having the highest value than case (2). For case (1) $Re = 50,000$ ROW 5 has the highest $HTC = 228.279 (W/m^2k)$ (Graph 22.2; Table 22.3).



Graph 22.2 Reynolds number dependence of the friction coefficient for case (1) experimental and case (2) for circle [13] and elliptical pin-fin

Table 22.3 Case (1) and case (2) friction coefficient and *Re.* no for circular [13] and elliptical pin fin design

<i>f</i>	<i>Re. no</i>	<i>f</i>	<i>Re. no</i>
0.241741	10,000	0.237909	10,000
0.238554	20,000	0.235256	20,000
0.236612	30,000	0.233659	30,000
0.234826	40,000	0.232087	40,000
0.232971	50,000	0.230706	50,000

22.4 Conclusion

In the current study, the flow and heat transfer characteristics of in-lined pin–fins in a wedge duct with two different coolants are analyzed using ANSYS CFX13. The conjugate heat transfer analysis of two cases of coolants case (1) and Case (2) for two different shapes like circular [13] and elliptical pin fin has come to the following conclusions:

- In the circular pin fin case [13], the expected results of the case of $\Delta T = 26$ K agree acceptably with the experimental data of two cases of coolants. Both the Nu at bottom end wall of the wedge duct and the Nu_d on the pin–fins for the case of $\Delta T = 26$ K are higher than values of case $\Delta T = 50$ K. In Case (2), the friction coefficient is very less and also having the high thermal performance factor than the case (1) condition. So, the case (2) is considered as better thermal performance factor for the circular pin fin design.
- For the elliptical pin fin design of two cases of coolants, the friction coefficient for case (2) is less when compared to the case (1). The Reynolds number 50,000 for case (2) gives the lowest friction coefficient when compared to other four

Reynolds number. So, the case (2) is considered as the lower friction coefficient for the elliptical pin fin configuration.

- For the elliptical pin fin, the thermal performance factor (η) for case (2) is higher than that of case (1). The $Re = 10,000$ of case (2) having the highest thermal performance factor. Conclusively, compared to circular and elliptical pin fin design, an elliptical fin pin of case (2) gives the higher thermal performance factor and produces the lower friction coefficient, which improves the heat transfer enhancement of the in-line wedge-shaped elliptical pin fins in the trailing edge of the turbine blade. So, elliptical pin fin design is considered as a better model for this CHT analysis.

References

1. Liao, G., Wang, X., Li, Jun, Zhang, F.: A numerical comparison of thermal performance of in-line pin-fins in a wedge duct with three kinds of coolant. *Int. J. Heat Mass Transf.* **77**, 1033–1042 (2014)
2. Sparrow, E.M., Ramsey, J.W.: Heat transfer and pressure drop for a staggered wall-attached array of cylinders with tip clearance. *Int. J. Heat Mass Transf.* **21**, 1369–1377 (1978)
3. Lau S.C., Kim, Y.S., Han, J.C.: Local endwall heat/mass-transfer distributions in pin fin channel. *J. Thermophys.* **1** (4) (1987) 365–372.
4. Li, Q.L., Chen, Z., Flechtner, U., Warnecke, H.J.: Heat transfer and pressure drop characteristics in rectangular channels with elliptic pin fins. *Int. J. Heat Fluid Flow* **19**, 245–250 (1988)
5. Li, X., Gaddis, J.L., Wang, T.: Modeling of heat transfer in a mist/steam impinging jet. *ASME J. Heat Transf.* **124**, 1086–1092 (2001)
6. Jeng, T.M.: Thermal performance of in-line diamond-shaped pin fins in a rectangular duct. *Int. Commun. Heat Mass Transfer* **33**, 1139–1146 (2006)
7. Sparrow, E.M., Ramsey, J.W., Altemani, C.A.C.: Experiments on in-line pin fin arrays and performance comparisons with staggered arrays. *ASME J. Heat Transfer* **102**, 44–50 (1980)
8. BabusHaq, R.F., Akintunde, K., Probert, S.D.: Thermal performance of a pin–fin assembly. *Int. J. Fluid Flow* **16**, 50–55 (1995)
9. Tahat, M., Kodah, Z.H., Jarrah, B.A., Probert, S.D.: Heat transfer from pin–fin arrays experiencing forced convection. *Appl. Energy* **67**, 419–442 (2000)
10. Liu, J., Gao, J.M., Gao, T.Y., Shi, X.J.: Heat transfer characteristics in steam-cooled rectangular channels with two opposite rib-roughened walls. *Appl. Therm. Eng.* **50**, 104–111 (2013)
11. Jeng, T.M., Tzeng, S.C.: Pressure drop and heat transfer of square pin–fin arrays in in-line and staggered arrangements. *Int. J. Heat Mass Transf.* **50**, 2364–2375 (2007)
12. Hwang, J.J., Lui, C.C.: Measurement of endwall heat transfer and pressure drop in a pin-fin wedge duct. *Int. J. Heat Mass Transfer* **45**, 877–889 (2002)
13. Deepthi, K.R., Madhubala, M.: Thermal analysis of wedge duct with in line pin fin configuration. *IJERT* **7** (2018)

Chapter 23

Computational Fluid Dynamic Analysis of Amphibious Vehicle



H. Jaouad, P. Vikram, E. Balasubramanian and G. Surendar

Abstract Development of unmanned amphibious vehicle for diverse applications including monitoring of oil-spills, military border and water quality measurement in remote water bodies are in the rise. These vehicles suffer for its stability and endurance due to the effect of drag in varied wind conditions. The present work focused on minimizing the drag and improving the aerodynamic performance characteristics. The computational fluid dynamic analysis is performed through considering various turbulent models such as $k-\omega$, $k-\varepsilon$ and SST $k-\omega$ (shear stress transport) to estimate the co-efficient of drag of the designed amphibious vehicle. Static analysis is performed through varying the angle of attack (AoA) from 0^0 to 10^0 under relative airspeed of 5, 8.3 and 10 m/sec. The velocity, pressure and turbulent kinetic energy contours predicted the streamline of air flow around the vehicle and instability regions.

Keywords Amphibious UAV · CFD · RANS model · Drag · Blunt body

23.1 Introduction

Unmanned aerial vehicles (UAVs) are predominantly used in diverse applications [1, 2] including precision agriculture, environmental monitoring, aerial photography, search and rescue, surveillance and reconnaissance, power line and telecom

H. Jaouad
Polytech Orleans, Orleans, France
e-mail: jaouad.hajjaji@gmail.com

P. Vikram · E. Balasubramanian (✉) · G. Surendar
Vel Tech Rangarajan Dr. Sagunthala R & D Institute of Science and Technology, Chennai, India
e-mail: esak.bala@gmail.com

P. Vikram
e-mail: vikram.veeran@gmail.com

G. Surendar
e-mail: suren.ganesh.2007@gmail.com

© Springer Nature Singapore Pte Ltd. 2020
C. Li et al. (eds.), *Advances in Engineering Design and Simulation*,
Lecture Notes on Multidisciplinary Industrial Engineering,
https://doi.org/10.1007/978-981-13-8468-4_23

tower inspections. However, usage of UAVs in water quality monitoring and collection of water samples in remote water bodies are scarce. Especially, the design of amphibian characteristics UAVs which can fly, land and glide along the water surface imposing a lot of challenges in terms of control in flight transition, selection of materials, propulsion, energy consumption and payload capacity [3]. In addition, other factors such as durability, reliability, safety and minimal cost are utmost important for industrial demand and customer requirement. There are few floating UAVs which have been developed and commercialized in the market [4]. However, integrating the characteristics of multirotor and hovercraft systems are not being explored in the literature. These vehicles are aimed to cover large areas of water bodies in a short span of time. Unlike other floating vehicles, due to the principle of hovercraft [5], the friction between the vehicle and water surface is avoided and thereby a huge amount of energy is saved. The vertical take-off and landing ability of vehicle can position the vehicle in precise water locations across rivers, ponds and other water bodies to collect water samples. One of the aerodynamic parameters influencing endurance of amphibious vehicle is a drag. There are few studies have been conducted to calculate the drag of fixed-wing and rotary-wing vehicles. Sitaraman and Baeder [6] carried out aerodynamic analysis of quadrotor using Navier–Stokes equation and wake interactions are studied. Stejil et al. [7] studied rotor and fuselage interaction using CFD analysis using a sliding plane technique. The turbulent flow characteristics [8] during inviscid and viscid fluids are simulated in CFD to analyse the behaviour of shrouds of the multirotor system. Biava et al. [9] examined the aerodynamic behaviour of the helicopter through CFD and experimental studies. Kusyumov et al. [10] carried out a CFD analysis of ANSAT helicopter to determine lift and drag forces in viscous flow conditions. Yoon et al. analysed [11] the flow distribution over fixed-wing aerofoil through varied AoA and co-efficient of drag and lift are obtained. Abudarag et al. [12] studied the flow separation between rotor and fuselage using CFD and turbulent flow characteristics are examined. The present work concentrates on performing CFD studies on various turbulent models [13–15] such as $k-\omega$, $k-\varepsilon$ and SST $k-\omega$ for determining the co-efficient of drag under various AoA and relative airspeed conditions.

23.2 Modelling

The conceptualization amphibian model is designed by inculcating the principles of the quadrotor and hovercraft. This vehicle is capable of flying in the air as a multirotor system and hovering in the water like a hovercraft. After many design iterations, the amphibious UAV model has 1.2 m of length 0.6 m of width and 0.48 m of height is finalized to carry a payload of 7 kg. Propeller has 0.7 m of diameter and 0.182 m of the pitch to generate 10 kg of thrust force. In order to reduce the computational effort, the model is scaled down to a factor of 1:0.25. Also, to maintain the Reynolds number with reference to the prototype, velocity is increased four times and various wind speed conditions are accounted for simulation studies (Fig. 23.1).

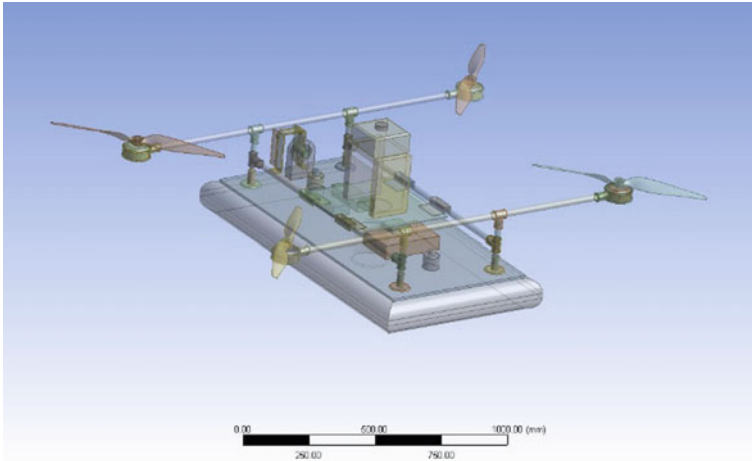


Fig. 23.1 Conceptualized model of amphibious vehicle

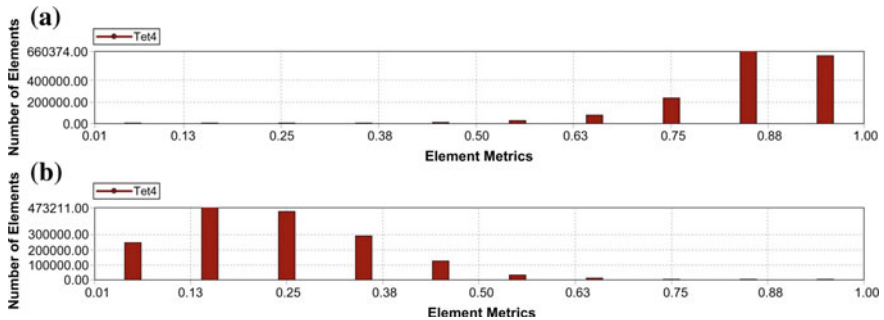


Fig. 23.2 a Orthogonality of elements. b Skewness of elements

The scaled down amphibian structure is meshed with tetrahedron element using ICEM tool. Grid quality is verified with orthogonality (Fig. 23.2a) and skewness and checks (Fig. 23.2b). The average mesh size of the element is maintained as 5,00,000 and 6,00,000 elements.

23.3 Computational Fluid Dynamic Analysis

The turbulent flows are computed by solving Reynolds-averaged Navier–Stokes equations (RANS). Shear stress transport (SST) $k-\omega$ model given in Eqs. (23.1) and (23.2) is utilized to calculate the near-wall flow characteristics using a blending function. It also estimates the flow properties away from the wall surface. In the SST $k-\omega$ model, a damped cross-diffusion term is used to determine the turbulent shear

stress through modifying the turbulent viscosity which ensures the selected model is more accurate and reliable for diverse flow fields

Kinematic eddy viscosity

$$v_T = \frac{\alpha_1 k}{\max(\alpha_1 k, SF_2)} \quad (23.1)$$

Turbulent kinetic energy

$$\frac{\partial k}{\partial t} + U_j \frac{\partial k}{\partial x_j} = P_k - \beta^* k \omega + \frac{\partial}{\partial x_j} \left[(v + \sigma_k v_T) \frac{\partial k}{\partial x_j} \right] \quad (23.2)$$

CFD analysis is performed through varying the AoA under various relative air velocity conditions. Simulation studies are conducted [10] for the following three cases of velocity conditions.

Case 1: 5 m/s

CFD analysis is performed through varying the angle of attack (AoA) from 0^0 – 10^0 at the relative airspeed of 5 m/sec (Fig. 23.3). During 0^0 AoA, high reverse flow region occurs behind the water sampler module region. While increasing the AoA, the velocity regimes are streamlined and at 8^0 AoA reverse flow around the amphibious vehicle is streamlined which reduces drag. Further, an increase of AoA leads to the formation of the turbulent region at the rear of the vehicle that may cause an increase of the drag. It is evident from pressure contours of varied AoA, up to 8^0 , there is a decrease in the trend of pressure and a further increase of AoA causes an increase in pressure in the upstream region and there is a possibility of instability vehicle. Also, above 8^0 of AoA, the intensity of turbulence is increased which may lead to vibration and unable to control the vehicle in the desired path.

Case 2: 8.3 m/s

A similar phenomenon is observed as in the case of 5 m/s. However, the intensity of velocity and pressure is quite high as compared to 5 m/s (Fig. 23.4).

Case 3: 10 m/s

The intensity of turbulence is increased at high relative airspeed which can be seen in Fig. 23.5. For various wind speed conditions and AoA, the co-efficient of drag and lift is estimated which is given in Table 23.1. It is observed that increase in AoA and wind speed causes an increase in drag and a decrease in lift. The lift-to-drag ratio for the wind speed of 8.3 m/s given in Table 23.2 reveals that at 8^0 AoA, high amount of lift is generated with minimal drag.

CFD analysis is performed for half- and full-scale model to validate the results obtained through simulation. It is evident from Table 23.3 that the minimal error is obtained and hence half-scale model can be utilized for CFD analysis to overcome the computational burden and save a lot of time.

For various turbulent models such as $k-\omega$, $k-\varepsilon$ and SST $k-\omega$, CFD analysis is performed and corresponding drag force is determined. Since, $k-\omega$ is considered as a standard model to measure the drag force, with reference to that error is calculated.

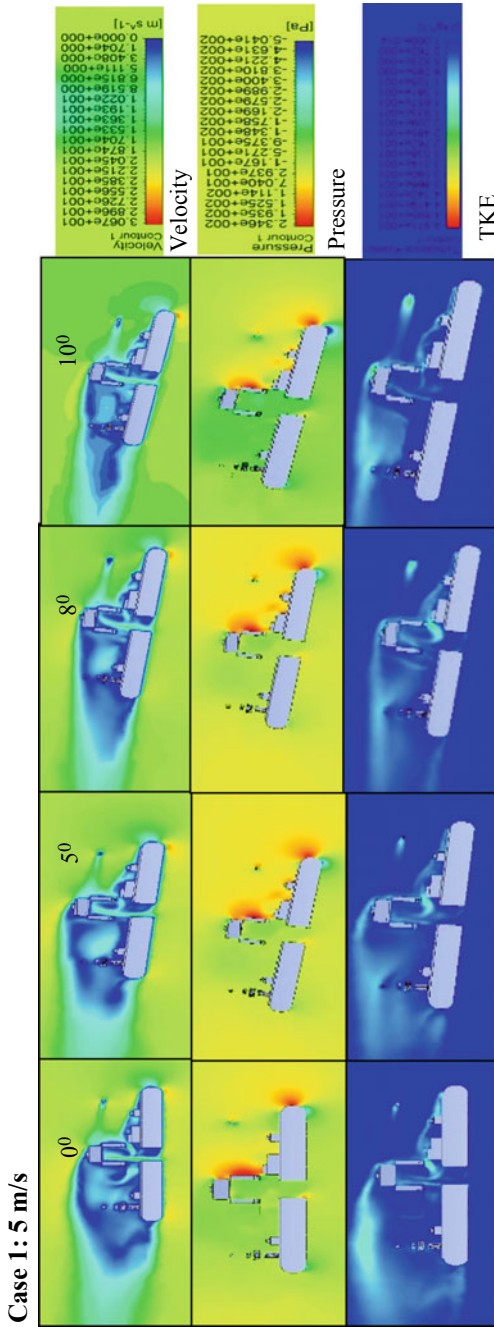


Fig. 23.3 Velocity, pressure and turbulence kinetic energy contours at 5 m/s

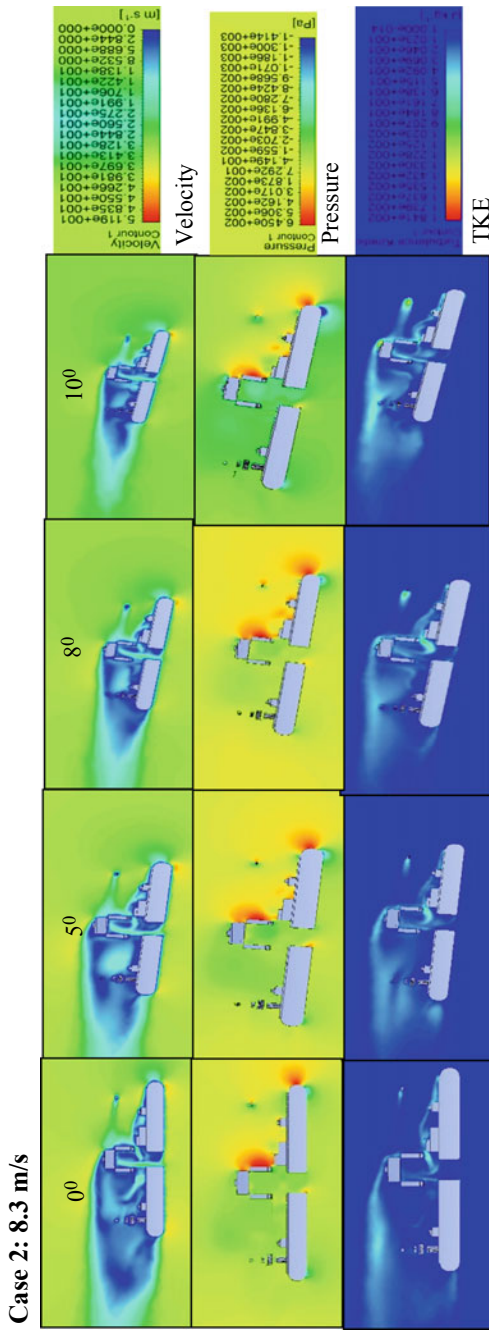


Fig. 23.4 Velocity, pressure and turbulence kinetic energy (TKE) contours at 8.3 m/s

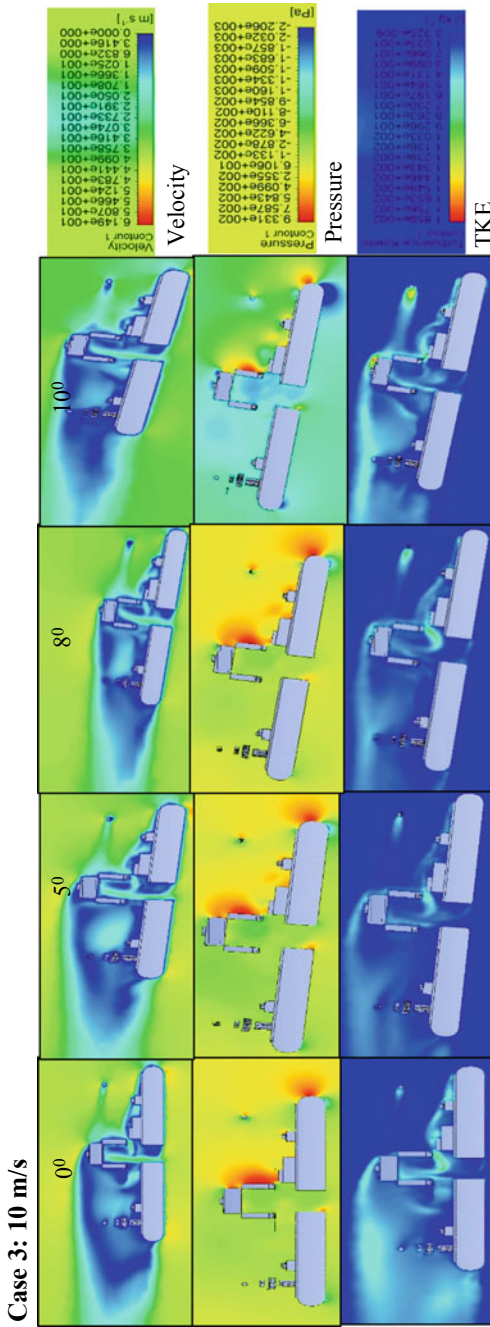


Fig. 23.5 Velocity, pressure and turbulence kinetic energy (TKE) contours at 10 m/s

Table 23.1 Estimation of drag for various AoA under different wind speed conditions

Wind speed (m/s)	Parameters	Angle of attack			
		0°	5°	8°	10°
5.0	C _D	0.489	0.346	0.364	0.382
	C _L	0.165	0.142	0.269	0.285
	Drag	1.32	1.27	1.327	1.529
8.3	C _D	0.489	0.352	0.364	0.382
	C _L	0.165	0.156	0.272	0.249
	Drag	3.639	3.582	3.654	4.213
10.0	C _D	0.489	0.349	0.367	0.379
	C _L	0.201	0.147	0.28	0.229
	Drag	5.28	5.157	5.358	6.059

Table 23.2 Lift-to-drag ratio at 8.3 m/sec

AoA (deg)	Drag (N)	Lift (N)	L/D ratio
0	3.639	1.265	0.348
5	3.582	1.591	0.444
8	3.654	2.731	0.747
10	4.213	2.745	0.652

Table 23.3 Comparison of drag for full- and half-scale amphibious model

AoA (deg)	Relative velocity (m/s)	Drag for full model (N)	Drag for the half model (N)	Error
5	5	2.617	1.278	0.061
	8.3	7.217	3.582	0.051
8	5	2.486	1.327	-0.168
	8.3	6.948	3.654	-0.36

Minimum error is obtained for these models which are given in Table 23.4, and they can be used to calculate the drag force.

At 8.3 m/sec two extreme AoA of conditions (0° and 8°), the velocity streamline pattern is shown in Figs. 23.6 and 23.7. It is observed that there is a severe recirculation zone at 0° and at 8° AoA. It is completely minimized. Hence, at 8° AoA, the amphibious vehicle experiences minimal drag.

Table 23.4 Computation of drag using various turbulent models

AoA (deg)	Relative velocity (m/s)	Drag (N) ($k-\omega$ model)	Drag (N) ($k-\varepsilon$ model)	Drag (N) (SST $k-\omega$ model)	Error ($k-\omega$ /SST $k-\omega$)	Error ($k-\omega$ / $k-\varepsilon$)
5	5	3.615	3.639	3.560	-0.055	-0.024
	8.3	3.582	3.577	3.593	0.011	0.005
8	5	3.654	3.743	3.701	0.047	-0.089
	8.3	4.213	4.298	4.312	0.099	-0.085

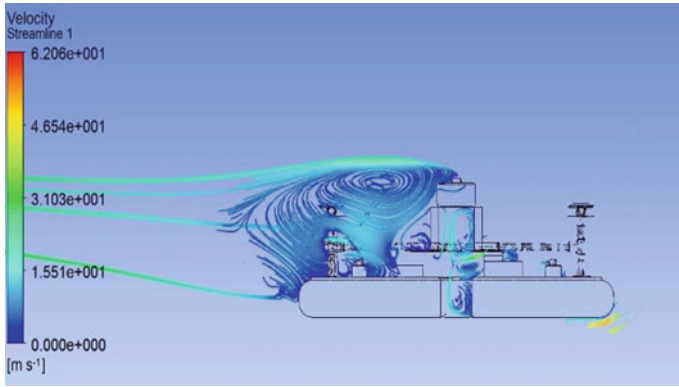


Fig. 23.6 Velocity Streamline 8.3 m/s at 0° AoA

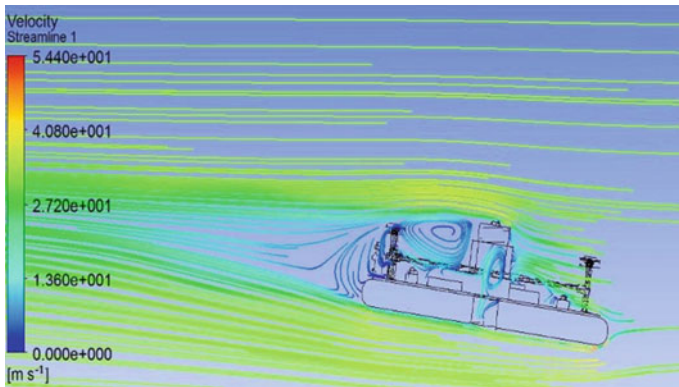


Fig. 23.7 Velocity Streamline 8.3 m/s at 8° AoA

23.4 Conclusion

CFD analysis is performed for the designed amphibian structure through varying the AoA from 0^0 to 10^0 under different wind speed conditions (5, 8.3 and 10 m/s) and corresponding co-efficient of drag and lift force is calculated. At 8.3 m/s and 8^0 AoA, the maximum L/D ratio is obtained in comparison with other operating conditions and hence it is well suited for cruise flight. In addition, CFD studies are conducted for half- and full-scale amphibious models and drag force is calculated. It is evident that the error between these models is minimal and hence the half-scale model can be further utilized to perform CFD analysis. Comparative evaluation of various turbulent models such as $k-\omega$, $k-\varepsilon$ and SST $k-\omega$ suggested that error between standard $k-\omega$ and other models is minimum and hence they can be also used for dynamic analysis.

References

1. Valavanis, K. P., Vachtsevanos, G. J.: Handbook of unmanned aerial vehicles. Springer (2014)
2. Hassanalain, M., Abdelkefi, A.: Classifications, applications, and design challenges of drones: a review. *Prog. Aerosp. Sci.* **91**, 99–131 (2017)
3. Pisanich, G., Morris, S.: Fielding an amphibious UAV—development, results, and lessons learned. *Digital Avionics Systems Conference*, vol. 2, pp. 8C4–8C4 (2002)
4. Boxerbaum, A.S., Werk, P., Quinn, R.D., Vaidyanathan, R.: Design of an autonomous amphibious robot for surf zone operation: Part I mechanical design for multi-mode mobility. In *Advanced Intelligent Mechatronics Proceedings, IEEE/ASME International Conference*, pp. 1459–1464 (2005)
5. Amyot, J.R.: *Hovercraft technology, economics and applications*, vol. 11. North Holland. (2013)
6. Sitaraman, J., Baeder, J.: Analysis of quad-tiltrotor blade aerodynamic loads using coupled CFD/free wake analysis. In *20th AIAA Applied Aerodynamics Conference*, p. 2813. (2002)
7. Steijl, R., Barakos, G., Badcock, K.: CFD analysis of rotor-fuselage aerodynamics based on a sliding mesh algorithm. (2007)
8. Grondin, G., Thipyopas, C., Moschetta, J.M.: Aerodynamic analysis of a multi-mission short shrouded coaxial UAV: part III-CFD for hovering flight. In *28th AIAA Applied Aerodynamics Conference*, p. 5073. (2010)
9. Biava, M., Khier, W., Vigevano, L.: CFD prediction of air flow past a full helicopter configuration. *Aerosp. Sci. Technol.* **19**(1), 3–18 (2012)
10. Kususumov, A., Mikhailov, S.A., Garipov, A.O., Nikolaev, E.I., Barakos, G.: CFD simulation of fuselage aerodynamics of the ANSAT helicopter prototype. *Trans. Control Mech. Syst.* **1**(7), 318–324 (2015)
11. Yoon, S., Lee, H. C., Pulliam, T.H.: Computational analysis of multi-rotor flows. In *54th AIAA Aerospace Sciences Meeting*, p. 0812. (2016)
12. Abudarag, S., Yagoub, R., Elfatih, H., Filipovic, Z.: Computational analysis of unmanned aerial vehicle (UAV). In *AIP Conference Proceedings*, vol. 1798, no. 1, p. 020001. AIP Publishing (2017, January)
13. Lesieur, M.: *Turbulence in fluids: stochastic and numerical modelling*. Nijhoff, Boston, MA (1987)

14. Versteeg, H.K., Malalasekera, W.: An introduction to computational fluid dynamics: the finite volume method. Pearson Education. (2007)
15. Ferziger, J.H., Peric, M.: Computational methods for fluid dynamics. Springer Science & Business Media. (2012)

Chapter 24

Finite Element Analysis of Amphibian UAV Structure



Ting Kee Sheng, Balasubramanian Esakki and Arunkumar Ponnambalam

Abstract Unmanned aerial vehicles are extensively exploited for diverse applications importantly surveillance, reconnaissance, defense, and military. Development of unmanned amphibious vehicle with integrating features of multicopter and hovercraft principles to navigate along and above water body, land surface, and also flying in the air is a challenging task. This article presents a conceptual design of amphibious vehicle for the payload capacity of 7 kg with an endurance of 20 min and provision for mounting water sampler to collect water samples in remote water bodies. Finite element analysis (FEA) is performed to evaluate the structural strength characteristics of each part of the amphibious vehicle, and the integrity of the structure is analyzed. FEA results indicated that the designed amphibious vehicle structure is well within the stress limit and the minimal displacement is obtained. Materials for various parts of vehicles are determined through structural analysis, and the overall amphibious structure is analyzed with a due consideration of lift carrying capacity, payload, battery, and other electronic module weights.

Keywords Amphibious UAV · Quadcopter · Hovercraft · Structural analysis · Finite element analysis

24.1 Introduction

Unmanned aerial vehicles (UAVs) are classified with reference to body shape and size are fixed, flapping and rotary wings [1]. These UAVs made a vivid impact in multifaceted applications including environmental monitoring, search and rescue, bridge inspection, traffic monitoring, mapping of mines, wildlife surveying, precision agriculture, etc. [2]. Design and development of aerial vehicles with diverse

T. K. Sheng
Polytech Orleans, Orléans, France

B. Esakki (✉) · A. Ponnambalam
Vel Tech Rangarajan Dr. Sagunthala R & D Institute of Science and Technology, Chennai, India
e-mail: esak.bala@gmail.com

© Springer Nature Singapore Pte Ltd. 2020
C. Li et al. (eds.), *Advances in Engineering Design and Simulation*,
Lecture Notes on Multidisciplinary Industrial Engineering,
https://doi.org/10.1007/978-981-13-8468-4_24

315

payload capacity and an ability to perform necessary missions pertaining to specific applications are in the rise. There are few research works on the development of amphibious vehicles [3–8]; the design of hovercraft systems [9–14] and many works have been carried out on the development of quadrotor systems. However, the usage of UAVs in water quality monitoring and collection of water samples in remote water bodies are scarce. Especially, the design of amphibian characteristics UAVs can fly, land, and glide along the water surface imposing a lot of challenges in terms of control in flight transition, selection of materials, propulsion, energy consumption, and payload capacity. In addition, other factors such as durability, reliability, safety, and minimal cost are utmost important for industrial demand and customer requirement. There are few floating UAVs which have been developed and commercialized in the market. However, integrating the characteristics of multirotor and hovercraft systems is not being explored in the literature. These vehicles are aimed to cover large areas of water bodies in a short span of time. Unlike other floating vehicles, due to the principle of hovercraft, the friction between the vehicle and water surface is avoided and thereby a huge amount of energy is saved. The vertical takeoff and landing ability of vehicle can position the vehicle in precise water locations across rivers, ponds, and other water bodies to collect water samples. Designing amphibious vehicle with sufficient strength characteristics to withstand lift conditions and carrying necessary payload are considered to be challenging. In this work, an amphibious model is developed to carry a payload of 7 kg. Finite element analysis is performed for UAV frame, hull, skirt, and amphibious structure through varying the materials to examine the structural strength and integrity of the structure.

24.2 Conceptual Model of Amphibious Vehicle

Amphibious model is conceptualized through integrating the principles of quadcopter and hovercraft as shown in Fig. 24.1. The basic H-UAV frame is used to act as quadrotor, and at the four corners, lightweight motors and propellers are assembled to generate sufficient thrust force to lift the entire vehicle. The lifting capacity can be increased by providing coaxial propellers so that payload carrying capacity may be increased. At the middle of the vehicle, a water sampler mechanism is placed, and at the rear, a duct fan is positioned to achieve directional control while in hovercraft mode. The batteries, electronic accessories, flight controllers, and other electrical elements are appropriately distributed to balance the center of gravity of the vehicle.

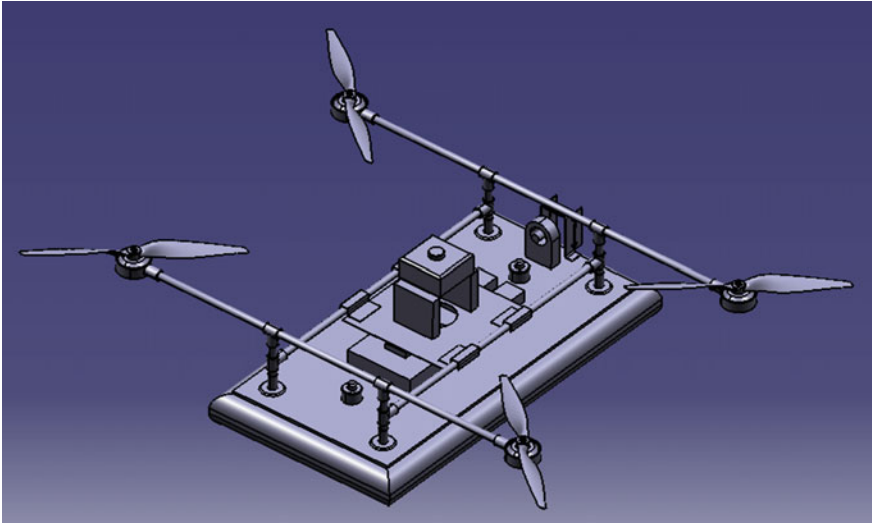


Fig. 24.1 Conceptualized model of amphibious vehicle

24.3 Finite Element Analysis of Amphibious Parts and Integrated Structure

In order to determine the suitable material for each amphibious part, structural analysis is performed through varying the materials. They are selected with respect to high strength-to-weight ratio, manufacturability, low cost, and also its availability.

24.3.1 Quadrotor Frame

The quadrotor frame is meshed (Fig. 24.2) with tetrahedron element having three degrees of freedom (DOF) with skewness of 0.978 and an aspect ratio of 2. The elements are maintained with maximum tetrahedron angle of 102° and length of the element is 6 mm. The generation of thrust force from each propeller of about 10 kg is applied at each corner of the motor frame; a central load of 7 kg as the payload is concentrated for payload; and batteries and other loads are distributed appropriately in the frame structure. For various materials (Table 24.1), structural analysis is carried out to determine the minimal displacement and stress. Aluminum obtained the maximum stress of 15 MPa (Fig. 24.3) and the displacement of 2.22 mm (Fig. 24.4).

It is also observed from Table 24.1 that carbon fiber and aluminum obtained better performance in comparison with other materials. However, with respect to cost and availability, aluminum is preferred.



Fig. 24.2 Finite element model with boundary conditions

Table 24.1 Structural analysis results of various materials for UAV frame

Materials	Max stress (MPa)	Max displacement (mm)	Structure mass (kg)
Aluminum	15.4	2.2	6.6
Carbon fiber	12.4	1.7	3.9
ABS	12.2	45.8	2.6
PEEK	12	30.5	3.2
ULTEM	11.9	39.4	3.1

Fig. 24.3 Stress contour of UAV frame-aluminum

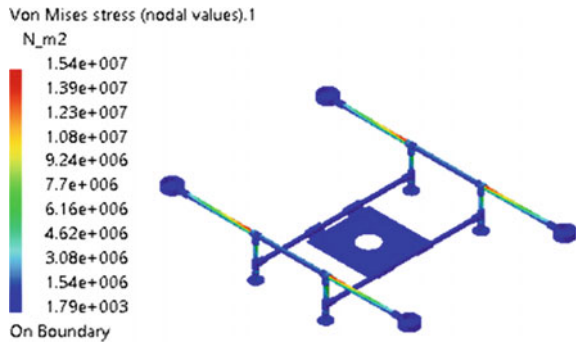


Fig. 24.4 Deformation of UAV frame-aluminum

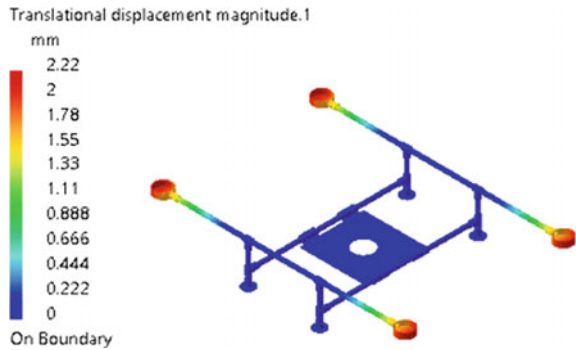


Fig. 24.5 Stress contour of hull

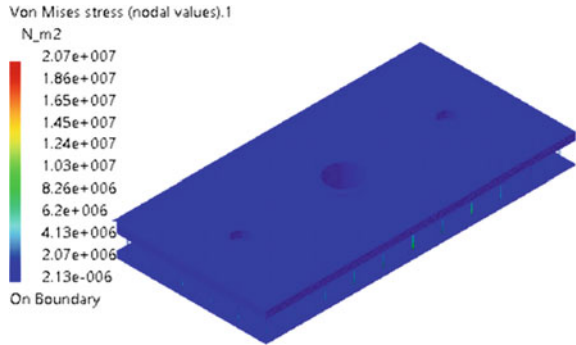
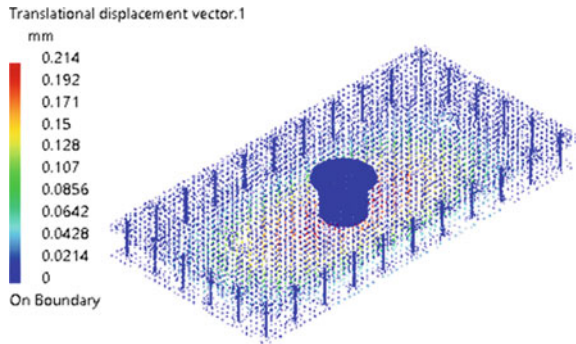


Fig. 24.6 Deformation of hull



24.3.2 Hull

It serves as a platform to fasten the frame of the quadrotor together and hold the electronics hub. It also incorporates all hardware units, propulsion, wireless communications, soldered circuitry, and battery. The structure is made up of wood/foam sandwich to achieve minimal weight. Finite Element Analysis (FEA) is performed for the internal hull pressure of 731 Pa, 10 kg battery weight and other loads of 1.5 kg are acting on the hull is also considered for the analysis. Simulation results indicated that maximum stress (Fig. 24.5) of 20 MPa and deformation of 0.21 mm (Fig. 24.6) are experienced at the hull structure.

24.3.3 Skirt

The skirt is inflated during hovering mode, and it creates a cushioning effect between the vehicle and surface. An internal pressure of 731 Pa is applied along the periphery of the structure, and the static analysis is performed for diverse materials as given in

Table 24.2 Structural analysis results for various skirt materials

Materials	Max stress (MPa)	Max displacement (mm)	Structure mass (kg)
Natural rubber	0.74	352	0.969
Nylon impregnated with urethane	0.743	0.307	1.204
Urethane nylon	0.736	0.43	1.332
Neoprene coated nylon	0.736	0.202	1.278

Fig. 24.7 Stress contour of skirt

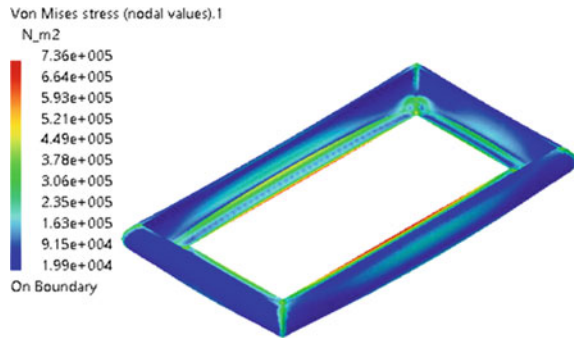


Fig. 24.8 Deformation of skirt

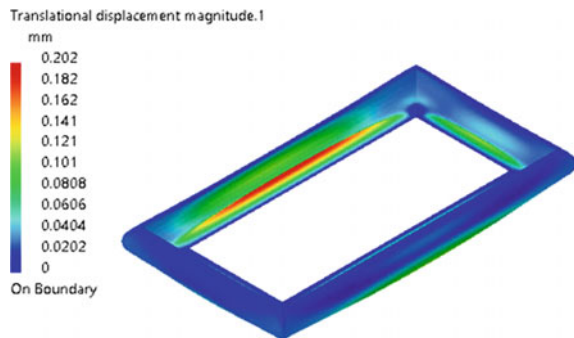


Table 24.2. Due to the pressure loading, the minimal stress of 0.74 MPa (Fig. 24.7) and the displacement of 0.2 mm (Fig. 24.8) are obtained for nylon family materials.

24.3.4 Integrated Structure

After integrating UAV frame, hull, and skirt for the earlier material properties and applying appropriate boundary conditions, FEA is carried out to evaluate the integrity and strength of the amphibious structure.

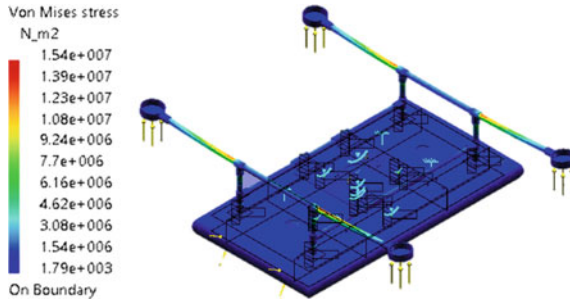


Fig. 24.9 Stress contour of amphibious structure

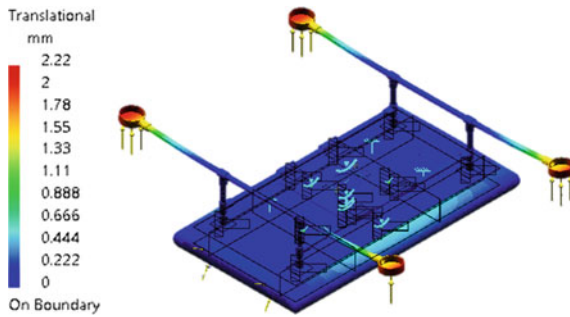


Fig. 24.10 Deformation of amphibious structure

Static analysis results indicate that the designed structure is well within the allowable stress (Fig. 24.9) and deformation of 2 mm can be seen at the four corners due to cantilever structure (Fig. 24.10).

The convergence of the solution is guaranteed with reference to analysis as shown in Fig. 24.11.

24.4 Conclusion

Amphibious vehicle is conceptualized for air, water, and land-borne operations to carry a payload capacity of 7 kg. Each part of an amphibious vehicle such as UAV frame, hull, and skirt is structurally evaluated with diverse material properties, and appropriate boundary conditions are considered. The following are the conclusions drawn from FEA:

- For the UAV frame, aluminum and carbon fiber obtained minimal displacement and stress. However, aluminum is cost-effective than carbon fiber.

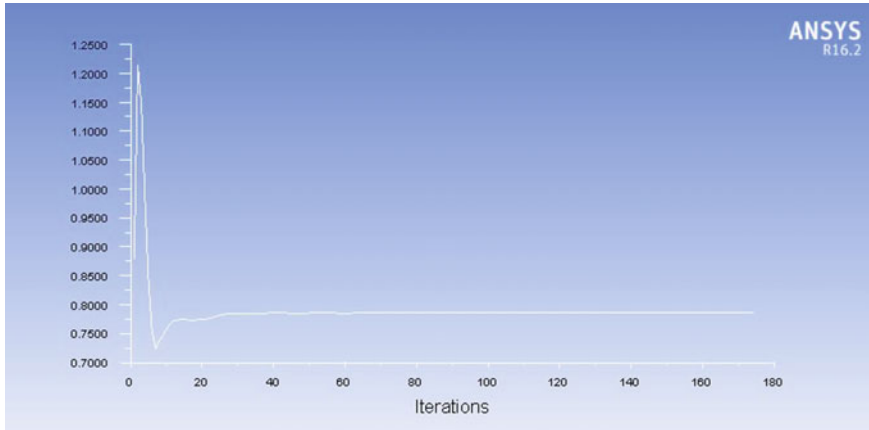


Fig. 24.11 Convergence of solution

- Hull material made of wood/foam sandwich structure has better load-carrying capacity to withstand the payload, weight of the battery, and other electronic modules.
- Neoprene-coated nylon obtained minimal displacement and stress in comparison with other nylon-based material, and it can be selected for the skirt.
- The integrated structure of quadrotor and hovercraft experienced minimal displacement and stress. Hence, the conceptualized amphibious structure can be built through these materials and it ensures the rigidity of the structure.

References

1. Valavanis, K.P., Vachtsevanos, G.J.: Handbook of unmanned aerial vehicles. Springer, New York (2014)
2. Hassanalian, M., Abdelkefi, A.: Classifications, applications, and design challenges of drones: a review. *Prog. Aerosp. Sci.* **91**, 99–131 (2017)
3. Collins, K.A.: A concept of unmanned aerial vehicles in amphibious operations. Doctoral dissertation, Monterey, California. Naval Postgraduate School (1993)
4. Boxerbaum, A.S., Werk, P., Quinn, R.D., Vaidyanathan, R.: Design of an autonomous amphibious robot for surf zone operation: Part I mechanical design for multi-mode mobility. In *Advanced Intelligent Mechatronics Proceedings, IEEE/ASME International Conference*, pp. 1459–1464 (2005)
5. Yayla, M., Sarsilmaz, S.B., Mutlu, T., Cosgun, V., Kurtulus, B., Kurtulus, D.F., Tekinalp, O.: Dynamic stability flight tests of remote sensing measurement capable amphibious unmanned aerial vehicle. In: *AIAC, 7th Ankara International Aerospace Conference*, Ankara, Turkey (2013)
6. Pisanich, G., Morris, S.: Fielding an amphibious UAV—development, results, and lessons learned. In: *Digital Avionics Systems Conference*, vol. 2, 8C4-8C4 (2002)
7. Hasnan, K., Ab Wahab, A.: First design and testing of an unmanned three-mode vehicle. *Int. J. Adv. Sci. Eng. Inf. Tech.* **2**(1), 13–20 (2012)

8. Frejek, M., Nokleby, S.: Design of a small-scale autonomous amphibious vehicle. In: *Electrical and Computer Engineering, CCECE Canadian Conference, IEEE*. 000781-000786 (2008)
9. Amyot, J.R.: *Hovercraft technology, economics and applications*, North Holland, 11 (2013)
10. Detweiler, C., Griffin, B., Roehr, H.: Omni-directional hovercraft design as a foundation for MAV education. *Intelligent Robots and Systems (IROS), IEEE/RSJ*, pp. 786–792 (2012)
11. Schleigh, J.: *Construction of a hovercraft model and control of its motion*. Doctoral dissertation (2006)
12. Rashid, A., Zamzuri, M., Aras, M., Shahrieel, M., Mohamed Kassim, A., Ibrahim, Z., Annisa, J.: Dynamic mathematical modeling and simulation study of small scale autonomous hovercraft. *Int. J. Adv. Sci. Tech.* **46**, 95–114 (2012)
13. Fuller, S.B., Murray, R.M.: A hovercraft robot that uses insect-inspired visual autocorrelation for motion control in a corridor. *Robotics and Biomimetics (ROBIO)*, pp. 1474–1481 (2011)
14. Amiruddin, A.K., Sapuan, S.M., Jaafar, A.A.: Development of a hovercraft prototype with an aluminium hull base. *Int. J. Phys. Sci.* **6**, 4185–4194 (2011)

Chapter 25

Investigation of 3D Printed Jet Fuel Atomizer



Raja Marudhappan, U. Chandrasekhar and K. Hemachandra Reddy

Abstract The simplex atomizer of an annular combustion chamber of an 1100-kW class aero-derivative turboshaft engine is designed. Three-dimensional CAD model of the atomizer is made. An attempt is made to fabricate the atomizer model in 3D printing using acrylonitrile butadiene styrene and fused deposition modeling technique. The quality of the 3D printed atomizer is studied for the suitability of functional testing. It is found that the surface finish and the smallest structural features of the 3D printed model are not meeting the functional requirements. Hence, the atomizer manufactured by conventional machining is considered in numerical modeling and performance testing using Jet A fuel. The transient 2D axisymmetric flow analysis is performed by solving Navier–Stokes equations. The fuel–air interface is tracked by following the Euler–Euler approach and using the volume of fluid (VOF) surface tracking mathematical model. The velocity fields across the swirl chamber and in the near exit zone are presented. The air core formation and hollow cone spray obtained from numerical modeling are compared to previously published reports. The atomizer is tested in an atmospheric test facility to assess the quality of jet penetration and hollow cone spray formation. The observed performance characteristics are compared to the published literature and found in order. Alternative techniques for 3D printing of the atomizer and the related issues are discussed.

Keywords 3D printing · Atomizer · Annular combustor · Turboshaft · Numerical modeling

R. Marudhappan (✉) · K. Hemachandra Reddy
JNTUA, Anantapur 515002, India
e-mail: raja.marudhappan@gmail.com

U. Chandrasekhar
Vel Tech University, Chennai 600062, India

© Springer Nature Singapore Pte Ltd. 2020
C. Li et al. (eds.), *Advances in Engineering Design and Simulation*,
Lecture Notes on Multidisciplinary Industrial Engineering,
https://doi.org/10.1007/978-981-13-8468-4_25

Nomenclature

x, y, z	Spatial coordinates
u, v, w	Instantaneous velocity along spatial coordinates x, y, z
V	Velocity vector field
ρ	Density
p	Pressure
τ	Shear stress
β	Liquid volume fraction
\dot{m}_{ab}	Mass transfer from phase a to phase b
\dot{m}_{ba}	Mass transfer from phase b to phase a
q	Body force per unit mass

25.1 Introduction

Atomization converts the bulk of fuel into small droplets. The atomization process comprises two separate processes. The first process also called the primary atomization converts the fuel stream into shreds and ligaments. Further secondary atomization leads to breaking of larger drops and globules resulted from primary atomization. There are two mechanisms of atomization of liquids, viz. classical mechanism and prompt mechanism. When the velocity of flow is lesser, classical atomization predominates. Prompt mechanism occurs when the flow velocity is larger. The atomization mechanism in gas turbine engines generally follows prompt mechanism. The major task of the atomizer is to provide sufficiently larger surface area by forming an increased number of fuel droplets. Hence, drop sizes and drop size distribution are important performance requirements of the atomizer. Another task of the atomizer is to distribute the drops as per the requirement in the combustion chamber in order to achieve a well-controlled air–fuel mixture distribution and rapid mixing.

25.2 Literature Review

Atomization can be achieved through different methods. These methods involve many basic processes such as hydraulics of flow inside the atomizers. The hydraulics govern the turbulence of the emerging liquid spray. The shape, penetration, and number density of drops are controlled by the development of the jet and the growth of small disturbances leading to the disintegration of the sheet into ligaments and then drops [1].

Atomizers are broadly classified into three distinct categories based on the basic process involved. The pressure atomization is achieved by forcing the liquid through a narrow orifice to obtain high velocity. The thin fluid atomization uses high-velocity air stream to disintegrate fuel jet. Rotary atomizers employ centrifugal forces to produce liquid sheet while flowing along the surface of a rotating disk [2].

The pressure atomization is the simplest method to atomize the liquid fuel. The pressure energy of the liquid is converted into kinetic energy inside the nozzle, and the liquid is forced through the orifice. When the liquid enters the orifice with a tangential velocity component, a hollow cone spray emerges in the downstream of the orifice. The spray cone angle of 60–100° can be achieved by controlling the flow properties closely.

The internal flow of water in a scaled pressure swirl atomizer is modeled numerically and experimentally by Hansen et al. [3]. The study is conducted to validate the applicability of commercial CFD code CFX-4.3 in modeling the atomization process. Laser Doppler anemometry (LDA) is used in experiments for measuring the flow velocity. The study reported the presence of Rankine-vortex-like phenomena in tangential velocity profile. The study is made based on turbulence and laminar flow. The numerical simulations managed to capture the characteristics of pressure swirl atomizer by capturing the air core and thin film of fluid in the orifice exit region.

Rezaeimoghaddam et al. [4] studied the effects of shear thinning and shear thickening fluids in a pressure swirl atomizer. The fluid flow inside the atomizer is simulated by solving Navier–Stokes equations time-independently and solving the transport equation for volume fraction by VOF model. The numerical study used different sizes of orifices. The results obtained from the numerical study are compared to Ma's experimental data [5]. The comparison shows that the tangential velocity decreases when the power law index increases.

The atomization of Jet A-1 fuel in a commercial pressure swirl atomizer is experimentally investigated by Marchione et al. [6]. Phase Doppler anemometry (PDA) is used for the characterization of drop sizes and velocity. The fluctuation of spray behavior is examined with a high-speed charge-coupled camera. The analysis of the digital image has confirmed that the instantaneous spray cone angle is approximately equal to the one obtained with a PDA. Two oscillation modes at 100 and 1800 Hz are reported.

Numerical simulation of the internal flow of swirl atomizer under ambient pressure is reported by Fu [7]. VOF method is used to track the interface of liquid and air. The steady-state flow analysis is performed on a 2D axisymmetric model. The effect of inlet pressure fluctuations on a spray cone angle and flow rate is reported. The VOF model is able to capture the liquid–air interface.

Mkvik et al. [8] performed a numerical investigation on a twin-fluid atomizer internal flow. The viscous aqueous Maltodextrin solution is used in the experiments. Twin-fluid atomizers use a pressurized gas stream to enhance the jet breakup. The simulation is performed on a commercial CFD code. The investigation reported the influence of mixing mechanism on internal flow dynamics.

Qian et al. [9] reported a numerical study of internal flow in a pressure swirl atomizer. The interface of liquid and air is modeled by VOF technique. The technique

called coupled level set/VOF solver is used for numerical modeling. The impact of different geometric parameters on atomization quality is reported. The numerical prediction of the internal flow field, spray cone angle, and velocity profiles are compared to the published literature. The comparison shows that the coupled level set/VOF method is able to predict the flow pattern more accurately than the conventional VOF method.

Cui et al. [10] visualized the internal flow in a pressure swirl atomizer and characterized the effect of orifice geometry on spray and flow field. Interferometer particle imaging (IPI) is used for droplet size measurement. The experiments are performed using water. The nozzles are manufactured from transparent methyl methacrylate. The effect of the flow field in different nozzles having manufacturing deviations under various injection pressures is reported. The Sauter mean diameter (SMD) of drops monotonously decreases with an increase in injection pressures.

The objectives of this study are to design a pressure swirl atomizer for use in an 1100-kW class aero-derivative gas turbine engine and to explore the possibility of additive manufacturing of atomizer by 3D printing. In case the 3D printing is not successful, it is planned to manufacture the atomizer by conventional machining methods and carry out numerical modeling of internal flow. The numerical results obtained are validated by experiments.

25.3 Governing Equations

The governing equations of fluid flow provide mathematical statements of the laws of conservation of physics. These are the continuity equation and momentum conservation equations. These equations are solved over the problem domain to obtain the instantaneous values of flow field variables [11].

These fluid flow governing equations are;

Continuity equation:

$$\frac{\partial \rho}{\partial t} + \nabla \cdot (\rho V) = 0 \quad (25.1)$$

X-momentum:

$$\frac{\partial(\rho u)}{\partial t} + \nabla \cdot (\rho u V) = -\frac{\partial p}{\partial x} + \frac{\partial \tau_{xx}}{\partial x} + \frac{\partial \tau_{yx}}{\partial y} + \frac{\partial \tau_{zx}}{\partial z} + \rho q_x \quad (25.2)$$

Y-momentum:

$$\frac{\partial(\rho v)}{\partial t} + \nabla \cdot (\rho v V) = -\frac{\partial p}{\partial y} + \frac{\partial \tau_{xy}}{\partial x} + \frac{\partial \tau_{yy}}{\partial y} + \frac{\partial \tau_{zy}}{\partial z} + \rho q_y \quad (25.3)$$

Z-momentum:

$$\frac{\partial(\rho w)}{\partial t} + \nabla \cdot (\rho w V) = -\frac{\partial p}{\partial z} + \frac{\partial \tau_{xz}}{\partial x} + \frac{\partial \tau_{yz}}{\partial y} + \frac{\partial \tau_{zz}}{\partial z} + \rho q_z \quad (25.4)$$

Apart from solving the continuity and momentum conservation equations, the interphase of the fuel and air is tracked by the solution of continuity equation for volume fraction of the fuel.

$$\frac{1}{\rho_b} \left[\frac{\partial}{\partial t} (\beta_b \rho_b) + \nabla \cdot (\beta_b \rho_b \vec{v}) \right] = \sum_{p=1}^n \dot{m}_{ab} - \dot{m}_{ba} \quad (25.5)$$

The volume fraction (β) of each finite volume is specified as

$$\beta = \begin{cases} 1 & \text{pure liquid (fuel)} \\ 0 < \beta < 1, & \text{gas-liquid interface} \\ 0 & \text{pure gas (air)} \end{cases}$$

The volume fraction of the b th liquid phase is calculated based on the constraint,

$$\sum_{b=1}^n \beta_b = 1 \quad (25.6)$$

25.4 Design of Atomizer

Radcliffe [12] did extensive research on the effect of geometrical parameters on atomization quality using a simplex atomizer. A large number of swirl atomizers with different geometric sizes are tested with water, and the results are published. These atomizers have two fixed parameters, the diameter of the swirl chamber (D) and swirl chamber cone angle (φ). The other geometric parameters are presented in Table 25.1.

The atomizer has a body, housing the swirl pin. The swirl pin is located centrally inside the body by a compression spring. A fuel filter normally of 10 μm mesh size is placed at the inlet of the atomizer and locked with a circlip. The swirl pin has three inclined swirl ports in such a way that the liquid enters the chamber with sufficient swirl velocity component. The schematic drawing of the atomizer is shown in Fig. 25.1. Figure 25.2 shows the sectional view of atomizer housing. Isometric view and front view of swirl pin are shown in Fig. 25.3.

Table 25.1 Atomizer design parameters

Parameters	Values
Orifice diameter	$d = 0.6 \text{ mm}$
Swirl chamber diameter	$D = 6d$
Size of tangential port	$P = 0.5 \times 0.5 \text{ mm}$
Length of final orifice	$t = 2d/3$
Length of cylindrical section of swirl chamber	$b = 2d$
Radius of offset of tangential ports	$r = D/2 - 3d/4$
Swirl chamber cone angle	$\Phi = 90^\circ$

Fig. 25.1 Schematics of swirl atomizer

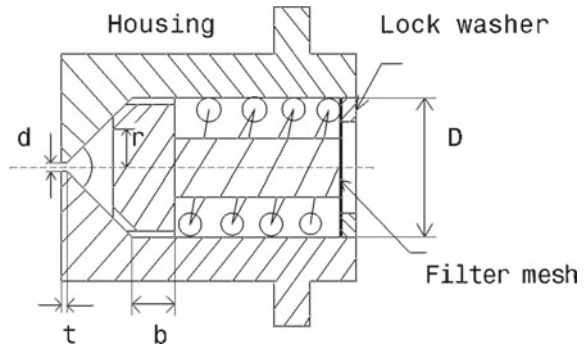


Fig. 25.2 Sectional view of atomizer housing

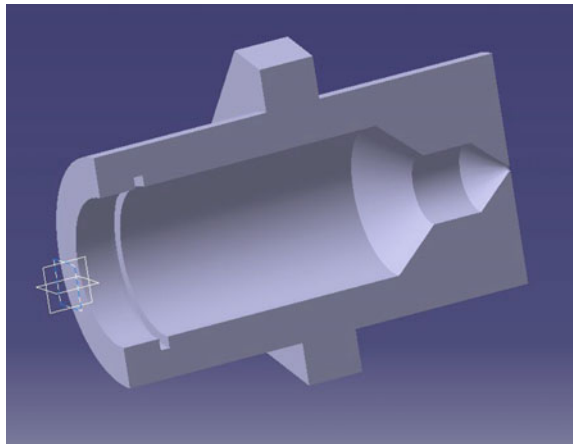
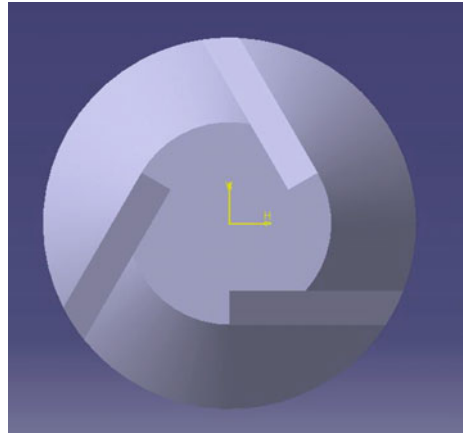
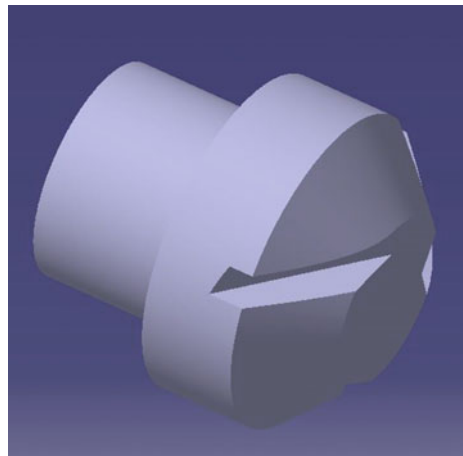


Fig. 25.3 Swirl pin

(a) Front view



(b) Isometric view

25.5 Rapid Prototyping and Manufacturing

25.5.1 Introduction

The term rapid prototyping and manufacturing (RP&M) is synonymously used for 3D printing. The earlier application of the technology was limited to manufacturing of prototypes. The earlier technology has not led to the manufacturing of functional parts. The 3D printing industry is fast maturing and opening up several avenues in manufacturing functional parts. The prototype provides an excellent visualization than a hundred pictures. The rapid prototyping makes the process of verification of design easier to examine whether the prototype carries all the desired features

and it carries any unwanted features. Though functional tests are not performed, the designers are able to hold in their hands the geometrically verified parts.

25.5.2 Methods of 3D Printing

The stereolithography (SLA) was developed by a Japanese researcher Dr. Hideo Kodama during early 1980. The process uses ultraviolet light to cure the photo-sensitive polymer in layer-by-layer additive manufacturing. Several distinct additive manufacturing processes have been evolved, and they differ in the method of layering, materials, and machines used. The early development of fused deposition modeling (FDM) has confined mostly to desktop platforms. This process has limitations since precision and repeatability are major concerns which prevent the applicability of the process in professional applications.

The selective laser sintering (SLS) or direct metal laser sintering (DMLS) is based on the selective fusion of a powder bed in layers as per the CAD model. The plastic-based process is referred to as SLS, and the metal based process is referred to as DMLS.

The printing time in conventional SLS/DMLS is very prohibitive. The development of mask-image projection-based stereolithography (MIP-SL) has drastically reduced the manufacturing time of homogenous objects.

25.5.3 Aeronautical Industry and 3D Printing

Aeronautical industry is an early adopter of 3D printing compared to other industries. Functional parts used in aerospace and defense applications are generally required to be manufactured with close dimensional tolerances. Moreover, development of a new component by conventional methods takes generally longer time due to the complex nature of geometrical features and subsection of many quality certification processes. The 3D printing offers an excellent tool for quick manufacturing of not only the prototype but also the functional components.

Though the 3D CAD model and drawings give a reasonable understanding of the components, a quick made physical model cannot be supplemented by drawings. This makes 3D printing an attractive platform to understand the intricacy of complicated components in the early stages of development. The manufacturing of an aircraft or an aero-engine requires hundreds of fixtures and jigs. When these are 3D printed, it saves roughly 60–90% of cost and development time compared to other conventional manufacturing processes [13].

Surrogates are the components which represent actual components but are used for educational and training purposes. These surrogates are normally used on the production floor. The 3D printing can be adopted for the manufacture of surrogates.

3D printing is successfully applied in the manufacturing of low-volume structures and metal brackets. These include mounts of oil and fuel accessories on an aero-engine or mounts of complex life-saving systems in an aircraft. Other functional parts suitable for 3D printing are combustion liners, air intake, and exhaust ducts. Surface finish is a critical requirement in the aeronautical industry. The surface finish of 3D printed components is not suitable for ready to use. The surface finish of additive manufactured components has been improved by the development of material jetting and binder jetting technologies. These can offer smooth, injection-molding-like finish with a little post-processing.

Major aerospace companies like Rolls-Royce, Turbomeca, and GE are foraying into manufacturing of aero-engine components by 3D printing to save time, money, and inventory. Rolls-Royce has a plan to fly the largest 3D printed part ever flown; however, it has not set any time frame. Rolls-Royce has printed the front bearing housing for the Trent XWB-97 engine from titanium with 1.5 m diameter [14]. GE has already manufactured titanium structures and bearing housing using electron beam melting technology (EBMT) [15]. The Indian aeronautical industry is yet to go a long way in adopting 3D printing of aero-engine components or aircraft structures. Recently, Hindustan Aeronautics Limited has forayed into manufacturing of centrifugal pump casing and nozzle guide vanes of developmental projects. However, these parts are yet to undergo a long certification process.

25.5.4 Raw Materials for 3D Printing

There are a variety of raw materials available for 3D printing. The selection of the right material for the intended application needs an extensive research. The acrylonitrile butadiene styrene (ABS) and polylactic acid (PLA) are most commonly used materials for preliminary research works. ABS belongs to thermoplastic polymer family and opaque. ABS is more popular because of its superior plastic properties. The major advantages of ABS are its abrasion resistance and affordability. The added advantages are its impact strength and lightweight. The melting temperature is 200 °C which makes ABS an ideal choice for use in safe machines. It is fire-retardant and also gives good surface quality. It is biocompatible and recyclable. However, oxidation of ABS at higher temperatures leads to yellowing color.

PLA is considered as an alternative to ABS. It is made from cornstarch. It melts at 150 °C. The PLA prints made for mechanical operations or when stored at high temperatures result in warping, cracking, or melting. It is also biodegradable.

Metal printing is the fastest growing segment in the rapid prototyping industry. The availability of low-cost metal powders is directly tied to the realization of potential and transformation of industrial production. Metal powders are generally manufactured either by water jet atomization or gas atomization. Gas-atomized powders are generally preferred over the water-jet-atomized powders because the later one produces irregularly shaped powders.

25.5.5 3D Printing of Atomizer

The swirl pin and the housing are the two important components of a pressure swirl atomizer. The accuracy and surface quality of fuel inlet ports on the swirl pin are the most important for achieving proper atomization. It is decided to manufacture these two components by 3D printing using FDM with ABS material. The print parameters are listed in Table 25.2.

The print quality of atomizer housing is better than the quality of swirl pin. The 3D printing has failed to print the 0.5×0.5 mm fuel inlet port at the swirl pin. The surface finish has not improved even after post-print cleaning, making the 3D printed components unsuitable for functional testing. The model is built in 0.12-mm-thick layers which is the minimum possible thickness by FDM. The finest feature of the swirl pin, the fuel inlet port 0.5×0.5 mm size is not printed by the chosen printing method. After a careful market research, 0.178-mm-diameter nozzle is used for printing. The chosen nozzle is the smallest size found in the market at present. The 3D printed swirl pin is shown in Fig. 25.4.

Subsequently, the atomizer housing and swirl pin are manufactured by wire cut electric discharge machining. Figure 25.5 shows the swirl pin manufactured by sub-

Table 25.2 Parameters of 3D printing

Model material	ABS
Model volume	50.0 mm ³
Filament diameter and length	1.00 and 30.00 mm
Diameter of print nozzle	0.2 mm
Temperature of nozzle tip	315 °C
Printer oven temperature	90 °C

Fig. 25.4 Swirl pin, 3D printed



Fig. 25.5 Swirl pin

tractive manufacturing. The stainless steel of grade SS347 is used for both housing and swirl pin. The swirl pin is assembled inside the housing using a compression spring, filter, and a circlip.

25.6 Numerical Modeling of Atomization

The 3D fluid flow domain is shown in Fig. 25.6. However, the atomizer internal flow analysis is performed in 2D axisymmetric model. The 2D model is discretized with mapped face mesh, Fig. 25.7. The computational domain is extended up to 2.00 mm down the orifice to study the spray structure.

The atomizer internal flow is classified as stratified where the two immiscible fluids, fuel and air are separated by a clearly defined interface boundary. The fluid mechanics offers two different approaches of mathematical modeling of multiphase flow, viz. Euler–Lagrange approach and Euler–Euler approach. The Euler–Euler approach assumes the phases are interpenetrating continua in this case fuel and air. This approach introduces a concept called phasic volume fraction since the volume of a phase is unique and cannot be occupied by any other phase. The VOF model is an interface surface tracking technique based on the Euler–Euler approach. There are certain limitations in using the VOF model. The model can only be used with pressure-based solver, and the control volume is always occupied by either of a phase in the case of two-phase flow. The thermophysical properties of Jet A used in the analysis are presented in Table 25.3.

The convection terms of the governing equations are discretized with least square cell-based method. The pressure equation is discretized with pressure staggering option (PRESTO) scheme. The momentum and swirl velocity equations are discretized with the second-order upwind scheme. The volume fraction equation is discretized with the first-order upwind scheme. The first-order implicit scheme is

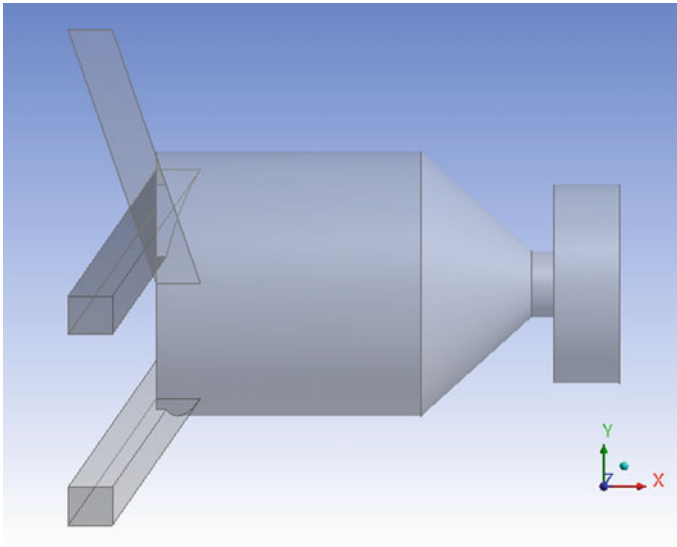


Fig. 25.6 Fluid flow model, 3D

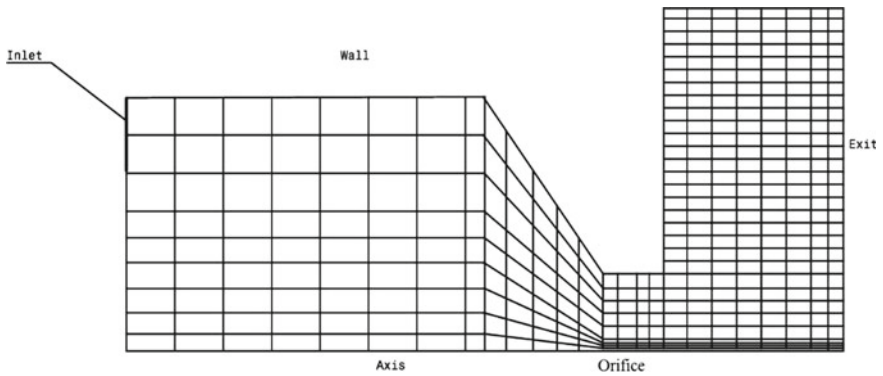


Fig. 25.7 Representative 2D axisymmetric model

Table 25.3 Thermophysical properties of Jet A

Fuel flow rate	0.0069 kg/s
Fuel inlet direction vector	$0.18 j - 0.98 k$
Density	800 kg/m^3
Upstream pressure	3.0, 4.0, 5.0 MPa
Downstream pressure	100 kPa
Surface tension	0.026 N/m
Dynamic viscosity	0.0067 kg/m-s
Fuel temperature	300 K

Table 25.4 Details of mesh independency study

Case	Minimum edge size (μm)	Mesh count (M)	Spray cone ($^\circ$)
Case 1	2.0	0.065	60
Case 2	1.6	0.100	60
Case 3	1.5	0.125	60

applied for discretizing transient formulation. All the flow field variables and volume fraction in the problem domain are transiently solved using pressure-based and coupled solver scheme. The time step of $1.0 \mu\text{s}$ is maintained throughout the transient solution procedure. The solution process is repeated for three upstream pressures 3.0, 4.0, and 5.0 MPa. The mesh independence study is performed on consecutively refined meshes. The details are presented in Table 25.4.

There are no appreciable improvements when the control volume is refined with finer meshes. Hence, the results obtained from Case 1 alone are considered for further discussion.

25.7 Testing of Atomizer

The atomizer after assembly is tested in a laboratory-scale atmospheric test facility using aviation jet fuel. The test setup has a fuel tank mounted on wheels with a pump fixed over it. The tank mounted fuel pump circulates the fuel to the test chamber. A pressure regulator is provided to adjust the supply pressure, according to the test requirements. A flow controller controls the flow rate. The drain line takes the fuel from the test chamber to the fuel storage tank through a suitable filtering mechanism. The fuel is collected in a measuring jar, and the flow rate is maintained as per the test requirements. A temperature indicator indicates the temperature of inlet fuel. The measuring jars are used to maintain the design fuel flow rate. The schematic diagram of the stand-alone atomizer test facility and the test stand are shown in Figs. 25.8 and 25.9. Table 25.5 shows the test parameters.

The fuel supply system is a centralized facility which can be used for many other requirements. The atomizer test facility is as a stand-alone unit. The test chamber can be separated from the fuel supply system. The atomizer is fitted in the downward direction. The facility can be used to test a single atomizer or a set of 16 atomizers simultaneously, and the fuel supply can be adjusted according to the requirement.

25.8 Results and Discussion

The prediction of flow field variables and spray cone structures under 3.0, 4.0, and 5.0 MPa injection pressures are studied. There are no appreciable differences in the results. Though the results show regular increasing trends in velocity fields for

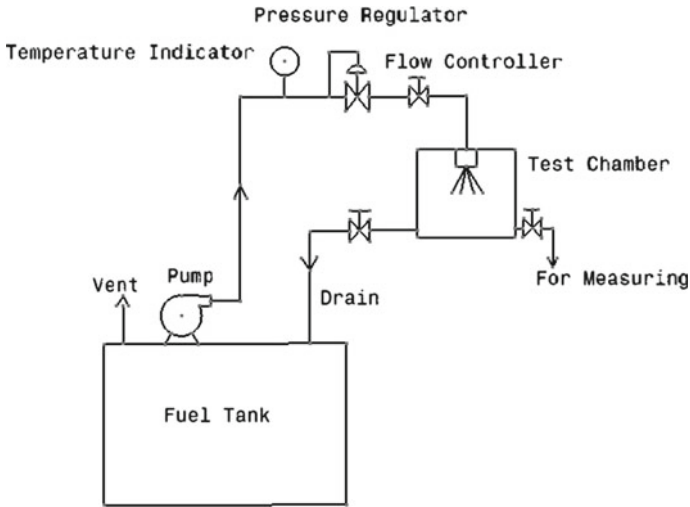


Fig. 25.8 Schematic diagram of a stand-alone atomizer test facility

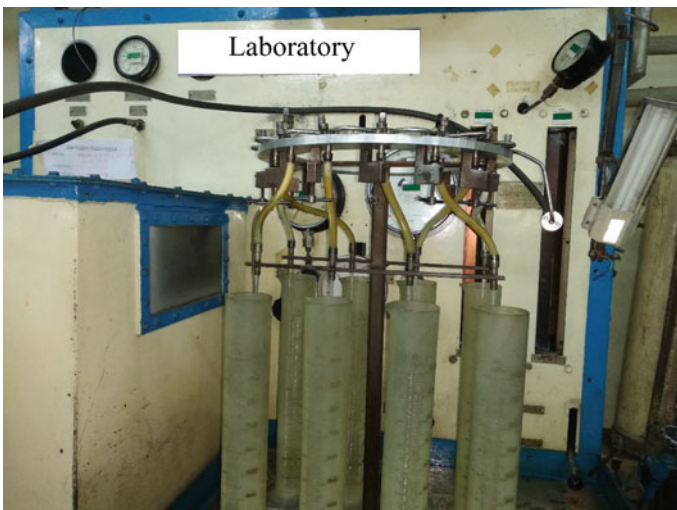


Fig. 25.9 Atomizer test stand

increasing injection pressures, the spray patterns remain nearly the same for all injection pressures. Three locations are chosen to study the velocity profiles, viz. 1.0 and 2.0 mm from the fuel inlet, and both fall inside the swirl chamber. The third location 4.0 mm from the fuel inlet falls just outside the orifice. Figures 25.10, 25.11, and 25.12 show the instantaneous axial, radial, and swirl velocity profiles along the swirl chamber and at the near exit of the orifice. There is no much variation in axial and radial velocity inside the swirl chamber. At the near exit of the orifice, there

Table 25.5 Atomizer test parameters

Fuel	Jet A
Flow rate	0.0069 kg/s
Upstream pressure	3.0, 4.0, 5.0 MPa

is a strong gradient in swirl velocity observed. The axial distance has no impact on swirl velocity inside the swirl chamber [16]. The swirl velocity at the orifice exit is zero approximately at 2/3rd height from the atomizer axis. This confirms the disintegration of the liquid sheet just after leaving the orifice.

The stream function plot, Fig. 25.13, confirms there is no mass flow in the air core region and inside the hollow cone spray. The plot also indicates that the region just at the beginning of nozzle converging zone experiences zero mass flow. The wrinkles at the beginning of the air core are clearly captured as reported by Sumer et al. [17]. The stream function plot also confirms that the flow inside the swirl chamber is highly stratified. The formation of Rankine vortex is confirmed from streamlines plot shown in Fig. 25.14.

The contour plot showing volume fraction of fuel confirms the formation of hollow cone spray measuring approximately 60°. as per the design, Fig. 25.15. The air core does not exhibit uniform size and is unstable in the beginning. It is minimum at the beginning and gradually increases to 0.4 mm at the end of the orifice. The spray sheet thickness is approximately measuring 0.10 mm.

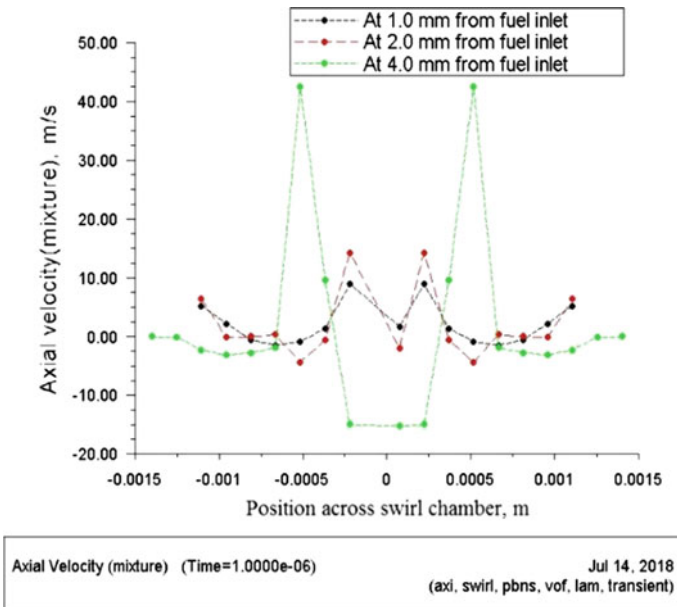


Fig. 25.10 Axial velocity, 3.0 MPa upstream pressure

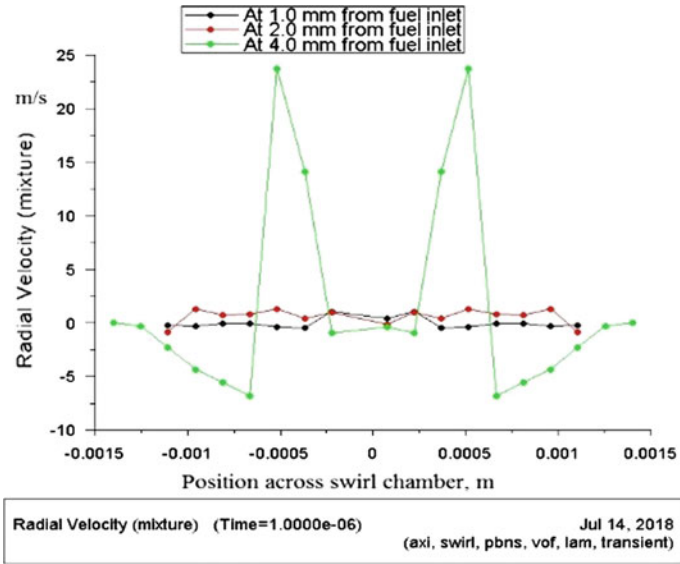


Fig. 25.11 Radial velocity, 4.0 MPa upstream pressure

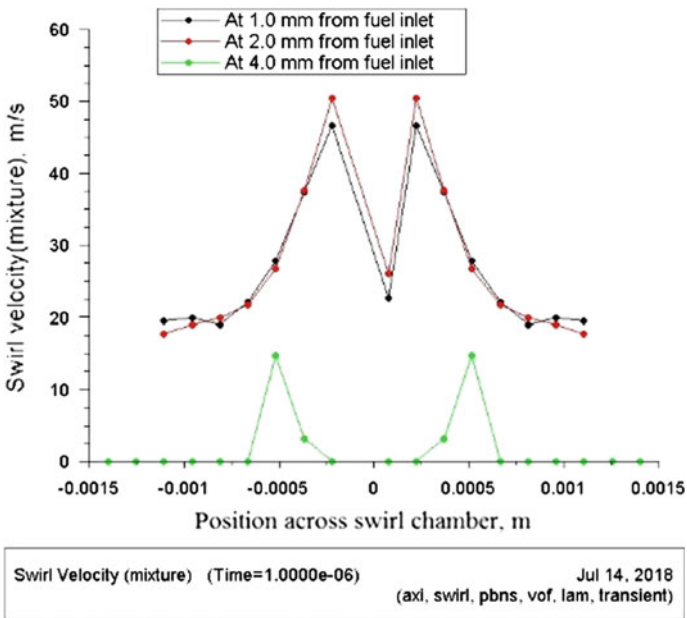


Fig. 25.12 Swirl velocity, 5.0 MPa upstream pressure

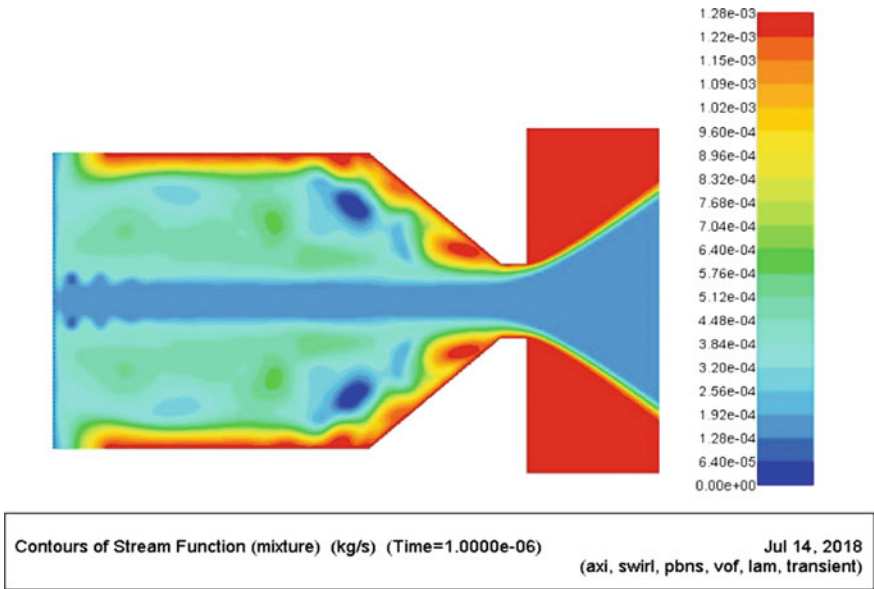


Fig. 25.13 Stream function showing air core at the center

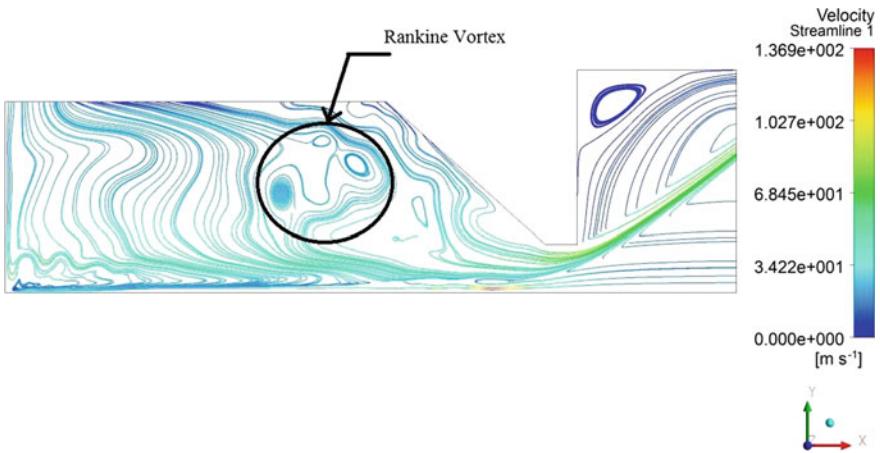


Fig. 25.14 Streamlines

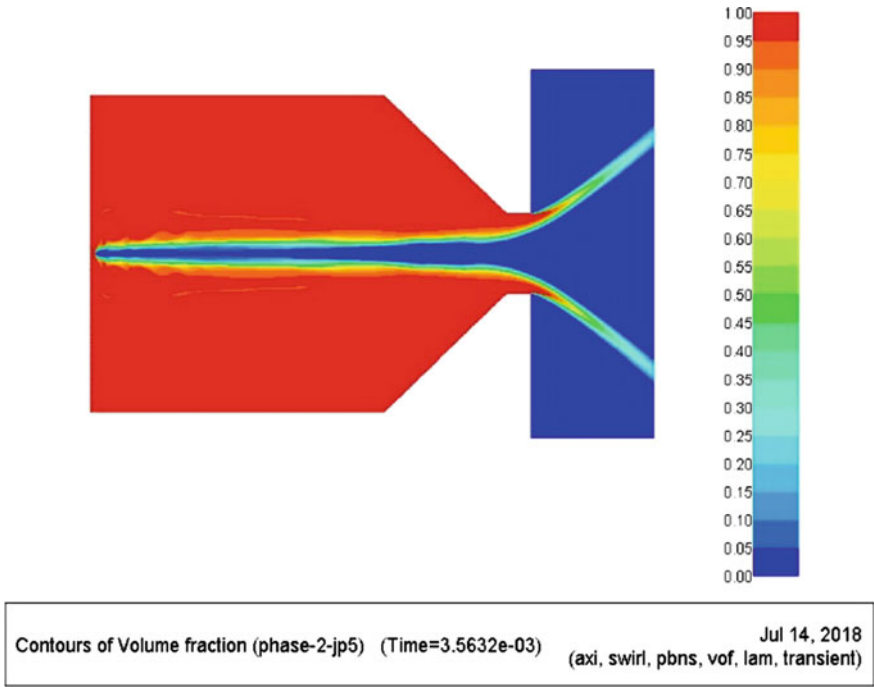
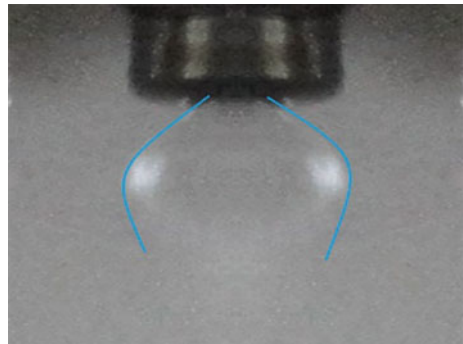


Fig. 25.15 Hollow cone spray

Fig. 25.16 Hollow cone spray at low pressure

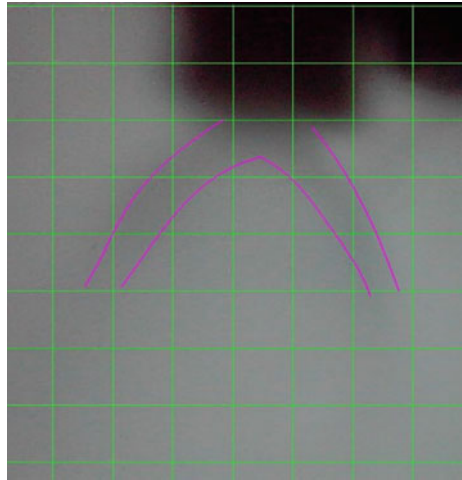


During testing of atomizer performance, at a low injection pressure, onion-shaped spray is observed. With the gradual increase in pressure, the onion-shaped spray transforms into a full-fledged stable hollow cone spray, Figs. 25.16 and 25.17. The spray cone angle is measured by capturing the image of the spray by a high-speed digital single-lens reflex camera (DSLR) with a 50.00-mm f1.8 lens. The spray structures observed during experimentation are similar to those reported by Moon et al. [18].

Fig. 25.17 Stable atomization at high pressure



Fig. 25.18 Jet penetration



The jet penetration is not clearly visible due to the presence of fuel mist inside the test chamber. The jet sheet is visible approximately about 3.0–4.0 mm as measured from a shadowgraph, Fig. 25.18. The jet breakup is almost similar to the one reported by Garai et al. [19].

25.9 Conclusion

The pressure swirl atomizer is designed for the intended application. An attempt is made to manufacture the atomizer by 3D printing using fused deposition modeling. The method failed to print the smallest geometrical feature like tangential fuel inlet port of swirl pin. The atomizer housing is also manufactured by 3D printing. However, the surface quality is not good enough, even after sufficient post-print cleaning. The 3D printed swirl pin and housing are not taken up for further functional testing.

Hence, the atomizer is manufactured by wire cut electrical discharge machining. The atomizer internal flow is modeled by solving unsteady Navier–Stokes equations over the 2D axisymmetric model. The air–fuel interface is tracked by solving the continuity equation for fuel volume fraction using the volume of fluid model of a commercial computational fluid dynamics code. The model is able to predict the flow field variables with reasonable accuracy. Also, the model is able to capture the air core formation and hollow cone spray structures. The atomizer is tested with Jet A fuel. The spray cone structure is compared to numerical prediction and to the published literature. The numerically predicted velocity fields are compared to previously published research work. No appreciable contradiction is noticed. The direct metal laser sintering is fast catching-up as the most preferred 3D printing choice in aerospace applications because of its ability to build the part by layer as thin as 20 μm using metal powders. This makes the process more suitable not only for manufacturing prototypes, but also functional parts. However, certain limitations like thermal distortion, porosity, surface roughness, and cost of DMLS printed parts need to be addressed thoroughly.

Acknowledgements The support for this work by laboratory technicians is thankfully acknowledged. Sincere thanks are also due to Ms. M. Ramalakshmi for her expert typing.

References

1. Lefebvre, A.H., Ballal, D.R.: Gas Turbine Combustion Alternative Fuels and Emissions. CRC Press, Boca Raton, FL (2013)
2. Winterfeld, G., Eickhoff, H.E., Depooter, K.: Combustion system design. In: Mellor, A.M. (ed.) Design of Modern Turbine Combustor. Academic Press, London (1990)
3. Hansen, K.G., Madsen, J., Trinh, C.M., Ibsen, C.H., Solberg, T., Hjertager, B.H.: A computational and experimental study of the internal flow in a scaled pressure-swirl atomizer. In: ILASS-Europe 2002 (2002)
4. Rezaeimoghaddam, M., Elahi, R., Razavi, M.R.M., Ayani, M.B.: Modeling of non-newtonian fluid flow within simplex atomizers. In: Proceedings of the ASME 2010 10th Biennial Conference on Engineering Systems Design and Analysis ESDA2010, Turkey, 2010
5. Ma, Z.: Investigation on the internal flow characteristics of pressure-swirl atomizer. Ph.D. Thesis, University of Cincinnati, Department of Aerospace Engineering and Engineering Mechanics of the College of Engineering (2001)
6. Marchione, T., Allouis, C., Amoresano, A., Beretta, F.: Experimental investigation of a pressure swirl atomizer spray. *J. Propuls. Power* **23**(5) (2007)
7. Fu, Q.: Numerical simulation of the internal flow of swirl atomizer under ambient pressure. *J. Mech. Eng. Sci.* **0**(0) (2015)
8. Mkvik, M., Smolar, M., Olsiak, R.: Numerical investigation of the twin-fluid atomizers internal flows. In: AIP Conference Proceedings 1768, 2016
9. Qian, W., Hui, X., Zhang, C., Xu, Q., Lin, Y.: A numerical study of the internal flow in a pressure swirl atomizer. In: Proceedings of ASME Turbo Expo 2017: Turbomachinery Technical Conference and Exposition GT2017, USA, 2017
10. Cui, J., Lai, H., Li, J., Ma, Y.: Visualization of internal flow and the effect of orifice geometry on the characteristics of spray and flow field in pressure-swirl atomizers. *Appl. Therm. Eng.* <http://dx.doi.org/10.1016/j.applthermaleng.2017.08.103>

11. Versteeg, H.K., Malalasekera, W.: An Introduction to Computational Fluid Dynamics the Finite Volume Method, Pearson, India (2007)
12. Radcliffe, A.: The performance of a type of swirl atomizer. *Proc. Inst. Mech. Eng.* **69**(1) (1995)
13. <https://www.3dhubs.com/knowledge-base/aerospace-3d-printing-applications>. Accessed 28 Aug 2018
14. <https://www.theengineer.co.uk/issues/june-2015-digi-issue/rolls-royce-breaks-additive-record-with-printed-trent-xwb-bearing>. Accessed 17 June 2018
15. <http://www.arcam.com/technology/electron-beam-melting>. Accessed 16 June 2018
16. Maly, M., Sapik, M., Jedelsky, J., Janackova, L., Jicha, M., Slama, J., Wigley, G.: Internal flow characteristics in scaled pressure-swirl atomizer. In: EPJ Web of Conference 180, 2018
17. Sumer, B., Erkan, N., Uzol, O., Tuncer, I.H.: Experimental and numerical investigation of a pressure swirl atomizer. In: 12th Triennial International Conference on Liquid Atomization and Spray Systems, Germany, 2012
18. Moon, S., Abo-Serie, E., Bae, C.: Air flow and pressure inside a pressure-swirl spray and their effects on spray development, *Exp. Therm. Fluid Sci.* **33**(2) (2009)
19. Garai, A., Pal, S., Mondal, S., Ghosh, S., Sen, S., Mukhopadhyay.: A Experimental investigation of spray characteristics of kerosene and ethanol-blended kerosene using a gas turbine hybrid atomizer. *Sadhana* **42**(4) (2017)